

**Development and Application of Genetically-Encoded
Sensors to Study the Role of Zinc in Biology**

by

Jungwon Genevieve Park

B.S., Massachusetts Institute of Technology, 2005

A thesis submitted to the
Faculty of the Graduate School of the
University of Colorado in partial fulfillment
of the requirements for the degree of
Doctor of Philosophy
College of Arts & Sciences Department of Chemistry & Biochemistry

2014

This thesis entitled:
Development and Application of Genetically-Encoded Sensors to Study the Role of Zinc in Biology
written by Jungwon Genevieve Park
has been approved for the College of Arts & Sciences Department of Chemistry & Biochemistry

Amy E. Palmer

Hang Hubert Yin

Date _____

The final copy of this thesis has been examined by the signatories, and we find that both the content and the form meet acceptable presentation standards of scholarly work in the above mentioned discipline.

Park, Jungwon Genevieve (Ph.D., Biochemistry)

Development and Application of Genetically-Encoded Sensors to Study the Role of Zinc in Biology

Thesis directed by Prof. Amy E. Palmer

Zinc is a micronutrient that is required for cellular growth, proliferation, and differentiation. Dozens of zinc transporters and zinc-buffering proteins regulate the intracellular concentration of zinc, and dysregulation of zinc homeostasis is implicated in the pathogenesis of several human diseases, including diabetes, cancer, and neurodegeneration. Even though zinc is important for many critical cellular processes, it is still unclear whether and how cells redistribute zinc in response to stimuli, and how changes in zinc affect signaling pathways. Our laboratory has developed several genetically-encoded, ratiometric, fluorescent sensors of zinc that can quantitatively report zinc concentrations in different organelles of individual living cells. In this work, I optimized and characterized genetically-encoded zinc sensors for two major applications: the estimation of mitochondrial zinc in multiple cell types and quantitative imaging of cytosolic zinc in insulin-secreting cells. I found that zinc is buffered in the mitochondrial matrix at sub-picomolar concentrations, which can vary significantly among different cell types. I also made the observation that zinc can modulate calcium signaling in glucose-stimulated insulin-secreting cells. In addition, I present a set of protocols for optimizing the use of genetically-encoded sensors in quantitative imaging, refined throughout the progress of experiments that generated the results of this thesis work. The development and application of new genetically-encoded zinc sensors enabled us to make novel observations that improve our understanding of the role of zinc in biology.

Dedication

To my family, friends, and colleagues.

Acknowledgements

I would like to acknowledge my parents, Young Chul and Elizabeth Park, for always supporting and encouraging me to do my best and pursue lofty goals.

I am also thankful for my friends, near and far, who encouraged me to find time to experience life outside of the lab, and who convinced me to keep going and not give up.

My colleagues have challenged and helped me throughout my time in graduate school. I especially want to thank all of the members of the Palmer lab and the students in the Biochemistry Graduate Program and in the Medical Scientist Training Program.

Last but not least, I thank my advisor, Dr. Amy Palmer, for her guidance, patience, and encouragement.

Contents

Chapter	
1	Introduction 1
1.1	The Biological Role of Zinc 1
1.2	Zinc Homeostasis in Mammalian Cells 2
1.2.1	Total Intracellular Zinc 3
1.2.2	Zinc-Containing Vesicles 3
1.2.3	Molecular Functions of Tightly-Bound Zinc 5
1.2.4	Labile Intracellular Zinc 7
1.2.5	Transporters and Regulators of Zinc Homeostasis 12
1.2.6	Tools for Studying Zinc in Biological Systems 16
1.3	An Overview of Genetically-Encoded Sensors of Calcium and Zinc 17
1.3.1	Sensor Design 18
1.3.2	The Binding Properties and Dynamic Range of a Sensor 19
1.3.3	Guidelines for Choosing a Sensor 23
1.3.4	Multiplexed Imaging with Additional Fluorescent Probes 24
1.4	Thesis Overview 28
2	Analytical Methods 30
2.1	Abstract 30
2.2	Introduction 30

2.3	Optimizing the Use of Genetically-Encoded FRET Sensors for Quantitative Measurements	31
2.3.1	Sample Preparation	32
2.3.2	Microscopy Systems for Imaging FRET Sensors	35
2.3.3	Optimization of Image Acquisition	38
2.3.4	Calibration of FRET Sensors in Cells	40
2.3.5	Estimation of Ion Concentrations	46
2.4	Titration of FRET Sensors in Living Cells	51
2.4.1	Experimental Protocol for <i>in situ</i> Titrations	51
2.4.2	Analysis of <i>in situ</i> Titration Data	52
2.5	Techniques for Image Analysis Automation	55
2.5.1	Image Collection	58
2.5.2	Image Registration	60
2.5.3	Image Segmentation	62
2.5.4	Automation of FRET Ratio Calculations	66
2.5.5	Creation of Images and Movies Pseudocolored by FRET Ratio	67
2.6	Summary	70
3	New Sensors for Quantitative Measurement of Mitochondrial Zinc	71
3.1	Abstract	71
3.2	Publication Status	71
3.3	Introduction	72
3.4	Results and Discussion	73
3.4.1	Sensor Design and Validation	73
3.4.2	Comparison of Mitochondrial to Cytosolic Zinc	82
3.4.3	Comparison of Mitochondrial Zinc in Different Cell Types	86
3.5	Methods	89

3.5.1	Sensor Construction	89
3.5.2	Cell Culture	89
3.5.3	Imaging	92
3.5.4	Mito-ZapCY1 Titrations	93
3.5.5	Statistical Analysis	93
3.5.6	Data Analysis	94
4	The Role of Zinc in Calcium Signaling in Insulin Secreting Cells	97
4.1	Abstract	97
4.2	Introduction	97
4.3	Results and Discussion	100
4.4	Methods	106
4.4.1	Cell Culture	106
4.4.2	Imaging	107
4.4.3	Data Analysis	108
5	Concluding Remarks and Future Directions	109
5.1	Conclusions	109
5.2	Future Directions	110
5.2.1	Further Characterization of Mitochondrial Zinc Homeostasis	110
5.2.2	Investigation of Zinc Homeostasis During Cell Division	112
	Bibliography	113
	Appendix	
A	Purification of a Cytosolic Zinc Sensor Using an Intein Purification System	127
A.1	Introduction	127

A.2	Cloning Strategy	128
A.3	Purification of NES-ZapCV2	131
A.3.1	Overview of <i>in vitro</i> Titrations	131
A.4	Titration of NES-ZapCV2 <i>in vitro</i>	132
A.4.1	Preparation of Metal-Chelate Buffered Solutions	134
A.4.2	Titration of NES-ZapCV2 Using a Microplate Reader	136
B	Image Analysis Protocols	140
B.1	Selection of Regions of Interest with FIJI	141
B.2	Automated Analysis of Manually-Selected ROIs in MATLAB	145
B.3	Standardized Ratio vs. Time Plots	147
B.4	Automated Registration of YFP FRET and CFP images	150
B.5	Optimization of Image Segmentation	151
B.6	Automation of ROI Selection in an Image Where Cells are of Different Intensities	153
B.6.1	Select cells using ImageJ	153
B.6.2	Run MATLAB script	154
B.7	Calculation of the Mean Intensity of an ROI Using a Binary Mask	156
B.8	Creating Ratiometric Images for Movies	157
B.9	Example MATLAB Script for ROI Selection, FRET Ratio Calculation, and Ratiometric Image Creation	158
B.10	Generating Ratio vs. Time Plots for a Movie	161
B.11	Techniques for Finishing Movies in ImageJ	164
C	Miscellaneous Protocols	168
C.1	Making Imaging Dishes	168
C.2	Widefield Microscopes Used in This Study	169
C.3	Creating Stable Cell Lines With the PiggyBac System	170
C.3.1	Introduction	170

C.3.2	PiggyBac Transposon Cloning	171
C.3.3	Co-transfection of PB plasmids	171
C.3.4	Selection with blasticidin	171
C.3.5	Example: HeLa NES-ZapCV2 cell line	172
C.4	Imaging Buffer Recipes	176
C.4.1	Chelex-treated ultrapure H ₂ O	176
C.4.2	Hank's Balanced Salt Solution (HBSS), Life Technologies Formulation	176
C.4.3	HEPES-buffered HBSS (HHBSS), pH 7.4	177
C.4.4	HHBSS without Ca ²⁺ , pH 7.4	178
C.4.5	HHBSS without phosphate	179
C.4.6	Krebs-Ringer Buffer with HEPES, pH 7.4	179
C.4.7	Alternative buffer for MIN6 Imaging, pH 7.4	180
C.4.8	Preincubation buffer for MIN6 cells, pH 7.4	180

Tables

Table

1.1	Estimates of total intracellular Zn^{2+} concentration	4
1.2	Estimates of Free Zn^{2+} Concentration	9
1.3	Estimates of Free Zn^{2+} Concentration, continued	10
1.4	Dissociation constants of cellular molecules for Zn^{2+}	11
1.5	Selected Ca^{2+} biosensors	25
1.6	Selected Zn^{2+} biosensors	26
1.7	Sensors targeted to subcellular locations	26
2.1	Optimized perturbations for cytosolic Ca^{2+} and Zn^{2+} calibrations	41
2.2	Reagents used to calibrate Ca^{2+} and Zn^{2+} sensors	47
2.3	Reagents used to titrate Ca^{2+} and Zn^{2+} sensors <i>in situ</i>	53
3.1	Characteristics of all mitochondrial Zn^{2+} sensors tested	77
3.2	Amino acid sequences of different Zn^{2+} binding domains	91
3.3	cpVenus PCR primers	91
3.4	mito-ZapCY1 measurements in different cells in one imaging experiment	96
3.5	mito-ZapCY1 measurements of ROIs within a cell	96
A.1	pH and temperature dependence of Ca^{2+} buffers	135
A.2	pH and temperature dependence of Zn^{2+} buffers	135
A.3	Metal-chelate buffers for sub- μ M Ca^{2+} and Zn^{2+} solutions	135

A.4	Metal-chelate buffers for a Zn^{2+} sensor titration	138
C.1	Widefield microscope components	170
C.2	Typical acquisition parameters for CFP/YFP FRET sensor imaging	170

Figures

Figure

1.1	Functional annotation of the human Zn^{2+} proteome	5
1.2	Structures of Zn^{2+} -binding proteins	6
1.3	Zn^{2+} concentrations compared to other cellular concentrations	8
1.4	Mammalian Zn^{2+} transporters from the ZnT and ZIP families	14
1.5	Basic design of a genetically-encoded FRET sensor	19
1.6	Binding properties and dynamic range of a FRET sensor	21
1.7	The effect of the empirical Hill coefficient on sensor measurements	22
1.8	The fractional saturation of commonly-used Ca^{2+} sensors	27
2.1	Overview of the sensor calibration optimization	33
2.2	Genetically-encoded sensors targeted to different organelles	36
2.3	Sensor mislocalization affects its response	37
2.4	FRET sensor dynamic range using different microscopes	39
2.5	Analysis of FRET sensor calibrations	44
2.6	Heterogeneity in sensor calibrations	45
2.7	Evaluating the effects of sensor concentration on FRET ratios	50
2.8	Image analysis of <i>in situ</i> titration data	54
2.9	Examples of <i>in situ</i> titration experimental results	54
2.10	One- and two-site binding models fit to titration data	56

2.11	Comparison of <i>in situ</i> and <i>in vitro</i> titrations	57
2.12	Workflow for automated image analysis	59
2.13	Edge effects due to image misalignment	61
2.14	Overlay of FRET and CFP images before and after registration	62
2.15	Top-hat filtering of mitochondrial and cytosolic sensor images	64
2.16	Comparison of global and adaptive thresholding	65
2.17	Single-cell segmentation method	65
2.18	Standardized plot of R over time	66
2.19	Ratiometric image of HeLa cells expressing mito-ZapCY1	68
2.20	Movie of ratiometric images and corresponding R vs. time plots	69
3.1	Design of genetically-encoded mitochondrial Zn^{2+} sensors	74
3.2	mito-ZapCY1 sensor calibration	75
3.3	Comparison of mito-ZifCY1 to mito-ZapCY1	76
3.4	Co-localization of mito-ZapCY1 with MitoTracker Red	78
3.5	Circular permutation of mito-ZifCY1 sensors	80
3.6	Calibrations of mito-ZifCY1 and mito-ZifCV1 variants	81
3.7	mito-ZapCY1 <i>in situ</i> titrations	82
3.8	ZapCY1 <i>in vitro</i> titrations	83
3.9	Fractional saturation of cytosolic and mitochondrial Zn^{2+} sensors	84
3.10	Pyrrithione treatment of different cell types	85
3.11	Comparison of mitochondrial Zn^{2+} in different cell types	87
3.12	Fractional saturation of mito-ZapCY1 at different sensor concentrations	88
3.13	Effects of changes in pH and redox state	90
3.14	Selection of ROIs	95
4.1	Genetically-encoded Zn^{2+} and Ca^{2+} sensors	101
4.2	Glucose induces heterogeneous Ca^{2+} oscillations in MIN6 cells	102

4.3	Zn ²⁺ decreases Ca ²⁺ oscillation frequency in MIN6 cells	104
4.4	Cytosolic Zn ²⁺ increases upon addition of glucose and Zn ²⁺	105
A.1	Comparison of two protein purification strategies	129
A.2	pTXB1-NES-ZapCV2 cloning strategy	130
A.3	Absorbance of purified NES-ZapCV2	131
A.4	Binding curves under conditions where the sensor concentration is much greater than the K_D'	133
A.5	Titration of NES-ZapCV2 <i>in vitro</i>	138
C.1	Widefield microscopes used in this thesis	169

Chapter 1

Introduction

1.1 The Biological Role of Zinc

For over 50 years, physicians have recognized the importance of zinc in human health and disease. In fact, numerous clinical studies have provided evidence that zinc supplementation is effective in decreasing the duration and severity of diarrhea and pneumonia, reducing stunting, and lowering mortality of infants and children in developing countries [1–3]. In addition, randomized, controlled studies of children in Denver in the 1970s and 1980s revealed that mild to moderate, growth-limiting, zinc deficiency is even prevalent in developed countries, and that supplementation improves growth, immune function, cognition, and behavior [2, 4]. The elderly population can also benefit from zinc supplementation, which has been shown to decrease inflammation and improve immune function [5, 6]. Acrodermatitis enteropathica is a heritable disease of severe zinc deficiency caused by mutations in a human zinc transporter gene, *hZIP4*, and it is associated with diarrhea, higher susceptibility to infections, and death during infancy and early childhood. Zinc supplementation alone rapidly resolves symptoms of this disease [2, 7]. Recently, mutations in another zinc transporter gene, *ZnT8*, have been associated with a lower risk of type 2 diabetes mellitus [8]. Other human diseases, including including Alzheimer’s disease and other forms of neurodegeneration, diabetes, and cancer, are also associated with changes in zinc homeostasis [9–11]. Thus, there is a vital need for zinc and a deeper understanding of its specific role in disease.

Studies with model organisms have led to some surprising discoveries of how zinc homeostasis affects physiology. One such example is the story of the “lethal milk” mouse, which was first discov-

ered and characterized at the Jackson Laboratories during the 1960s. Adult mice homozygous for the mutation appeared normal [12], but when such a mouse nursed pups of any genotype, the pups were stunted, had dermatitis, and died before weaning. It was found that “lethal milk” contains less zinc than normal milk (8 $\mu\text{g}/\text{mL}$ and 12 $\mu\text{g}/\text{mL}$, respectively), and that zinc supplementation rescues the normal phenotype [13]. The mutation was later mapped to *ZnT4*, which encodes a Zn^{2+} transporter highly expressed in the mammary glands [14]. Interestingly, mutations in human *ZnT2* are associated with a reduction of zinc in milk, and infants fed exclusively with this milk are zinc deficient [15].

Genetic studies in other model organisms have also revealed unexpected roles of Zn^{2+} in signaling cascades. Forward genetic screens, designed to identify *Caenorhabditis elegans* mutants that suppress constitutively active EGF signaling, resulted in the identification and characterization of *cdf-1* and *sur-7* mutants and a role for Zn^{2+} in cell signaling [16, 17]. Loss of function of Cdf-1 or Sur-7, both of which are transmembrane proteins capable of transporting Zn^{2+} , caused zinc hypersensitivity and inhibited Ras signaling. It became clear that Zn^{2+} homeostasis played an important role in EGF signaling and was regulated by multiple, tissue-specific transporters in *C. elegans*. During the past decade, many different Zn^{2+} transporters have been knocked out in mice, and these studies have revealed that zinc homeostasis is controlled by a complex network of multiple transporters and buffers, and that the consequences of Zn^{2+} dysregulation can be dire and are poorly understood [18, 19].

1.2 Zinc Homeostasis in Mammalian Cells

Given the importance of Zn^{2+} in the function of living cells, it is not surprising that mammalian cells control their Zn^{2+} uptake, efflux, storage, and distribution with an impressive number of membrane transporters and Zn^{2+} -binding proteins. At least two dozen Zn^{2+} transporters and a dozen isoforms of metallothionein, a major metal-binding protein, are expressed in a cell- and tissue-specific manner [18–20]. There are many examples of cells altering the expression or localization of Zn^{2+} -regulating proteins during differentiation, proliferation, or in response to different

signaling molecules [10,21–24]. This section presents an overview of intracellular Zn^{2+} homeostasis and the transporters and regulators that maintain it.

1.2.1 Total Intracellular Zinc

Total Zn^{2+} ($[\text{Zn}^{2+}]_{total}$) includes the labile pools of exchangeable, or *free* Zn^{2+} ($[\text{Zn}^{2+}]_{free}$) in cells as well as the Zn^{2+} that is tightly bound by macromolecules. The vast majority of intracellular Zn^{2+} is bound by protein and serves essential structural and catalytic roles (see Section 1.2.3). $[\text{Zn}^{2+}]_{total}$ is consistently about 10 to 100 times more concentrated inside cells than in the extracellular environment. In mammalian cells this is estimated to be about 100-300 μM (see Table 1.1). In comparison, $[\text{Zn}^{2+}]_{total}$ in serum is estimated to be about 1-15 μM [25–29]. Some specialized mammalian cells, such as glutaminergic neurons, pancreatic β -cells, prostatic epithelial cells, and lactating mammary epithelial cells, are known to concentrate a much higher $[\text{Zn}^{2+}]_{total}$, and this supplemental Zn^{2+} is likely to be stored in vesicles (see Section 1.2.2 and [30]). Even so, all cells require a substantial amount of Zn^{2+} for basic physiological functions, which supports the observation that intracellular $[\text{Zn}^{2+}]_{total}$ is typically 100 μM or greater.

1.2.2 Zinc-Containing Vesicles

Most cells stained with fluorescent, small-molecule Zn^{2+} dyes, such as FluoZin-3, have a punctate pattern of fluorescence, these puncta being vesicles containing high concentrations of Zn^{2+} [37,38]. Some cell types store a significant amount of Zn^{2+} in vesicles, including pancreatic β cells, which package Zn^{2+} with insulin in secretory granules, and hippocampal and cortical neurons, which package 5-15% of their intracellular Zn^{2+} with glutamate in synaptic vesicles [39]. Computational modeling of Zn^{2+} homeostasis also supports the existence of membrane-bound Zn^{2+} storage compartments, in addition to Zn^{2+} -binding molecules, that maintain Zn^{2+} homeostasis [40,41]. The Zn^{2+} -containing vesicles are not well characterized, but they represent another pool of Zn^{2+} in mammalian cells.

Table 1.1: Estimates of total intracellular $[\text{Zn}^{2+}]$ in different cell types. Methods of measuring $[\text{Zn}^{2+}]_{total}$ —inductively coupled plasma mass spectrometry (ICP-MS) and atomic absorption spectroscopy (AAS)—are presented in Section 1.2.6. When $[\text{Zn}^{2+}]_{total}$ was reported as ng/mg protein, it was converted to μM under the assumption that the intracellular protein concentration is ~ 100 mg/mL [31].

Cell type	$[\text{Zn}^{2+}]_{total}$ (μM)	Method	Ref
Human erythrocytes (primary cells)	150	AAS	[25]
<i>E. coli</i>	200	ICP-MS	[32]
HT-29 (human colorectal adenocarcinoma line)	264	AAS	[33]
Murine cortical neurons (primary cells)	445	ICP-MS	[34]
Isolated mitochondria from rat liver	500	AAS	[35, 36]
Murine astrocytes (primary cells)	730	ICP-MS	[34]

1.2.3 Molecular Functions of Tightly-Bound Zinc

In mammalian cells, Zn^{2+} is a structural component of thousands of proteins and a cofactor for hundreds of enzymes. Recent analyses of currently available protein structures and sequences predict that about 3,000 human proteins—10% of the human proteome—bind Zn^{2+} [42–44]. Figure 1.1 illustrates the diversity of Zn^{2+} -binding proteins, and Figure 1.2 displays the structures of a few of these proteins. Enzymes requiring a catalytic Zn^{2+} are found in five of the six classes of enzymes: oxidoreductases, transferases, hydrolases, lyases, and isomerases [45–48]. The concentrations of some of these enzymes can be close to that of $[\text{Zn}^{2+}]_{total}$. For example, human red blood cells can contain high μM concentrations of active carbonic anhydrase II, which catalyzes the conversion of carbon dioxide to bicarbonate ion by using Zn^{2+} as a Lewis acid [25, 49].

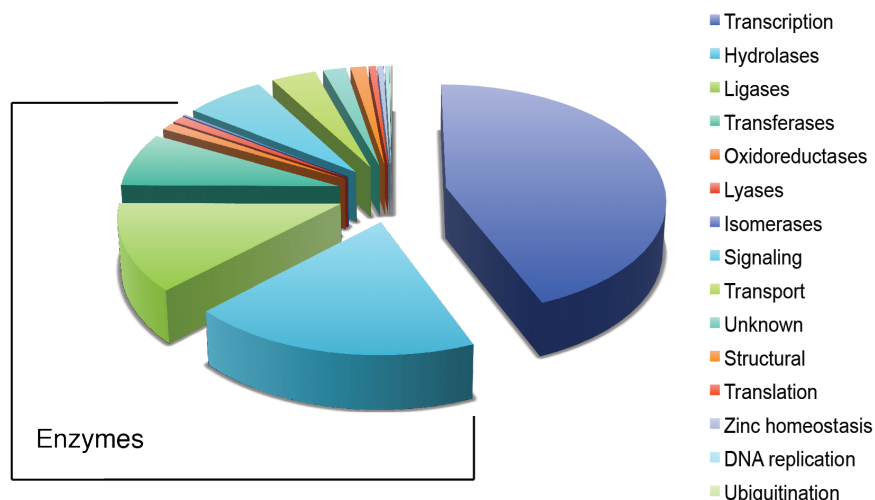


Figure 1.1: Functional annotation of the human Zn^{2+} proteome. An estimated 10% of the human proteome binds at least one Zn^{2+} ion; over 40% of these Zn^{2+} -binding proteins are transcription factors. Adapted from [42, 43].

Zinc fingers, compact protein domains consisting of only 20–40 amino acids stabilized by a Zn^{2+} ion, are ubiquitous in mammalian cells [51, 52]. Zinc fingers are necessary for sequence-specific DNA binding of many transcription factors and can also mediate protein-RNA and protein-protein interactions [53]. The Swiss-Prot database (accessed on 2014-02-17) has 793 human pro-

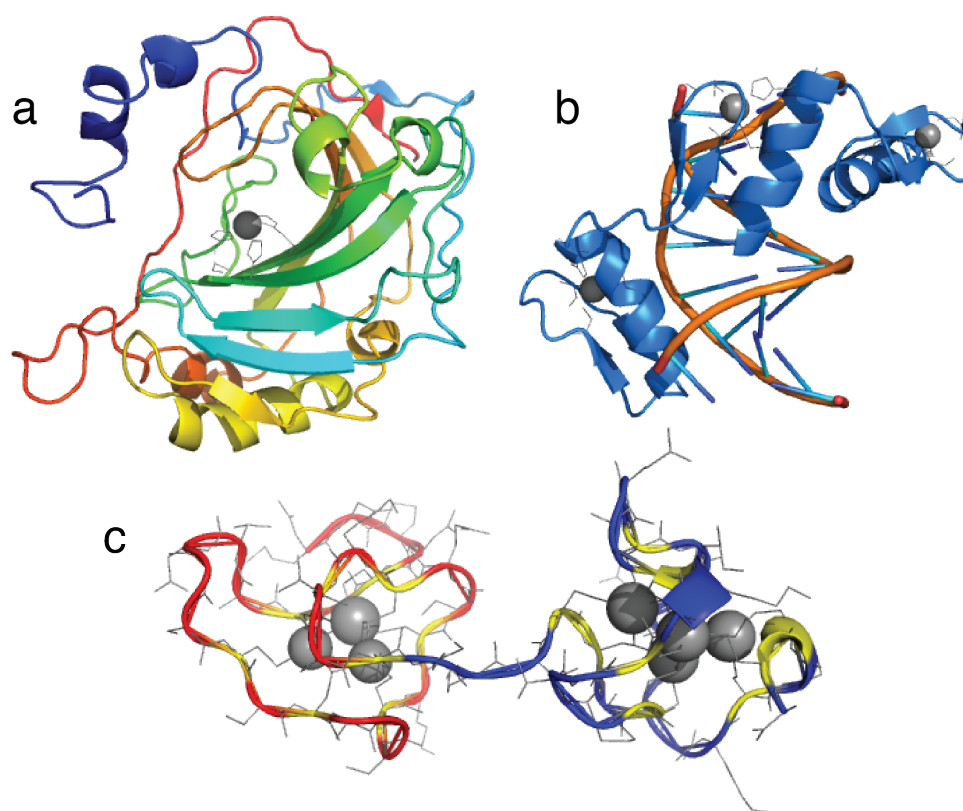


Figure 1.2: Structures of Zn^{2+} -binding proteins. a) Human carbonic anhydrase II (PDB entry 1ca2) contains a Zn^{2+} ion in its active site coordinated by three histidine residues (side chains shown in gray). b) Three C_2H_2 zinc fingers of mouse Zif268 wrap around the major groove of the DNA binding site (PDB entry 1zaa). c) Rat metallothionein 2 (PDB entry 4mt2) can bind up to 7 Zn^{2+} with different affinities spanning 4 orders of magnitude [50]. It has an alpha domain (blue) and a beta domain (red) that collectively contain 20 cysteine residues (yellow).

teins containing at least one zinc finger domain, including transcription factors, ubiquitin ligases, histone-modification enzymes, protein kinases, and many proteins of unknown function. Efforts toward identifying and annotating the Zn^{2+} -binding proteome continue to progress, but our understanding is far from complete and is biased towards already-characterized proteins [54, 55]. Mass spectrometry-based methods show promise in identifying Zn^{2+} -binding proteins in specific cell types or under different experimental conditions [34, 56–58]. In addition, Zn^{2+} binds metabolites, such as cysteine and glutathione, which are at mM concentrations in cells. By these estimates, it is reasonable to say that cells contain at least as many Zn^{2+} -binding sites as Zn^{2+} ions, and that changes in Zn^{2+} homeostasis could alter the occupancy of sites that bind Zn^{2+} less tightly.

Indeed, many studies have shown that there are many unoccupied intracellular Zn^{2+} -binding sites. A study using human colon cancer cells (HT-29) showed that the concentration of available Zn^{2+} -binding sites in resting cells is $\sim 28 \mu\text{M}$ [33]. In several different cell types, 10-50% of metallothionein, a protein that can bind 7 Zn^{2+} ions, exists in its metal-free apo form [59, 60]. Biochemical studies with purified protein have revealed that some enzymes are inhibited or activated when specific Zn^{2+} -binding sites are occupied, suggesting that Zn^{2+} occupancy may modulate protein activity [61–63]. The excess of Zn^{2+} -binding sites is important for cellular Zn^{2+} homeostasis and buffers Zn^{2+} .

1.2.4 Labile Intracellular Zinc

Intracellular Zn^{2+} -binding molecules buffer the labile pool of Zn^{2+} ($[\text{Zn}^{2+}]_{free}$) in a range corresponding to their affinities for Zn^{2+} , which is about 6 orders of magnitude lower than $[\text{Zn}^{2+}]_{total}$ (see Table 1.2). An intracellular $[\text{Zn}^{2+}]_{free}$ buffer is analogous to a pH buffer, which can maintain the pH of the solution within an order of magnitude of its pK_a . Many of the dissociation constants (K_D 's) of various intracellular proteins for Zn^{2+} , listed in Table 1.4, are in the pM to nM range, certainly capable of buffering $[\text{Zn}^{2+}]_{free}$ in the high pM range. Figure 1.3 compares both $[\text{Zn}^{2+}]_{total}$ and $[\text{Zn}^{2+}]_{free}$ to the concentrations of other important molecules.

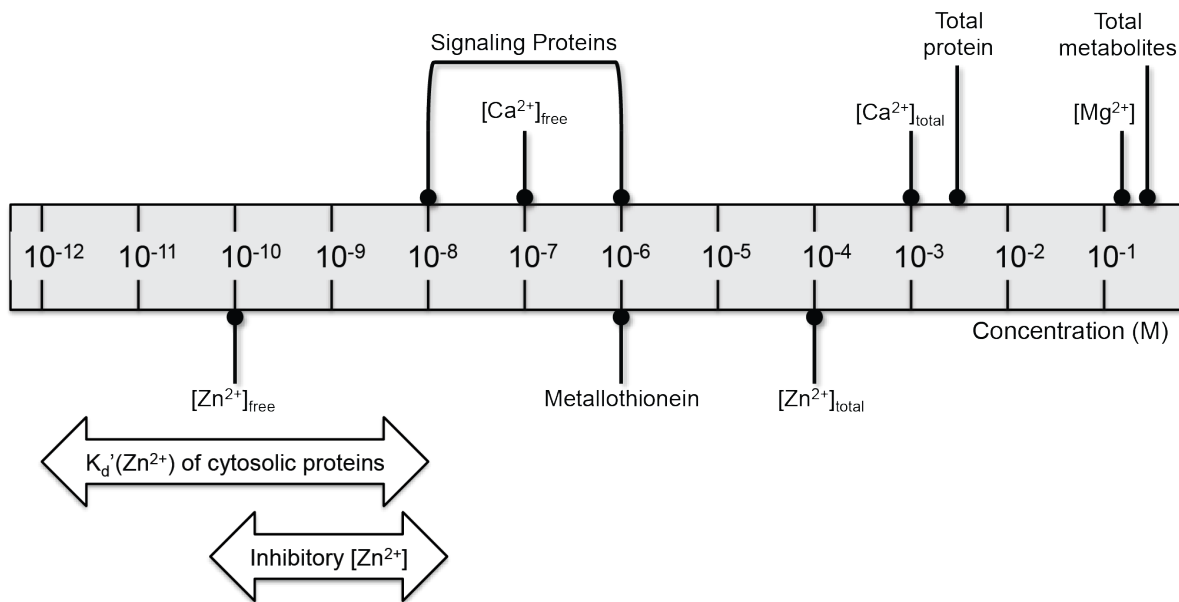


Figure 1.3: Zn^{2+} concentrations compared to other cellular concentrations. $[\text{Zn}^{2+}]_{\text{total}}$ is orders of magnitude greater than $[\text{Zn}^{2+}]_{\text{free}}$. Zn^{2+} -binding molecules have K_D 's for Zn^{2+} in the pM to nM range. Intracellular Ca^{2+} is also buffered, but its concentration is much greater than that of Zn^{2+} .

Investigators have estimated $[\text{Zn}^{2+}]_{\text{free}}$ using many different methods since 1971, when the first estimate of 100 pM in rabbit muscle was made. The membrane-permeant fluorescent Zn^{2+} sensor FluoZin-3 AM, developed in 2002, has been used in a variety of cell types to estimate $[\text{Zn}^{2+}]_{\text{free}}$ [33, 71]. However, the intracellular localization of this dye is not well-characterized, and its intracellular concentration can affect $[\text{Zn}^{2+}]_{\text{free}}$ estimation [33, 66]. In addition, the K_D ' of FluoZin-3 for Zn^{2+} is 15 nM, and so it is problematic to precisely estimate $[\text{Zn}^{2+}]_{\text{free}}$ in the pM range by measuring the fractional saturation of FluoZin-3 [37]. Genetically-encoded, ratiometric sensors, which have a wider range of K_D 's, have been used since 2006 to more precisely estimate $[\text{Zn}^{2+}]_{\text{free}}$ in a variety of cell types (see Section 1.3 and [87]). Even though there is some variation in $[\text{Zn}^{2+}]_{\text{free}}$ estimation in mammalian cells, the majority of measurements fall within 10-500 pM.

It is also clear that different organelles in the same cell can buffer $[\text{Zn}^{2+}]_{\text{free}}$ at very different concentrations. Ratiometric, genetically-encoded sensors, targeted to the endoplasmic reticulum (ER), Golgi, nucleus, and mitochondria, have been used to observe sub-pM $[\text{Zn}^{2+}]_{\text{free}}$ in these

Table 1.2: Estimates of $[\text{Zn}^{2+}]_{free}$ in different cell types and organelles. FluoZin-3, AM (Life Technologies) is a Zn^{2+} -responsive fluorescent dye that concentrates in the cytosol and vesicles of mammalian cells. Its subcellular localization is not determined [37, 64, 65].

Cell Type	Subcellular Location	$[\text{Zn}^{2+}]_{free}$ (pM)	Method	Ref
<i>E. coli</i>	Not determined	< 1	Transcription assay was used to measure the sensitivity of key Zn^{2+} regulatory enzymes	[32]
HeLa (human cervical cancer line)	Mitochondrial matrix	0.14	Genetically-encoded ratiometric ZapCY1 sensor	[66]
PC-12 (rat adrenal pheochromocytoma line)	Mitochondrial matrix	0.2	Ratiometric carbonic anhydrase II sensor	[67]
HeLa (human cervical cancer line)	Golgi	0.6	Genetically-encoded ratiometric ZapCY1 sensor	[66]
HeLa (human cervical cancer line)	ER	0.9	Genetically-encoded ratiometric ZapCY1 sensor	[66]
PC-12 (rat adrenal pheochromocytoma line)	Cytosol	10	Ratiometric carbonic anhydrase II sensor	[68]
Human erythrocytes (primary cells)	Not determined	24	Total Zn^{2+} was measured in cells incubated with different buffered Zn^{2+} solutions.	[25]
HeLa (human cervical cancer line)	Nucleus	58	Genetically-encoded ratiometric ZapCY2 sensor	Y. Qin, unpublished data
HeLa (human cervical cancer line)	Cytosol	80	Genetically-encoded ratiometric ZapCY2 sensor	[66]
Homogenized rabbit muscle	Not determined	100	Catalysis of endogenous phosphoglucomutase, which is inhibited by Zn^{2+}	[69]

Table 1.3: Estimates of Free Zinc Concentration, continued from Table 1.2.

Cell Type	Subcellular	$[\text{Zn}^{2+}]_{free}$ (pM)	Method	Ref
	Location			
Human peripheral blood mononuclear cells from elderly donors (primary)	Not determined	160	The fractional saturation of FluoZin-3 AM in trypsinized cells was measured with a flow cytometer.	[70]
Human peripheral blood mononuclear cells (primary)	Not determined	170	The fractional saturation of FluoZin-3 AM in trypsinized cells was measured with a flow cytometer.	[71]
Human peripheral blood mononuclear cells from young donors (primary)	Not determined	320	The fractional saturation of FluoZin-3 AM in trypsinized cells was measured with a flow cytometer.	[70]
Jurkat (human T-lymphocyte cells)	Not determined	350	The fractional saturation of FluoZin-3 AM in trypsinized cells was measured with a flow cytometer.	[71]
INS-1 (rat insulin-secreting beta cell line)	Cytosol	400	Genetically-encoded ratiometric eCALWY sensors	[72]
E367 rat neuroblastoma cell line	Not determined	500	^{19}F -NMR of cells loaded with 5F-BAPTA	[73]
HT-29 (human colorectal adenocarcinoma line)	Not determined	614	The fractional saturation of FluoZin-3 AM in trypsinized cells was measured with a spectrofluorimeter.	[33]

Table 1.4: Dissociation constants of cellular molecules for Zn^{2+}

	Zn^{2+} binding molecule	K_D' (M)	Ref
Catalytic	Human carbonic anhydrase II	4×10^{-12}	[74]
	Rabbit angiotensin-converting enzyme	6.4×10^{-10}	[75]
	<i>E. coli</i> alkaline phosphatase	6×10^{-11} ; 2×10^{-8}	[76]
	Sheep liver sorbitol dehydrogenase	6.3×10^{-12}	[60]
Structural	Human BRCA1	3×10^{-8} ; 8×10^{-6}	[77]
	HIV-1 nucleocapsid protein NCp7	4×10^{-15} ; 2×10^{-14}	[78]
	Rat neural zinc finger factor 1	1.4×10^{-10}	[79]
	<i>Xenopus</i> transcription factor IIIA	1×10^{-8} ; 2.6×10^{-5}	[80]
	<i>S. cerevisiae</i> Zap1	4.6×10^{-9}	[81]
	Horse liver alcohol dehydrogenase	1.4×10^{-10}	[82]
Protein interface	Human growth hormone and prolactin receptor	3.3×10^{-11}	[83]
Exchangeable	Human metallothionein 2A	2×10^{-8} ; 1×10^{-10} ; 4×10^{-11} ; 2×10^{-12}	[50]
	Human serum albumin	4×10^{-7}	[84, 85]
	Cysteine	4×10^{-9}	[86]
	Glutathione	2×10^{-6}	[86]

organelles [66, 67, 88]. The reasons for this are not clear, but these organelles are capable of Zn^{2+} uptake during Zn^{2+} overload, which could decrease Zn^{2+} toxicity [65, 66].

Given the volume of a HeLa cell and these estimates of $[\text{Zn}^{2+}]_{free}$, there are only about 100 unbound Zn^{2+} ions in the cytosol, and none in the ER, Golgi, or mitochondrial matrix. This supports the idea that Zn^{2+} remains bound to ligands as it is trafficked around the cell, and any surplus of unbound Zn^{2+} ions is sequestered in other membrane-bound organelles. It is poorly understood how proteins with K_D 's for Zn^{2+} spanning a few orders of magnitude (see Table 1.4) obtain Zn^{2+} , but it is possible that Zn^{2+} is either exchanged directly from a Zn^{2+} chaperone or that transient local changes in $[\text{Zn}^{2+}]_{free}$ distribute Zn^{2+} to specific proteins.

1.2.5 Transporters and Regulators of Zinc Homeostasis

Cells are equipped with a toolbox of transporters, sensors, and storage units so that they can precisely modulate both $[\text{Zn}^{2+}]_{free}$ and $[\text{Zn}^{2+}]_{total}$. Over two dozen mammalian transporters move Zn^{2+} in and out of the cell and between different subcellular compartments, including specialized Zn^{2+} storing vesicles. Metallothionein is arguably the cell's most important Zn^{2+} buffering protein, and cells can adjust its expression in response to changes in Zn^{2+} status. In addition, several regulators of Zn^{2+} homeostasis, including transcription factors, hormones, and nitric oxide, have been described in the literature. This section provides an overview of some of the known transporters and regulators of cellular $[\text{Zn}^{2+}]_{free}$ and $[\text{Zn}^{2+}]_{total}$.

Zn^{2+} transporters. All cells contain multiple Zn^{2+} transporters that can be expressed or redistributed in response to physiological or pathological stimuli [89, 90]. The Zn^{2+} transport machinery appears to be unique to each cell type and is particularly specialized in secretory cells, such as hippocampal neurons, lactating mammary epithelial cells, pancreatic cells, and prostatic epithelial cells [30, 91, 92]. Two major families of proteins—ZnT and ZIP transporters—are known to transport Zn^{2+} in mammalian cells (reviewed in [5, 11, 18, 19, 41, 89, 93–96]). Other transporters are also known to transport Zn^{2+} , but they are less commonly evaluated in studies of Zn^{2+} homeostasis. Figure 1.4 shows the distribution of some of the most widespread ZnT and ZIP transporters in

mammalian cells.

There are 10 members in the mammalian ZnT family, also known as the solute carrier family 30 (SLC30). These proteins are known to transport Zn^{2+} from the cytosol to the extracellular medium or into an organelle, and are key players in every cell's Zn^{2+} homeostasis. For example, extracellular Zn^{2+} induces the expression of ZnT1 to prevent Zn^{2+} overload [97]. Interestingly, the brains of ZnT3 knockout mice have only 70-80% of total Zn^{2+} compared to those of their wildtype counterparts [39]. ZnT3 is thought to transport Zn^{2+} from the cytosol to the lumen of a vesicle, thus increasing Zn^{2+} stored in neuronal vesicles. This family is part of an ancient superfamily of proteins, the cation diffusion facilitator (CDF) superfamily, which contains members in all kingdoms of life. Mammalian ZnT proteins usually have 6 transmembrane domains, and the N- and C-termini are found on the cytosolic side of the membrane. A loop between the fourth and fifth transmembrane domains is rich in serine and histidine residues and thought to be important for Zn^{2+} recognition and transport. ZnTs also have a large C-terminal domain that may function in dimerization and/or Zn^{2+} recognition. Currently, no mammalian ZnT protein structures are available, but the structure of the *E. coli* YiiP protein (a CDF) was published in 2007. The YiiP protein is a homodimer and has Zn^{2+} binding sites at its cytosolic interface and in its transmembrane domain [98, 99]. The ZnT's mechanism of transport is not clearly understood, but it has been hypothesized that ZnTs are $\text{H}^+/\text{Zn}^{2+}$ antiporters [100, 101].

The other major family of Zn^{2+} transporting proteins, the ZIP (Zrt-, Irt-like proteins; SLC39A) family, imports Zn^{2+} into the cytosol from the extracellular environment or from an organelle. There are 14 ZIPs encoded in the human genome. ZIPs have 8 transmembrane domains, and the N- and C-termini are on the non-cytosolic side. A loop between transmembrane domains 3 and 4 has many histidine residues that probably function in Zn^{2+} binding. The proposed mechanism of ZIPs is energy-independent $\text{Zn}^{2+}/(\text{HCO}_3^-)_2$ symport [102, 103]. Most mammalian ZIPs have been shown to transport Zn^{2+} by measuring $^{65}\text{Zn}^{2+}$ uptake. Some ZIPs are less selective and transport other divalent cations as well (ZIP14 also transports iron and ZIP8 transports cadmium) [18, 104, 105]. ZIP1 is widespread and is one of the first responders to Zn^{2+} -limiting

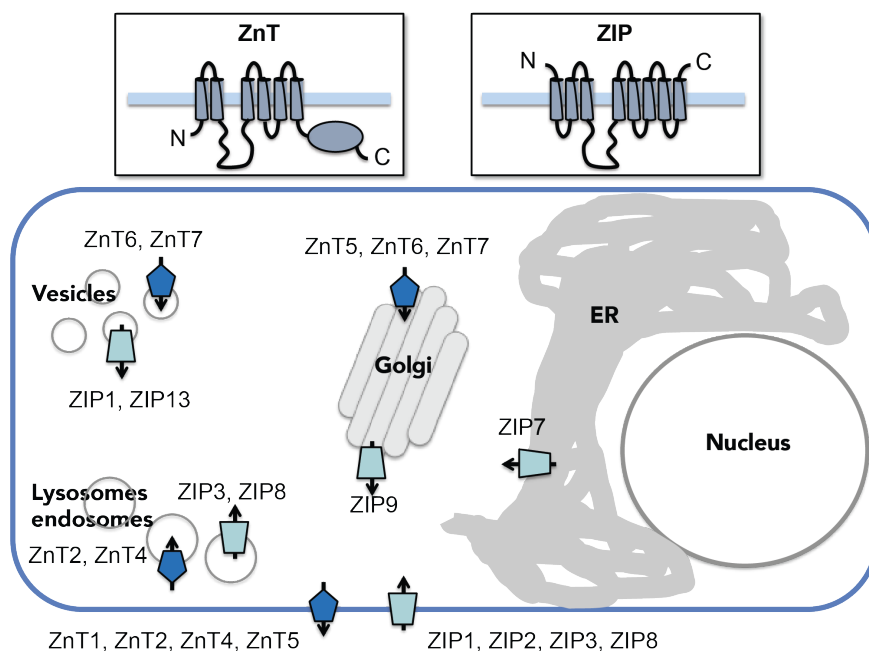


Figure 1.4: Mammalian Zn^{2+} transporters from the ZnT and ZIP families. Over two-dozen mammalian transporters have been shown to regulate intracellular $[\text{Zn}^{2+}]_{free}$ and $[\text{Zn}^{2+}]_{total}$. Members of the ZnT family (SLC30) transport Zn^{2+} out of the cytosol, while members of the ZIP family (SLC39) transport Zn^{2+} into the cytosol. Proteins known to be expressed by a variety of cells are shown in this depiction of a cell. Some transporters, such as ZIP1, are found in multiple locations in the cell.

conditions, at which point ZIP1 redistributes from vesicles to the plasma membrane [103]. In peripheral blood mononuclear cells, ZIP1, ZIP2, and ZIP3 expression increase up to 100-fold in Zn^{2+} -deficient conditions [70]. Decreased ZIP13 expression is associated with decreased cytosolic $[\text{Zn}^{2+}]_{free}$ [106].

Some transient receptor potential (TRP) channels appear to play an important role in Zn^{2+} homeostasis. TRP channels are expressed in both excitable and non-excitable cell types and some are mechano-sensitive or respond to changes in temperature [107]. Interestingly, some of these channels are permeable to Zn^{2+} ; in some cases, they conduct Zn^{2+} more readily than other, smaller metal ions like Ca^{2+} and Mg^{2+} [108, 109]. In a *Drosophila* model, null mutation of dTRPM leads to a growth defect, decreased total Zn^{2+} , and decreased expression of metallothionein and a ZnT family protein; this phenotype can be rescued with Zn^{2+} supplementation [108]. Zn^{2+} can enter pancreatic β cells through TRPM3, and this mechanism of entry may be important for replenishing Zn^{2+} , which is crystallized with insulin in secretory granules [110, 111].

Another Zn^{2+} influx pathway in excitable cells is through the voltage-gated calcium channels [112]. Upon depolarization, Zn^{2+} can enter pancreatic β cells and neurons through voltage-gated calcium channels [113–116]. There is also evidence to support the entry of Zn^{2+} into the mitochondrial matrix through the mitochondrial Ca^{2+} uniporter [117, 118].

Metallothionein. Over a dozen isoforms of metallothionein (MT) are encoded by the human genome [20]. MT2A, one of the most prevalent forms, is a 61-amino acid protein containing 20 cysteine residues (see Figure 1.2). It can chelate Zn^{2+} and other metals, including lead, copper, cadmium, mercury, silver, and platinum. It binds up to 7 Zn^{2+} ions, which have a range of K_D 's over four orders of magnitude (see Table 1.4). MTs can be transported into mitochondria and the nucleus and thus may be Zn^{2+} chaperones that redistribute Zn^{2+} throughout the cell [36, 119]. Increased MT expression is associated with increased $[\text{Zn}^{2+}]_{total}$.

Other regulators of Zn^{2+} homeostasis. The only characterized Zn^{2+} sensing protein in mammalian cells is the metal response element-binding transcription factor (MTF-1), which binds Zn^{2+} with a dissociation constant of 31.4 pM [120, 121]. MTF-1 induces transcription of ZnT1 and

ZnT2 and represses transcription of ZIP10, and it can interact with p300, PTEN, and HIF-1 α [122]. Hormones, such as prolactin, testosterone, estrogen, and glucocorticoids, and cytokines like TNF- α can activate MTF-1 and/or induce transcription of ZnTs or ZIPs [5, 89]. Nitric oxide and reactive oxygen species can react with thiols and release Zn²⁺ from thiol ligands, leading to an increase in $[Zn^{2+}]_{free}$ [123–125].

In summary, $[Zn^{2+}]_{free}$ is maintained at several orders of magnitude lower than $[Zn^{2+}]_{total}$. Cells use a variety of molecular tools to control both $[Zn^{2+}]_{free}$ and $[Zn^{2+}]_{total}$ in response to a variety of signals. Intracellular $[Zn^{2+}]_{free}$ buffering allows for acute signaling through transient changes in zinc levels and supports the exchange of zinc between different ligands that bind it in the pM-nM range.

1.2.6 Tools for Studying Zinc in Biological Systems

There are several methods that can be used to measure $[Zn^{2+}]_{free}$ or $[Zn^{2+}]_{total}$, but few can truly capture the dynamic nature of Zn²⁺ in biology. Most of these methods are briefly presented in this section because they have been reviewed extensively [38, 87, 126–129].

The first methods used to study Zn²⁺ at the tissue and cellular level were histochemical stains for Zn²⁺ and other transition metals [38]. Such stains showed that Zn²⁺ was concentrated in vesicles in the mammalian hippocampus and cortex. Another method of visualizing Zn²⁺ is x-ray fluorescence microscopy [127, 130]. This method can measure total Zn²⁺ (and other metals) with limited spatial resolution, and it requires an advanced x-ray source.

$[Zn^{2+}]_{total}$ of a population of cells is usually measured with atomic absorption spectroscopy (AAS) or inductively coupled plasma mass spectrometry (ICP-MS) [34, 126, 127]. ICP-MS is more sensitive, but AAS is more widely available. Presently, there are not any methods for measuring $[Zn^{2+}]_{total}$ in individual, living cells.

Many fluorescent probes for monitoring labile Zn²⁺ have been recently developed. For a thorough review of Zn²⁺-responsive probes, the reader is referred to recent reviews [126, 128]. In general, these probes can be categorized as small-molecule dyes, which must be added to cells

before imaging, or genetically-encoded sensors, which are encoded on DNA that is introduced into cells by transfection or transduction. Many small-molecule Zn^{2+} -sensitive probes are modified versions of Ca^{2+} probes that respond more specifically to Zn^{2+} . The most popular small-molecule probes are ZinPyr-1 [131] and FluoZin-3 [37]. Both of these probes have an increased fluorescence intensity when bound to a Zn^{2+} ion. FluoZin-3 is not membrane-permeable, but the addition of acetoxymethyl ester groups makes it membrane-permeable and leads to intracellular concentration. However, it is difficult to control the intracellular concentration and localization of these probes.

On the other hand, genetically-encoded sensors can be targeted to subcellular locations by adding an N- or C-terminal localization sequence [126]. They can also be expressed at low concentrations using stable cell lines or an inducible promoter system [132, 133]. The currently available genetically-encoded Zn^{2+} sensors are ratiometric, and so they can be used to estimate $[\text{Zn}^{2+}]_{free}$ and to monitor changes in $[\text{Zn}^{2+}]_{free}$ in living cells. Genetically-encoded sensors of Ca^{2+} and Zn^{2+} are discussed in greater detail in Section 1.3.

It is clear that Zn^{2+} has great importance in biological processes, and that it is tightly regulated by many different proteins in a cell. New tools are needed for monitoring Zn^{2+} in different subcellular compartments and assessing the occupancy of the Zn^{2+} proteome, which would help us study how changes in Zn^{2+} affect cell signaling, growth, differentiation, and death.

1.3 An Overview of Genetically-Encoded Sensors of Calcium and Zinc

Fluorescent biosensors are valuable tools for observing dynamic changes in intracellular ion concentrations. I will briefly compare and contrast ratiometric to intensimetric sensors, describing how to select an appropriate genetically-encoded, ratiometric, fluorescent, metal ion sensor in living cells. I will also discuss some important complexities and limitations of quantitative measurements using these sensors. Detailed protocols for using these sensors correctly are presented in Chapter 2.

In practice, there are two major types of fluorescent biosensors for metal ions: *intensimetric* biosensors that change fluorescence intensity when bound to an ion, and *ratiometric* biosensors, in

which there is a shift in the absorption or emission spectra when bound to an ion. The fluorescence intensity of an intensimetric sensor is dependent on the sensor concentration in each cell and the path length (*i.e.* the thickness of a cell) in addition to the ion concentration; hence ratiometric biosensors are preferred for quantitative measurements. On the other hand, ratiometric biosensors have several experimental limitations, which include lower sensitivity (*i.e.* smaller dynamic range), a larger spectral bandwidth, and the need to acquire images with two combinations of fluorescence excitation and emission filters.

In this Section, I focus on genetically-encoded biosensors: proteins encoded by DNA that is introduced into living cells by transient transfection or viral transduction. In contrast to small molecule biosensors, which are chemically synthesized and are introduced to cells immediately before the experiment, genetically-encoded biosensors are manufactured by the cell and become functional without further intervention by the investigator. Genetically-encoded biosensors are readily targeted to subcellular locations by appending localization sequences to the DNA sequence, a major advantage when the investigator desires the ability to monitor ion concentrations in organelles, such as the ER, Golgi, nucleus, or mitochondria [126]. Subcellular targeting to some locations like vesicles is hindered by the size of some sensors (typically 60-65 kDa).

1.3.1 Sensor Design

Almost all available genetically-encoded, ratiometric, fluorescent metal ion sensors have the following design: a donor fluorescent protein (FP) is attached to an acceptor FP by a linker containing the metal-binding domain (see Figure 1.5). The chromophore of an FP forms autocatalytically from three amino acid residues inside of a beta barrel. The biosensor undergoes a conformational change upon binding the metal ion, changing the distance and orientation between the two FPs and consequently the efficiency of Förster resonance energy transfer (FRET) (reviewed in [134, 135]). The change in FRET alters the emission spectra of the biosensor, decreasing the peak of donor FP emission and increasing the peak of acceptor FP emission. The FRET ratio (R) is defined as the ratio of the acceptor FP emission intensity to the donor FP emission intensity. R

can be converted to an ion concentration when three parameters are known: (1) the sensor affinity in terms of K_D' , (2) R in the absence of the ion (R_{free}), and (3) R when the sensor is saturated with the ion (R_{bound}). The sensor affinity can be measured either *in vitro* or *in situ* (*i.e.* in cells) and is usually published in the literature, as discussed below. R_{free} and R_{bound} are measured at the end of each experiment. Typically, R_{free} is the minimum FRET ratio (R_{min}) and R_{bound} is the maximum FRET ratio (R_{max}), but sometimes the sensor response is inverted and the opposite is true [72, 88].

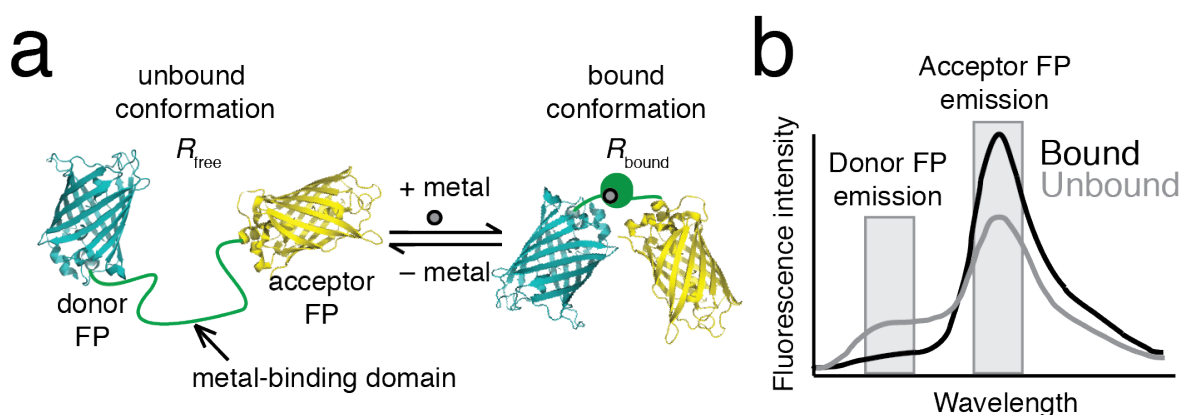


Figure 1.5: Basic design of a genetically-encoded FRET sensor of Ca^{2+} or Zn^{2+} . a) A genetically-encoded, fluorescent, ratiometric sensor contains a Ca^{2+} or Zn^{2+} binding domain fused to a donor FP (usually cyan FP) at its N-terminal end and an acceptor FP (usually yellow FP) at its C-terminal end. When Ca^{2+} or Zn^{2+} reversibly binds to its binding domain, the sensor changes conformation, which leads to a change in FRET efficiency. b) shows how the change in FRET efficiency changes R , which is the ratio of acceptor FP to donor FP emission intensity upon donor FP excitation. Thus, R of the unbound sensor (R_{free}) is distinct from that of the bound sensor (R_{bound}).

1.3.2 The Binding Properties and Dynamic Range of a Sensor

Every biosensor is sensitive to changes within a range of ion concentrations, which spans about two orders of magnitude. This range is largely determined by the sensor's binding affinity for an ion (or ions) and dynamic range (DR). The binding constant is reported as the K_D' , which is equal to the ion concentration when 50% of the sensor is bound (see Figure 1.6). Occasionally,

when a sensor has multiple binding sites with different binding affinities, multiple K_D' values are reported. A K_D' is determined by fitting a binding curve to experimental data from a sensor titration experiment, in which R of the sensor is measured at different ion concentrations. Chapter 2 and Appendix A describe how to determine the K_D' of a sensor in cells or *in vitro*, respectively.

A K_D' is determined by fitting a binding curve to experimental data from a sensor titration experiment, in which R is measured at different ion concentrations. The simplest binding equation is used to describe the titration data, even though it may not represent actual binding events. For example, the Ca^{2+} sensor D3cpV is fit to a single-site binding equation, even though each sensor binds to 4 Ca^{2+} ions [137]. It is important to note that temperature, salt concentration, pH, and other factors can affect the K_D' , and that most titrations are performed *in vitro* with protein purified from a bacterial expression system. However, experiments performed in our group and others indicate that the K_D' *in vitro* and in cells are often comparable [66, 72, 88]. This is something that each investigator can verify in his or her own experimental system using the protocol outlined in Section 2.4.

DR has many definitions in the literature, but it is essentially an indicator of a sensor's measurement sensitivity and its signal-to-noise ratio (SNR). Common definitions of DR include the fold-change in FRET ratio ($DR = R_{max}/R_{min}$); or, the maximum change in FRET ratio ($DR = R_{max} - R_{min}$). SNR is also described as the ratio of R to the standard deviation of R at baseline [138, 139]. Several factors can significantly affect a sensor's DR (or SNR), including the microscopy system used for measurement, the cell type expressing the sensor, and the subcellular location (see Section 2.3). Accordingly, reported DRs are most useful for relative comparisons and will not always be the same in a different experimental system. Moreover there are numerous examples of sensors exhibiting decreased DR in cells compared to *in vitro* and hence researchers are encouraged to seek out and compare R_{max} and R_{min} values from *in situ* experiments.

A sensor is most sensitive to changes in ion concentration when it is close to 50% bound because a change in ion concentration near the K_D' results in a greater change in fraction bound, which is proportional to the change in R (see Figure 1.6). For example, if a sensor's K_D' is 1

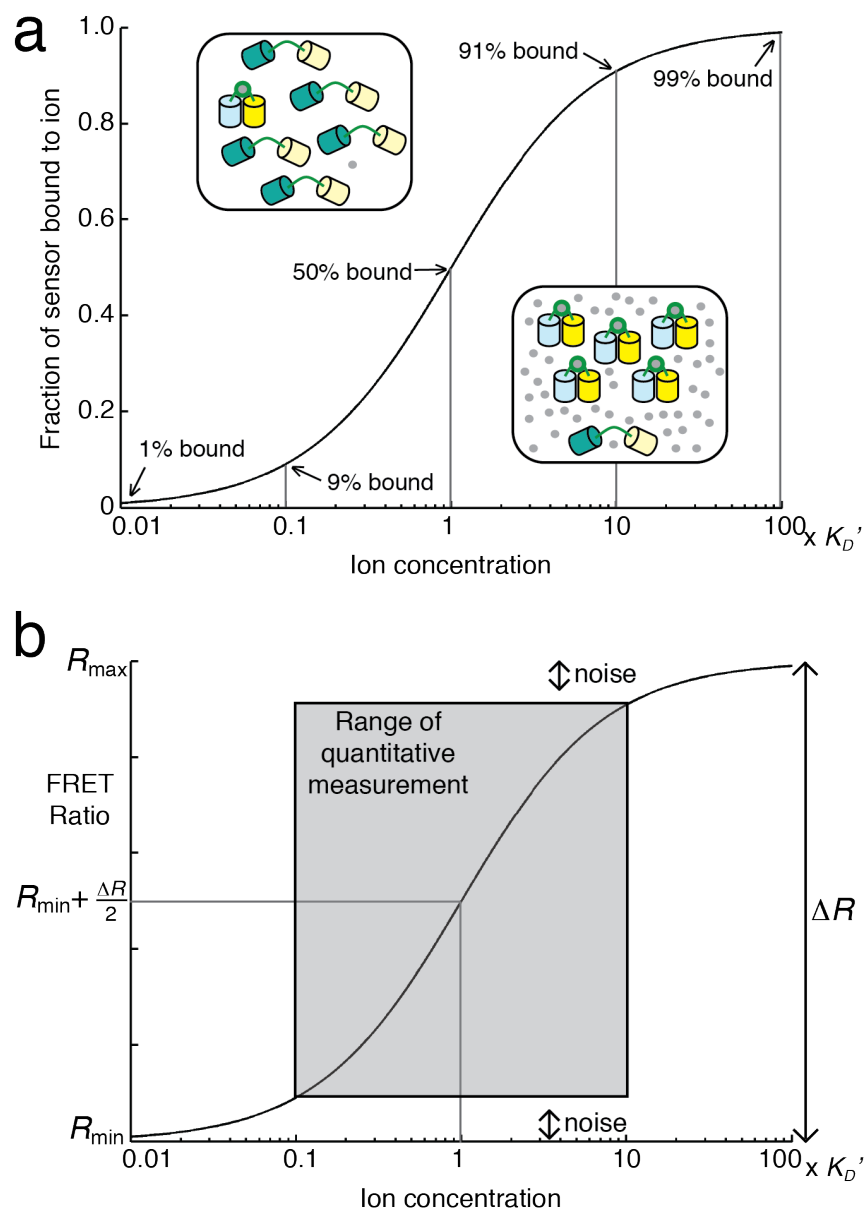


Figure 1.6: A sensor's sensitivity to changes in Ca^{2+} or Zn^{2+} concentration is related to its K_D' . a) When the ion concentration ($[\text{ion}]$) is the same as the sensor's K_D' , 50% of a population of sensors (1-20 μM in cells [65, 136]) is bound to the ion. The fraction of sensor bound changes the most when the $[\text{ion}]$ varies within 10-fold of the sensor's K_D' . b) R is a linear function of the fraction bound, and so the midpoint of R_{min} and R_{max} corresponds to an $[\text{ion}]$ equal to the sensor's K_D' . The signal-to-noise ratio and the K_D' limit the range of the $[\text{ion}]$ that can be quantified by the sensor.

μM , a change in ion concentration from $0.1 \mu\text{M}$ to $1 \mu\text{M}$ results in an increase from 9% to 50% fraction bound, whereas a change from $0.01 \mu\text{M}$ to $0.1 \mu\text{M}$ results an increase from 1% to 9% fraction bound. Consequently, changes in ion concentration close to the sensor's K_D' are more readily detected. R_{min} and R_{max} correspond to 0% and 100% fraction bound, respectively. The variance of R , or noise, relative to the overall change in R (ΔR), determines the range of fraction bound that a sensor can reliably report. Thus, a sensor with a larger SNR can be used to measure a greater range of ion concentrations.

The empirical Hill coefficient, n , reflects the steepness of the binding curve. When n greater than 1, the binding curve is steeper (see Figure 1.7). A steeper curve also means that R can be more precise near the K_D' but the range of ion concentration that the sensor can report is smaller. In Figure 1.7, a change in ion concentration from $1 \times K_D'$ to $2 \times K_D'$ results in a larger change in R when $n=1.5$ than when $n=0.5$.

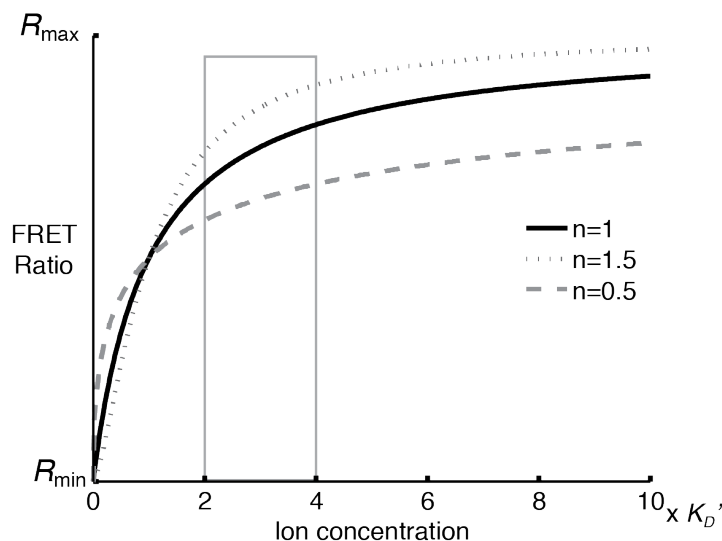


Figure 1.7: The effect of the empirical Hill coefficient on a sensor's measurement precision and range. If the [ion] changes from $2 \times K_D'$ to $4 \times K_D'$, the change in R is greater when n is larger.

1.3.3 Guidelines for Choosing a Sensor

Currently, many biosensors are available for Ca^{2+} or Zn^{2+} imaging, so the investigator must attempt to choose the one best suited to the experimental system. The K_D' and the DR are the most important factors to consider, along with the other factors discussed below, but often the best sensor is revealed by empirical testing of multiple sensors [140].

First, fluorescence properties of the donor and acceptor FPs affect each sensor. The cyan FP and yellow FP donor-acceptor pair is by far the most common. Single or multiple amino acid mutations in an FP can change its excitation and/or emission wavelengths, brightness, maturation time, or photostability, and so there are several different cyan FPs and yellow FPs with slightly different fluorescence properties [141, 142]. A word of caution regarding yellow FPs is that their fluorescence is quenched by acid and hence it may be challenging to use a sensor containing a yellow FP in an acidic compartment. Circularly permuted (cp) variants of FPs are constructed by changing the N- and C-termini to different loops within the FP. Although circular permutation does not significantly change the fluorescence properties, the incorporation of a cp FP into a sensor can change the DR by altering the relative orientation of the two FPs in the bound and/or unbound conformation of the sensor [143, 144]. In addition, circular permutation can affect the pH sensitivity by changing the pK_a of the chromophore, and rearrangement of cysteine residues can affect its sensitivity to oxidizing organelles. We have found that sensors containing a cpVenus FP have decreased DR and SNR in the ER due to the low signal from the cpVenus FP. Red-green FRET pairs are preferred in acidic compartments, such as the secretory pathway, since sensors containing yellow FPs can be much dimmer at low pH (<6.5) [145, 146]. The substitution of different FPs into a sensor can alter its K_D' and DR in unpredictable ways, so the investigator should evaluate each sensor's performance *in situ* before performing important experiments.

Replacement or mutation of the binding domain also alters the sensor's properties. To monitor increases in ion concentration, it's useful to pick a sensor that is $\sim 20\%$ saturated at baseline, whereas a sensor that is $\sim 50\%$ saturated is better for comparing differences in resting ion con-

centrations in different cells or different environmental conditions. Cameleon-Nano sensors have lower K_D 's and are better for quantitative measurement of cytosolic Ca^{2+} in some cell types [138], whereas D1ER is preferred for ER measurement because Ca^{2+} levels are high in the ER and the K_D ' of D1ER is much higher than other Cameleons [144]. Tables 1.5 and 1.6 summarize K_D 's and DRs of some current sensors, and Table 1.7 summarizes sensors used in specific subcellular compartments. In addition to a sensor's K_D ' and DR, the investigator may consider properties such as sensitivity to other biologically relevant metal ions, pH, redox balance, salt concentration, or sensor concentration. It is also important to consider the on and off rates of ion binding when attempting to observe dynamic changes in ion concentrations [138, 140, 147, 148].

1.3.4 Multiplexed Imaging with Additional Fluorescent Probes

In an imaging experiment, genetically-encoded, ratiometric sensors can be used in conjunction with other fluorescent probes, such as small molecule dyes, fluorescently-tagged proteins, or another genetically-encoded sensor. If multiple fluorescent probes are used, they must be orthogonal: that is, their excitation and emission wavelengths should not interfere with each other. For example, a CFP/YFP FRET sensor could be used with a red fluorescent protein, but not a green fluorescent protein.

Many published studies have successfully monitored two different fluorescent probes simultaneously. A red fluorescent protein, targeted to the mitochondrial intermembrane space, was used to visualize mitochondrial outer membrane permeabilization in cells expressing CFP/YFP FRET reporters of caspase activity; using these tools, the authors were able to show that initiator caspases, but not executioner caspases, are activated hours before mitochondrial outer membrane permeabilization during apoptosis [153]. Nuclear and cytosolic Zn^{2+} uptake were monitored simultaneously using a CFP/YFP FRET sensor targeted to the cytosol and a tSapphire/RFP FRET sensor targeted to the nucleus [145]. In another study, RhoC was found to be activated around but not inside invadopodia by using a CFP/YFP FRET RhoC biosensor and an RFP-cortactin fusion, which marks invadopodia [154]. Several multiplexed imaging protocols have been published [132, 145, 155, 156].

Table 1.5: This table presents the binding properties of some currently used, genetically encoded, ratiometric, Ca^{2+} biosensors. Publications of other sensors within these families (Yellow Cameleon, Yellow Cameleon Nano, Cameleon D, and TroponinC) are referenced in the last column, and Ca^{2+} sensors are more comprehensively reviewed elsewhere [127,141,148,149]. Abbreviations: calmodulin (CaM), CaM-binding M13 peptide (M13p), mutant CaM and M13 peptide (mCaM and mM13p), modified EF hands I-IV from chicken skeletal muscle troponin C (mTpC).

	Sensor	Ca^{2+} - responsive elements	K_D' for Ca^{2+} (nM)	n	Comments	Ref
Yellow Cameleon series	YC2.60	CaM, M13p	93.5	2.7		[138, 143]
Yellow Cameleon series	YC3.60	CaM E104Q, M13p	215; 779	3.6; 1.2	High dynamic range	[138, 143]
Yellow Cameleon Nano series	YC-Nano50	CaM, M13p	52.5	2.5	Optimized for detecting subtle cytosolic Ca^{2+} transients in living organisms	[138]
D-family Cameleons	D1	mCaM, mM13p	800; 6×10^5	1.18; 1.67	Does not bind endogenous CaM; optimized for ER	[144]
D-family Cameleons	D3cpV	mCaM, mM13p	600	0.74	Does not bind endogenous CaM; optimized for cytosol and mitochondria	[137]
TroponinC family	TN-XXL	mTpC	800	1.5	Optimized for imaging of neurons; fast response	[147]

Table 1.6: This table presents the binding properties of some currently used, genetically encoded, ratiometric, Zn^{2+} biosensors. Abbreviations: first two zinc fingers of *Saccharomyces cerevisiae* Zap1 (Zap), mutant Zap with decreased affinity for Zn^{2+} (mZap).

	Sensor	Zn^{2+} -responsive elements	K_D' for Zn^{2+} (pM)	n	Comments	Ref
eCALWY family	eCALWY4	Atox1 and the WD4 domain of ATP7B	630	1	Optimized for cytosol	[72]
ZinCh family	eZinCh	Zn^{2+} -coordinating residues on CFP and YFP connected by a flexible linker	8.2×10^6	1	Targeted to vesicles by fusion to VAMP2	[72, 150]
Zap family	ZapCY1	Zap	2.53	1	Optimized for ER, Golgi, and mitochondria; high dynamic range	[66]
Zap family	ZapCY2	mZap	811	0.44	Optimized for cytosol	[66]

Table 1.7: This table summarizes sensors that have been targeted to different subcellular locations by adding a genetically encoded localization tag. Untargeted sensors are typically found in both the cytosol and the nucleus.

Subcellular location	Ca^{2+} sensors	Zn^{2+} sensors	Ref
ER	D1ER	ER-ZapCY1	[66, 144]
Golgi	—	Golgi-ZapCY1	[66]
Vesicles	Ycam2	eZinCh	[72, 151]
Mitochondria	4mt-D3cpV	Mito-ZapCY1	[88, 137]
Nucleus	D3cpV	ZapCY2	[66, 137]
Cytosol	D3cpV	eCALWY-4, ZapCY2	[66, 72, 137]

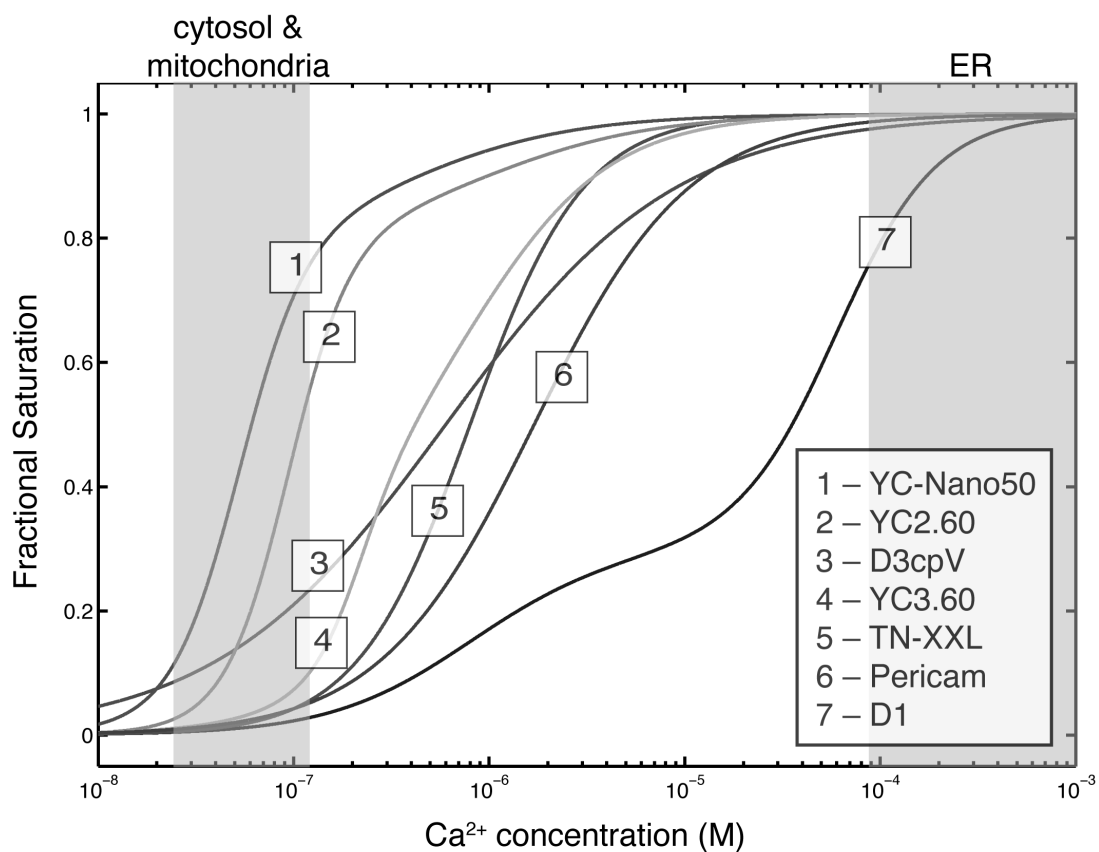


Figure 1.8: The fractional saturation of commonly-used Ca^{2+} sensors in the cytosol, mitochondria, and ER of HeLa cells at rest. The figure shows Ca^{2+} binding curves of Pericam, YC-Nano50, YC2.60, YC3.60, TN-XXL, D3cpV, and D1 [137, 138, 143, 144, 147, 152]. D3cpV is 20% saturated in the cytosol or mitochondria, and D1 is 80% saturated in the ER.

In summary, genetically-encoded, ratiometric sensors are excellent tools for quantitative measurement. The guidelines presented in this section can help the investigator select the best sensor for an experiment. The imaging and calibration conditions should then be optimized to obtain the best results, as described in Chapter 2.

1.4 Thesis Overview

Genetically-encoded, ratiometric sensors are tools ideally suited for observing dynamic processes with live cell imaging and for making quantitative measurements in living cells. They can be used with a variety of different cell types for long term imaging with several different types of microscopy systems. Chapter 2 is a discussion of methods that I have developed to maximize the usefulness of a FRET sensor—Ca²⁺ or Zn²⁺ sensors in particular. First, I discuss how to calibrate a sensor and maximize its stability and dynamic range in a microscopy system. This not only verifies the sensor’s functionality in cells, it also is necessary for estimation of $[\text{ion}]_{free}$. The accuracy of $[\text{ion}]_{free}$ measurement is also dependent on determining the binding properties of the sensor in the environmental conditions in which it will be used. I discuss a protocol for titrating a sensor *in situ*, in the cells and/or the organelle of interest. Lastly, I present methods for automated analysis of the data, which allows the researcher to work efficiently, organize results, and create ratiometric movies.

The analytical methods described in Chapter 2 enabled us to make novel observations about mitochondrial Zn²⁺ homeostasis, which are presented in Chapter 3. In this study, I constructed and tested several of new mitochondrial Zn²⁺ sensors and identified three sensors with high dynamic range. One of these sensors, mito-ZapCY1, was used to quantify mitochondrial Zn²⁺ in different cell types. I also discovered that this sensor is fully saturated in the cytosol but almost unsaturated in the mitochondrial matrix, showing that different subcellular compartments regulate Zn²⁺ differently. In this Chapter, I validated the methods presented in Chapter 2 and developed new sensors to observe mitochondrial Zn²⁺ homeostasis in intact, living cells.

In Chapter 4, genetically-encoded sensors, specific to Ca²⁺ or Zn²⁺, were used to explore

potential crosstalk between Zn^{2+} and other ions in insulin-secreting cells. These cells package insulin- Zn^{2+} crystals into secretory vesicles, and there is some evidence that when these vesicles are released, Zn^{2+} participates in autocrine or paracrine signaling. I decided to investigate the role of Zn^{2+} in Ca^{2+} oscillations stimulated by glucose. Genetically-encoded sensors are excellent tools for these studies because they can discriminate between Ca^{2+} and Zn^{2+} and can be used to observe dynamic signaling processes with good spatial and temporal resolution. I found that changes in intracellular Zn^{2+} are associated with changes in Ca^{2+} oscillations, which may have downstream effects on insulin secretion, a topic that I plan to explore further.

Chapter 2

Analytical Methods

2.1 Abstract

Quantitative imaging of genetically-encoded, ratiometric Ca^{2+} and Zn^{2+} sensors enables investigators to observe real-time changes in ion concentrations with subcellular resolution. However, the precision, accuracy, and repeatability of these experiments rely on the optimization of imaging, sensor calibration, and analysis protocols for each sensor and cell type. I have developed a workflow for identifying the image acquisition and calibration conditions that maximize a sensor's dynamic range. I also provide a protocol for estimating the ion concentration from a series of images of cells expressing a FRET sensor, and discuss when and how to determine a sensor's binding properties in living cells in order to improve the accuracy of the estimation. Techniques for automating the analysis of imaging experiments are discussed in the last section of this Chapter.

2.2 Introduction

Genetically-encoded, fluorescent sensors have enabled scientists to observe dynamic processes in living cells and organisms with great specificity and spatiotemporal resolution. These sensors, which are discussed in detail in Chapter 1, are more easily targeted to subcellular organelles and persist longer than small-molecule probes. The concentration of genetically-encoded sensors in cells can also be carefully controlled in order to minimize their interference with endogenous signaling pathways. In addition, they can be designed to sense different cellular signals, including metal ion concentrations, kinase activity, and GTPase activity. Furthermore, ratiometric FRET sensors

are used to quantitatively measure Ca^{2+} and Zn^{2+} concentrations with superior specificity. This Chapter presents a set of protocols and a standard workflow that can be used to optimize the performance of a FRET sensor in live-cell imaging experiments, leading to precise, accurate, and repeatable observations.

FRET sensors often appear to respond differently in different cell types or in the hands of different investigators. For this reason, a standardized procedure for optimization is very helpful when dealing with a new sensor or cell type. Chapter 1 contains practical considerations for choosing the most promising sensor for a particular application; here, the focus is generating high quality data. Although these protocols are directed toward investigators dealing with a Ca^{2+} or Zn^{2+} sensor, they can be adapted for other types of ratiometric sensors.

Section 2.3 describes how to verify a sensor's functionality in a particular cell type and optimize its performance as a ratiometric sensor for quantitative measurement. When accurate estimation of Ca^{2+} or Zn^{2+} is essential, measurement of the sensor's K_D' in the cellular environment becomes very important. The protocol for an *in situ* titration is presented in Section 2.4. This assay can complement *in vitro* titration, which is described in Appendix A. It is important to validate and characterize sensors inside of cells, since the *in vitro* conditions can mimic but not replicate a complex intracellular or subcellular environment.

Once an experimental workflow has been established, automation of data analysis can improve productivity and consistency. Several techniques for improving image analysis of FRET sensor experiments are described in Section 2.5, and detailed protocols can be found in Section B.

2.3 Optimizing the Use of Genetically-Encoded FRET Sensors for Quantitative Measurements

It is important to identify the correct protocol for calibrating a FRET sensor in every cell type before beginning a set of experiments that rely on proper use of the sensor. A sensor calibration consists of measuring its minimum and maximum FRET ratios (R_{min} and R_{max}) in cells. For sensors that detect ions such as Ca^{2+} or Zn^{2+} this is accomplished using chelators or ionophores to

deplete or saturate the sensor. Conversion of the FRET ratio (R) to Ca^{2+} or Zn^{2+} concentration requires accurate measurement of R_{min} and R_{max} . The experimental conditions needed to obtain R_{min} and R_{max} are not necessarily the same for every sensor or cell type, and so a variety of conditions are tested to obtain the maximum dynamic range (DR). Sensor calibration is even valuable when there is no intention to convert R to the free ion concentration ($[\text{ion}]_{free}$) because it verifies that the sensor is functional and that experimental conditions allow for the greatest signal-to-noise ratio (SNR).

This section provides a workflow for optimizing the calibration of a FRET sensor in single cells using live-cell fluorescence microscopy. An overview of this procedure is shown in Figure 2.1. First, the sensor should be correctly localized when expressed in the cells of interest (Section 2.3.1). Next, a microscope capable of FRET imaging should be chosen for the experiments (Section 2.3.2). Section 2.3.3 explains how to adjust image acquisition settings to obtain a stable R with the least phototoxicity. The procedure of calibrating a sensor is described in Section 2.3.4. Lastly, the analysis of sensor calibration data and conversion of R to ion concentration is discussed in Section 2.3.5.

As shown in Figure 2.1, optimizing the sensor calibration is an iterative process of adjusting image acquisition parameters and conditions for reaching R_{min} and R_{max} . Quantitative measurement requires determining R_{min} and R_{max} in each cell imaged because the values can vary from cell to cell; sources of variation likely include partial proteolysis or oxidation of sensors in different cells. The optimization process can be applied to other types of sensors, such as kinase and GTPase sensors, to identify imaging conditions that verify their function and maximize the DR.

2.3.1 Sample Preparation

The way in which cells are prepared for imaging—cell culture, plating density, or transfection conditions—can significantly affect the success of an experiment. Optimizing these protocols can improve localization and decrease toxicity due to overexpression of the sensor, thus improving the quality of data collected.

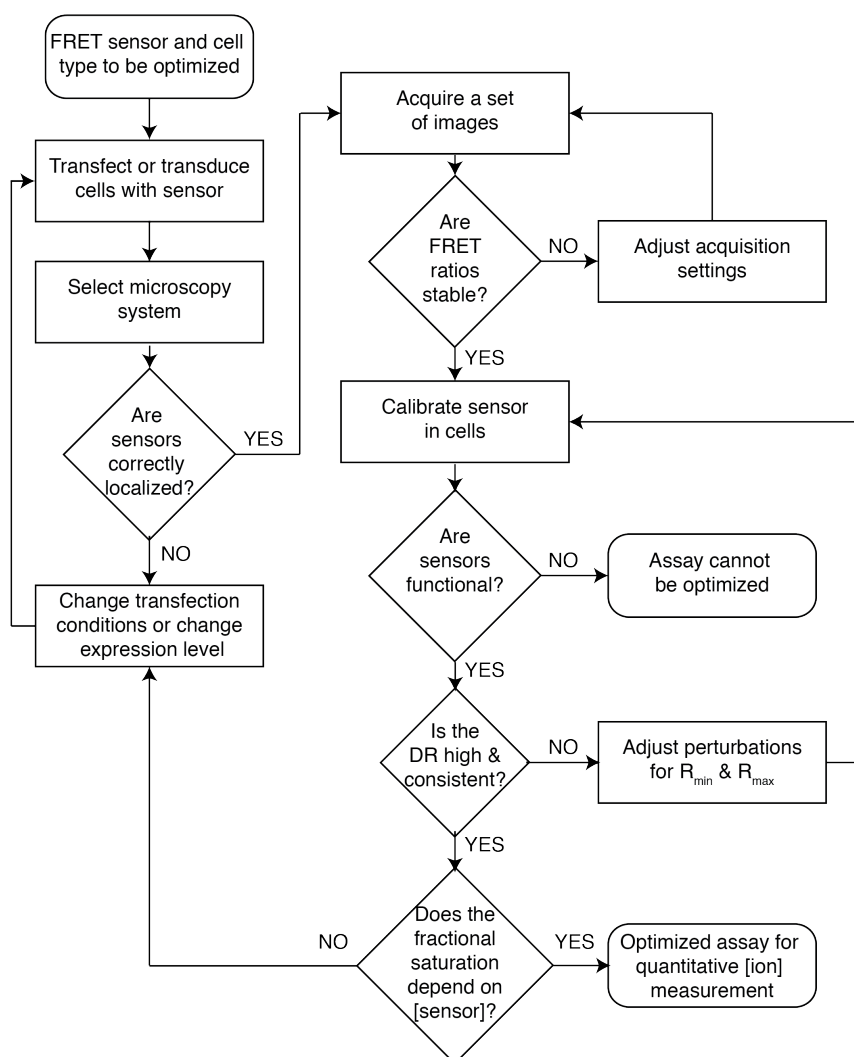


Figure 2.1: An overview of the optimization of FRET sensor calibrations. Once the investigator has selected a cell type and FRET sensor for quantitative imaging, the sensor calibration protocol should be optimized in order to obtain the most repeatable and reliable results. First, one should establish a suitable method of transfecting the cells of interest with the sensor, so that the sensor is correctly localized and does not perturb cell function and proliferation. Next, the acquisition settings should be optimized for the most stable signal and the least amount of phototoxicity. Then, a standard protocol of chemical perturbations, used to calibrate the FRET sensor, should be established that maximizes the DR of the sensor. At this point, the sensor can be calibrated at the end of an experiment to determine R_{min} and R_{max} , which are needed to convert R to $[ion]_{free}$.

Cells expressing the genetically-encoded sensor of choice should be seeded on glass-bottomed imaging dishes or plates for experiments. A protocol for economically making 35 mm imaging dishes can be found in Section C.1. Dishes coated with fibronectin, gelatin, or poly-lysine may increase the adherence of some cell types. It is more difficult to measure the background fluorescence intensity when cells are more dense and therefore optimal imaging conditions ensure the cells are not over-crowded.

There are many different methods of introducing DNA encoding the sensor into mammalian cells. Transient transfection, including lipofection or electroporation, is a convenient way to introduce plasmid DNA. For example, I plate HeLa cells on 35 mm imaging dishes 24-48 hours before transiently transfecting a plasmid encoding a cytosolic Zn^{2+} or Ca^{2+} sensor using lipofection. Viral transduction can be more successful in some cell lines that are difficult to transfect (*e.g.* primary cells). Making a stable cell line may be more convenient and less costly when many experiments must be performed with the same cell type and sensor. In addition, stable cell lines often express lower levels of sensor, and so this could decrease toxicity or mislocalization due to sensor overexpression. FRET sensor overexpression (particularly sensors of GTPase activity) has been known to change cellular signaling and affect cell proliferation and death [138, 156, 160, 161]. A protocol for making a stable cell line using a PiggyBac transposon system can be found in Section C.3. In our experience, it is very important to identify conditions that minimize cell toxicity, promote biosensor expression levels detectable by the microscope, and maximize the number of cells displaying correct sensor localization.

In our laboratory, the most common mislocalization problems are mitochondrial sensors found in both the mitochondria and the cytosol, and Golgi (or other secretory pathway) sensors incorrectly localized to the endoplasmic reticulum (ER). In addition, because of the breakdown of the nuclear envelope during mitosis, nuclear-targeted sensors are temporarily cytosolic during mitosis. Co-localization of a sensor and an organelle marker can be quantified by running a Pearson's correlation analysis [66, 88]. Another method often employed is to quantify the percentage of cells displaying incorrect localization when optimizing conditions for the best localization [149]. Images of cells

expressing genetically-targeted sensors are shown in Figure 2.2.

Consistently correct localization of sensors is important for several reasons. When the sensor is correctly localized in only a proportion of cells, experiments yield less data, the analysis is harder to automate, and it is more difficult to sort stable cell lines with fluorescence-activated cell sorting. Mislocalized sensors can lead to inaccurate FRET sensor data because $[\text{ion}]_{\text{free}}$ can differ by orders of magnitude in different subcellular compartments. For example, Figure 2.3 shows an image of cells transiently transfected with the same Zn^{2+} sensor, named mito-ZifCV1.173 (Section 3.4.1). This sensor is genetically targeted to the mitochondrial matrix, but in some cells, it is also found in the cytosol and nucleus. This sensor is almost completely unbound when correctly targeted, but almost saturated in the cytosol and nucleus (a protocol for determining the fractional saturation of a sensor can be found in Section 2.3.4). This could lead to estimates of Zn^{2+} that differ by ~ 2 orders of magnitude (Section 3.4.2). Clearly, localization is important for accurate quantification using genetically-encoded FRET sensors.

2.3.2 Microscopy Systems for Imaging FRET Sensors

Several types of microscopy systems are capable of imaging CFP/YFP FRET sensors, including widefield epifluorescence microscopes, laser-scanning or spinning-disk confocal microscopes, or two-photon microscopes, each with advantages and disadvantages. Even though images acquired with widefield microscopes are more blurred than those acquired with laser scanning confocal microscopes, widefield microscopes collect more emitted light and so have a better SNR while exposing the sample to less light [132, 160, 162]. Some cell types, such as primary neurons, may be more sensitive to the increased light exposure in confocal microscopy. It is not uncommon to verify sensor localization and obtain publication-quality images with a confocal microscope, while collected the majority of the data using a widefield system [72, 145, 163, 164]. A comparison of data collected of cells expressing a mitochondrial sensor on a widefield system or confocal system is shown in Figure 2.4. While the mitochondrial localization is much more obvious in the confocal images, the SNR is better in the widefield data. Two widefield microscopy systems, used in our laboratory, are

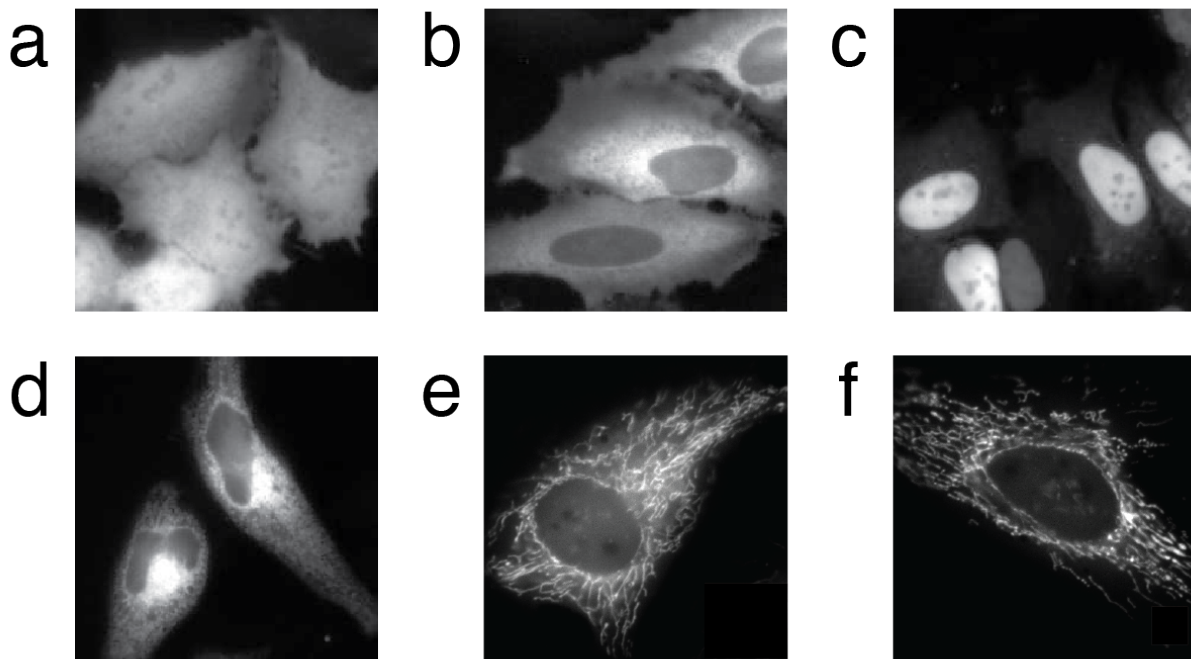


Figure 2.2: Images of HeLa cells transfected with subcellularly targeted sensors. a) Untargeted sensors are found in both the cytosol and nucleus. b) Sensors with an N-terminal nuclear export signal (MLQLPPLERLTLSDP) are retained in the cytosol. c) Sensors with an N-terminal nuclear localization sequence (MPKKKRKVEDASDPM) are retained in the nucleus. d) Sensors with an N-terminal calreticulin signal sequence (MLLPVLLLGLLGAAAD) and a C-terminal ER-retention sequence (KDEL) localize to the ER. e) and f) A significant fraction of mitochondrial sensors are found in both the cytosol and mitochondria, but changing the transfection conditions can result in good mitochondrial localization.

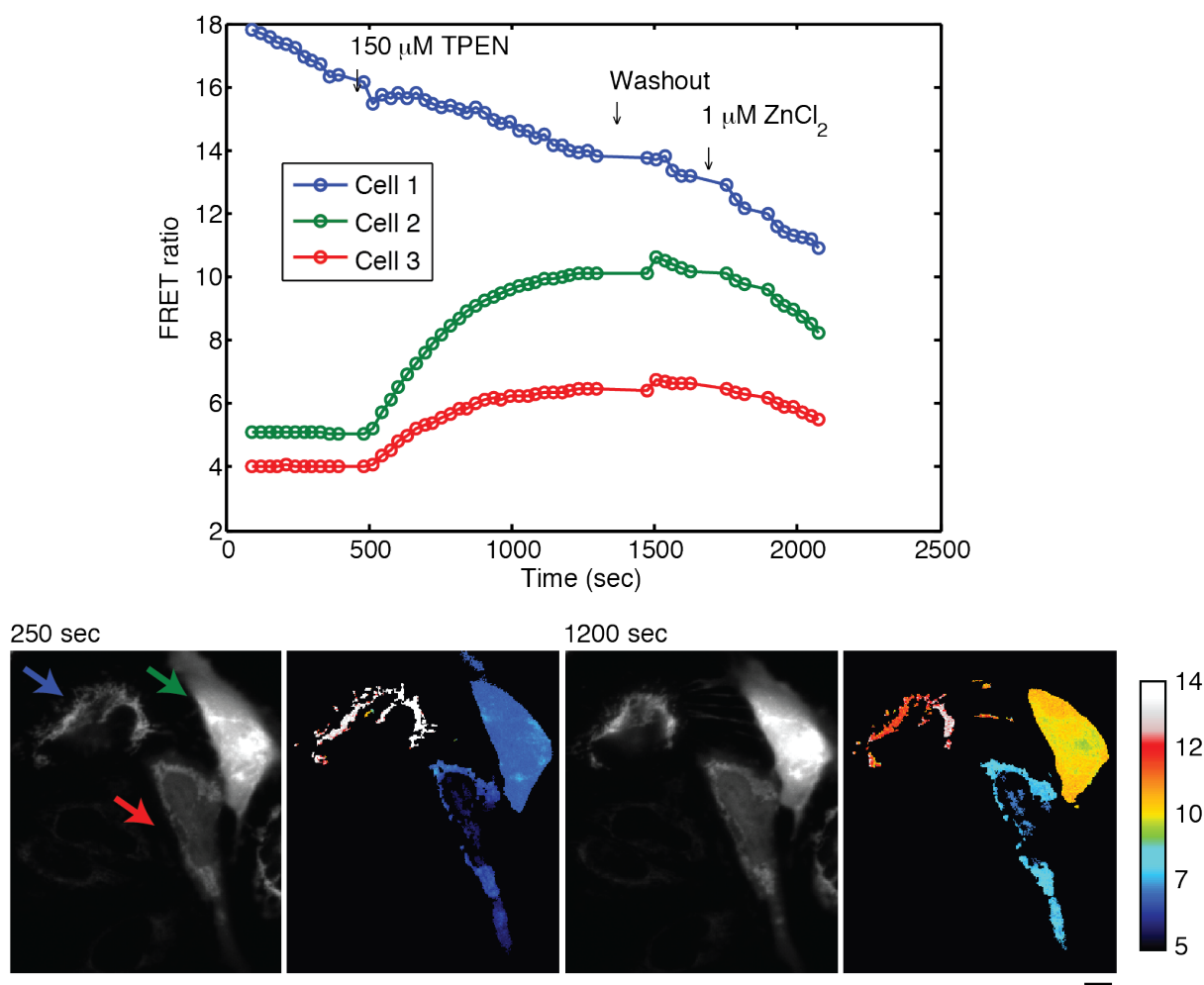


Figure 2.3: Sensor mislocalization affects its response to changes in $[\text{ion}]_{\text{free}}$. HeLa cells were transfected with mito-ZifCV1.173, a sensor that has an N-terminal mitochondrial matrix localization sequence (Section 3.4.1). This sensor has an inverted response to Zn^{2+} , and so R increases concomitantly with a decrease in $[\text{Zn}^{2+}]_{\text{free}}$. The plot shows that Cell 1, in which mito-ZifCV1.173 is correctly localized, displays a much higher R at rest than Cells 2 and 3, in which the sensor appears to be in both the mitochondria and cytosol. Images of the YFP intensity and pseudocolored ratiometric images at 250 and 1200 sec are displayed below the plot. The calibration bar shows the colors that correspond to different R , and a $10 \mu\text{m}$ scale bar is shown below the images.

described in further detail in Section C.2.

In some cases, confocal microscopy may result in a greater SNR than widefield microscopy. This is true when imaging membrane-targeted sensors [143, 165, 166]. Imaging of tissues or other thick samples often requires two-photon imaging to increase the depth of light penetration [138, 140]. Another consideration is that detection of rapid signal fluctuations, due to movement or changes in FRET ratio, may require simultaneous measurement of YFP FRET and CFP emission. This is possible using confocal microscopy, a dual-view emission system (Section C.2), or a two-camera system [155, 160]. Methods for collecting and analyzing data from a dual-view emission system have been included in this thesis (Section 2.5 and Appendix B). Lastly, environmental chambers that control temperature, %CO₂, and humidity should be used for long-term imaging or any temperature-dependent experiment.

2.3.3 Optimization of Image Acquisition

Before beginning a live-cell imaging experiment, image acquisition settings should be optimized to minimize photobleaching and phototoxicity and to obtain an adequate signal. The same acquisition settings on the same microscope should be used for all experiments. Furthermore, it is good to be aware of when the bulb of an arc lamp has been changed because this can change the light intensity emitted by the lamp.

The CFP and YFP FRET fluorescence intensity of the sensor should not saturate the camera and ideally each signal should be at least two times the background intensity. Increasing the excitation light intensity or exposure time can increase the fluorescence intensity captured in an image, but it can also lead to photobleaching and phototoxicity, which can affect cellular phenotypes and lead to artifacts. Phototoxicity can be decreased or eliminated by decreasing the exposure time, decreasing light intensity (using neutral density filters), or increasing the acquisition interval [149, 167].

One way to identify the best acquisition settings is to acquire YFP FRET, CFP, and YFP images of resting cells that express the sensor (excitation and emission filter settings can be found

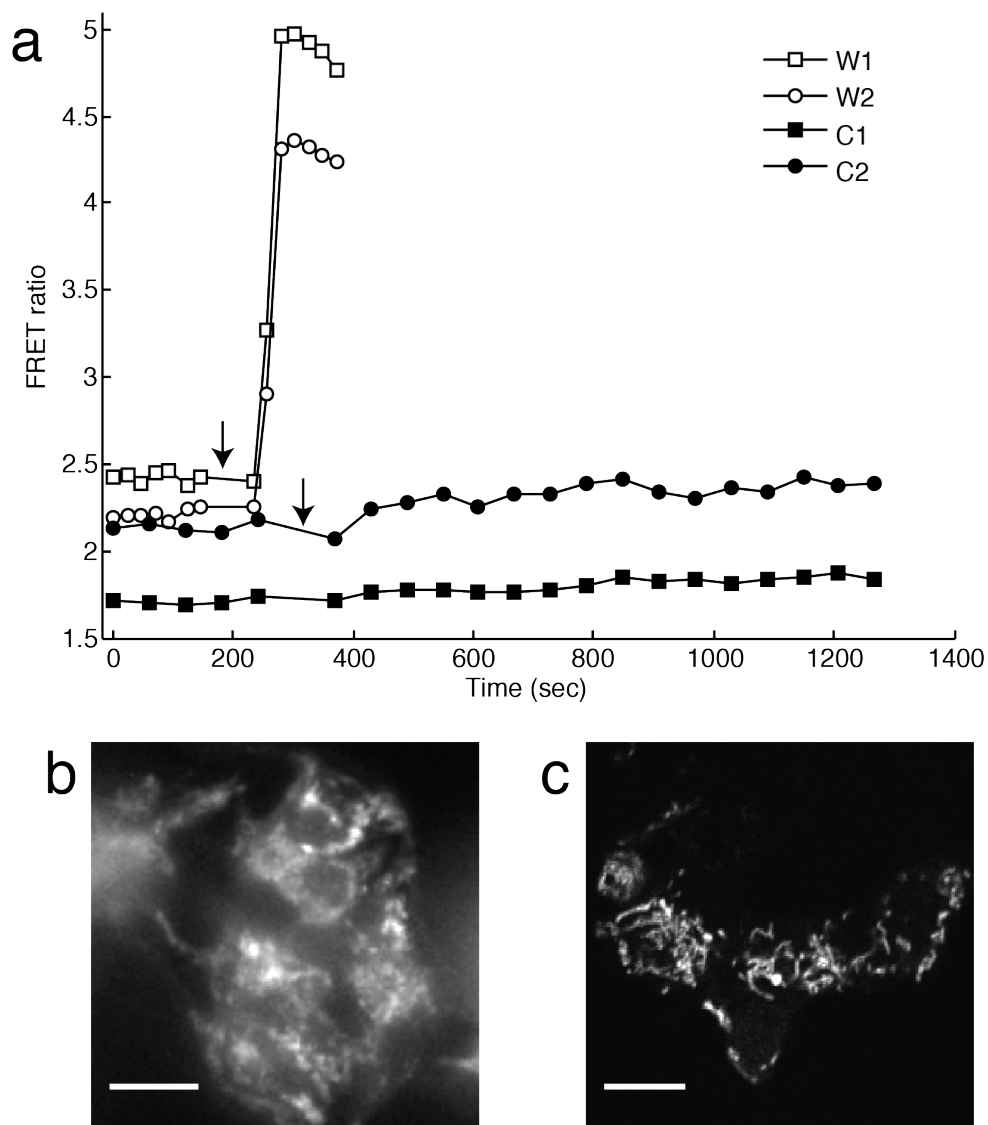


Figure 2.4: Comparison of FRET sensor results on widefield and confocal microscopy systems. Panel a) shows the change in mean R of single cells when $5 \mu\text{M}$ pyrithione is added (vertical arrows) to MIN6 cells expressing mito-ZapCY1. W1 and W2 are two different cells in the cluster of cells shown in b), that were imaged on a widefield microscope; C1 and C2 are single cells, in the field of view shown in c), imaged with a laser-scanning confocal microscope. The addition of pyrithione results in a rapid increase in $[\text{Zn}^{2+}]_{\text{free}}$ (Section 3.4.2), but this change is not apparent in cells monitored by confocal microscopy. However, the mitochondrial localization of mito-ZapCY1 is much clearer in c). The scale bars represent $10 \mu\text{m}$.

in Section C.2). Typically, resting cells do not have fluctuations of Ca^{2+} or Zn^{2+} , and so one can assume R should not change over a short time interval of 3-5 min. The YFP images are used to monitor photobleaching; this intensity is independent of FRET changes and is dependent on the concentration of fluorescent YFP in the cell. Many software programs controlling image acquisition allow the investigator to select regions of interest and calculate the ratio of two images or regions of interest (ROIs) during acquisition. This function is helpful because it allows the investigator to observe the sensor response during the experiment. An unstable R is usually the consequence of too much light exposure. Decreasing the frequency of image acquisition, decreasing the exposure time, or using a neutral density filter can be very helpful. If it is not possible to obtain a stable FRET ratio, data can be corrected off-line [162]. Typically, several iterations of acquiring a set of images and adjusting acquisition parameters are required.

2.3.4 Calibration of FRET Sensors in Cells

The sensor calibration is used to measure R_{min} and R_{max} , and these values, along with the K_D' of the sensor, are used to convert R to $[\text{ion}]_{free}$. Accordingly, identifying the conditions needed to deplete or saturate sensors (in cells) of the ion of interest are critical to accurate estimation of $[\text{ion}]_{free}$. R_{min} and R_{max} can vary from cell to cell, so they should be measured at the end of every experiment. Furthermore, R_{min} and R_{max} can be used to calculate the DR of the sensor and evaluate the functionality and performance of the sensor in both qualitative and quantitative experiments. The first part of this section is an overview of the sensor calibration protocol, and the second section will discuss ways to optimize this protocol for a particular sensor and cell type.

Sensor calibration protocol. When the cell density and sensor expression level are appropriate (usually 24-72 hours after transient transfection), the cell culture media is removed and cells are washed 3-5 times in imaging buffer. Examples of different imaging buffers can be found in Section C.4. Optically clear solutions are preferred for cellular imaging because the autofluorescence of phenol red and serum in complete media increases background fluorescence. In addition, components of complete media, such as amino acids and proteins, bind metal ions and can affect

sensor calibrations. Our laboratory routinely uses HEPES-buffered Hank’s Balanced Salt Solution (HHBSS) as our imaging solution. A 35 mm imaging dish comfortably holds 2 mL media and is amenable to manual mixing and changing of solutions.

Next, R_{min} is measured by chelating intracellular Ca^{2+} or Zn^{2+} . This can be done by carefully washing cells 3-5 times in fresh imaging buffer, without moving the imaging dish, before adding the appropriate chelating solution, such as the one described in Table 2.1. After the last wash, 1 mL of imaging buffer is added to the imaging dish. A 2X concentrated chelating solution in 1 mL of imaging buffer is made and added drop by drop to the imaging dish. When working with Ca^{2+} sensors, the addition of ionomycin will initially increase R in the cytosol, nucleus, and mitochondria due to the permeabilization of the ER and release of Ca^{2+} stores. Images are acquired until R reaches its minimum (5-60 min, depending on the sensor and cell type). An alternative is to monitor R for 15-20 min, fit the data to an exponential decay, and extrapolate to R_{min} .

Table 2.1: Reagents used to determine R_{min} and R_{max} of cytosolic Ca^{2+} and Zn^{2+} sensors. These concentrations have been optimized for HeLa cells transfected with D3cpV (Ca^{2+} sensor) or ZapCV2 (Zn^{2+} sensor). Other cell types or sensors may require different concentrations of these reagents or alternative reagents (see Table 2.2).

	Reagent	Stock concentration	Working concentration	Volume added to 2 mL buffer	Imaging buffer
R_{min} (Zn^{2+})	TPEN	25 mM	50-150 μ M	4-12 μ l	HHBSS
R_{max} (Zn^{2+})	Pyridithione	500 μ M	1-5 μ M	4-20 μ l	Phosphate-free HHBSS
	$ZnCl_2$	400 μ M	5 μ M	50 μ l	
R_{min} (Ca^{2+})	Ionomycin	1 mM	5 μ M	10 μ l	Ca^{2+} free HHBSS
	EGTA	0.5 M	5 mM	20 μ l	
R_{max} (Ca^{2+})	Ionomycin	1 mM	5 μ M	10 μ l	HHBSS
	$CaCl_2$	1 M	5 mM	10 μ l	

A similar procedure is used to measure R_{max} following the measurement of R_{min} . The cells

are washed 3-5 times with fresh imaging buffer to remove the excess chelator. Then, an excess of Ca^{2+} or Zn^{2+} and an ionophore or permeabilizing agent are added to the imaging buffer to saturate the sensor (see an example in Table 2.1). The rapid influx of ions, especially Ca^{2+} ions, when measuring R_{max} usually causes membrane permeabilization and cell death within minutes. Therefore, R_{max} is usually measured at the end of the experiment.

To calibrate ER-targeted Ca^{2+} sensors, R_{max} is measured first. Since the ER contains high amounts of Ca^{2+} under resting conditions, and the FRET based Ca^{2+} sensor (D1ER) is almost or fully saturated [144], it is difficult to increase the level of Ca^{2+} in the ER. Note that addition of ionomycin and Ca^{2+} will actually facilitate release of Ca^{2+} from the ER, and after such treatment, it is difficult to attain the original resting ratio before cell death. Thus, to measure R_{max} , our protocol involves permeabilizing the plasma membrane exclusively and adding Ca^{2+} , Mg^{2+} , and ATP to facilitate uptake of Ca^{2+} into the ER by the sarco/endoplasmic reticulum Ca^{2+} -ATPase (SERCA). As a last resort, if it is not certain R_{max} has been attained, I perform a partial calibration in which I measure R and R_{min} and report the relative changes as $\Delta R = R - R_{min}$. This allows quantitative comparison of the relative amount of Ca^{2+} in different cell types or under different environmental conditions, but does not allow for conversion to $[\text{Ca}^{2+}]_{free}$.

A general image analysis workflow is shown in Figure 2.5. After image acquisition, ROIs are defined in the field of view, and the mean intensity in each ROI is measured in every image. The mean R of each ROI is calculated using Equation 2.1.

$$R = \frac{FRET - BG_{FRET}}{CFP - BG_{CFP}} \quad (2.1)$$

The background intensities (BG_{FRET} and BG_{CFP}) are subtracted from the mean intensities of each ROI in the CFP (CFP), YFP FRET ($FRET$), and YFP images, and R is calculated by dividing the ROI's background-subtracted mean intensity in the YFP FRET image by that in the CFP image at each time point. Then, these results are visualized by plotting R over time. A detailed explanation of how to select and analyze ROIs in ImageJ can be found in Section B.1, and automation of this analysis is discussed in Section 2.5. Then, R_{min} , R_{max} , and DR can be

determined for each ROI. DR can be defined as Equation 2.2, 2.3, or 2.4. These results are used to evaluate different sensor calibration protocols and identify the best conditions; after calibration conditions are standardized, the sensor calibration data can be used to estimate $[\text{ion}]_{\text{free}}$ (Section 2.3.5).

$$\text{Dynamic Range} = \frac{R_{\text{max}}}{R_{\text{min}}} \quad (2.2)$$

$$\text{Dynamic Range} = R_{\text{max}} - R_{\text{min}} \quad (2.3)$$

$$\text{Dynamic Range} = \frac{R_{\text{max}} - R_{\text{min}}}{R_{\text{min}}} \quad (2.4)$$

Optimization of the sensor calibration protocol. A sensor calibration is optimized by adjusting the reagents (and their working concentrations) used to deplete or saturate the sensor, the duration of the chemical perturbations, or the order of the perturbations (*i.e.* measuring R_{min} or R_{max} first). A metric, such as the DR, can be used to evaluate different calibration conditions and select the best ones. The DR can also be used to compare the sensor’s response to that achieved in previously published work. Then, the same conditions should be used consistently throughout the series of experiments using a specific sensor and cell type.

Of note, R_{min} and R_{max} need not be consistent from cell to cell as long as the DR is comparable. Sources of variation in R likely include partial proteolysis or oxidation of sensors in different cells. Cell-to-cell heterogeneity in R is not as apparent when R is converted to fractional saturation. For example, in one field of view of cells expressing the Zn^{2+} sensor mito-ZapCY1, R_{min} was 1.9 ± 0.1 and R_{max} was 6.5 ± 0.8 . When fractional saturation of mito-ZapCY1 in resting cells is calculated from R_{min} and R_{max} of each cell (see Equation 2.5), its coefficient of variation is 0.2; calculated from population average R_{min} and R_{max} , it is 0.3. The range of R_{min} and R_{max} values and the benefit of performing single-cell calibrations can be appreciated in Figure 2.6.

$$\text{Fractional Saturation} = \frac{R - R_{\text{min}}}{R_{\text{max}} - R_{\text{min}}} \quad (2.5)$$

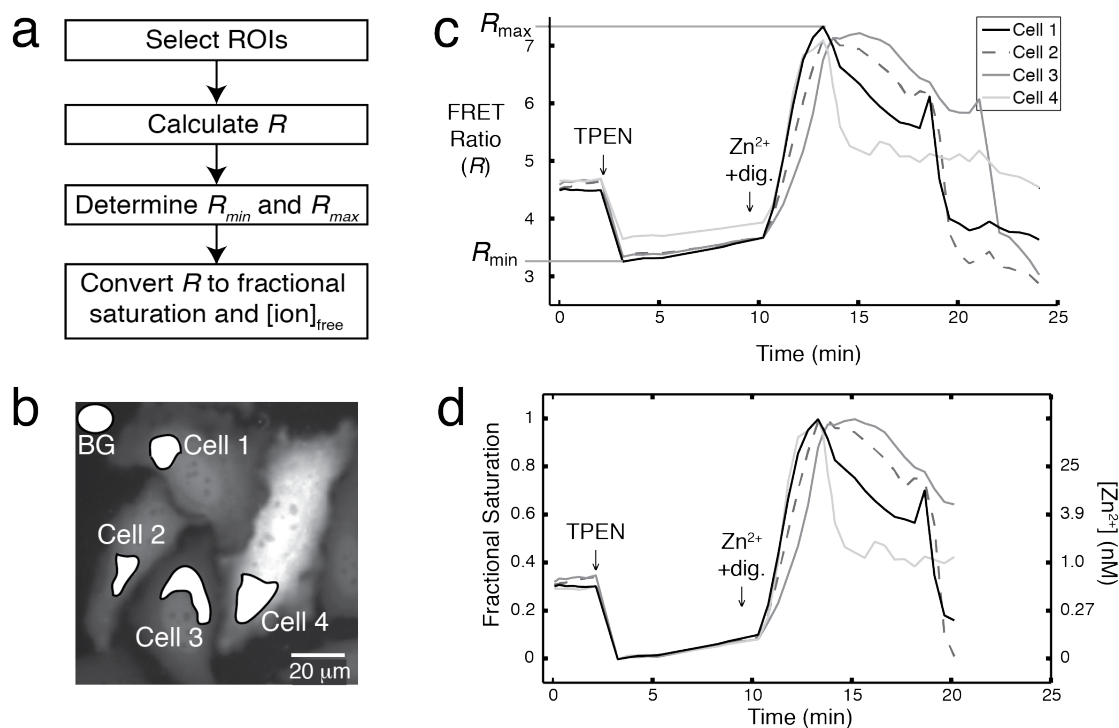


Figure 2.5: Analysis of imaging data from FRET sensor calibrations. The major steps in this analysis are listed in a). b) A background (BG) ROI and an ROI for each cell are defined within the acquired images. These data are taken from a calibration of the Zn^{2+} sensor ZapCV2 in HeLa cells. The mean intensities of these ROIs in the FRET and CFP images are used to calculate R . c) The mean R of each cell is plotted over the course of the sensor calibration, and each line in the plot corresponds to R of an ROI in a different cell. Notice the relatively stable R before any perturbations, the decrease upon the addition of $150 \mu\text{M}$ TPEN, and increase upon the addition of $20 \mu\text{M}$ ZnCl_2 and $10 \mu\text{M}$ digitonin. R_{min} is reached ~ 3 min and $R_{max} \sim 13$ min. d) R values are converted to fractional saturation of the sensor using R_{min} and R_{max} and $[\text{Zn}^{2+}]_{free}$ using the sensor's K_D' and n . The steps in this analysis are described in Sections 2.3.4 and 2.3.5.

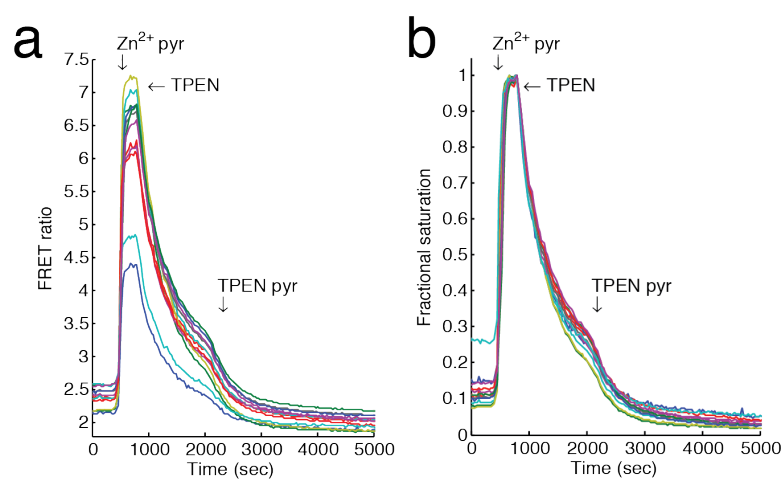


Figure 2.6: Comparison of cell-to-cell variability in sensor calibration results plotted in terms of R or fractional saturation. HeLa cells transfected with mito-ZapCY1 were subjected to treatment with $5 \mu\text{M}$ ZnCl_2 and $1 \mu\text{M}$ pyrithione, $150 \mu\text{M}$ TPEN, and $150 \mu\text{M}$ TPEN and $1 \mu\text{M}$ pyrithione. The same results are plotted in terms of R in a) and fractional saturation in b). Each line corresponds to the mean R of one cell.

Ideal calibration conditions result in a DR that is consistent among cells, experiments, and published values. The chemical perturbations should result in reaching R_{min} and R_{max} as quickly as possible while keeping cells intact and attached to the dish. Ratiometric sensors are much less sensitive to changes in shape and thickness, and therefore R_{min} and R_{max} can be measured even if cells are shrinking or changing in shape. When measuring R_{max} , sometimes R spikes and declines before reaching a plateau. This phenomenon typically arises because the cell dies before the sensor has an opportunity to be saturated. The solution is to optimize the concentration of ion and ionophore used in the calibration. Table 2.2 lists reagents that have successfully been used in sensor calibrations. Some reagents are better suited to calibrations of sensors targeted to organelles. For example, digitonin can be used to permeabilize the plasma membrane, but it is less effective in permeabilizing the mitochondrial inner membrane before cells detach from the dish. Pyrithione is relatively stable in solution and can be kept at 4 °C for weeks, but ionomycin and alamethicin should be aliquoted for single use only and stored at -20 °C. In our experience, adjusting the concentration of $ZnCl_2$ used to obtain R_{max} can be very useful. R increases to a much more stable maximum when 5 μM rather than 100 μM $ZnCl_2$ (with 1 μM pyrithione) is used to calibrate mito-ZapCY1 in HeLa cells. Once the sensor calibration conditions have been chosen, a calibration performed at the end of an experiment can be used to convert R to $[ion]_{free}$.

2.3.5 Estimation of Ion Concentrations

When a sensor calibration is performed at the end of an experiment and the K_D' of the sensor is known, R can be converted to $[ion]_{free}$. Section 2.3.4 describes how to optimize the protocol for consistent R_{min} and R_{max} measurements. It is equally important to use an accurate K_D' . The K_D' s of most Ca^{2+} and Zn^{2+} sensors have been published; these values are tabulated in Tables 1.5 and 1.6. It is also possible experimentally determine the K_D' under the same conditions used in an experiment (*i.e.*, *in situ*; see protocol in Section 2.4). The first part of this section explains how to convert R to $[ion]_{free}$, and the second part of this section discusses important controls to make

Table 2.2: Reagents used to calibrate Ca^{2+} and Zn^{2+} sensors. These reagents must be optimized for each sensor and cell type [149, 168–170].

	Reagent	Final concentration	Notes about usage
Chelators	EGTA	1-5 mM	Membrane-impermeable chelator that is selective for Ca^{2+} over Mg^{2+} ; pH dependent; also chelates Zn^{2+}
	BAPTA	0.5-1 mM	Membrane-impermeable, Ca^{2+} -specific, chelator that is less pH dependent than EGTA but expensive
	BAPTA-AM	5-50 μM	Membrane-permeable BAPTA
	TPEN	50-150 μM	Membrane-permeable Zn^{2+} chelator; chelates other heavy metal ions
Ionophores	Ionomycin	2-10 μM	More selective for Ca^{2+} over Mg^{2+}
	Bromo-A23187	0.1-20 μM	More effective than ionomycin at lower pH
	Pyrrithione	0.5-20 μM	Zn^{2+} ionophore
Permeabilizing agents	Digitonin	5-100 μM	Low concentrations permeabilize the plasma membrane; higher concentrations permeabilize internal membranes
	Alamethicin	40-50 $\mu\text{g/mL}$	Permeabilizes plasma membrane and outer mitochondrial membrane; used to reach R_{max} in sensors targeted to the mitochondrial matrix
	<i>S. aureus</i> α toxin	–	
Ions	ZnCl_2 or ZnSO_4	1-100 μM	Routinely used with pyrrithione or digitonin to reach R_{max}
	CaCl_2	5-20 mM	Routinely used with ionomycin to reach R_{max}
	Buffered Ca^{2+} and Zn^{2+} solutions	–	Used to control $[\text{Ca}^{2+}]_{free}$ and $[\text{Zn}^{2+}]_{free}$ at sub- μM concentrations
Other	Thapsigargin	0.2-4 μM	SERCA inhibitor that decreases both $[\text{Ca}^{2+}]$ and $[\text{Zn}^{2+}]$ in ER

sure the sensor itself is not perturbing the observed R and thus the estimation of $[\text{ion}]_{\text{free}}$.

Conversion of R to $[\text{ion}]_{\text{free}}$. Depending on the sensor, binding data can be fit to a one-site (*i.e.* one K_D') or two-site (*i.e.* two K_D' s) with or without the empirical Hill coefficient (n). If using a sensor with one K_D' , the $[\text{ion}]_{\text{free}}$ can be calculated by Equation 2.6.

$$[\text{ion}]_{\text{free}} = K_D' \left(\frac{R - R_{\text{min}}}{R_{\text{max}} - R} \right)^{\frac{1}{n}} \quad (2.6)$$

Equation 2.6 is related, but not identical, to Equation 2.7 derived for small molecule fluorescent indicators.

$$[\text{ion}]_{\text{free}} = K_D' \left(\frac{R - R_{\text{min}}}{R_{\text{max}} - R} \right) \frac{S_{f2}}{S_{b2}} \quad (2.7)$$

This original expression contains an instrument factor ($\frac{S_{f2}}{S_{b2}}$) that naturally fell out of the derivation and represents the ratio of the fluorescence intensity of the free to bound sensor at wavelength 2 [171]. The instrument factor is absent from all expressions used to convert R to $[\text{ion}]_{\text{free}}$ because the genetically-encoded sensors don't adhere to a strict 1:1 complexation, an assumption used to derive the above expression.

If using a sensor with two K_D' s, the data are converted to fractional saturation using the experimentally derived R , R_{min} , and R_{max} values (see Equation 2.5). Then, an iterative approximation approach can be used to solve Equation 2.8 for $[\text{ion}]_{\text{free}}$. Iterative approximation involves making an initial guess for the $[\text{ion}]_{\text{free}}$, then calculating fractional saturation, and successively repeating that until the calculated and experimental fractional saturation are the same.

$$\text{Fraction Bound} = F_1 \frac{[\text{ion}]^{n_1}}{(K_D'_{1})^{n_1} + [\text{ion}]^{n_1}} + F_2 \frac{[\text{ion}]^{n_2}}{(K_D'_{2})^{n_2} + [\text{ion}]^{n_2}} \quad (2.8)$$

In Equation 2.8, F_1 and F_2 are scaling factors, n_1 and n_2 are empirical Hill coefficients, and $K_D'_{1}$ and $K_D'_{2}$ are dissociation constants. These calculations can be incorporated into automated data analysis.

Evaluating the effect of sensor concentration on $[\text{ion}]_{\text{free}}$ estimation. Perhaps one of the single greatest advantages of using ratiometric biosensors is that it is possible to rigorously define the intracellular concentration of the sensor and assess whether the sensor itself perturbs

$[\text{ion}]_{\text{free}}$. This can be done because the fluorescence intensity of the acceptor FP, upon direct excitation, is independent of the level of free ion within the cell and proportional to its concentration. In contrast, the fluorescence intensity of the donor FP is dependent on its concentration and the FRET efficiency. Thus, a standard curve relating the acceptor FP intensity to the sensor concentration can be made by measuring the intensity of purified sensor protein, at a range of known concentrations, using a fluorescence microscope under conditions identical to a live cell imaging experiment. The standard curve can then be used to calculate the sensor concentration from a fluorescence image of an unknown sample (*i.e.* a cell). This method necessitates creating microcuvettes with volumes similar to that of cell, as has been done using the wedge method [172, 173], glass capillaries [136], and microwells fabricated in polydimethylsiloxane [65]. Having a means to quantify the sensor concentration in cells allows researchers to assess whether the measured concentration is independent of the sensor's concentration. I have found that for most sensors under control of a standard CMV promoter there is a wide range of sensor expression levels, typically varying from 1 to 20 μM [65, 66, 136] and hence there is natural variation of sensor concentration that enables researchers to examine estimated ion concentration as a function of sensor concentration. For sensor concentrations ranging from 1 to 20 μM , I have observed little perturbation of resting ion measurement. In contrast, small molecule probes with acetoxymethyl (AM) esters are known to concentrate in cells at levels close to hundreds of μM [64, 169].

Thus, the fractional saturation of a sensor in cells should be plotted against the YFP intensity, which is proportional to the sensor concentration (fictional data are shown in Figure 2.7). If fractional saturation is constant over a range of YFP intensities, one can assume that $[\text{ion}]_{\text{free}}$ is not dependent on the sensor concentration and have greater confidence in estimated $[\text{ion}]_{\text{free}}$. On the other hand, if the fractional saturation depends on the sensor concentration, $[\text{ion}]_{\text{free}}$ may be inaccurate. One solution to this problem is to fit this dependence to a linear function and extrapolate to a value where there is no sensor [33, 136].

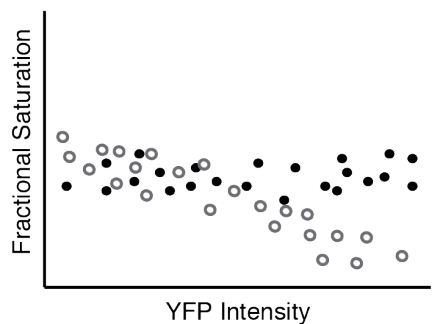


Figure 2.7: Evaluating the effect of sensor concentration on $[\text{ion}]_{free}$ estimation. Each cell's fractional saturation, before any perturbation, can be plotted against its mean YFP intensity, which is directly proportional to the sensor's intracellular concentration. In this plot, the fractional saturation of a sensor in resting cells is plotted against its YFP intensity (fictionalized data). In one experiment (open circles), increased sensor expression decreases its fractional saturation, indicating that sensor expression levels perturb resting $[\text{ion}]_{free}$. In another experiment (closed circles), the fractional saturation does not appear to depend on the sensor concentration, and so expression levels do not perturb resting $[\text{ion}]_{free}$.

2.4 Titration of FRET Sensors in Living Cells

This section explains how to adapt the sensor calibration protocol to a set of *in situ* titration experiments. The binding parameters derived from *in vitro* titrations of ratiometric Ca^{2+} and Zn^{2+} sensors are often used to convert experimental R to the corresponding $[\text{ion}]_{free}$ (Section 2.3.5). An *in situ* titration can be performed in cells when experimental conditions differ from *in vitro* conditions and accurate estimation of ion concentration is critical [72, 174–176].

The first part of this Section is a general protocol and a discussion of practical considerations for performing an *in situ* titration of a Ca^{2+} or Zn^{2+} sensor. The second part explains how to analyze the data and determine the K_D' . The success of this experiment is dependent on establishing conditions for reaching R_{min} and knowing the expected DR, both of which are discussed in Section 2.3.4.

2.4.1 Experimental Protocol for *in situ* Titrations

The sensor calibration, optimized in Section 2.3, can be easily adapted into an experiment that determines the *in situ* K_D' of a sensor. The difference is that R at different $[\text{ion}]_{free}$ is measured after obtaining R_{min} , and measurement of R_{max} is omitted. The R (or $R - R_{min}$) values are used to fit a single-site or two-site binding model and thus determine K_D' and n .

Cytosolic sensors under a CMV promoter are expressed in concentrations typically varying from 1 to 20 μM [65, 66, 136]. This is equal to or greater than the expected K_D' of most Ca^{2+} and Zn^{2+} sensors, and so one cannot assume $[\text{ion}]_{total} \approx [\text{ion}]_{free}$. For this reason, metal-chelate buffers are used to control the $[\text{ion}]_{free}$ in these experiments. For a sensor titration, at least 10 linearly-spaced concentrations should be chosen within the range of ~ 10 -fold above and below the expected K_D' . A thorough explanation and examples of metal-chelate buffer solutions can be found in Section A.4.1.

In this experiment, at least one 35 mm imaging dish is needed for each $[\text{ion}]_{free}$. All solutions and cells should be kept at the desired temperature, humidity, $\% \text{CO}_2$, and $\% \text{O}_2$. When the cell

density and sensor expression level are appropriate, the cell culture media is removed and cells are washed 3-5 times in 2 mL imaging buffer. R_{min} is measured by adding a chelating solution. This can be done by removing 1 mL of imaging buffer from the dish, mixing it with stock solutions to make a 2X concentrated chelating solution, and adding it drop by drop to the imaging dish (which already contains 1 mL imaging buffer). Table 2.3 specifies the reagents used to perform *in situ* titrations of cytosolic Ca^{2+} and Zn^{2+} sensors in HeLa cells.

Then, R is measured as cells are permeabilized in the presence of a metal-chelate buffer solution that precisely defines the $[\text{ion}]_{free}$. First, cells are washed 3-5 times with 2 mL imaging buffer to remove the chelating solution used to measure R_{min} . Then, 1 mL imaging buffer is removed from the dish and the appropriate amount of stock solutions are added to it to make a 2X metal-chelate buffer/permeabilizing solution. The 2X solution is added drop by drop to the imaging dish, and immediately afterwards images are acquired every 10-20 seconds until R stabilizes. This experiment is repeated with a fresh dish of cells for every $[\text{ion}]_{free}$ in the titration.

It is necessary to identify the most effective permeabilizing agent and appropriate working concentration empirically for each cell line. Some of the reagents available for *in situ* titrations are listed in Table 2.2. In our experience, an *in situ* titration of a mitochondrial matrix sensor is most successful using alamethicin as the permeabilization agent, which effectively permeabilizes the mitochondrial membranes to ions and small molecules while retaining the sensor in the matrix (Chapter 3 and [170]). Excellent additional resources for parameters to optimize for *in situ* calibrations include a paper by Thomas *et al.* that details *in situ* calibrations for a range of small molecule Ca^{2+} indicators [174].

2.4.2 Analysis of *in situ* Titration Data

The image analysis workflow, outlined in Figure 2.8, is similar to the sensor calibration analysis presented in Section 2.3.4. Instead of measuring R_{max} , an R_{final} is determined for each cell in an *in situ* experiment. Examples of *in situ* titration results are displayed in Figure 2.9.

Next, $R_{final} - R_{min}$ is plotted against $[\text{ion}]_{free}$ to generate a binding curve. The data are fit

Table 2.3: Reagents used to titrate Ca^{2+} and Zn^{2+} sensors *in situ*. These concentrations have been optimized for HeLa cells expressing cytosolic sensors. Other cell types or sensors may require different concentrations of these reagents or alternative reagents.

	Reagent	Stock concentration	Working concentration	Volume added to 2 mL buffer	Imaging buffer
$R_{\min}(\text{Zn}^{2+})$	TPEN	25 mM	150 μM	12 μl	HHBSS
$R_{\text{final}}(\text{Zn}^{2+})$	Digitonin	3 mM	10 μM	6.67 μl	Ca^{2+} -, Mg^{2+} -, and phosphate-free HHBSS
	Metal-chelate buffer	100 mM	1 mM	20 μl	
$R_{\min}(\text{Ca}^{2+})$	Ionomycin	1 mM	5 μM	10 μl	Ca^{2+} free HHBSS
	EGTA	0.5 M	5 mM	20 μl	
$R_{\text{final}}(\text{Ca}^{2+})$	Ionomycin	1 mM	5 μM	10 μl	Ca^{2+} - and Mg^{2+} -free HHBSS
	Metal-chelate buffer	1 M	100 mM	20 μl	

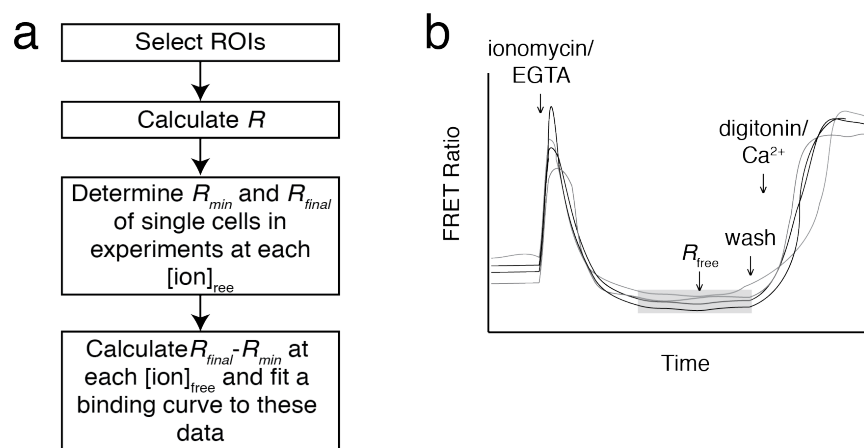


Figure 2.8: Image analysis of *in situ* titration data. a) Steps in the analysis of a set of *in situ* titration experiments. b) Fictional results from an *in situ* titration of a Ca^{2+} sensor. Each line is the mean R over time of a cell in a field of view. A solution of ionomycin and EGTA, is added to the imaging buffer, which initially increases R (due to permeabilization of the ER) but eventually stabilizes at R_{min} . The chelating solution is washed out of the imaging dish, and a solution of digitonin and buffered Ca^{2+} is added. Then, R stabilizes at R_{final} .

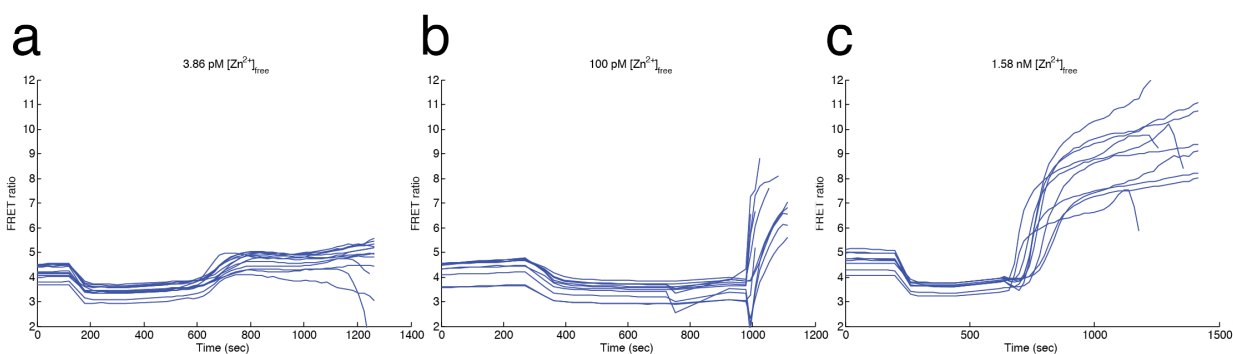


Figure 2.9: ZapCV2 titration experiments at three different $[\text{Zn}^{2+}]_{free}$ concentrations. HeLa cells expressing ZapCV2 in the cytosol were used to perform an *in situ* titration of the sensor. Data from three different imaging experiments are shown. In each experiment, R decreases after the addition of TPEN (membrane permeable) and increases after the addition of digitonin and a buffered $[\text{Zn}^{2+}]_{free}$ solution. In contrast to the results shown in Figure 2.8, the addition of TPEN does not initially increase R , it simply declines to R_{min} . Each line shows R of a single cell. R_{min} is the minimum R during TPEN treatment, and R_{final} is the maximum R after the addition of Zn^{2+} /digitonin and before cell death. $R_{final} - R_{min}$ is 1.55 ± 0.32 in a) (3.86 pM free Zn^{2+}), 3.38 ± 0.82 in b) (100 pM free Zn^{2+}), and 5.77 ± 1.18 in c) (1.58 nM free Zn^{2+}).

with a one-site (Equation 2.9) or two-site binding expression (Equation 2.10).

$$R_{final} - R_{min} = \Delta R \frac{[ion]^n}{(K_D')^n + [ion]^n} + C \quad (2.9)$$

$$R_{final} - R_{min} = F_1 \frac{[ion]^{n_1}}{(K_{D'1})^{n_1} + [ion]^{n_1}} + F_2 \frac{[ion]^{n_2}}{(K_{D'2})^{n_2} + [ion]^{n_2}} + C \quad (2.10)$$

To determine the most appropriate binding expression, the binding model used to fit *in vitro* data should be consulted first when it is available. Then, data are fit by several binding expressions, illustrated in Figure 2.10, using the least-squares method. As a general principle, one should use the simplest expression that yields the best fit. Lastly, binding models should be evaluated visually, since expressions with more parameters (*i.e.* two-site models with or without Hill coefficients) often yield better fits as judged by the R^2 value, but are sometimes physically unrealistic as shown in Figure 2.10. Figure 2.11 compares an *in situ* to an *in vitro* titration of NES-ZapCV2 in HeLa cells at room temperature (refer to the *in vitro* titration method and results in Appendix A).

2.5 Techniques for Image Analysis Automation

Standardizing the image analysis workflow is just as important as establishing experimental conditions. Automating an analysis, tailored to a specific type of experiment, is one way to keep consistent records of and standardize the results of numerous experiments. In addition, automation can save time and decrease user bias [177, 178]. Modern microscopes with motorized x-y-z stages can easily collect gigabytes of data in a matter of hours, and automated analysis can make large-scale, high-throughput experiments tractable for many laboratories. In this section, several image processing techniques will be introduced; these techniques can be combined to produce a standardized analysis that can be automated.

Many groups have implemented automated analysis and data collection, which has been the subject of many recent reviews [178–181]. Image analysis can be automated at many different levels: macros written for commercial software, like Microsoft Excel, MetaFluor (Molecular De-

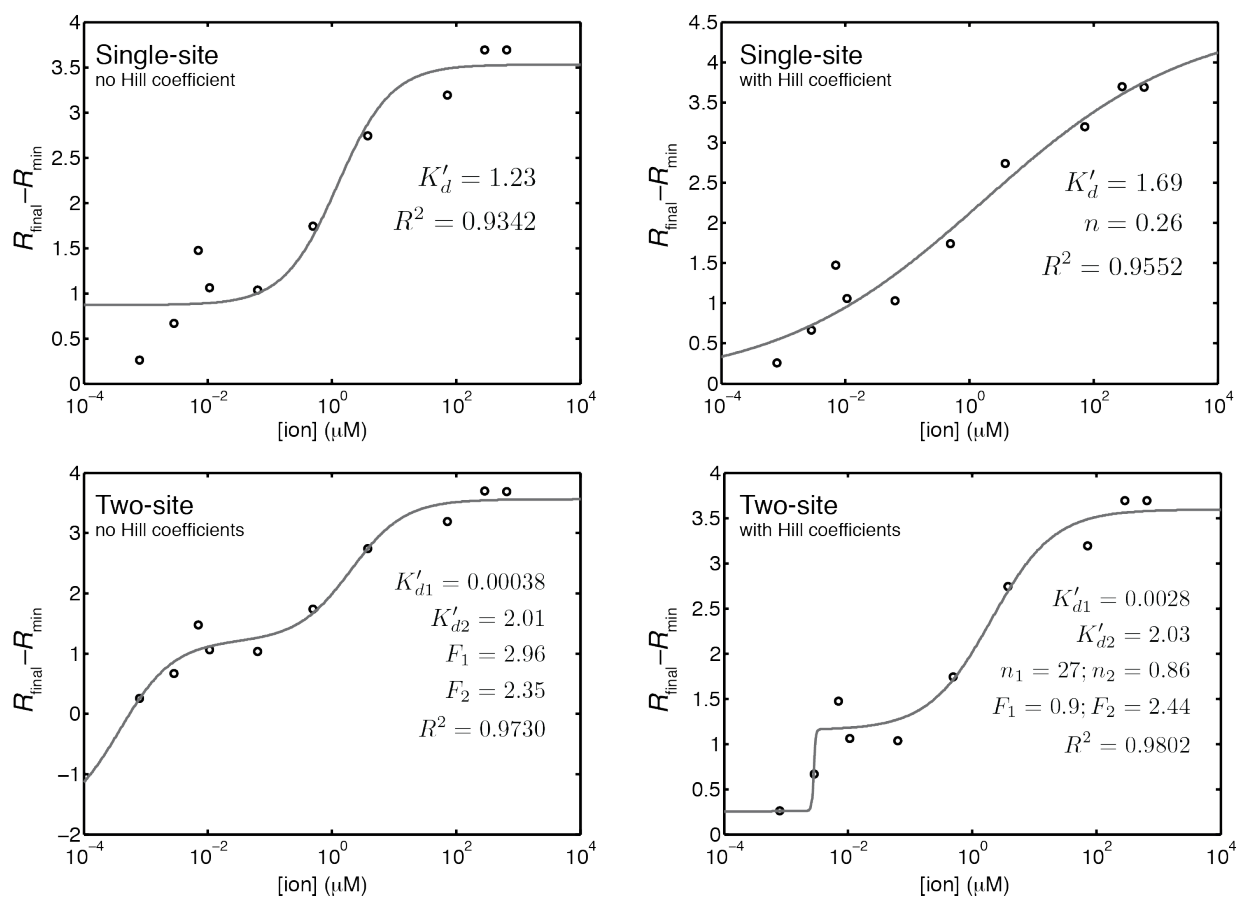


Figure 2.10: One- and two-site binding models fit to *in situ* titration data of a sensor with a $K_D' \sim 1 \mu\text{M}$. The same dataset was fit using the one-site or two-site model, with or without a Hill coefficient(s) (Equations 2.9 and 2.10).

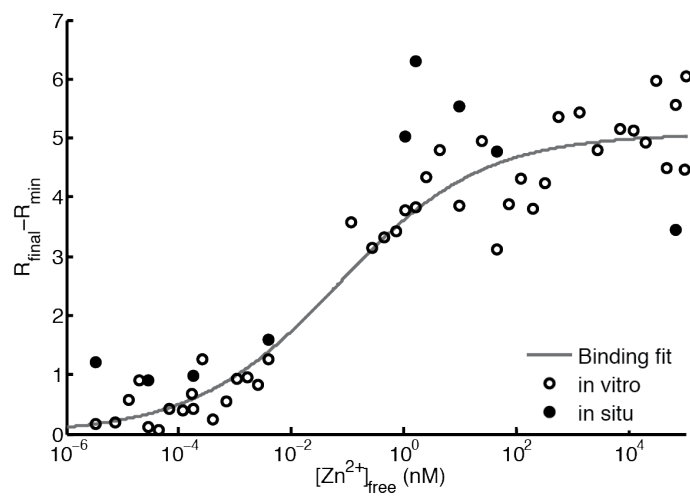


Figure 2.11: Comparison of *in situ* and *in vitro* titrations of NES-ZapCV2. The data are fit to a one-site binding expression with a K_D' of 70 pM and n of 0.34.

vices), or NIS Elements (Nikon Instruments); macros/plugins written for open-source software, like FIJI/ImageJ [182] or Icy [183]; functions and scripts in MATLAB (MathWorks); or a combination of several of these.

This approach is not without challenges for the wet-lab scientist, who may not have programming experience. Fortunately, many resources are available, including didactic courses and websites [184]. Several open-source software programs, such as FIJI [185] or CellProfiler [186], were developed as platforms, accessible to both computer scientists and wet-lab scientists, that encourage interdisciplinary collaboration [182, 187–189]. However, a basic knowledge of programming enables the wet-lab scientist to independently test and tailor different parts of the image analysis workflow.

This section presents several image processing techniques that have been useful for automating the analysis of experiments similar to those described in this Chapter. Figure 2.12 outlines how the different techniques in this section can fit together into a logical workflow for tracking R over time and creating images pseudocolored by R . Examples of the implementation of these techniques in ImageJ or MATLAB are included in Appendix B. Excellent reviews of additional techniques applicable to FRET sensor image analysis have been published [156, 160, 162].

2.5.1 Image Collection

Storing images in a standard format that contains the raw, uncompressed data facilitates automation of image analysis. The raw images contain quantitative information about the fluorescence intensity of the sample. The fluorescence emitted from a FRET biosensor is captured in a digital image made up of an array of pixels. Current microscopy systems capture digital images with a camera equipped with charge-coupled device (CCD) photon detector, which is a two-dimensional array of light-sensitive wells. During each image acquisition, each well collects electrical charge proportional to the incident light intensity, and the electrical signal is recorded as an intensity value corresponding to that particular well. The raw digital image is a representation of an array of integer intensity values, which are called pixels. Thus, the raw digital image contains quantitative information that is used to calculate R and thus the sensor's activity.

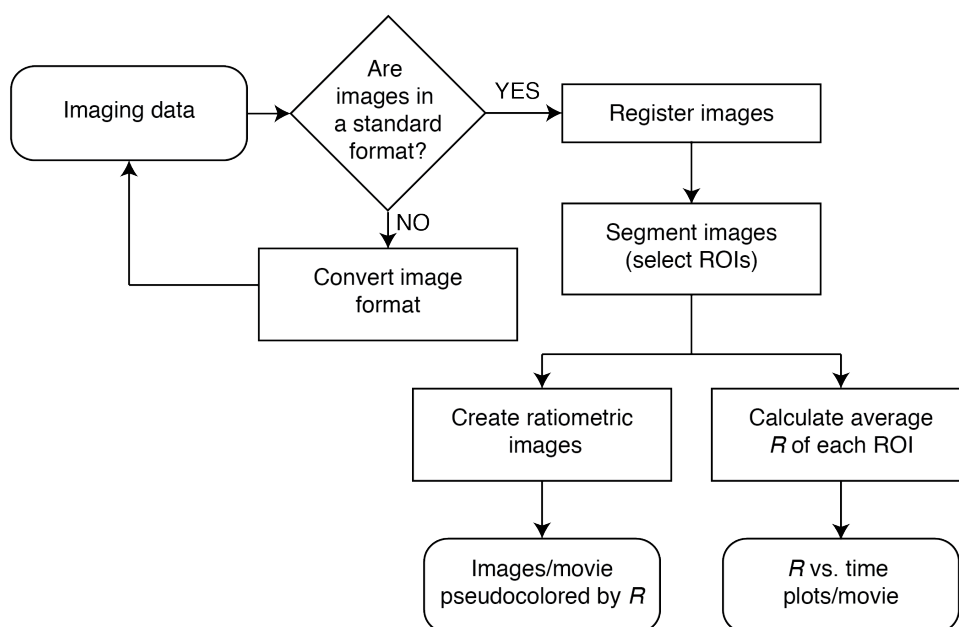


Figure 2.12: Automated analysis of imaging data from a ratiometric FRET sensor experiment. First, images are converted to a format that can be imported by different image analysis programs. Then, acceptor emission (YFP FRET) and donor emission (CFP) images are aligned in a process called image registration. ROIs are selected using automated segmentation. The segmented images can be used to create movies from ratiometric images and to calculate average R of each ROI. These techniques are discussed in this Section, and detailed protocols are in Appendix B.

Digital images are usually captured as 8-bit images (pixel values between 0 and 255), 12-bit images (pixel values between 0 and 4095), or 16-bit images (pixel values between 0 and 65535). Almost all microscopy systems are controlled by proprietary software, which save raw images with metadata in a proprietary image format. It is not difficult to mistakenly export these images in a format that rescales the images (*i.e.* changes the intensity values to increase their DR) or performs lossy compression on the image (*e.g.* JPEG compression). For quantitative image analysis, one must take care to perform the analysis on the raw images, which are often saved as .tiff files. An overview of different image data types and microscopy software programs can be found in [178, 180, 187, 190].

To address this issue, the Open Microscopy Environment has developed software called Bio-Formats to convert images saved in over 120 file formats to a standard format [191, 192]. Bio-Formats is compatible with several different image analysis programs, including MATLAB and ImageJ, and it can be very helpful for using the same analysis workflow on image data acquired with different microscopy systems.

2.5.2 Image Registration

It is important to register (*i.e.* align) the acceptor emission channel (YFP FRET) and donor emission channel (CFP) images as closely as possible because even sub-pixel misalignments can result in misleading edge effects, as demonstrated in Figure 2.13 and [133, 162]. This is particularly important when imaging samples with features that are only a few pixels in diameter, such as ER, vesicles, or mitochondria.

Registration is also necessary when acquiring images simultaneously with two cameras [160, 162] or with a dual-view emission splitting system, which acquires images in the two fluorescence channels simultaneously. The dual-view system can be easily misaligned and tedious to re-align; so, offline image alignment is more time-efficient.

Many methods for sub-pixel image registration have been developed for a variety of uses, which are reviewed in [193–197]. For quantitative analysis of FRET sensor images, it is usually sufficient to optimize a geometric transformation that maps each pixel of the CFP image (the

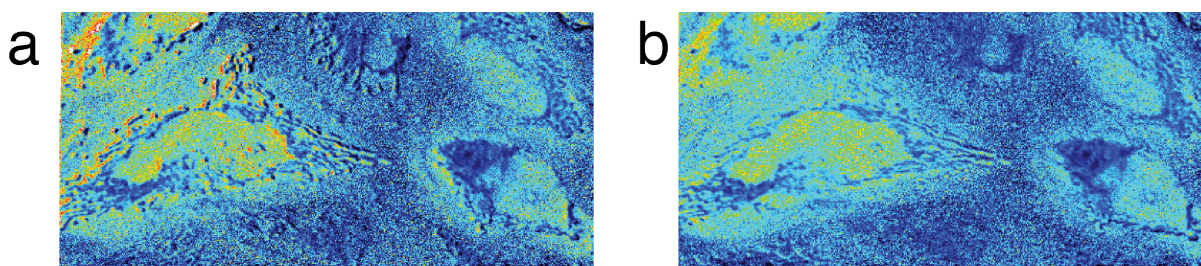


Figure 2.13: Edge effects are one consequence of the misalignment of YFP FRET and CFP images. Displayed is a ratiometric image created from YFP FRET and CFP images a) misaligned by 2 pixels and b) successfully aligned images. Sections 2.5.5 and B.8 describe how these ratiometric images are created from YFP FRET and CFP images.

distorted image) on to the YFP FRET image (the reference image). When one can assume that the YFP FRET and CFP images are misaligned in the same way throughout the experiment, the same geometric transformation can be applied to all of the CFP images in the experiment, which is much faster than aligning every pair of images in the series. The MATLAB Image Processing Toolbox (Version R2013b) includes the functions `imregtform` and `imwarp`, which optimize the geometric transformation and perform gray-level interpolation, respectively. An example of performing image registration in MATLAB can be found in Section B.4. Figure 2.14 shows the results of registering images with a dual-view emission system.

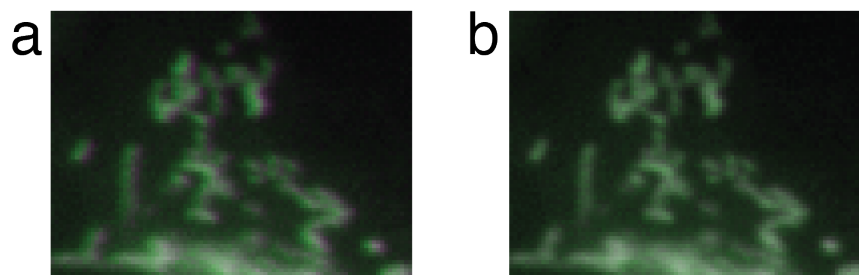


Figure 2.14: Overlay of FRET and CFP images before and after registration. The 2D correlation coefficient before registration is 0.9658; after registration it is 0.9785. The `imregtform` and `imwarp` MATLAB functions were used to calculate the geometric transformation to align the images, and the `imfuse` and `imshowpair` MATLAB functions were used to overlay the images. Section B.4 goes through this method of automated image registration.

2.5.3 Image Segmentation

Another critical step in image analysis is selecting objects of interest within an image—like a cell or organelle—and defining them as ROIs. ROIs can be drawn within an image or image sequence in image analysis programs. Then, features of each ROI, such as intensity, texture, or size, can be measured and exported to a data file. A simple workflow using ImageJ can be found in Section B.1.

However, manual selection of ROIs becomes tedious when a cell or subcellular organelle is changing shape, moving, or going in and out of focus during an experiment. In this situation,

automated ROI selection is more efficient, and takes much less time, and with automation, analysis of larger datasets becomes reasonable. Automated image segmentation has been reviewed extensively [178, 179, 196, 198], but these algorithms must be tailored to each type of experiment. Proprietary software programs are capable of applying several different types of segmentation methods, but it can be difficult to access or make changes to the algorithms they use. On the other hand, simple automated analysis workflows can be evaluated and implemented in ImageJ or MATLAB with better transparency.

One method that has worked well to segment nuclei, mitochondria, and cells of different sizes is to use MATLAB to perform top-hat filtering followed by image thresholding. A top-hat filter brings out elements smaller and brighter than a structuring element (*e.g.* a 2x2-pixel square); the size and shape of the structuring element can be adjusted to different types of foreground objects. Figure 2.15 shows how the size of the structuring element affects image segmentation. A global threshold for the filtered image can be computed using Otsu's method [199], and this can be used to make a binary mask. Uncomplicated scripting in MATLAB can be used to determine which structuring element works best for a specific experiment (see Section B.5).

Most experiments contain cells of different intensities, and so selecting a threshold based on the entire image will not segment all the cells in the same way (see Figure 2.16). Many solutions to this problem have been proposed, including adaptive threshold and seeded watershed algorithms, which have been reviewed elsewhere [178, 179, 200]. An approach that works for smaller-scale experiments is to divide the image into sections, each of which contains one cell. Segmentation is performed on each individual cell; the binary masks of each cell can be combined to make a binary mask containing all the cells in the image. This is shown in Figure 2.17 and explained further in Section B.6.

Equally important is the selection of a background ROI. The mean intensity of the background ROI in each image is used to perform background subtraction and accurately calculate R .

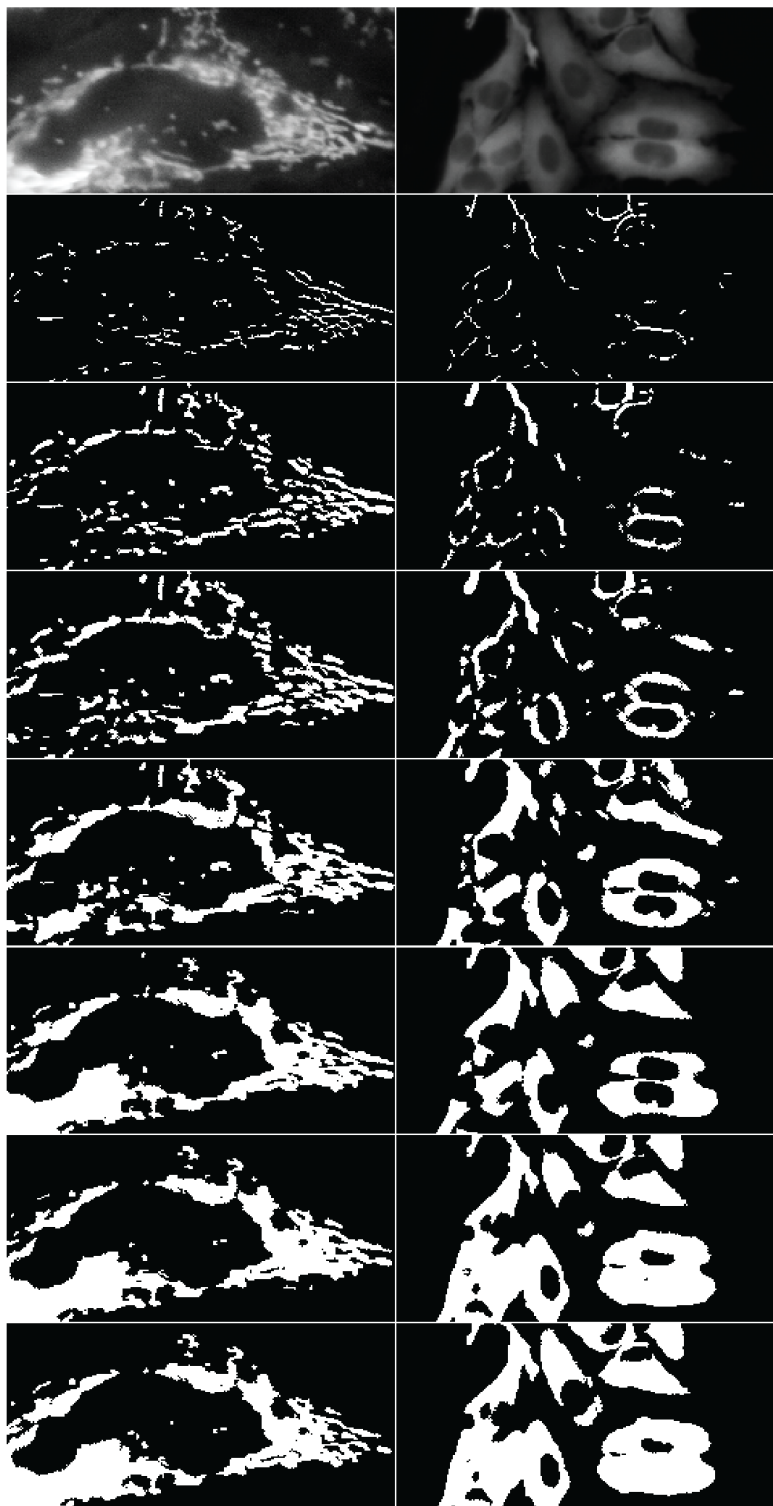


Figure 2.15: Comparison of top-hat filtering of mitochondrial and cytosolic sensor images with structuring elements of increasing size. From top to bottom, the structuring element used with the `imtophat` function was a diamond shape of 1, 3, 5, 10, 25, 50, or 100 pixels. A detailed protocol is included in Section B.5.

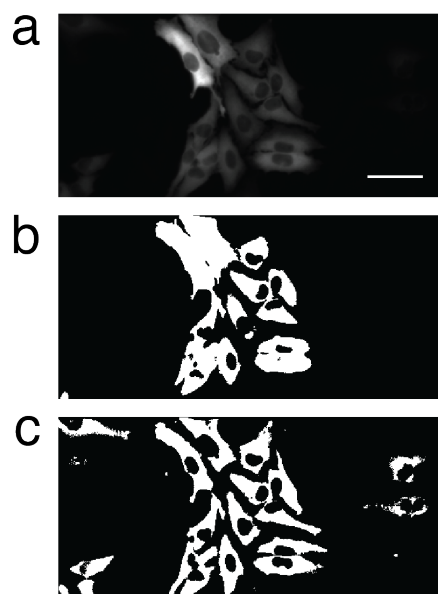


Figure 2.16: Comparison of global and adaptive thresholding of images of cells expressing a cytosolic sensor. The image in a) was thresholded using b) Otsu's method or c) adaptive thresholding using ImageJ.

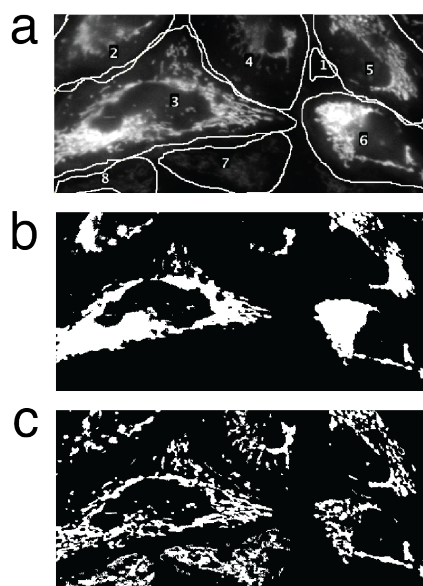


Figure 2.17: Single cells were thresholded individually and combined into one mask. a) The original image is divided into regions containing individual cells. A background ROI is also selected. b) Global thresholding of the image does not capture all cells. c) Segmentation of each cell region separately gives better results.

2.5.4 Automation of FRET Ratio Calculations

The endpoint for many experiments is the calculation of average R of each ROI over time. This information can be used to calculate R_{min} and R_{max} of sensor calibrations or titrations, the DR, and the fractional saturation of the sensor (as described in Sections 2.3 and 2.4). An example of a standardized plot of the results of an experiment is shown in Figure 2.18. MATLAB scripts that calculate these values from ROI intensity data and output this plot can be found in Sections B.2 and B.3.

Automated calculation of the mean intensities of an ROI (and consequently R) can be implemented by masking the aligned YFP FRET and CFP images with binary masks created during image segmentation. A more detailed description can be found in Section B.7.

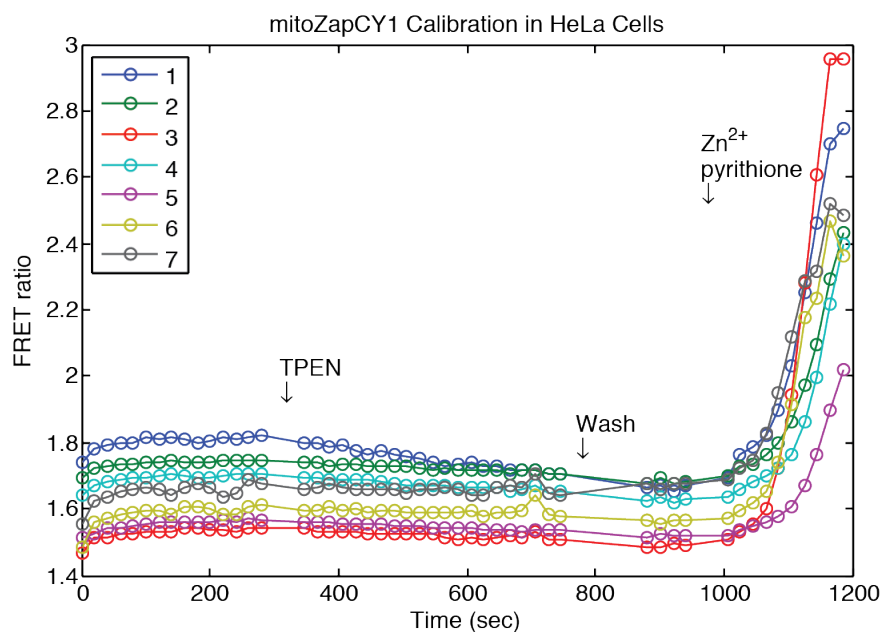


Figure 2.18: A customized MATLAB function was used to generate a standard labeled plot of the experiment shown in Figure 2.17. Each colored line corresponds to the average FRET ratio in mitochondria of a single cell in the field of view.

2.5.5 Creation of Images and Movies Pseudocolored by FRET Ratio

Another way to visualize the results of a FRET sensor experiment is to create images in which the cells (or organelles) are color-coded by R . To do this, each pixel of the aligned YFP FRET and CFP images are background-subtracted and divided (Equation 2.11).

$$R_{ij} = \frac{FRET_{ij} - BG_{FRET}}{CFP_{ij} - BG_{CFP}} SF \quad (2.11)$$

The background intensities (BG_{FRET} and BG_{CFP}) are subtracted from the mean intensities of each pixel at position (i, j) in the CFP (CFP) and YFP FRET ($FRET$) images, and R_{ij} calculated for every pixel. SF is a scaling factor that increases the DR of the ratiometric image. In our laboratory, R typically falls between 1.5 and 7, and images are made up of pixels with integer values. So, the ratios are multiplied by a scaling factor in order to expand the DR of the ratiometric image. This is sometimes called a floating-point correction [133, 162]. Without background subtraction, higher-intensity cells can appear to have higher R but ratiometric images are less noisy. However, it is visually misleading and not quantitative without background subtraction.

The background-subtracted ratiometric image often has hotspots in the background, and these can take the viewer's focus away from the features of interest. If this happens, the ratiometric image can be masked so that all the values outside of the ROI are replaced with 0. A ratiometric image that has been masked in this way is shown in Figure 2.19.

A series of ratiometric images can be assembled into a movie using ImageJ, complete with scale bars, calibration bars, and time stamps. Another way to visualize the changes in R is to save a series of plots (see Figure 2.20), the first plot containing just the first timepoint, the second containing the first two timepoints, *etc.* The series of plots can be combined with the series of images using the Combine function in ImageJ to make one movie. Appendix B includes a tutorial of how to add these finishing touches.

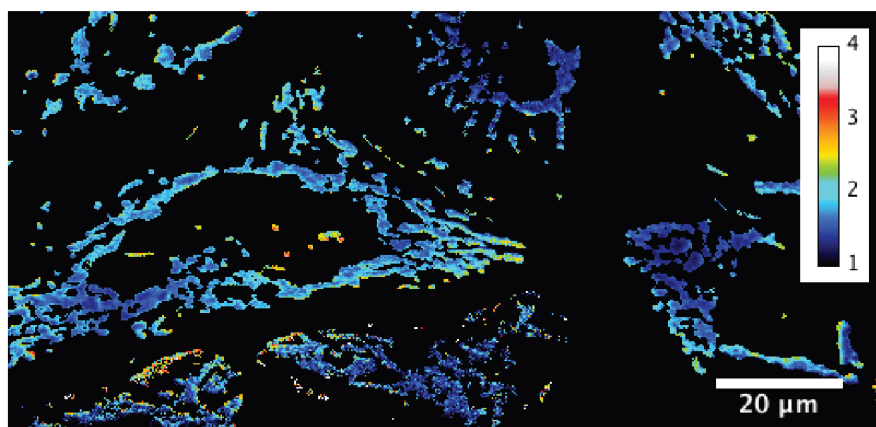


Figure 2.19: Ratiometric image of HeLa cells expressing mito-ZapCY1. This image was generated using an automated MATLAB script (see Section B.8). The colors correspond to R between 1 and 4. The scale bar represents 20 μm .

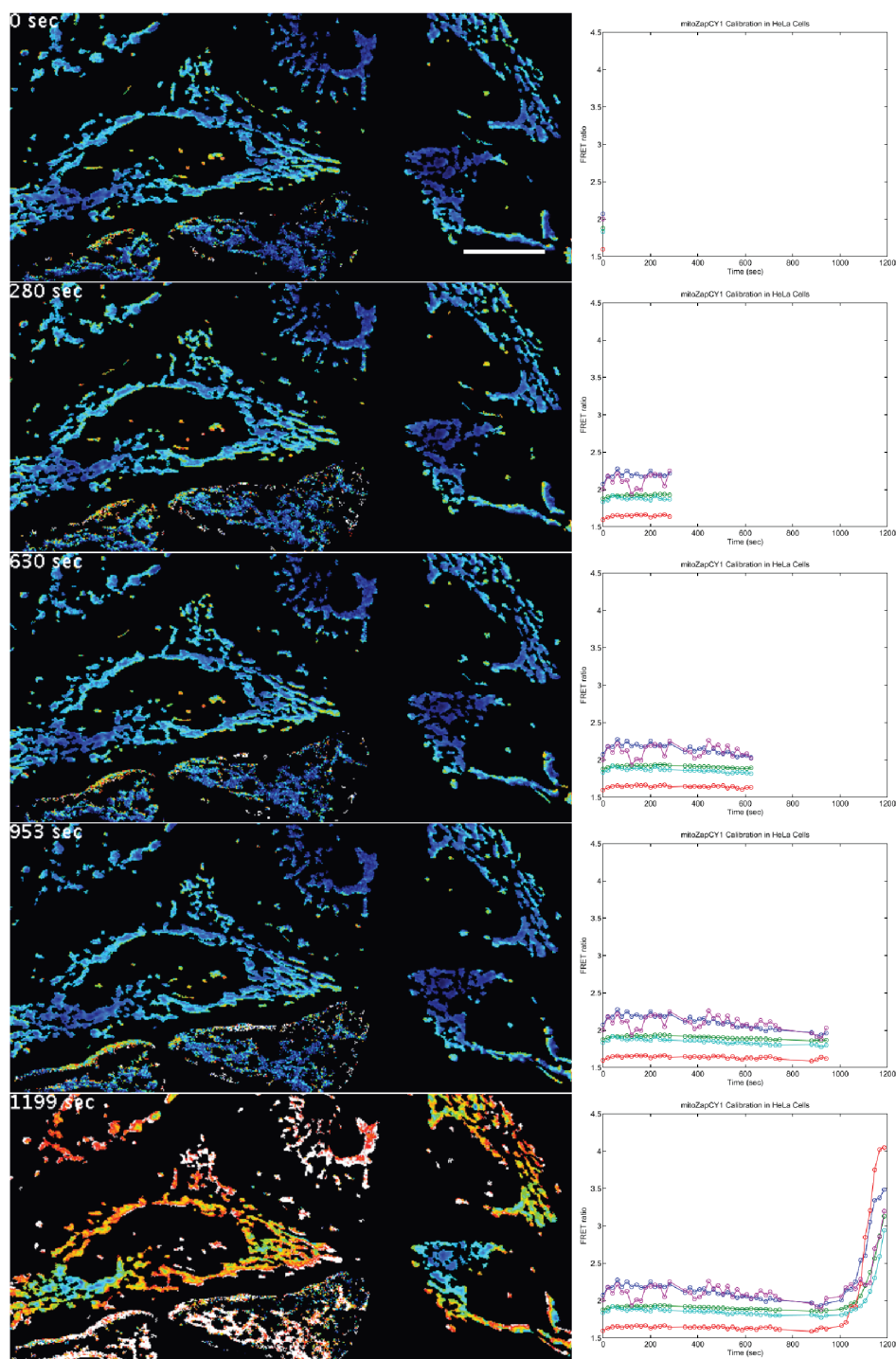


Figure 2.20: Frames from a movie of ratiometric images and corresponding R vs. time plots. HeLa cells, expressing mitoZapCY1, were treated with $150 \mu\text{M}$ TPEN and then with Zn^{2+} /pyrithione. A customized MATLAB script was used to generate the series of ratiometric images and R vs. time plots. The movie was annotated using ImageJ. The details of this protocol can be found in Sections B.8, B.10, and B.11.

2.6 Summary

Genetically-encoded, ratiometric sensors of metal ions are often used to quantitatively measure changes in ion concentrations in living cells. Optimization of imaging, calibration, and analysis can significantly improve the repeatability and precision of these experiments. This Chapter presents a workflow for performing this optimization, which was refined as the work for this thesis was performed. Determining the *in situ* K_D' under experimental conditions improves the accuracy of the estimation of ion concentrations, and so a protocol for an *in situ* titration is also included in this Chapter. Lastly, automation of some or all of the image analysis increases efficiency and standardizes the results. Techniques for automating image analysis are also discussed in this Chapter. The quality of data obtained from any experiment using a genetically-encoded FRET sensor is directly related to the correct use of the sensor. Thus, it is essential to perform an optimization, such as the one described in this Chapter, before embarking on a set of experiments using a FRET sensor to monitor ion concentrations in a particular cell type.

Chapter 3

New Sensors for Quantitative Measurement of Mitochondrial Zinc

3.1 Abstract

Zinc (Zn^{2+}) homeostasis plays a vital role in cell function, and the dysregulation of intracellular Zn^{2+} is associated with mitochondrial dysfunction. Few tools exist to quantitatively monitor the buffered, free Zn^{2+} concentration in mitochondria of living cells ($[\text{Zn}^{2+}]_{\text{mito}}$). I have validated three high dynamic range, ratiometric, genetically-encoded, fluorescent, Zn^{2+} sensors that I have successfully used to precisely measure and monitor $[\text{Zn}^{2+}]_{\text{mito}}$ in several cell types. Using one of these sensors, called mito-ZapCY1, I report observations that free Zn^{2+} is buffered at concentrations about 3 orders of magnitude lower in mitochondria than in the cytosol, and that HeLa cells expressing mito-ZapCY1 have an average $[\text{Zn}^{2+}]_{\text{mito}}$ of 0.14 pM, which differs significantly in other cell types. These optimized mitochondrial Zn^{2+} sensors could improve our understanding of the relationship between Zn^{2+} homeostasis and mitochondrial function.

3.2 Publication Status

Reproduced in part with permission, from Park JG, Qin Y, Galati DF, Palmer AE. New sensors for quantitative measurement of mitochondrial Zn^{2+} . *ACS Chem Biol.* 2012 Oct 19;7(10):1636-40. doi:10.1021/cb300171p. Epub 2012 Aug 10. PubMed PMID: 22850482. Copyright 2012 American Chemical Society.

3.3 Introduction

Zn^{2+} is a micronutrient that is required for human life, and deficiency can lead to impaired cognition, immune dysfunction, diarrhea, and death, particularly in children under the age of 5 years [2]. Although Zn^{2+} is essential for cell function, accumulation of Zn^{2+} to toxic levels leads to cell death. The human genome encodes two-dozen Zn^{2+} -specific transporters and many metal-buffering proteins, which are expressed in a tissue-specific manner [95]. Our current understanding of Zn^{2+} homeostasis is that intracellular Zn^{2+} is distributed into a large pool of structural or catalytic Zn^{2+} that is tightly bound, and two smaller pools of Zn^{2+} : free Zn^{2+} and exchangeable Zn^{2+} bound loosely to small molecule or protein partners [33,40]. Zn^{2+} homeostasis can be altered in diseases, such as neurodegeneration [9]. In order to effectively study Zn^{2+} biology, we must be able to observe and manipulate Zn^{2+} specifically with subcellular resolution.

Cellular Zn^{2+} homeostasis affects mitochondrial function through poorly understood mechanisms. Zn^{2+} toxicity can lead to the release of cytochrome c from the intermembrane space, caspase activation, and apoptosis [118,124,201]. Changes in Zn^{2+} availability can affect metabolism, including oxidative phosphorylation [202,203]. Intracellular Zn^{2+} can depolarize mitochondria and decrease mitochondrial movement [204–206]. Lastly, it is likely that mitochondria are a source and sink of Zn^{2+} in neurons and other cells [40,117,136,207]. To understand how Zn^{2+} homeostasis affects mitochondrial function, we must be able to measure and monitor mitochondrial Zn^{2+} .

Few tools exist to observe mitochondrial Zn^{2+} homeostasis in living cells with high specificity. Small-molecule, fluorescent probes are arguably the most popular tools. FluoZin-3 increases in intensity upon binding Zn^{2+} and has been used to observe free Zn^{2+} in isolated mitochondria [37,208]. Positively charged probes, such as RhodZin-3, concentrate within mitochondria of intact cells due to the negative mitochondrial inner membrane potential ($\Delta\Psi_m$) [37,209]. Consequently, it is problematic to monitor Zn^{2+} in depolarized mitochondria using such probes because a decrease in fluorescence intensity could be caused by either a decrease in Zn^{2+} or in $\Delta\Psi_m$. Other mitochondrial sensors consist of both a small-molecule fluorophore and a protein component, which

can be genetically targeted to mitochondria. This approach was used to target the fluorescent Zn^{2+} probe Zinpyr1 to mitochondria, and to exclusively express an excitation ratiometric Zn^{2+} sensor derived from carbonic anhydrase in mitochondria [67,210]. Other genetically encoded Zn^{2+} sensors, such as the eCALWY family, have not yet been targeted to mitochondria [72]. Our group previously constructed mito-ZifCY1 (renamed from mito-Cys₂His₂), a genetically-encoded, ratiometric, Zn^{2+} -specific sensor targeted to mitochondria, but its measurements are limited by its small dynamic range [136].

In this study, I show that increasing the dynamic range of genetically encoded Zn^{2+} sensors improves their precision. I make novel comparisons of the $[\text{Zn}^{2+}]_{\text{mito}}$ of different cell types using improved sensors. I find $[\text{Zn}^{2+}]_{\text{mito}}$ is about 3 orders of magnitude lower than the cytosolic free Zn^{2+} concentration and varies considerably among different cell types.

3.4 Results and Discussion

3.4.1 Sensor Design and Validation

The Zn^{2+} sensors constructed in this study are variants of previously published cytosolic ZapCY1 and ZifCY1 sensors, which respond specifically to Zn^{2+} over other biologically relevant divalent cations, including calcium, magnesium, iron, and copper [66, 136]. Our mitochondrial sensor design is shown in Figure 3.1. The conformational change upon Zn^{2+} binding changes the Förster resonance energy transfer (FRET) efficiency, and thus the sensor's fluorescence emission reports the proportion of bound sensor. I report the magnitude of FRET as the FRET ratio (R), which is the fluorescence intensity of the acceptor fluorescence protein (FP) divided by that of the donor FP when only the donor FP is excited. Estimation of *free* Zn^{2+} is possible when the sensor's affinity for Zn^{2+} is known and an *in vivo* sensor calibration is performed. Importantly, these sensors cannot estimate *total* Zn^{2+} .

In order to identify an improved mitochondrial Zn^{2+} sensor, several new sensors were constructed with different Zn^{2+} binding domains. Specifically, I sought to identify sensors that have an

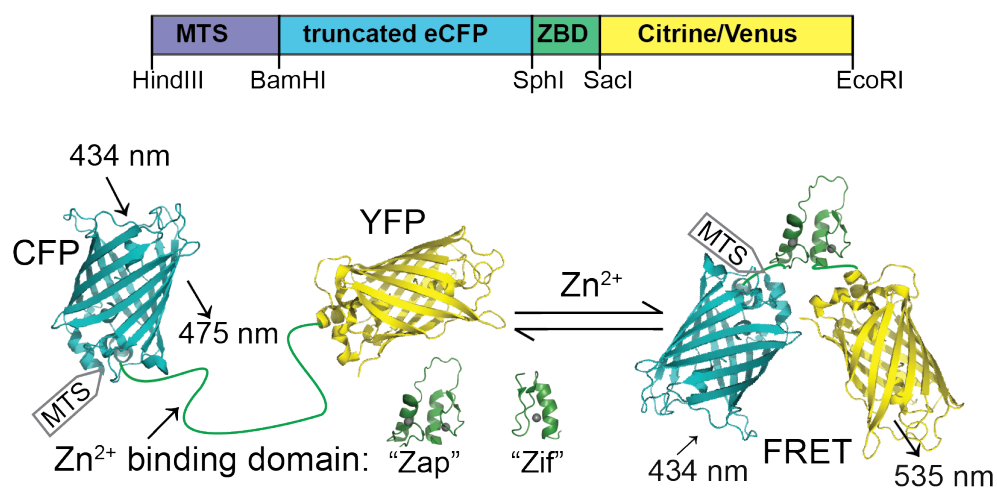


Figure 3.1: Design of genetically-encoded mitochondrial Zn^{2+} sensors. These sensors undergo a conformational change upon binding Zn^{2+} , which leads to a change in FRET from the donor FP (truncated eCFP) and the acceptor FP (Citrine or Venus). The Zn^{2+} binding domain (ZBD) used in the Zap and Zif sensors consists of the first two Zn^{2+} fingers of the *Saccharomyces cerevisiae* protein Zap1 or the first Zn^{2+} finger from the mammalian protein Zif268, respectively. The mitochondrial targeting sequence (MTS) is appended to the N-terminus of the sensor. The MTS was cloned into the pcDNA3.1 multiple cloning site between *HindIII* and *BamHI*. The sensor is flanked by *BamHI* and *EcoRI* restriction sites, and the ZBD lies between *SphI* and *SacI* restriction sites.

appropriate dissociation constant (K'_D) for Zn^{2+} allowing detection of both decreases and increases in Zn^{2+} concentration and with an improved dynamic range (defined as the maximum R (R_{max}) divided by the minimum R (R_{min})). In most cases, the Zn^{2+} -saturated sensor reports R_{max} and Zn^{2+} -free sensor reports R_{min} , but some display inverted responses [72]. Measurement of R_{max} and R_{min} was achieved by performing *in situ* calibrations of single HeLa cells expressing each sensor (Figure 3.2). In a typical *in situ* calibration, R is measured in cells treated with $150 \mu\text{M}$ of the Zn^{2+} chelator N, N, N', N' -Tetrakis(2-pyridylmethyl)ethylenediamine (TPEN), followed by $0.75 \mu\text{M}$ pyrithione (a Zn^{2+} ionophore) and $10 \mu\text{M}$ ZnCl_2 . The fractional saturation, which is more consistent from cell-to-cell than R , is calculated as shown in Equation 3.1.

$$\text{Fractional Saturation} = \frac{R - R_{min}}{R_{max} - R_{min}} \quad (3.1)$$

A comparison of R and fractional saturation values that illustrates the consistency of the fractional saturation as opposed to R can be found in the Methods (Section 3.5).

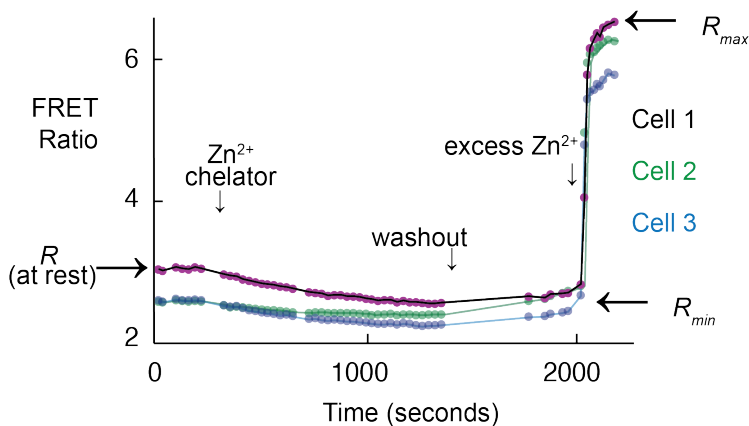


Figure 3.2: An *in situ* calibration of mitochondrial Zn^{2+} sensor mito-ZapCY1. A sensor calibration is performed to determine the fractional saturation of mito-ZapCY1 in HeLa cells by measuring R (at rest), R_{min} , and R_{max} . The mean R of each of 3 different cells is plotted over time.

I also hoped to identify partially saturated sensors, which are best for quantitative measurements. Table 3.1 reports the dynamic range and fractional saturation of all the sensors tested and reveals mito-ZapCY1 as a robust sensor with a resting fractional saturation of $8.7 \pm 5.8\%$ and the

current largest dynamic range of 3.2, significantly better than the previously reported mito-ZifCY1 sensor, which has a dynamic range of 1.2 [136]. The improved dynamic range is illustrated in Figure 3.3, which shows the calibration of both sensors in the same plot.¹

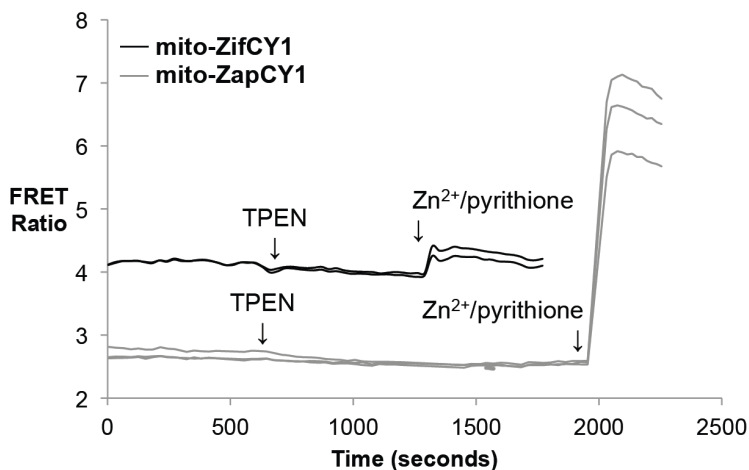


Figure 3.3: Comparison of the dynamic ranges of mito-ZifCY1 to mito-ZapCY1. Representative calibration traces from HeLa cells expressing either mito-ZapCY1 or mito-ZifCY1 illustrate the significant improvement in dynamic range.

Sensors were targeted to the mitochondrial matrix by appending an N-terminal mitochondrial targeting sequence. As shown in Figure 3.4, they display a high degree of co-localization with MitoTracker Red in HeLa cells, MIN6 cells, and HC11 cells, as quantified by the Pearson’s correlation coefficient.

Estimates of mitochondrial free Zn^{2+} in HeLa cells based on mito-ZapCY1 dramatically differ from those based on mito-ZifCY1. Using mito-ZifCY1 (ZifCY1’s *in vitro* K_D' is $1.7 \pm 0.2 \mu M$), we previously observed a fractional saturation of $\approx 41\%$, identical to what I observe in the present study (see Table 3.1) leading to an estimate of $[Zn^{2+}]_{mito}$ of 680 ± 140 nM in HeLa cells. In contrast, measurements using mito-ZapCY1 (ZapCY1’s *in vitro* K_D' is 2.53 pM at pH 7.4) estimate a $[Zn^{2+}]_{mito}$ of 0.22 pM in HeLa cells. I hypothesized that the poor dynamic range of mito-ZifCY1

¹ For comparison, the recently developed mito-CA probe, which was successfully used to estimate $[Zn^{2+}]_{mito}$ in PC-12 cells, is excitation ratiometric (excitation at 360 nm and 540 nm, emission at 615 nm) and yields a dynamic range of 1.6 and $R_{max} - R_{min}$ of 0.32 in isolated mitochondria [67]. The ratio of mito-CA could be perturbed by differential loading of its small molecule fluorophore component, dapoxyl sulfonamide [33, 65].

Table 3.1: Characteristics of mitochondrial Zn^{2+} sensors constructed and tested in this study. The sensors are named according to their donor and acceptor fluorescent proteins (FPs) and Zn^{2+} -binding domain. The Zn^{2+} -binding domains are described in 3.2. CFP is a truncated eCFP which is described in [136]. cpVenus FPs are circularly permuted at the residue number indicated (see text in this Section for details). The dynamic range is defined as R_{max}/R_{min} . Fractional saturation and R of the bound and unbound sensor were determined as described in Equation 3.1 and Section 3.5.

Sensor name	Zinc binding domain	Donor FP	Acceptor FP	Dynamic Range	Fractional Saturation at Rest	FRET ratio of unbound sensor	FRET ratio of bound sensor	$R_{max} - R_{min}$	Total # of cells measured	Total # of experiments performed
mito-ZapCY1	Zap	CFP	Citrine	3.22 ± 0.57	0.09 ± 0.06	2.13 ± 0.24	6.78 ± 0.87	4.65	31	3
mito-ZapCY2	Zap mutant #2	CFP	Citrine	1.26 ± 0.01	0.34 ± 0.01	2.26 ± 0.06	2.86 ± 0.09	0.60	6	2
mito-ZapCV2.49	Zap mutant #2	CFP	cpVenus ₄₉	1.16 ± 0.01	0.17 ± 0.05	2.11 ± 0.10	2.45 ± 0.12	0.34	17	1
mito-ZapCV2.173	Zap mutant #2	CFP	cpVenus ₁₇₃	1.50 ± 0.06	0.04 ± 0.01	3.07 ± 0.20	4.59 ± 0.25	1.52	28	1
mito-ZapCY4	Zap mutant #4	CFP	Citrine	1.13 ± 0.02	0.49 ± 0.14	2.06 ± 0.16	2.33 ± 0.19	0.27	15	1
mito-ZapCY5	Zap mutant #5	CFP	Citrine	1.14 ± 0.04	0.47 ± 0.18	2.04 ± 0.23	2.33 ± 0.20	0.29	18	2
mito-TFIIBC Y1	ZF from TFIIB	CFP	Citrine	1.10 ± 0.02	0.89 ± 0.02	2.28 ± 0.21	2.51 ± 0.19	0.23	2	1
mito-MTF35CY1	ZF 3 and 5 of MTF-1	CFP	Citrine	1.13 ± 0.02	0.18 ± 0.11	1.98 ± 0.14	2.23 ± 0.16	0.25	11	2
mito-ZifCY1	Zif	CFP	Citrine	1.17 ± 0.09	0.42 ± 0.27	3.52 ± 0.29	4.24 ± 0.31	0.72	10	3
mito-ZifCV1.49	Zif	CFP	cpVenus ₄₉	2.49 ± 0.38	0.10 ± 0.12	14.19 ± 2.42	5.16 ± 1.26	9.03	16	3
mito-ZifCV1.157	Zif	CFP	cpVenus ₁₅₇	1.22 ± 0.13	0.16 ± 0.09	2.32 ± 0.23	2.83 ± 0.35	0.51	19	2
mito-ZifCV1.173	Zif	CFP	cpVenus ₁₇₃	2.56 ± 0.46	0.05 ± 0.08	14.70 ± 4.63	5.35 ± 0.68	9.35	12	2
mito-ZifCV1.195	Zif	CFP	cpVenus ₁₉₅	1.15 ± 0.04	0.28 ± 0.20	4.01 ± 0.45	3.48 ± 0.35	0.53	14	2
mito-ZifCV1.229	Zif	CFP	cpVenus ₂₂₉	1.04 ± 0.02	0.42 ± 0.21	3.24 ± 0.57	3.10 ± 0.51	0.14	13	2

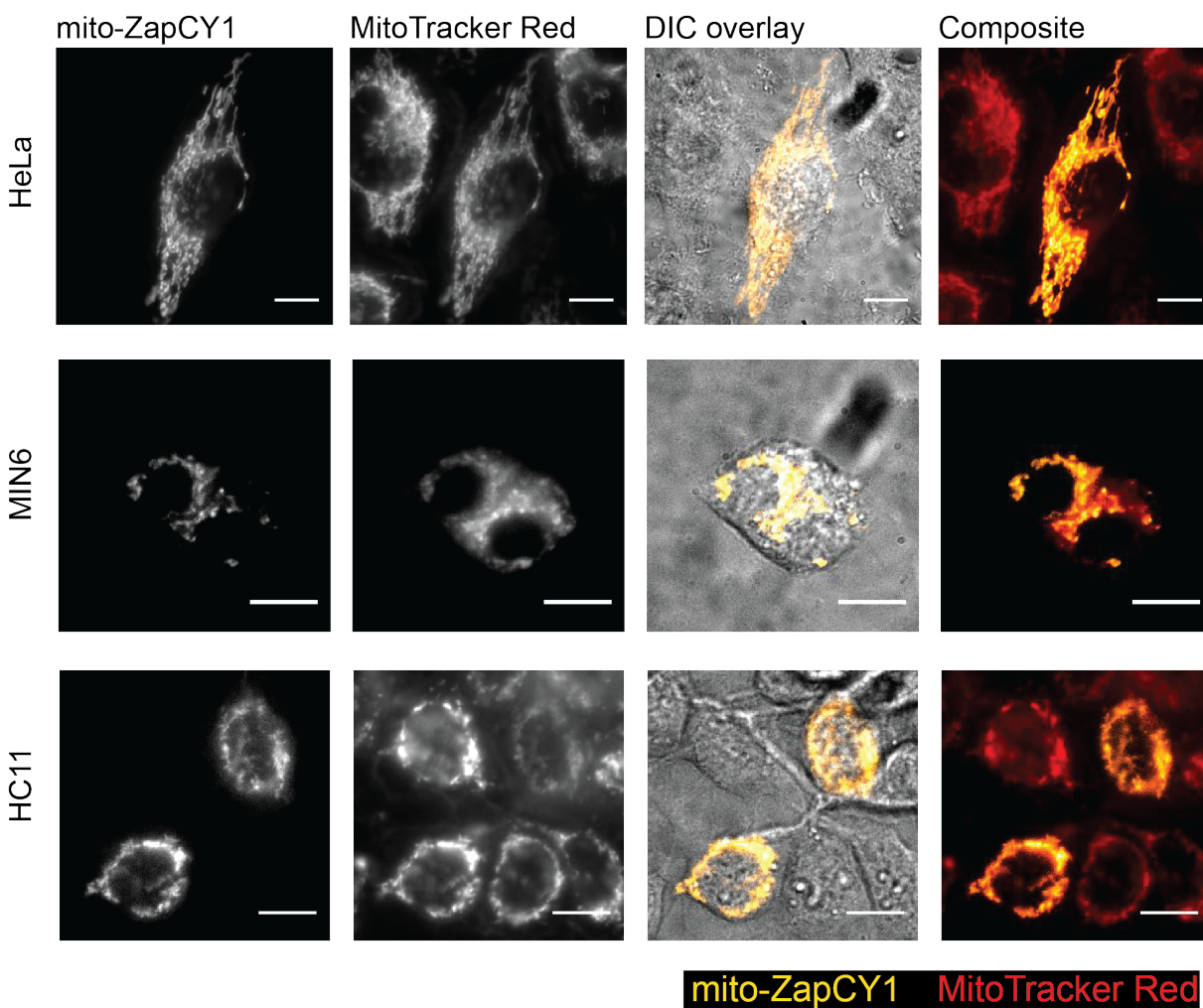


Figure 3.4: Mito-ZapCY1 colocalizes with MitoTracker Red in HeLa cells, MIN6 cells, and HC11 cells. Cells were transfected with mito-ZapCY1 and imaged 48-72 hours later, and MitoTracker Red dye was loaded into cells 1 hour prior to imaging. Pearsons coefficients for the HeLa cell is 0.938; two different images of MIN6 cells are 0.831 and 0.88; for two images of HC11 cells are 0.953 and 0.818. Microscope filter combinations for FRET and CFP: ex 430/24 excitation filter, 455 dichroic, 535/25, and 470/24 emission filters, respectively; for MitoTracker 577/20 excitation filter, 595 dichroic, 630/60 emission filter. Scale bars represent 10 μm .

results in unreliable estimates of $[Zn^{2+}]_{mito}$ and set out to improve its dynamic range.

Circular permutation of FPs, which involves relocating the N- and C- termini to different loops, has been shown to impact the dynamic range of FRET sensors by changing the orientation of the two FPs [137, 152, 211]. I screened 5 variants of circularly permuted Venus (cpV), each permuted at a different location, within the framework of mito-ZifCY1. Figure 3.5 presents the dynamic range and fractional saturation of these sensors and Figure 3.6 presents representative calibration traces. The 5 variants yielded significantly different fractional saturation and dynamic ranges, resulting in two sensors with increased dynamic ranges. These sensors were named mito-ZifCV1.49 and mito-ZifCV1.173, where the "49" denotes that Venus was circularly permuted at amino acid position 49. The high dynamic ranges of mito-ZifCV1.49 and mito-ZifCV1.173, which display inverted responses to Zn^{2+} , result from increased FRET in the unbound state and little change in FRET in the Zn^{2+} -bound state. I found that the fractional saturation decreases as the dynamic range increases, even though the Zn^{2+} binding domains are identical. It has been demonstrated that incorporation of cpV can decrease the K_D' 2-10-fold [137], but even variation of the K_D' cannot explain the strong correlation between the fractional saturation and dynamic range, suggesting that as hypothesized, measurements made using low dynamic range sensors can be inconsistent.

Converting the fractional saturation to $[Zn^{2+}]_{mito}$ requires accurate estimation of the K_D' . The molecular environment of mitochondrial matrix differs from cytosol, and the pH and redox balance can change significantly under different conditions. The pH in the mitochondrial matrix is typically ~ 8.0 without perturbation, but it can vary from about 6.5 to 8.5 under different conditions. Using Mito-pHRed [212], I estimated the mitochondrial matrix pH to be ~ 8.0 in resting HeLa cells. Therefore, I titrated mito-ZapCY1 in mitochondria of living cells by adding Zn^{2+} , buffered at different free concentrations, to Ca^{2+} -, Mg^{2+} -, and phosphate-free imaging media in the presence of 50 $\mu g/mL$ alamethicin. Alamethicin is an antimicrobial peptide that can permeabilize the mitochondrial inner membrane to small molecules only [170]. Using this method, I found mito-ZapCY1 has *in situ* K_D' s of 1.6 pM and 17 pM at pH 8.0 and 7.4, respectively (Figure 3.7). These

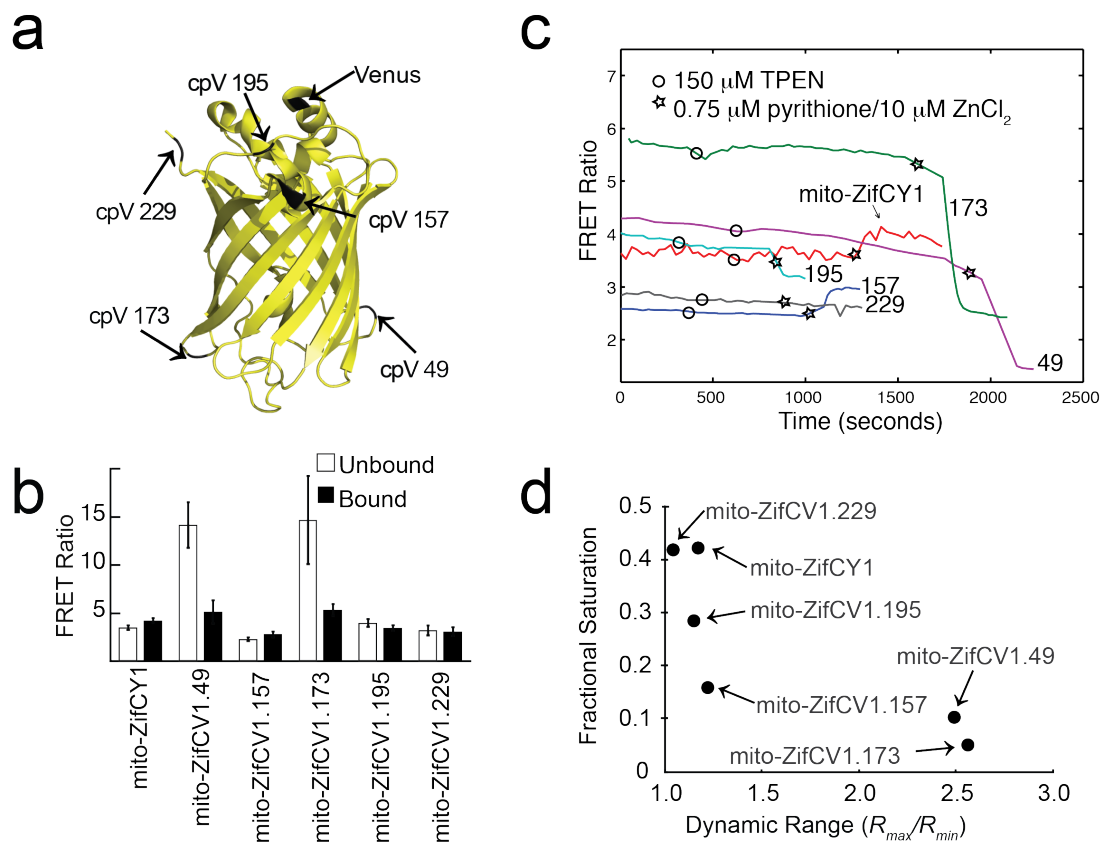


Figure 3.5: Circular permutation of mito-ZifCY1 dramatically increases its dynamic range. a) The N- and C- termini of cpVenus FPs are relocated to 5 different loops of the original Venus FP at the amino acid positions 49, 157, 173, 195, and 229. b) The average R of the unbound and bound sensors, in at least 10 cells from 2 or more independent experiments, acquired using identical exposure times, are summarized. c) Comparison of *in situ* calibrations of circularly permuted mito-ZifCY1 variants. d) High dynamic range sensors report lower fractional saturation.

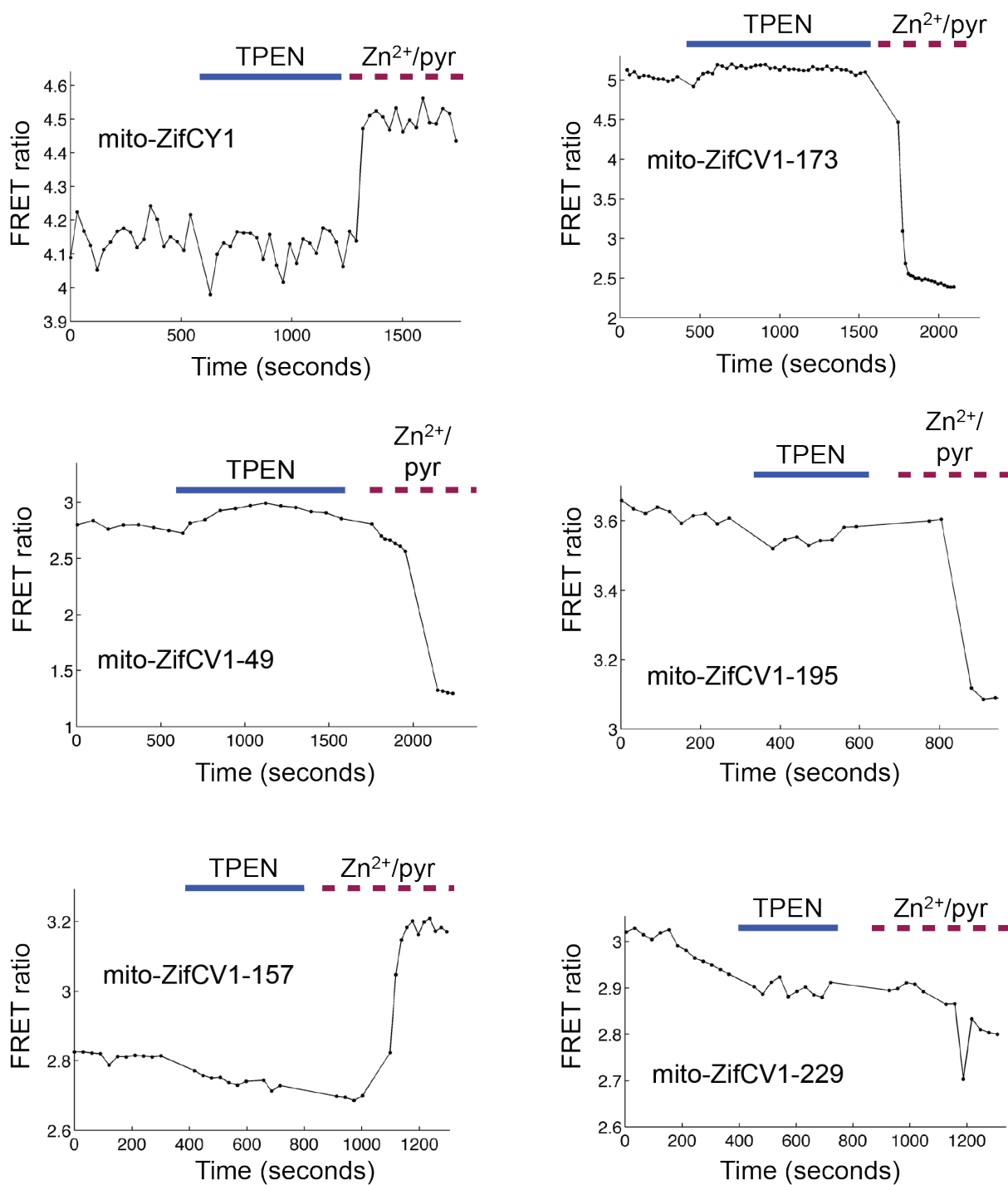


Figure 3.6: Representative calibration traces of mito-ZifCY1 and its circularly permuted variants. 150 μM TPEN was used to deplete Zn^{2+} and 10 μM ZnCl_2 and 0.75 μM pyrithione were used to saturate the sensor with Zn^{2+} . FRET ratios differ from those reported in Table 3.1 and Figure 3.5 due to different exposure times. The mito-ZifCV1.49 and mito-ZifC1.173 calibrations shown above were monitored using shorter YFP FRET exposure times and longer CFP exposure times, resulting in more stable resting FRET ratios, smaller R_{min} and R_{max} , and comparable dynamic ranges.

in situ K_D' s are comparable to those measured *in vitro* at different pH values (Figure 3.8). Our mito-ZapCY1 calibrations estimate $[Zn^{2+}]_{mito}$ to be 0.14 pM in resting HeLa cells.

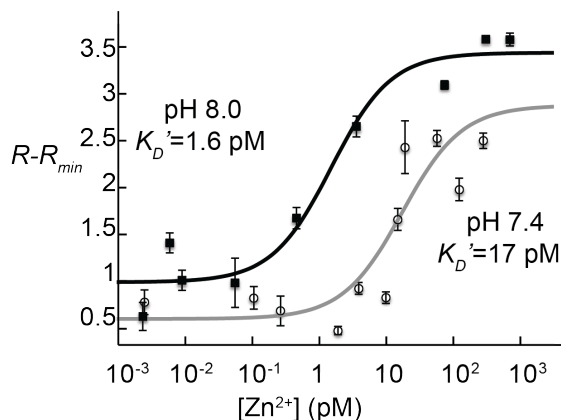


Figure 3.7: The *in situ* K_D' of mito-ZapCY1 was determined in HeLa cells at pH 7.4 and 8.0. Each point represents the average ($R - R_{min}$) of at least 3 cells.

3.4.2 Comparison of Mitochondrial to Cytosolic Zinc

Next, I confirmed that two high-dynamic-range sensors with different Zn^{2+} binding domains yield consistent estimates of $[Zn^{2+}]_{mito}$. As shown in Figure 3.9, the fractional saturations of mito-ZapCY1 and mito-ZifCV1.173 in HeLa cells were $16 \pm 10\%$ and $5.8 \pm 3.1\%$, respectively, while the corresponding sensors in the cytosol were almost completely saturated ($90 \pm 7.3\%$ and $95 \pm 1.1\%$, respectively). These data indicate that under resting conditions in HeLa cells, the free Zn^{2+} is buffered at concentrations about 3 orders of magnitude lower in mitochondria than in the cytosol.

If in fact, $[Zn^{2+}]_{mito}$ is buffered at a lower concentration than free cytosolic Zn^{2+} , the addition of a Zn^{2+} ionophore, in the absence of extracellular Zn^{2+} , should dissipate the Zn^{2+} gradient between these two subcellular compartments. Indeed, treatment of several cell types expressing mito-ZapCY1 with 5 μ M pyrithione caused a rapid increase in $[Zn^{2+}]_{mito}$, which was reversed by the addition of 150 μ M TPEN (Figure 3.10). Our interpretation of these results is that pyrithione moves Zn^{2+} into mitochondria from other subcellular compartments, such as the cytosol, which buffer free Zn^{2+} at higher concentrations.

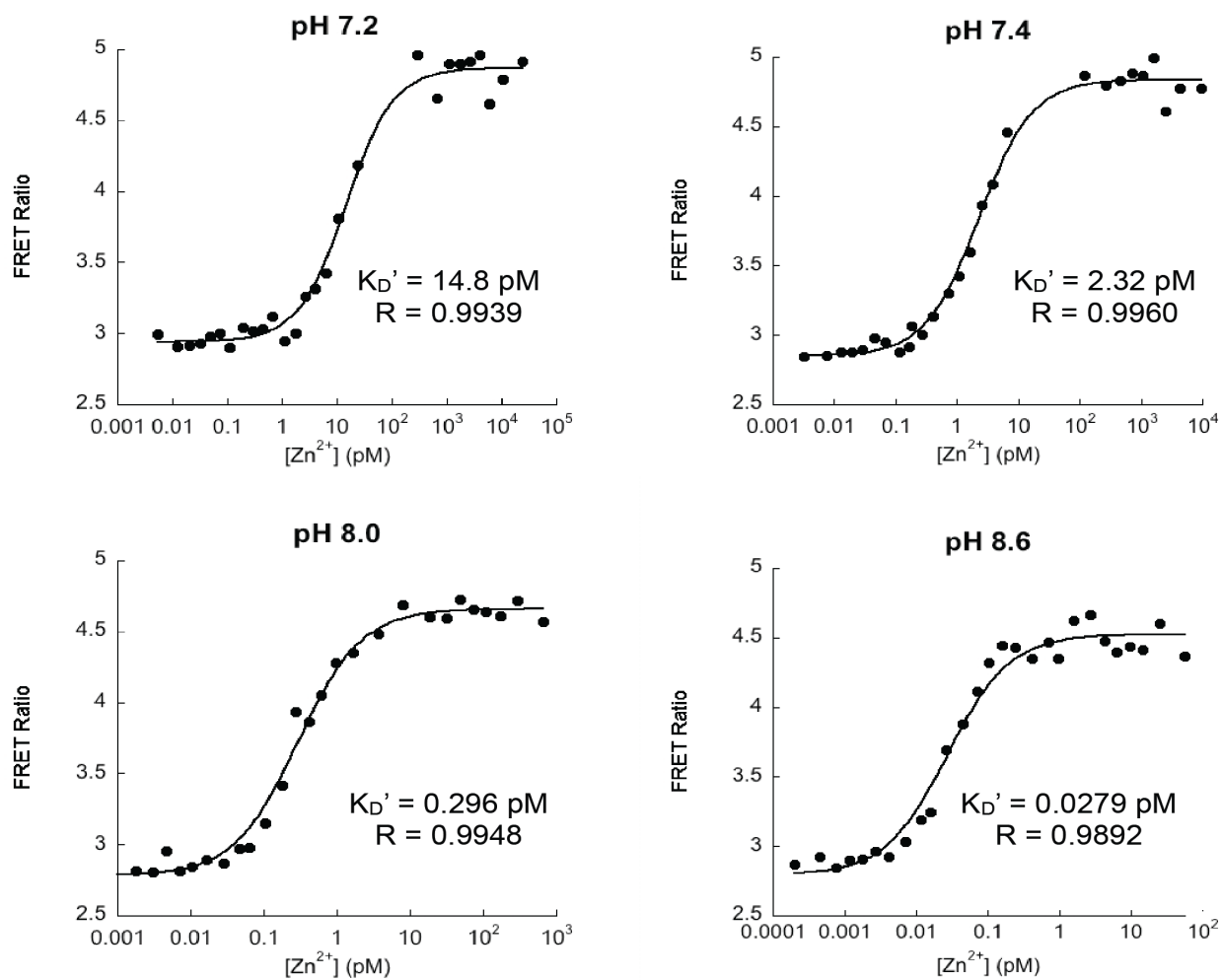


Figure 3.8: The pH dependence of the K_D' of ZapCY1 *in vitro*. Titrations of the same protein preparation of ZapCY1 were performed *in vitro* at pH 7.2, 7.4, 8.0, and 8.6. Data were fit to a single-site binding equation using the least-squares method in KaleidaGraph software.

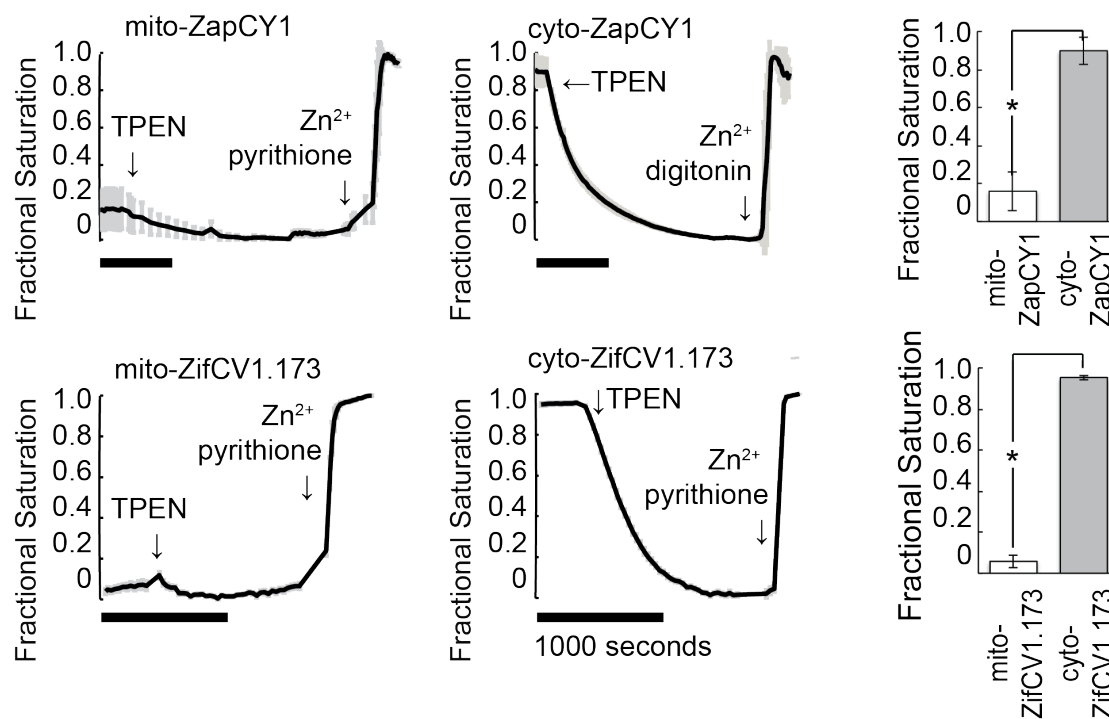


Figure 3.9: The fractional saturation of Zn²⁺ sensors is lower in mitochondria than in the cytosol. Representative calibrations of ZapCY1 and ZifCV1.173 expressed in the mitochondrial matrix or the cytosol of HeLa cells are shown. Comparison of the fractional saturation of each sensor illustrates the difference in mitochondrial and cytosolic Zn²⁺ ($p < 0.0001$, Student's T-test). Horizontal black bars represent 1000 seconds. At least 3 cells were measured in each experiment.

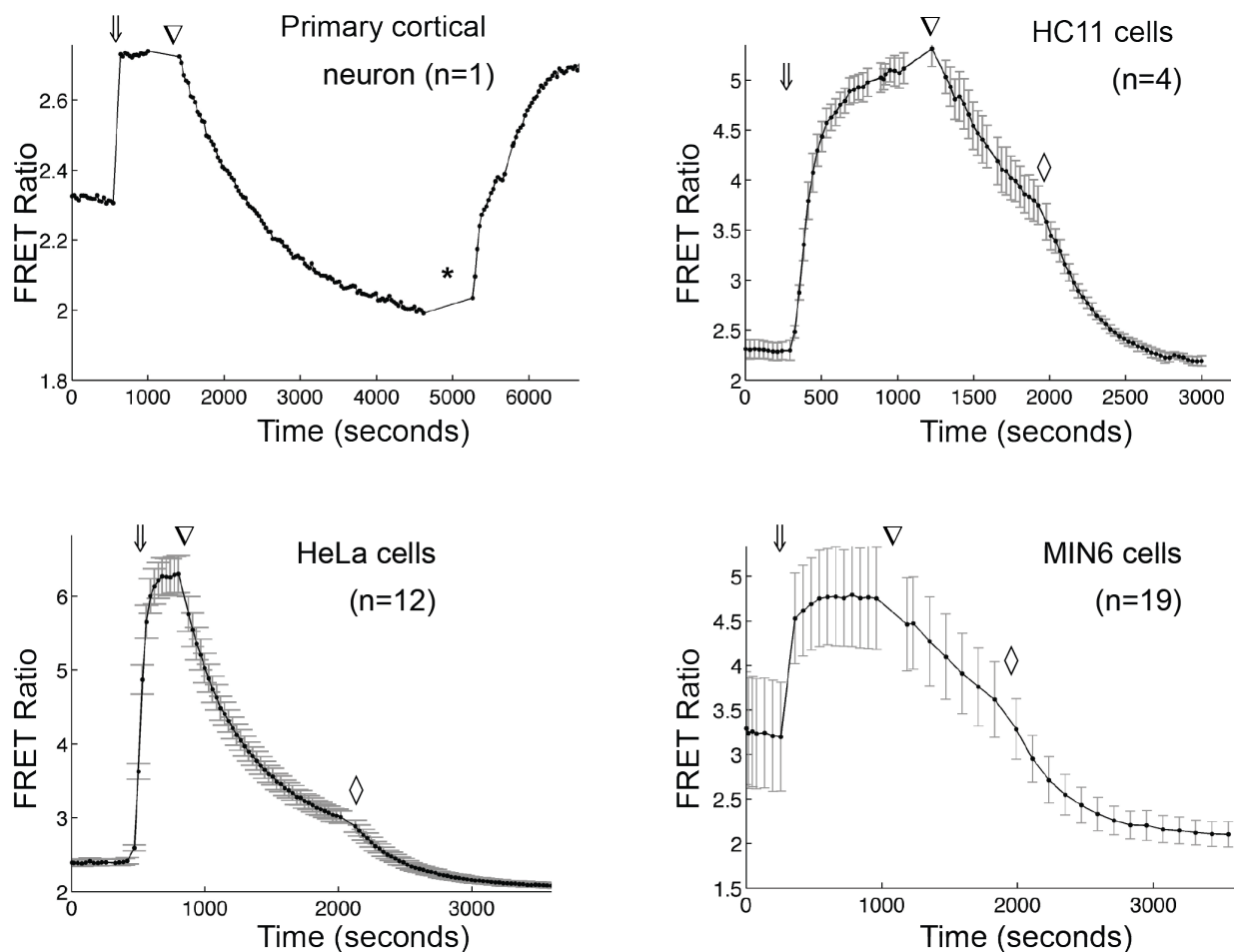


Figure 3.10: Pyrithione treatment alone saturates mito-ZapCY1 in 4 different cell types. Each plot shows the mean \pm standard deviation of n cells over the course of an experiment. The symbol \downarrow marks when cells were treated with 5 μ M (HC11 and HeLa cells) or 250 μ M (neuron and MIN6 cells) pyrithione (pyr). Next, at ∇ , the cells were treated with 150 μ M TPEN. Finally, cells were treated with 5 μ M pyrithione and 10 μ M $ZnCl_2$ (*) or 150 μ M TPEN (\diamond).

3.4.3 Comparison of Mitochondrial Zinc in Different Cell Types

I used mito-ZapCY1 to quantitatively compare $[\text{Zn}^{2+}]_{\text{mito}}$ in different cell types and under different conditions. Mito-ZapCY1 was expressed in HeLa cells, MIN6 cells (a mouse insulinoma cell line), primary mouse cortical neurons, and HC11 cells (a mouse mammary epithelial cell line). Resting R , R_{min} , and R_{max} were measured in individual cells to determine the fractional saturation of mito-ZapCY1 in each of the different cell types. Figure 3.11 presents a summary of mito-ZapCY1's fractional saturation in different cell types and pseudocolor images of cells at rest, upon TPEN treatment, and upon addition of Zn^{2+} /pyrithione. Significant differences among cell types were observed, including lower fractional saturation of mito-ZapCY1 in HeLa cells ($8.7 \pm 5.8\%$) than in MIN6 cells ($41 \pm 18\%$) or neurons ($59 \pm 20\%$). I also compared the fractional saturation of mito-ZapCY1 in HC11 cells grown in basal media ($-\text{prolactin}$) to those in lactogenic media ($+\text{prolactin}$) and found that $[\text{Zn}^{2+}]_{\text{mito}}$ is significantly higher in non-lactogenic HC11 cells than in lactogenic HC11 cells ($p=0.0022$, Student's T-test). This is particularly intriguing given that HC11 cells have been shown to undergo massive redistribution of intracellular Zn^{2+} pools and alterations in Zn^{2+} transporter expression upon lactogenic stimulation [21, 130]. These results suggest that $[\text{Zn}^{2+}]_{\text{mito}}$ is regulated differently in several cell types and under different environmental conditions. While at this point we do not know how cells maintain different levels of free Zn^{2+} in the mitochondrial matrix, I speculate that they will likely exhibit different levels of Zn^{2+} transporters, buffers, and other regulatory proteins, that are necessary to ensure appropriate Zn^{2+} management for each specialized cell.

In summary, I constructed and validated three genetically encoded, high dynamic range mitochondrial Zn^{2+} sensors. Although sensors of low dynamic range are capable of detecting relative changes in Zn^{2+} , high dynamic range sensors are necessary for making consistent and quantitative comparisons of Zn^{2+} between different cell types. Using mito-ZapCY1, I estimate $[\text{Zn}^{2+}]_{\text{mito}}$ to be 0.14 pM in HeLa cells. A recent study reports a similar $[\text{Zn}^{2+}]_{\text{mito}}$ of 0.2 pM measured with a different ratiometric Zn^{2+} biosensor in the PC12 rat pheochromocytoma cell line [67]. I believe

that these mitochondrial Zn^{2+} sensors can be used to address the complex interplay between Zn^{2+} homeostasis and mitochondrial function.

It is not known if and to what extent the level of Zn^{2+} sensor expression changes the total Zn^{2+} concentration and the Zn^{2+} -buffering capacity of the cell. Figure 3.12 shows that fractional saturation of mito-ZapCY1 does not change as the sensor expression increases, suggesting that in contrast to small-molecule sensors, these sensors do not deplete the mitochondrial Zn^{2+} pool [33,64]. The lack of perturbation of resting $[\text{Zn}^{2+}]_{\text{mito}}$ also suggests that, similar to cytosolic Zn^{2+} , mitochondrial Zn^{2+} is buffered, and the sensor concentration is much lower than the concentration of the buffer.

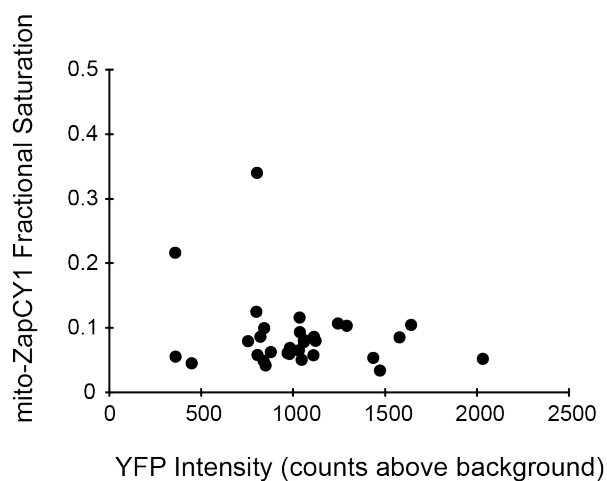


Figure 3.12: The fractional saturation of mito-ZapCY1 does not change as its concentration increases in HeLa cells. Each marker represents a single cell. The YFP intensity is an indicator of sensor concentration because YFP excitation and emission (ex/em) is not affected by FRET. The mito-ZapCY1 resting FRET ratio, in contrast to its fractional saturation, does appear to have some dependence on the YFP intensity, as shown in the right panel.

A potential limitation of the Zn^{2+} -finger binding domains of the mito-ZapCY1 or mito-ZifCV1 sensors is their sensitivity to oxidation and changes in pH. However, I observe little perturbation due to acidification by acetic acid or treatment with H_2O_2 . I performed parallel experiments with the sensors mito-pHRed and mito-RoGFP2 and observed little change in pH or oxidation in the

process of sensor calibration (Figure 3.13) [212, 213].

In conclusion, I created improved mitochondrial Zn^{2+} sensors to measure *free* $[\text{Zn}^{2+}]$ in the mitochondrial matrix with superior accuracy and precision. These new sensors complement and expand our fluorescent toolbox for studying Zn^{2+} and other ions in complex, biological systems.

3.5 Methods

3.5.1 Sensor Construction

Four repeats of the coding sequence for the first 29 amino acids of the human cytochrome c oxidase subunit 8a (mitochondrial precursor, accession number NP004065) precede the coding sequence of each sensor in the mammalian expression vector pcDNA3.1, as previously described [136]. The amino acid sequences of the ZBDs used in this study can be found in Table 3.2. Mito-ZapCY1 was constructed from two previously published constructs: the pcDNA3.1 (Life Technologies) vector backbone and mitochondrial targeting sequence of mito-ZifCY1 [136], and the sensor construct ZapCY1 [66]. Both plasmids were digested with *Bam*HI and *Eco*RI (New England Biolabs), gel-purified, and the ZapCY1 sensor was ligated into the pcDNA3.1-mito backbone. Mito-ZifCV1 sensor variants were constructed from the ZifCY1 sensor in a pBAD vector (a modified vector obtained from R.Y. Tsien). The restriction sites *Sac*I and *Eco*RI were appended on to the 5' and 3' ends, respectively, of each cpVenus (a gift of A. Miyawaki), using PCR amplification. The PCR primer sequences can be found in Table 3.3. pBAD-ZifCY1 was digested with *Sac*I and *Eco*RI (which removes Citrine from the construct) and each cpVenus was ligated in place of the original Citrine. Then, each pBAD-ZifCV1 construct was digested with *Bam*HI and *Eco*RI and ligated into the pcDNA3-mito vector described above.

3.5.2 Cell Culture

HeLa cells were maintained in high glucose Dulbeccos Modified Eagle Medium (DMEM) with 10% fetal bovine serum (FBS) and 1x penicillin/streptomycin (pen/strep). MIN6 cells were cultured

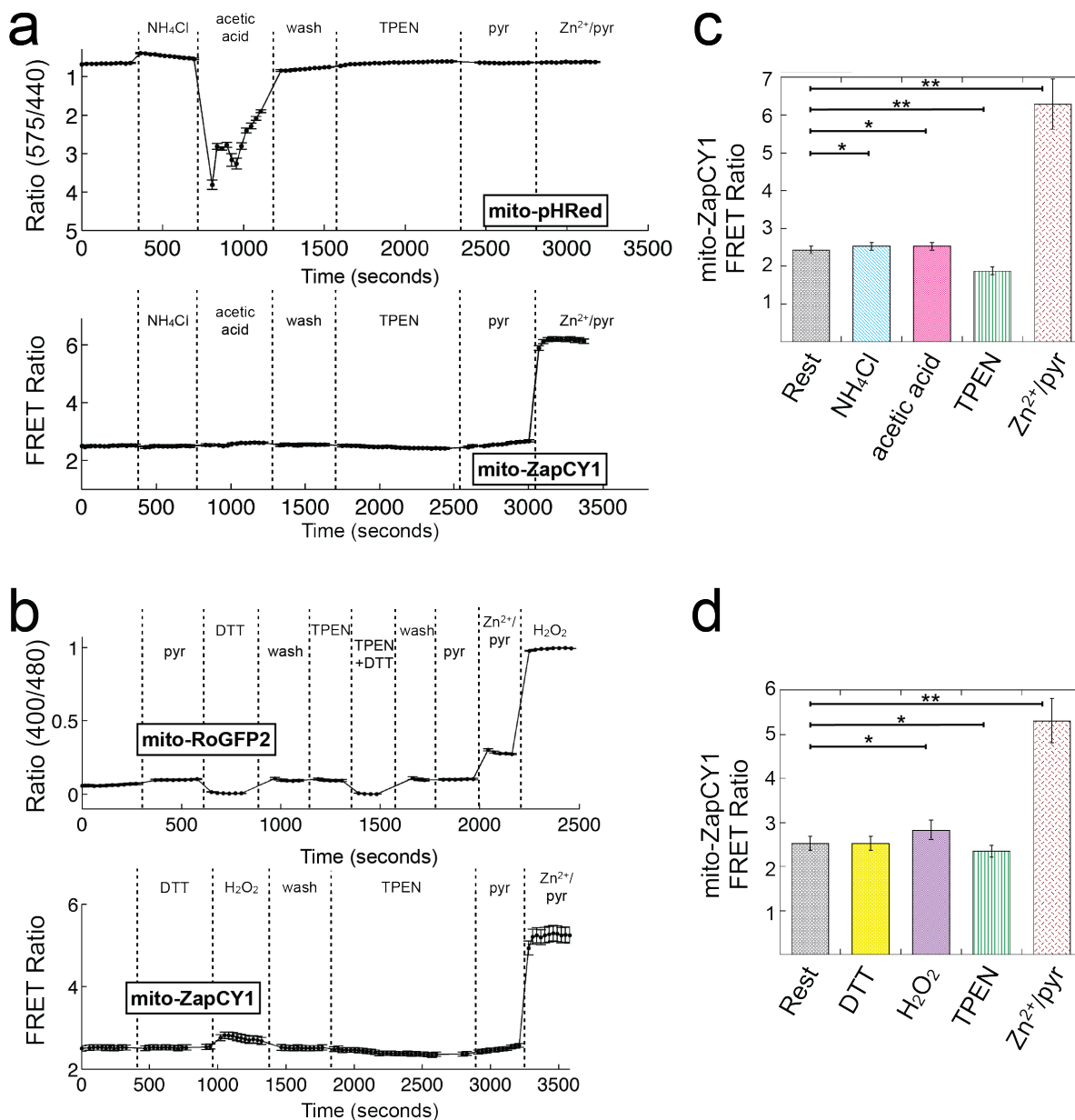


Figure 3.13: The FRET ratio of mito-ZapCY1 is minimally perturbed by changes in pH or redox balance. a) The FRET ratios of HeLa cells transfected with mito-pHRed or mito-ZapCY1 were measured in the presence of 10 mM NH₄Cl, 10 mM acetic acid, 150 μM NH₄Cl, 250 μM TPEN, 250 μM pyrithione, or 10 μM ZnCl₂ and 250 μM pyrithione. b) The FRET ratios of HeLa cells transfected with mito-RoGFP2 or mito-ZapCY1 were measured in the presence of 250 μM DTT, 250 μM H₂O₂, 150 μM TPEN, or 10 μM ZnCl₂ and 250 μM pyrithione. Each plot of FRET ratio over time represents n more than 5 cells in a single experiment. Quantification of the FRET ratios (mean ± standard deviation of more than 12 cells from at least 2 independent experiments) are shown in c) and d) (*p < 0.05; **p < 0.0001).

Table 3.2: Amino acid sequences of the different Zn²⁺ binding domains (ZBDs) used in this study. The Zn²⁺ binding domain (ZBD) used in the Zap sensors consists of the first two Zn²⁺ fingers of the *Saccharomyces cerevisiae* protein Zap1; Zap2-5 are mutants of Zap1. The ZBD used in the TFIIB sensor is from transcription factor IIB. The MTF1-F345 binding domain consists of the third, fourth, and fifth zinc fingers of the metal regulatory transcription factor 1. The ZBD used in the Zif sensors consists of the first Zn²⁺ finger from the mammalian protein Zif268. Cysteine and histidine residues that ligate Zn²⁺ are colored red and blue.

ZBD	Amino Acid Sequence
Zif	ERPYA C PV E SCDRRFSRSD ELTR H I R I H T GQK
TFIIB	MASTRLDALPRVT C PN H PDAILVEDYRAGDM I C PE C GLVVGDR VIDVGSEWRTFSNDKATK
MTF1-F345	FE C DVQ G CEKAFNTLYRLKA H QRL H TGKTFN C ESE G CSKYFTT L S DLRK H IR T H T G E KPF R CD H D G CGKAFAASHHLK T H V RT H TGERP
Zap1 (wt)	KNNDLK C KW K EC P ES C SSLFDLQR H LLK D H V SQDFKHPMEP L A C N W E D C DFLGDDTCSIV N H I NC Q H G I
Zap2	KNNDLK H KW K EC P ES C SSLFDLQR H LLK D H V SQDFKHPMEP L A H N W E D C DFLGDDTCSIV N H I NC Q H G I
Zap3	KNNDLK H KW K EC P ES C SSLFDLQR H LLK D H V SQDFKHPMEP L A H N W E D C DFLGDDTCSIV N H I NC Q H G I
Zap4	KNNDLK H KW K EC D ES C SSLFDLQR H LLK D H V SQDFKHPMEP L A H N W E D C DFLGDDTCSIV N H I NC Q H G I
Zap5	KNNDLK H KW K EC H ES C SSLFDLQR H LLK D H V SQDFKHPMEP L A H N W E D H DFLGDDTCSIV N H I NC Q H G I

Table 3.3: Primers used to construct mito-ZifCV1 variants. *SacI* and *EcoRI* restriction sites are underlined.

Primer name	Sequence (5' to 3')
SacI-cpV49 Fwd	cca <u>GAGCTC</u> ATG ACC GGC AAG CTG CC
SacI-cpV157 Fwd	cca <u>GAGCTC</u> ATG CAG AAG AAC GGC ATC AAG G
SacI-cpV173 Fwd	cca <u>GAGCTC</u> ATG GAC GGC GGC GTG
SacI-cpV195 Fwd	cca <u>GAGCTC</u> ATG CTG CCC GAC AAC CAC
SacI-cpV229 Fwd	cca <u>GAGCTC</u> ATG ATC ACT CTC GGC ATG GAC G
EcoRI-cpV Rev	CAG CCG GAT CAA GCT <u>TCG</u> AAT <u>TCT</u> TA

in D-MEM supplemented with 10% (v/v) FBS, L-glutamine, sodium pyruvate, β -mercaptoethanol, and penicillin/streptomycin. HC11 cells were maintained, as previously published, in non-lactogenic medium, which was replaced with lactogenic medium 24-48 prior to imaging [130]. All cells, except neurons, were transfected 48-72 hours before imaging with TransIT-LT1 (Mirus) or electroporated with the Neon system (Life Technologies).

Cerebral cortex was isolated from P0 rat pups, minced with a surgical scalpel and digested with papain for 30 minutes at room temperature. Following digestion, tissue chunks were successively triturated in D-MEM supplemented with 10% FBS and pen/strep using a fire polished glass pipet. Neurons were plated onto poly-D-lysine coated 35 mm glass bottom dishes at a density of 250,000 cells cm^2 at day in vitro (DIV) 0. At DIV 1, cultures were transferred to Neurobasal A supplemented with B-27 and the antimetabolic AraC. At DIV 8, cultures were transfected with 1 μg plasmid (750 ng plasmid of interest/250 ng empty vector) using Lipofectamine 2000.

Transfected cells were stained with MitoTracker Red (Life Technologies) for co-localization studies. To calculate the Pearson's correlation coefficient, images were cropped to include only one transfected cell. The JACoP plugin for FIJI [182, 214] was used to calculate the Pearson's coefficient.

During all experiments except *in situ* titrations, cells were imaged in phosphate-free HEPES-buffered Hanks Balanced Salt Solution (HHBSS), pH 7.4.

3.5.3 Imaging

Cells were plated on 35 mm, glass bottom imaging dishes 24-48 hours before transfection, and imaged 24 to 72 hours after transfection. Before imaging, cells were washed 3 times in phosphate-free HEPES buffered Hanks Balanced Salt Solution (HHBSS), containing 1.26 mM calcium chloride, 5.4 mM potassium chloride, 1.1 mM magnesium chloride, 137 mM sodium chloride, 16.8 mM D-glucose, 20 mM HEPES, pH 7.4, 20-25 °C. Phosphate-free HHBSS was used as the imaging buffer except in cases where mitochondria were permeabilized with alamethicin.

Image acquisition and analysis were performed as previously published [66]. Microscope filter

combinations for FRET and CFP were 430/24 nm excitation filter, 455 nm dichroic mirror, 535/25 nm and 470/24 nm emission filters, respectively.

The following solutions were used for mitochondrial Zn^{2+} calibrations: 150 μM TPEN (25 mM in 100% DMSO stock solution) to remove Zn^{2+} from sensors; 0.75 μM pyrithione (500 μM in 100% DMSO stock solution) and 10 μM ZnCl_2 (400 μM in phosphate-free HHBSS stock solution) to saturate Zn^{2+} sensors. During *in situ* titration experiments, the imaging buffer was exchanged to Ca^{2+} -, Mg^{2+} -, and phosphate-free HHBSS immediately before membrane permeabilization with 50 $\mu\text{g}/\text{mL}$ alamethicin (10 mg/mL in 100% DMSO stock solution).

3.5.4 Mito-ZapCY1 Titrations

ZapCY1 was expressed in *E. coli* and purified for use in *in vitro* titrations as previously described [66]. Zn^{2+} solutions used for the titration of mito-ZapCY1 were buffered using Zn^{2+} chelators (EGTA, EDTA, and HEDTA) as previously described [66] with the following modifications. Solutions for both *in vitro* and *in situ* titrations were adjusted to the specified pH, and the free $[\text{Zn}^{2+}]$ in each Zn^{2+} /chelator buffered solution was calculated for different pH. One imaging experiment was performed at each free Zn^{2+} concentration and the average R of at least 3 cells was used to fit the binding isotherm. Cells were imaged in phosphate-free HHBSS, pH 7.4 throughout Zn^{2+} chelation with 150 μM TPEN, which was then replaced with phosphate-, Ca^{2+} -, and Mg^{2+} -free HHBSS, pH 7.4 or pH 8.0 with 125 μM dithiothreitol (to prevent sensor oxidation) and a free Zn^{2+} buffer. Cells and mitochondria were permeabilized using 50 $\mu\text{g}/\text{ml}$ alamethicin. All chemicals were purchased from Sigma.

3.5.5 Statistical Analysis

Statistical analysis was performed using the Student's T-test or ANOVA with Tukey's HSD post-hoc test in the KaleidaGraph program.

3.5.6 Data Analysis

Data analysis was performed using FIJI (ImageJ) and MATLAB software.

First, regions of interest (ROIs) were manually selected to encompass an area within a cell with dense mitochondria, usually surrounding the nucleus (Figure 3.14). A background region was also selected.

FIJI was used to measure the mean intensity of each ROI in the FRET and CFP images, and then the mean intensity of a background ROI was subtracted from that value. FRET ratios were calculated using Equation 3.2.

$$R = \frac{\text{FRET} - \text{BG}_{\text{FRET}}}{\text{CFP} - \text{BG}_{\text{CFP}}} \quad (3.2)$$

Next, the FRET ratios were plotted over time. R_{Rest} was the mean R over the initial 5 minutes of imaging (10-15 acquisitions). R_{min} was calculated by taking the minimum R before TPEN was washed out. In some cases, the decrease in R over time was fit to an exponential decay function to extrapolate R_{min} . R_{max} was the maximum R after the addition of Zn^{2+} /pyrithione. If R did not stabilize at R_{max} for more than one acquisition, the data were discarded. Typically, R_{max} was stable for at least 5 minutes. These values were used to calculate the fractional saturation of the sensor at rest (Equation 3.1). The following equation was used to convert R to $[\text{Zn}^{2+}]$:

$$[\text{Zn}^{2+}] = K_D' \frac{R - R_{\text{min}}}{R_{\text{max}} - R} \quad (3.3)$$

The results of one mito-ZapCY1 calibration experiment are in Tables 3.4 and 3.5. These results correspond to the ROIs shown in Figure 3.14.

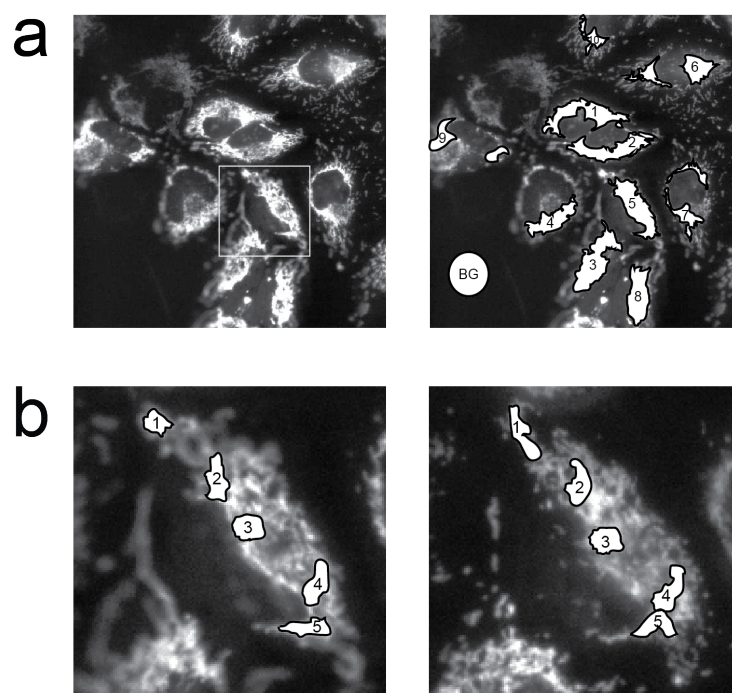


Figure 3.14: Selection of ROIs in HeLa cells expressing mito-ZapCY1. a) ROIs in one field of view numbered 1-10. FIJI was used to calculate the mean intensity of each ROI, including the background (BG) ROI, in the FRET and CFP images. The results calculated from each ROI are presented in Table 3.4. b) shows an attempt to select multiple ROIs within cell 5. The image on the left is the first acquisition and the image on the right is the last acquisition. Note that the mitochondria move and change shape and the focal plane changes throughout the experiment, so it is nearly impossible to track individual mitochondria during an experiment using widefield fluorescence microscopy. The results calculated from each ROI within this cell are presented in Table 3.5.

Table 3.4: mito-ZapCY1 measurements in different cells in one imaging experiment. The ROIs are shown in Figure 3.14.

Cell #	R_{rest}	R_{free}	R_{bound}	Fractional Saturation	Estimated free $[Zn^{2+}]_{mito}$ (pM)
1	2.38	1.91	7.05	0.0921	0.162
2	2.42	1.89	5.93	0.131	0.242
3	2.48	1.96	6.82	0.108	0.193
4	2.19	1.76	7.27	0.078	0.136
5	2.48	1.98	6.72	0.107	0.192
6	2.39	1.92	6.20	0.110	0.198
7	2.36	1.83	6.30	0.119	0.217
8	2.60	2.05	6.83	0.115	0.207
9	2.20	1.75	7.16	0.0838	0.146
10	2.16	1.76	4.45	0.150	0.282
Average	2.37	1.88	6.47	0.109	0.198
Standard Deviation	0.14	0.10	0.83	0.022	0.044

Table 3.5: mito-ZapCY1 measurements in different ROIs in cell. The ROIs are shown in Figure 3.14.

ROI #	R_{rest}	R_{free}	R_{bound}	Fractional Saturation	Estimated free $[Zn^{2+}]_{mito}$ (pM)
1	2.47	2.09	7.14	0.0745	0.129
2	2.45	2.04	7.01	0.0835	0.146
3	2.49	2.07	6.81	0.0891	0.156
4	2.48	2.03	6.84	0.0937	0.165
5	2.48	2.09	6.91	0.0810	0.141
Average	2.47	2.06	6.94	0.0843	0.147
Standard Deviation	0.01	0.03	0.13	0.0074	0.014

Chapter 4

The Role of Zinc in Calcium Signaling in Insulin Secreting Cells

4.1 Abstract

There is evidence of crosstalk between intracellular calcium and zinc in many cell types, including neurons and pancreatic β cells. In this study, a mouse insulinoma cell line, MIN6, is used to investigate crosstalk between calcium and zinc in the glucose-stimulated insulin secretion pathway. Genetically-encoded, ratiometric sensors of calcium and zinc were used to monitor changing ion concentrations in the cytosol as cells were stimulated with glucose in the presence or absence of extracellular zinc. I found that the addition of zinc during high glucose stimulation changed the temporal pattern of the changes in cytosolic calcium concentration. Additionally, I found that zinc enters cells when it is present as cells are stimulated with glucose. These results support the hypothesis that there is crosstalk between calcium and zinc in MIN6 cells, and they provide an interesting context for future studies in this model system.

4.2 Introduction

Zinc (Zn^{2+}) is a micronutrient that is required for human life. In fact, the human body contains about 2 grams of Zn^{2+} (for comparison, the human body contains about 5 grams of iron) [2]. Older infants and toddlers, pregnant women, and the elderly are at risk for Zn^{2+} deficiency in North America, and even mild Zn^{2+} deficiency can result in growth delays, anorexia, impaired immune function, and poor wound healing [2]. Furthermore, changes in Zn^{2+} distribution at the tissue, cellular, and subcellular levels are associated with several diseases, including Alzheimer's

disease and other forms of neurodegeneration, diabetes, and cancer (of the pancreas, prostate, and breast) [9–11, 24, 30, 215]. It is known that Zn^{2+} plays an essential role in all cells because it is necessary for the function of up to 10% of the proteome, including numerous transcription factors, metalloenzymes, E3 ubiquitin ligases, and enzymes required for RNA/DNA maintenance [42, 43]. However, it is poorly understood how and why Zn^{2+} dysregulation is associated with disease, or if changes in cellular Zn^{2+} interact with major cell signaling pathways, ultimately resulting in changes in cell physiology.

One intriguing hypothesis is that changes in intracellular Zn^{2+} homeostasis influence concentrations of other metal ions, namely calcium (Ca^{2+}). Ca^{2+} undeniably regulates multiple signaling pathways, and free Ca^{2+} concentrations ($[\text{Ca}^{2+}]$) in the cytosol, endoplasmic reticulum (ER) and mitochondria are very dynamic [216–218]. Several pieces of evidence, pooled from different areas of biological study, support this hypothesis. Zn^{2+} can enter cells through many different Ca^{2+} channels, including voltage-gated Ca^{2+} channels, nicotinic acetylcholine receptors, glutamate receptors, and transient receptor potential channels, and Zn^{2+} may in fact modulate Ca^{2+} entry through these channels [112]. For example, in a somatosensory neuron model, Zn^{2+} can augment Ca^{2+} influx through the transient receptor potential channel A1 [219]. In rat ventricular cardiomyocytes, Zn^{2+} modulates the inward Ca^{2+} current through voltage-gated Ca^{2+} channels [220]. There is also evidence that subcellular fluxes of Ca^{2+} and Zn^{2+} are related. Ca^{2+} entry into cultured neurons is correlated with Zn^{2+} release from intracellular stores [221]. Studies in our laboratory indicate the Zn^{2+} concentration in the ER decreases concomitantly with an increase in cytosolic Ca^{2+} [66].

Until recently, it has been difficult to study the dynamics of Ca^{2+} and Zn^{2+} signaling in living cells because many Ca^{2+} -sensitive fluorescent dyes also respond to Zn^{2+} . During the past decade, many Zn^{2+} -specific genetically-encoded, fluorescent sensors have been developed and optimized for live-cell imaging [66, 72, 136, 222]. Genetically-encoded sensors of Ca^{2+} or Zn^{2+} can be used to differentiate changes in $[\text{Ca}^{2+}]$ from changes in $[\text{Zn}^{2+}]$, and thus are ideal for studying metal crosstalk in living cells.

I decided to use a mouse insulinoma cell line, MIN6, as a model system for investigating

crosstalk between intracellular Ca^{2+} and Zn^{2+} in the well-characterized glucose-stimulated insulin secretion pathway. The main stimulus of insulin secretion from pancreatic β cells is a glucose concentration above 5-7 mM [223–226]. In this canonical pathway, glucose enters a cell through a glucose transporter and is metabolized by glycolysis and oxidative phosphorylation. The increased ATP to ADP ratio inhibits K^+ channels on the plasma membrane, which leads to membrane depolarization and the opening of voltage-dependent Ca^{2+} channels. The Ca^{2+} influx triggers fusion of insulin-containing vesicles to the plasma membrane and oscillations in $[\text{Ca}^{2+}]$; these oscillations are thought to drive pulsatile insulin secretion [218, 227, 228]. Ensuing oscillations in cyclic AMP and inositol triphosphate can regulate the pattern of $[\text{Ca}^{2+}]$ oscillations, which in turn can lead to different cellular responses, including, but not limited to, the amount and pattern of insulin secretion [218, 227, 229, 230].

Zn^{2+} has been shown to be important in pancreatic β cell physiology and insulin secretion, but the extent of its interaction with Ca^{2+} is poorly understood. One human zinc transporter, ZnT-8 (SLC30A8), has been implicated in the pathogenesis of type 1 diabetes, as it is a major autoantigen associated with the disease [231, 232]. In a recent study, mutations in human *ZnT-8* were found to be associated with a decreased risk for type 2 diabetes [8]. Interestingly, Zn^{2+} is crystallized with insulin in secretory vesicles, and ZnT-8 increases the Zn^{2+} content in these vesicles [232]. There have been many observations that changes in cellular Zn^{2+} are associated with changes in Zn^{2+} transporter and metallothionein expression, responsiveness to glucose stimulation, and insulin secretion [11, 30, 233–236]. However, the changes in Zn^{2+} in these experiments have not been quantified nor have they been localized to subcellular locations. Zn^{2+} can enter pancreatic β cells via multiple zinc transporters [237], voltage-gated Ca^{2+} channels, and the transient receptor potential channel M3 (TRPM3) [65, 110, 111, 113, 114]. Zn^{2+} may interact with the stimulus-secretion pathway by modulating Ca^{2+} influx into the cell and between different subcellular compartments or by interfering with insulin synthesis and secretion.

Previous work in our laboratory has shown that genetically-encoded Zn^{2+} sensors can be expressed and are functional in the cytosol and mitochondria of MIN6 cells [65, 88], and moreover

we can detect changes in the cytosolic Zn^{2+} concentration upon membrane depolarization with high extracellular KCl concentrations [65]. Our platform of genetically-encoded FRET sensors enables real-time observation of dynamic changes in the concentration of specific ions in specific subcellular locations. In this study, I use genetically-encoded sensors to observe fluctuations in cytosolic Ca^{2+} and Zn^{2+} concentrations upon stimulation with glucose, in the presence or absence of Zn^{2+} . I find that the addition of 10-20 μM ZnCl_2 to the imaging media dampens cytosolic Ca^{2+} oscillations stimulated by glucose and increases cytosolic Zn^{2+} . Understanding how Zn^{2+} affects Ca^{2+} oscillations could provide insight into how Zn^{2+} homeostasis affects glucose-stimulated insulin secretion.

4.3 Results and Discussion

In this study, genetically-encoded, ratiometric sensors of Ca^{2+} and Zn^{2+} were targeted to the cytosol by incorporating an N-terminal nuclear export sequence (NES) into the DNA sequence encoding these sensors (see Figure 4.1 and Section 4.4). The Ca^{2+} sensor, D3cpV, is a high-dynamic range sensor that has been used successfully in many different cell types [137,144]. The Zn^{2+} sensor, ZapCV2, is a modified version of the ZapCY2 sensor in which the citrine fluorescent protein is replaced with venus fluorescent protein circularly-permuted at amino acid 173 [65,66,143]. Both sensors localized well to the cytosol of MIN6 cells, and they were verified to be functional using the methods described in Chapter 2 (data not shown).

Next, I confirmed that high concentrations of glucose (16-18 mM) can induce Ca^{2+} oscillations, detectable by NES-D3cpV, in MIN6 cells cultured in low-glucose (5.5 mM) for 24-48 hours. These results are consistent with previous studies that revealed switching from low to high glucose media induces oscillations in Ca^{2+} in insulin-secreting cell lines [223, 227, 228, 238, 239]. Figure 4.2 shows that the oscillations in $[\text{Ca}^{2+}]$ are heterogeneous, as previously reported [227, 240, 241]. However, the peak frequency clearly increases after the addition of glucose. No response in cytosolic Ca^{2+} was observed upon glucose stimulation of HeLa cells, which should not be sensitive to a change in glucose concentration (data not shown).

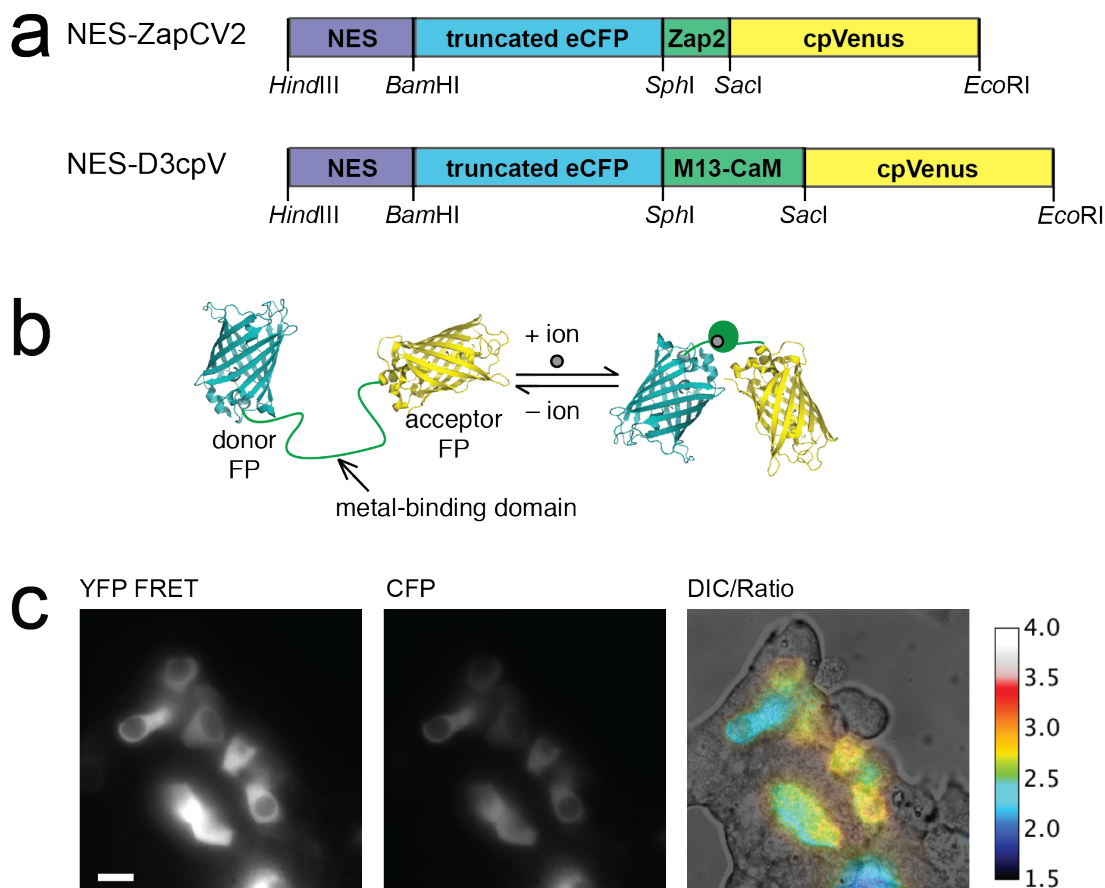


Figure 4.1: Genetically-encoded Zn^{2+} and Ca^{2+} sensors used in this study. a) The Zn^{2+} sensor NES-ZapCV2 and the Ca^{2+} sensor NES-D3cpV were used to monitor cytosolic ion concentrations. Both sensors consist of a binding domain sandwiched between a truncated enhanced cyan fluorescent protein (eCFP) [136] and Venus fluorescent protein circularly permuted at amino acid 173 (cpVenus) [137, 143]. There is an N-terminal nuclear export sequence (NES) that targets the sensors to the cytosol. b) The distance and orientation of the donor FP (eCFP) to the acceptor FP (cpVenus) are different in the ion-bound and ion-free conformations. Consequently, the Förster resonance energy transfer (FRET) efficiency differs in the two conformations. The FRET ratio (R) can be monitored with fluorescence microscopy. c) Images of MIN6 cells expressing NES-D3cpV imaged with an epifluorescence microscope. An image pseudocolored by R (a calibration bar is shown on the right) is overlaid on the DIC image. The scale bar represents 10 μm .

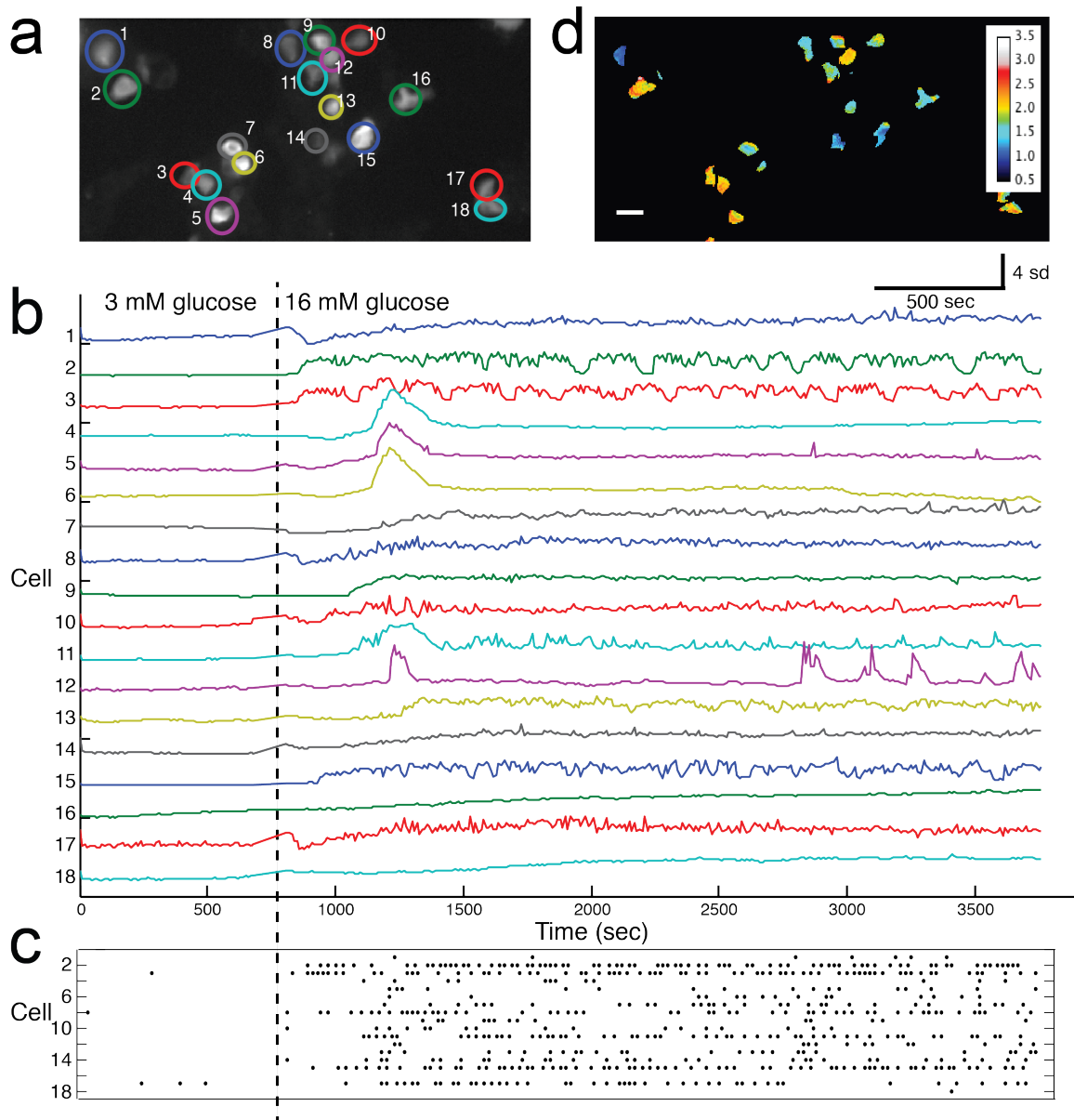


Figure 4.2: Glucose stimulates Ca^{2+} oscillations in MIN6 cells. MIN6 cells, transfected with NES-D3cpV, were stimulated with 16 mM glucose to induce Ca^{2+} oscillations. a) The mean R of each cell (numbered 1-18) was measured over the time course (see Section 4.4 for details). b) The changes in $[\text{Ca}^{2+}]$, as reported by NES-D3cpV, when cells are incubated in 3 mM glucose and 16 mM glucose are shown for each cell in the field of view. Changes in R are displayed as standard deviations from the mean. c) Each peak of the Ca^{2+} oscillation traces is plotted over time. d) An image of MIN6 cells pseudocolored by the initial R . A calibration bar shows the colors corresponding to R values. The scale bar represents 20 μm .

In order to test our hypothesis that Zn^{2+} can modulate glucose-stimulated Ca^{2+} oscillations, I monitored Ca^{2+} oscillations with NES-D3cpV in the presence or absence of Zn^{2+} . In these experiments, both glucose and Zn^{2+} were increased simultaneously, and images were acquired every 10 seconds for 30-90 minutes. The Ca^{2+} oscillatory pattern was classified into four categories: no response (no peaks higher than the standard deviation of R of NES-D3cpV), slow oscillations (peaks that are longer than 1 min in duration with a period longer than 2 min), or fast oscillations (peaks that have a period of less than 1 min). The presence of 10-20 μM extracellular Zn^{2+} during glucose stimulation decreased the the number of oscillations observed in 30 min. This is shown in Figure 4.3. Glucose stimulation did not induce any response in Ca^{2+} oscillations when 100 μM extracellular Zn^{2+} was present (data not shown).

I used NES-ZapCV2 to monitor increases in Zn^{2+} when glucose and Zn^{2+} are added to cells at the same time. I found that the addition of 10-20 μM ZnCl_2 extracellularly, while cells are incubated in imaging buffer, increases cytosolic Zn^{2+} significantly. Figure 4.4 shows the difference in cytosolic $[\text{Zn}^{2+}]$ upon glucose stimulation in the presence or absence of ZnCl_2 , displayed as the fractional saturation of NES-ZapCV2. Unexpectedly, the addition of glucose results in an initial decrease in the fractional saturation of NES-ZapCV2. This decrease in R could represent an actual decrease in cytosolic $[\text{Zn}^{2+}]$; it could also be caused by an increase in pH [212] that affects the fluorescence of eCFP and cpVenus, resulting in a change in R .

These results support our hypothesis that Zn^{2+} can modulate cytosolic Ca^{2+} oscillations stimulated by high concentrations of glucose, but it remains to be determined if this modulation affects insulin secretion or other downstream signaling. It is also unclear whether intracellular or extracellular Zn^{2+} is affecting cytosolic Ca^{2+} ; this could be tested using a cell-impermeant Zn^{2+} chelator [242]. Another avenue for further investigation is to see if Zn^{2+} modulation of Ca^{2+} signals are dependent on intracellular or extracellular Zn^{2+} .

Zn^{2+} may also be involved in regulating cellular metabolism and mitochondrial function, which could influence ATP production, membrane depolarization, and Ca^{2+} influx leading to insulin secretion. Changes in Zn^{2+} availability can affect metabolism, including glycolysis and oxidative

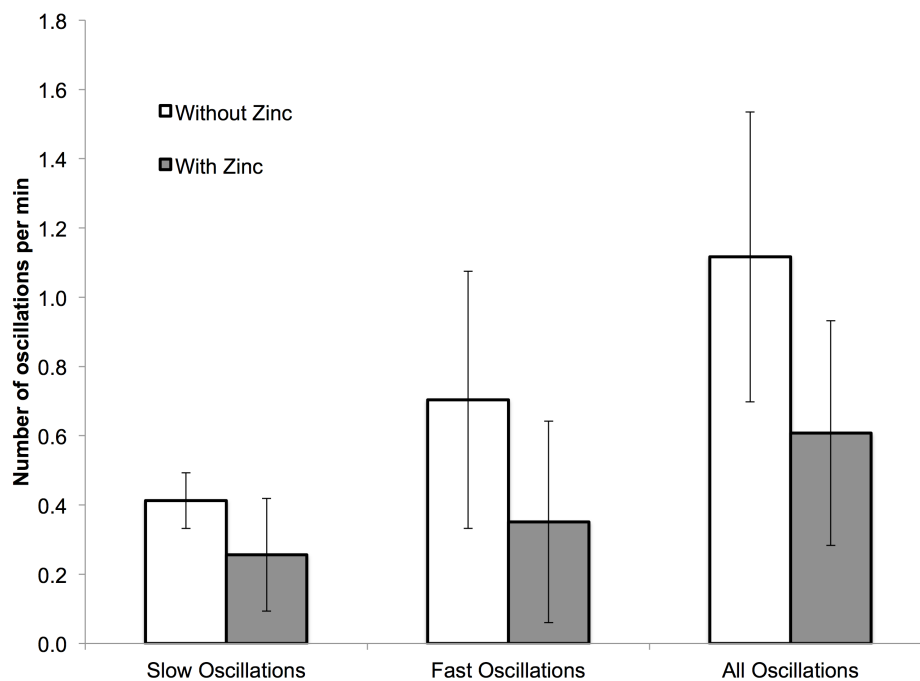


Figure 4.3: The presence of Zn^{2+} decreases Ca^{2+} oscillation frequency in MIN6 cells. The changes in cytosolic $[Ca^{2+}]$ in response upon glucose stimulation were monitored by the sensor NES-D3cpV. The oscillatory peaks during the 30 min immediately after the addition of 16 mM glucose, in the presence or absence of 10-20 μM extracellular $ZnCl_2$, were used to calculate the peak frequency of individual cells in 3 side-by-side experiments (10-30 cells per experiment).

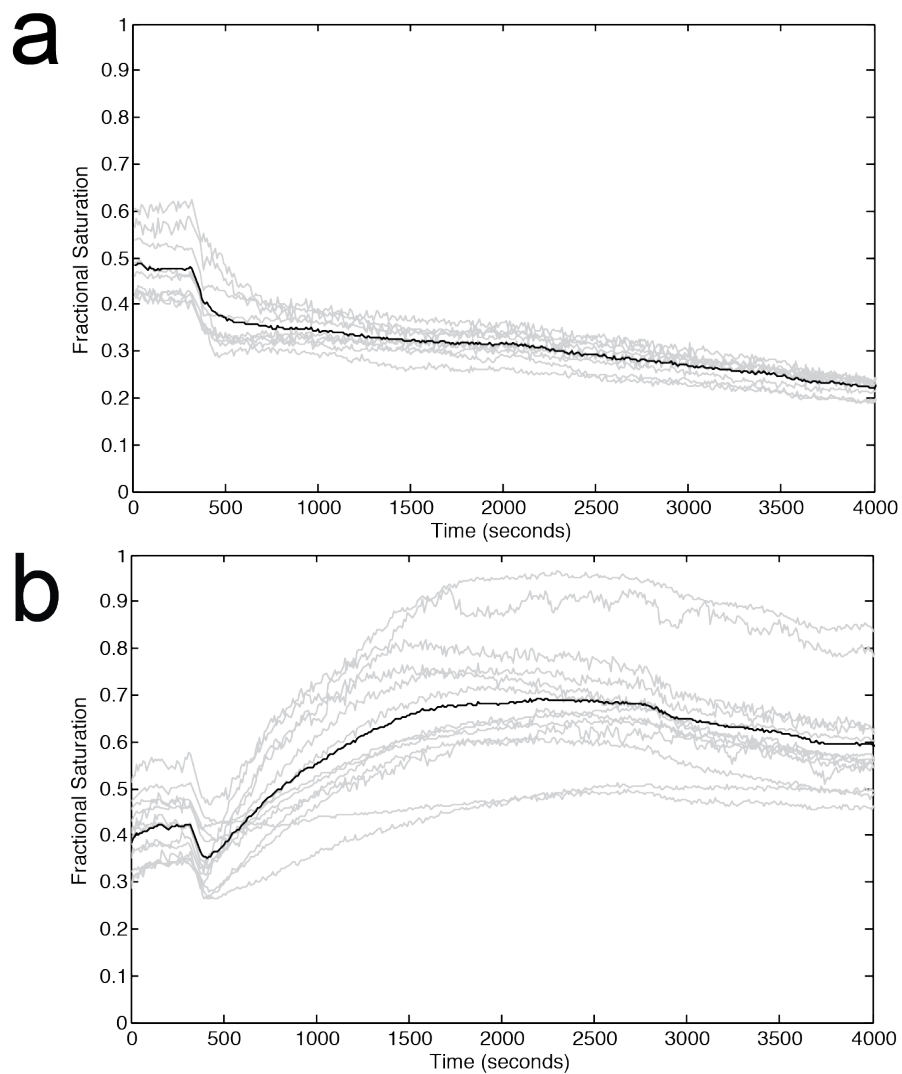


Figure 4.4: Cytosolic Zn²⁺ increases upon addition of glucose and Zn²⁺. Results of two different imaging experiments of MIN6 cells expressing the Zn²⁺ sensor NES-ZapCV2 are shown in this Figure. MIN6 cells, initially incubated in 2 mM glucose, were stimulated with a) 16 mM glucose alone, or b) 16 mM glucose and 20 μM ZnCl₂ after ~300 sec of imaging.

phosphorylation, in isolated mitochondria [202,208]. Zn^{2+} can also change mitochondrial dynamics, which are important for ATP availability, Ca^{2+} homeostasis, and differentiation [204–206]. The effect of Zn^{2+} on the ATP to ADP ratio could be monitored using a genetically-encoded sensor called Perceval [158,212]. Monitoring Zn^{2+} , Ca^{2+} , and other metabolites in living cells with fluorescence microscopy has the potential to uncover and decipher the complexities of the crosstalk between metal ions and other second messengers.

4.4 Methods

The Zn^{2+} sensor ZapCV2 and the Ca^{2+} sensor D3cpV were cloned, using the *Bam*HI and *Eco*RI restriction sites, into a pcDNA3.1 vector containing a nuclear export signal (NES) N-terminal to the sensor construct [145]. The amino acid sequence of the NES is LQLPPLERLTL. The two sensors have different ion-sensing domains, but otherwise they are identical (see Figure 4.1). The Zap2 sensing domain is a mutant of the first two Zn^{2+} fingers of *Saccharomyces cerevisiae* Zap1 [66], and the D3 sensing domain is a modified version of the M13 peptide and calmodulin binding pair [137].

4.4.1 Cell Culture

HeLa cells were maintained in high glucose Dulbecco's Modified Eagle Medium (D-MEM) with 10% fetal bovine serum (FBS) and 100 U/mL penicillin/streptomycin (pen/strep). MIN6 cells were cultured in D-MEM (25 mM glucose; Gibco #11995065) supplemented with 10% (v/v) FBS, 5.5 mM L-glutamine, 1.8 mM sodium pyruvate, 70 μM β -mercaptoethanol, and 100 U/mL pen/strep. For 24-48 hours prior to imaging, MIN6 cells were maintained in low-glucose D-MEM (5.6 mM glucose; Gibco #31600083) supplemented with 10% (v/v) FBS, 5.5 mM L-glutamine, 1.8 mM sodium pyruvate, 70 μM β -mercaptoethanol, and 100 U/mL pen/strep. For imaging, HeLa cells were plated on 35 mm glass-bottom dishes (uncoated) at a density of 1.5×10^5 cells per dish; MIN6 cells were plated on 35 mm glass-bottom dishes coated with poly-L-lysine at a density of 2.5×10^5 cells per dish.

HeLa cells were transiently transfected with TransIT-LT1 (Mirus Bio), using 5 μl of TransIT-LT1 and 1.5 μg of plasmid DNA for each 35 mm imaging dish. MIN6 cells were transiently transfected with TransIT-LT1, using 3 μl of TransIT-LT1 and 1 μg of plasmid DNA for each 35 mm imaging dish. Alternatively, MIN6 cells were electroporated with the Neon Transfection System (Life Technologies). 2×10^6 MIN6 cells were resuspended in 100 μl buffer and mixed with 10 μg plasmid DNA for electroporation (2 pulses of 1200 volts for 20 ms each).

HeLa and MIN6 stable cell lines expressing NES-ZapCV2 were made using the PiggyBac transposon system (reviewed in [243]; detailed protocol in Section C.3). HeLa cells were transfected and MIN6 cells were electroporated with two plasmids: a mammalian expression plasmid carrying PiggyBac transposase and another mammalian expression plasmid containing NES-ZapCV2 and blasticidin resistance flanked by inverted repeats. Cells were maintained in selection media containing 6 $\mu\text{g}/\text{mL}$ blasticidin for 3 days to select for cells expressing NES-ZapCV2.

4.4.2 Imaging

Two different microscopy systems, described in Section C.2 were used to image cells. Briefly, a Zeiss Axiovert 200M equipped with a Xenon XBO 75 lamp (Zeiss), a Cascade 512B camera (Photometrics), a Lambda 10-3 filter wheel and shutter control system (Sutter Instruments), and 40X oil and 100X oil objectives was used for imaging at room temperature (21-22 $^{\circ}\text{C}$). The filter settings were 430/24 nm excitation, 455 nm dichroic, and 535/25 nm emission for YFP FRET; 430/24 nm excitation, 455 nm dichroic, and 470/24 nm emission for CFP. A Nikon Eclipse Ti equipped with a Lambda XL with liquid light guide (Sutter Instruments), a iXon3 EMCCD camera (Andor), a DV2 emission splitting system (Photometrics), a LiveCell Stage Top Incubation System (Pathology Devices), and 20X air and 60X oil objectives was used for imaging at 37 $^{\circ}\text{C}$. The DV2 emission splitting system contains the following filters: 438/24 nm excitation filter, 483/32 nm emission filter for CFP, a 542/27 nm emission filter for YFP FRET, and a 458 nm dichroic mirror (Semrock Brightline filter set, Part #FRET-CFP/YFP-B-000).

Cells were imaged in either phosphate-free HEPES-buffered Hank's Balanced Salt Solution

(HHBSS) or Krebs Ringer Buffer with HEPES (KRBH), both at pH 7.4. HHBSS contains 137 mM sodium chloride, 5.4 mM potassium chloride, 1.1 mM magnesium chloride, 1.26 mM calcium chloride, and 20 mM HEPES. KRBH contains 130 mM sodium chloride, 4.8 mM potassium chloride, 1.2 mM magnesium sulfate, 2 mM calcium chloride, 5 mM sodium bicarbonate, 1 mg/mL bovine serum albumin, and 10 mM HEPES. Glucose concentration was adjusted to be between 0 and 18 mM with freshly made 1 M D-glucose (dextrose).

Before imaging, cells were washed 3 times in imaging buffer and incubated in 2 mL imaging buffer for 1-2 hours. Cells were also washed 3-5 times with 2 mL imaging buffer between chemical perturbations. The stock solutions used to perform chemical perturbations during imaging experiments were 1 M D-glucose (Fisher) in Chelex-treated water, 400 μ M ZnCl₂ (Sigma-Aldrich) in HHBSS, 25 mM *N,N,N',N'*-Tetrakis(2-pyridylmethyl)ethylenediamine (TPEN; Sigma-Aldrich) in 100% DMSO, 0.5 mM 2,2'-Bipyridyl (pyrithione; Sigma Aldrich) in 100% DMSO, 1 mM ionomycin (Calbiochem) in 100% DMSO.

4.4.3 Data Analysis

Data analysis was performed using ImageJ [182] and MATLAB (The MathWorks) using a customized script. First, cell boundaries were selected in ImageJ. Then, images were registered by calculating a geometric transformation and applying it to all images in the experiment. Automated selection of ROIs with each cell, calculation of R values and fractional saturation, and creation of ratiometric images were performed using a customized script in MATLAB. Details of these methods can be found in Chapter 2 and Appendix B. Peaks were identified using the `find peaks` function in the MATLAB Signal Processing Toolbox.

Chapter 5

Concluding Remarks and Future Directions

5.1 Conclusions

Zn^{2+} is a micronutrient essential for human life, and it is necessary for all major cellular functions. For over 50 years, physicians have recognized the important role of Zn^{2+} in human nutrition, immunity, and brain function, and in the last decade, scientists have discovered that the body's Zn^{2+} balance and distribution can be different in diseases including diabetes, Alzheimer's disease, and breast and prostate cancer [2, 9, 244]. However, it is poorly understood how Zn^{2+} dysregulation affects specific cell signaling pathways and cellular processes in human health and disease. In this thesis, I developed and used genetically-encoded Zn^{2+} sensors to improve our understanding of the biological role of Zn^{2+} in mitochondria and in insulin-secreting cells.

The methods for optimizing the use of genetically-encoded Ca^{2+} or Zn^{2+} sensors, presented in Chapter 2, have been critical to the completion of the work presented in Chapters 3 and 4. Optimization of a sensor's calibration protocol and determination of its *in situ* K_D' enabled us to make more precise, accurate, and repeatable estimates of the *free* Zn^{2+} concentration in different organelles. Automation of image analysis increased our data analysis efficiency, allowing us to analyze higher throughput experiments, which tracked dozens of cells, within a reasonable time frame. Furthermore, other investigators can use the MATLAB scripts and functions, which were written for specific types of imaging experiments performed in this thesis, to analyze new data in exactly the same way. I believe the methods discussed in Chapter 2 will improve the consistency of experimental results not only within our laboratory, but also among different laboratories.

In Chapter 3, I constructed and tested several of new mitochondrial Zn^{2+} sensors and identified three sensors with a high dynamic range. One of these sensors, mito-ZapCY1, was used to quantify the *free* Zn^{2+} concentration in mitochondria of different cell types. The sub-picomolar concentrations of *free* mitochondrial Zn^{2+} that I observed in this study was unexpected, as several other studies had predicted much higher concentrations [117, 118, 124, 136]. Our estimates of *free* Zn^{2+} concentration in mitochondria have been corroborated by estimates made using another recently developed sensor [67]. The mito-ZapCY1 sensor is an excellent tool for future studies of mitochondrial Zn^{2+} homeostasis, which is discussed further in Section 5.2.1.

I explored potential crosstalk between Ca^{2+} and Zn^{2+} in Chapter 4 by applying our expertise in genetically-encoded sensors of metal ions. Cytosolic Ca^{2+} and Zn^{2+} sensors were used to observe changing ion concentrations in a pancreatic β cell line during stimulation with high glucose concentrations. Importantly, these sensors enabled us to observe changes in Ca^{2+} or Zn^{2+} specifically and with minimal perturbation of endogenous Ca^{2+} and Zn^{2+} homeostasis [65, 137]. I found that the addition of Zn^{2+} during high glucose stimulation changed the pattern of ensuing changes in cytosolic Ca^{2+} concentration. The work presented in this Chapter should be supplemented with other assays, such as the measurement of insulin secretion, to investigate the downstream consequences of these changes in Ca^{2+} oscillations.

5.2 Future Directions

5.2.1 Further Characterization of Mitochondrial Zinc Homeostasis

A valuable research goal is to evaluate the potential role of Zn^{2+} homeostasis in mitochondrial function, which is supported by several observations. First, Zn^{2+} appears to be an antioxidant in several cell types, and mitochondria are a major source of reactive oxygen species (ROS). Zn^{2+} homeostasis may affect metallation of Cu/Zn superoxide dismutase, which is a major regulator of ROS [245, 246]. Second, changes in Zn^{2+} availability can affect energy production, including glycolysis and oxidative phosphorylation [202]. Third, Zn^{2+} can change mitochondrial dynamics, which

are important for ATP availability, Ca^{2+} homeostasis, and differentiation [205, 206, 208]. Fourth, toxic increases in intracellular Zn^{2+} lead to apoptosis through the intrinsic pathway [118, 201]. Also, Zn^{2+} can play a role in mitochondrial protein import by binding to the translocase of the inner membrane proteins [247]. Lastly, many investigators support the hypothesis that mitochondria are a source and sink of Zn^{2+} , which could affect all the mitochondrial functions mentioned above [40, 117, 207].

Our high dynamic range mitochondrial Zn^{2+} sensor, mito-ZapCY1, could be used to monitor changes in mitochondrial Zn^{2+} homeostasis when mitochondrial function is perturbed. Possible perturbations include inhibition of oxidative phosphorylation with protonophores, such as carbonyl cyanide-p-trifluoromethoxyphenylhydrazone (FCCP) and 2,4-dinitrophenol (DNP); electron transport chain inhibitors, such as rotenone and Antimycin A; and ATP synthase inhibitors, such as oligomycin. Zn^{2+} has also been hailed as an antioxidant [248–250], and mitochondria are the major generators of ROS, which have a signaling role in most cells [251, 252]. Zn^{2+} homeostasis could be monitored during treatment with oxidizing agents, such as 2-2' dithionpyridine (DTDP) and 5,5'-dithiobis-(2-nitrobenzoic acid) (DTNB), or antioxidants, such as MitoQ (Antipodean Pharmaceuticals).

In Chapter 3, mito-ZapCY1 was used to measure the *average* free Zn^{2+} concentration of all mitochondria in a cell. Mito-ZapCY1 has the potential to be used to assay the free Zn^{2+} concentration of individual mitochondria and to correlate these concentrations to mitochondrial shape, size, or movement. Mito-ZapCY1 could also be used with other sensors of mitochondrial function that do not overlap significantly with its spectral bandwidth (CFP/YFP), such as sensors of mitochondrial membrane potential (JC-1, Life Technologies), a sensor of mitochondrial outer membrane permeabilization (RFP-tagged Smac protein [153]), or an intensimetric Ca^{2+} sensor (R-GECO [253]).

5.2.2 Investigation of Zinc Homeostasis During Cell Division

Zn^{2+} is required for cell growth and proliferation [47] because it has a catalytic or structural role in up to 10% of human proteins, many of which function in DNA replication and transcription [23,42,43]. Too much Zn^{2+} can be toxic, but Zn^{2+} deficiency results in poor growth [29,108,254–256]. The labile Zn^{2+} concentrations in the nucleus and cytosol have never been monitored or quantified in individual cells during cell division, even though some evidence suggests that Zn^{2+} fluxes are correlated with particular phases of the cell cycle [257,258]. Fluxes in Zn^{2+} could activate or inhibit subsets of proteins important for the progression of the cell cycle [10,23,61,259]. The methods and sensors developed in this thesis could be used to make novel observations about cellular Zn^{2+} homeostasis during cell division by using genetically-encoded Zn^{2+} sensors targeted to the cytosol, nucleus, or other organelles. Preliminary work indicates that these experiments are feasible but would benefit from further development of automated analysis protocols.

Bibliography

- [1] Bhutta, Z. A, Ahmed, T, Black, R. E, Cousens, S, Dewey, K, Giugliani, E, Haider, B. A, Kirkwood, B, Morris, S. S, Sachdev, H. P. S, Shekar, M, & Maternal and Child Undernutrition Study Group. (2008) *Lancet* **371**, 417–440.
- [2] Hambidge, M. (2000) *J Nutr* **130**, 1344S–9S.
- [3] Bhutta, Z. A, Black, R. E, Brown, K. H, Gardner, J. M, Gore, S, Hidayat, A, Khatun, F, Martorell, R, Ninh, N. X, Penny, M. E, Rosado, J. L, Roy, S. K, Ruel, M, Sazawal, S, & Shankar, A. (1999) *J. Pediatr.* **135**, 689–697.
- [4] Walravens, P. A, Hambidge, K. M, & Koepfer, D. M. (1989) *PEDIATRICS* **83**, 532–538.
- [5] John, E, Laskow, T. C, Buchser, W. J, Pitt, B. R, Basse, P. H, Butterfield, L. H, Kalinski, P, & Lotze, M. T. (2010) *Journal of Translational Medicine* **8**, 118.
- [6] Haase, H & Rink, L. (2009) *Immun Ageing* **6**, 9.
- [7] Wang, K, Zhou, B, Kuo, Y.-M, Zemansky, J, & Gitschier, J. (2002) *Am. J. Hum. Genet.* **71**, 66–73.
- [8] Flannick, J, Thorleifsson, G, Beer, N. L, Jacobs, S. B. R, Grarup, N, Burt, N. P, Mahajan, A, Fuchsberger, C, Atzmon, G, Benediktsson, R, Blangero, J, Bowden, D. W, Brandslund, I, Brosnan, J, Burslem, F, Chambers, J, Cho, Y. S, Christensen, C, Douglas, D. A, Duggirala, R, Dymek, Z, Farjoun, Y, Fennell, T, Fontanillas, P, Forsén, T, Gabriel, S, Glaser, B, Gudbjartsson, D. F, Hanis, C, Hansen, T, Hreidarsson, A. B, Hveem, K, Ingelsson, E, Isomaa, B, Johansson, S, Jørgensen, T, Jørgensen, M. E, Kathiresan, S, Kong, A, Kooner, J, Kravic, J, Laakso, M, Lee, J.-Y, Lind, L, Lindgren, C. M, Linneberg, A, Masson, G, Meitinger, T, Mohlke, K. L, Molven, A, Morris, A. P, Potluri, S, Rauramaa, R, Ribel-Madsen, R, Richard, A.-M, Rolph, T, Salomaa, V, Segrè, A. V, Skärstrand, H, Steinthorsdottir, V, Stringham, H. M, Sulem, P, Tai, E. S, Teo, Y. Y, Teslovich, T, Thorsteinsdottir, U, Trimmer, J. K, Tuomi, T, Tuomilehto, J, Vaziri-Sani, F, Voight, B. F, Wilson, J. G, Boehnke, M, McCarthy, M. I, Njølstad, P. R, Pedersen, O, Groop, L, Cox, D. R, Stefansson, K, & Altshuler, D. (2014) *Nat Genet.*
- [9] Frederickson, C. J, Koh, J.-Y, & Bush, A. I. (2005) *Nat Rev Neurosci* **6**, 449–462.
- [10] Yamasaki, S, Sakata-Sogawa, K, Hasegawa, A, Suzuki, T, Kabu, K, Sato, E, Kurosaki, T, Yamashita, S, Tokunaga, M, Nishida, K, & Hirano, T. (2007) *J Cell Biol* **177**, 637–645.

- [11] Devirgiliis, C, Zalewski, P. D, Perozzi, G, & Murgia, C. (2007) *Mutat Res* **622**, 84–93.
- [12] Piletz, J. E & Herschman, H. R. (1982) *Biochem Genet* **20**, 1221–1233.
- [13] Piletz, J. E & Ganschow, R. E. (1978) *Science* **199**, 181–183.
- [14] Huang, L & Gitschier, J. (1997) *Nat Genet* **17**, 292–297.
- [15] Itsumura, N, Inamo, Y, Okazaki, F, Teranishi, F, Narita, H, Kambe, T, & Kodama, H. (2013) *PLoS ONE* **8**, e64045.
- [16] Bruinsma, J. J, Jirakulaporn, T, Muslin, A. J, & Kornfeld, K. (2002) *Developmental Cell* **2**, 567–578.
- [17] Yoder, J. H, Chong, H, Guan, K.-L, & Han, M. (2004) *EMBO J* **23**, 111–119.
- [18] Jeong, J & Eide, D. J. (2013) *Molecular Aspects of Medicine* **34**, 612–619.
- [19] Huang, L & Tepasamorndech, S. (2013) *Molecular Aspects of Medicine* **34**, 548–560.
- [20] Babula, P, Masarik, M, Adam, V, Eckschlager, T, Stiborova, M, Trnkova, L, Skutkova, H, Provaznik, I, Hubalek, J, & Kizek, R. (2012) *Metallomics* **4**, 739–750.
- [21] Kelleher, S. L, Seo, Y. A, & Lopez, V. (2009) *Genes Nutr* **4**, 83–94.
- [22] Kitamura, H, Morikawa, H, Kamon, H, Iguchi, M, Hojyo, S, Fukada, T, Yamashita, S, Kaisho, T, Akira, S, Murakami, M, & Hirano, T. (2006) *Nat Immunol* **7**, 971–977.
- [23] Beyersmann, D & Haase, H. (2001) *Biometals* **14**, 331–341.
- [24] Li, M, Zhang, Y, Liu, Z, Bharadwaj, U, Wang, H, Wang, X, Zhang, S, Liuzzi, J. P, Chang, S.-M, Cousins, R. J, Fisher, W. E, Brunicardi, F. C, Logsdon, C. D, Chen, C, & Yao, Q. (2007) *Proc Natl Acad Sci USA* **104**, 18636–18641.
- [25] Simons, T. (1991) *The Journal of membrane biology* **123**, 63–71.
- [26] Gandhi, M. S, Deshmukh, P. A, Kamalov, G, Zhao, T, Zhao, W, Whaley, J. T, Tichy, J. R, Bhattacharya, S. K, Ahokas, R. A, Sun, Y, Gerling, I. C, & Weber, K. T. (2008) *J Cardiovasc Pharmacol* **52**, 245–252.
- [27] Stoecker, B. J, Abebe, Y, Hubbs-Tait, L, Kennedy, T. S, Gibson, R. S, Arbide, I, Teshome, A, Westcott, J, Krebs, N. F, & Hambidge, K. M. (2009) *Eur J Clin Nutr* **63**, 916–918.
- [28] Gibson, R. S, Hess, S. Y, Hotz, C, & Brown, K. H. (2008) *Br. J. Nutr.* **99 Suppl 3**, S14–23.
- [29] Bozym, R. A, Chimienti, F, Giblin, L. J, Gross, G. W, Korichneva, I, Li, Y, Libert, S, Maret, W, Parviz, M, Frederickson, C. J, & Thompson, R. B. (2010) *Exp. Biol. Med. (Maywood)* **235**, 741–750.
- [30] Kelleher, S. L, McCormick, N. H, Velasquez, V, & Lopez, V. (2011) *Adv Nutr* **2**, 101–111.
- [31] Milo, R, Jorgensen, P, Moran, U, Weber, G, & Springer, M. (2010) *Nucleic Acids Research* **38**, D750–3.

- [32] Outten, C. E & O'Halloran, T. V. (2001) *Science* **292**, 2488–2492.
- [33] Krezel, A & Maret, W. (2006) *J Biol Inorg Chem* **11**, 1049–1062.
- [34] Hare, D. J, Grubman, A, Ryan, T. M, Lothian, A, Liddell, J. R, Grimm, R, Matsuda, T, Doble, P. A, Cherny, R. A, Bush, A. I, White, A. R, Masters, C. L, & Roberts, B. R. (2012) *Metallomics* **5**, 1656–1662.
- [35] Liu, Y, Franklin, R. B, & Costello, L. C. (1997) *Prostate* **30**, 26–32.
- [36] Ye, B, Maret, W, & Vallee, B. L. (2001) *Proc Natl Acad Sci USA* **98**, 2317–2322.
- [37] Gee, K, Zhou, Z.-L, Ton-That, D, Sensi, S, & Weiss, J. (2002) *Cell Calcium* **31**, 245–251.
- [38] Frederickson, C. (2003) *Sci STKE* **2003**, 18pe–18.
- [39] Cole, T. B, Wenzel, H. J, Kafer, K. E, Schwartzkroin, P. A, & Palmiter, R. D. (1999) *Proc Natl Acad Sci USA* **96**, 1716–1721.
- [40] Colvin, R. A, Holmes, W. R, Fontaine, C. P, & Maret, W. (2010) *Metallomics* **2**, 306.
- [41] Colvin, R. A, Bush, A. I, Volitakis, I, Fontaine, C. P, Thomas, D, Kikuchi, K, & Holmes, W. R. (2008) *AJP: Cell Physiology* **294**, C726–C742.
- [42] Andreini, C, Banci, L, Bertini, I, & Rosato, A. (2006) *J Proteome Res* **5**, 196–201.
- [43] Bertini, I, Decaria, L, & Rosato, A. (2010) *J Biol Inorg Chem* **15**, 1071–1078.
- [44] Andreini, C, Bertini, I, & Cavallaro, G. (2011) *PLoS ONE* **6**, e26325.
- [45] Auld, D. S. (2001) *Biometals* **14**, 271–313.
- [46] McCall, K. A, Huang, C, & Fierke, C. A. (2000) *J Nutr* **130**, 1437S–46S.
- [47] Vallee, B. L & Falchuk, K. H. (1993) *Physiol Rev* **73**, 79–118.
- [48] Waldron, K. J, Rutherford, J. C, Ford, D, & Robinson, N. J. (2009) *Nature* **460**, 823–830.
- [49] Lukaski, H. C. (2005) *Am J Clin Nutr* **81**, 1045–1051.
- [50] Krezel, A & Maret, W. (2007) *J Am Chem Soc* **129**, 10911–10921.
- [51] Krishna, S. S, Majumdar, I, & Grishin, N. V. (2003) *Nucleic Acids Research* **31**, 532–550.
- [52] Maret, W & Li, Y. (2009) *Chem Rev* **109**, 4682–4707.
- [53] Brayer, K. J & Segal, D. J. (2008) *Cell Biochem Biophys* **50**, 111–131.
- [54] Yannone, S. M, Hartung, S, Menon, A. L, Adams, M. W. W, & Tainer, J. A. (2012) *Curr Opin Biotechnol* **23**, 89–95.
- [55] Maret, W. (2010) *Metallomics* **2**, 117.

- [56] Cvetkovic, A, Menon, A. L, Thorgersen, M. P, Scott, J. W, Ii, F. L. P, Jenney, Jr, F. E, Lancaster, W. A, Praissman, J. L, Shanmukh, S, Vaccaro, B. J, Trauger, S. A, Kalisiak, E, Apon, J. V, Siuzdak, G, Yannone, S. M, Tainer, J. A, & Adams, M. W. W. (2010) *Nature* **466**, 779–782.
- [57] She, Y.-M, Narindrasorasak, S, Yang, S, Spitale, N, Roberts, E. A, & Sarkar, B. (2003) *Mol Cell Proteomics* **2**, 1306–1318.
- [58] Barnett, J. P, Scanlan, D. J, & Blindauer, C. A. (2012) *Anal Bioanal Chem* **402**, 3311–3322.
- [59] Yang, Y, Maret, W, & Vallee, B. L. (2001) *Proc Natl Acad Sci USA* **98**, 5556–5559.
- [60] Krezel, A & Maret, W. (2008) *J Biol Inorg Chem* **13**, 401–409.
- [61] Maret, W. (2013) *Biometals* **26**, 197–204.
- [62] Wilson, M, Hogstrand, C, & Maret, W. (2012) *Journal of Biological Chemistry* **287**, 9322–9326.
- [63] Velázquez-Delgado, E. M & Hardy, J. A. (2012) *Journal of Biological Chemistry* **287**, 36000–36011.
- [64] Dineley, K. E, Malaiyandi, L. M, & Reynolds, I. J. (2002) *Mol Pharmacol* **62**, 618–627.
- [65] Qin, Y, Miranda, J. G, Stoddard, C. I, Dean, K. M, Galati, D. F, & Palmer, A. E. (2013) *ACS Chem Biol* **8**, 2366–2371.
- [66] Qin, Y, Dittmer, P. J, Park, J. G, Jansen, K. B, & Palmer, A. E. (2011) *Proc Natl Acad Sci USA* **108**, 7351–7356.
- [67] Mccranor, B. J, Bozym, R. A, Vitolo, M. I, Fierke, C. A, Bambrick, L, Polster, B. M, Fiskum, G, & Thompson, R. B. (2012) *J Bioenerg Biomembr*.
- [68] Bozym, R. A, Thompson, R. B, Stoddard, A. K, & Fierke, C. A. (2006) *ACS Chem Biol* **1**, 103–111.
- [69] Peck, E. J & Ray, W. J. (1971) *J Biol Chem* **246**, 1160–1167.
- [70] Giacconi, R, Malavolta, M, Costarelli, L, Busco, F, Galeazzi, R, Bernardini, G, Gasparini, N, & Mocchegiani, E. (2012) *J. Nutr. Biochem.* **23**, 1256–1263.
- [71] Haase, H, Hebel, S, Engelhardt, G, & Rink, L. (2006) *Anal Biochem* **352**, 222–230.
- [72] Vinkenborg, J. L, Nicolson, T. J, Bellomo, E. A, Koay, M. S, Rutter, G. A, & Merckx, M. (2009) *Nat Meth* **6**, 737–740.
- [73] Benters, J, Flögel, U, Schäfer, T, Leibfritz, D, Hechtenberg, S, & Beyersmann, D. (1997) *Biochem J* **322** (Pt 3), 793–799.
- [74] Ippolito, J. A, Baird, T. T, McGee, S. A, Christianson, D. W, & Fierke, C. A. (1995) *Proc Natl Acad Sci USA* **92**, 5017–5021.
- [75] Schullek, J. R & Wilson, I. B. (1988) *Archives of Biochemistry and Biophysics* **265**, 346–350.

- [76] Cohen, S. R & Wilson, I. B. (1966) *Biochemistry* **5**, 904–909.
- [77] Roehm, P. C & Berg, J. M. (1997) *Biochemistry* **36**, 10240–10245.
- [78] Mély, Y, De Rocquigny, H, Morellet, N, Roques, B. P, & Gérard, D. (1996) *Biochemistry* **35**, 5175–5182.
- [79] Berkovits, H. J & Berg, J. M. (1999) *Biochemistry* **38**, 16826–16830.
- [80] Makowski, G. S & Sunderman, F. W. (1992) *Journal of Inorganic Biochemistry* **48**, 107–119.
- [81] Wang, Z, Feng, L. S, Matskevich, V, Venkataraman, K, Parasuram, P, & Laity, J. H. (2006) *J Mol Biol* **357**, 1167–1183.
- [82] Bergman, T, Zhang, K, Palmberg, C, Jörnvall, H, & Auld, D. S. (2008) *Cell. Mol. Life Sci.* **65**, 4019–4027.
- [83] Cunningham, B. C, Bass, S, Fuh, G, & Wells, J. A. (1990) *Science* **250**, 1709–1712.
- [84] Blindauer, C. A, Harvey, I, Bunyan, K. E, Stewart, A. J, Sleep, D, Harrison, D. J, Berezenko, S, & Sadler, P. J. (2009) *Journal of Biological Chemistry* **284**, 23116–23124.
- [85] Lu, J, Stewart, A. J, Sadler, P. J, Pinheiro, T. J. T, & Blindauer, C. A. (2008) *Biochem. Soc. Trans.* **36**, 1317–1321.
- [86] Walsh, M. J & Ahner, B. A. (2013) *Journal of Inorganic Biochemistry* **128**, 112–123.
- [87] Vinkenborg, J. L, Koay, M. S, & Merckx, M. (2010) *Current Opinion in Chemical Biology* **14**, 231–237.
- [88] Park, J. G, Qin, Y, Galati, D. F, & Palmer, A. E. (2012) *ACS Chem Biol* **7**, 1636–1640.
- [89] Cousins, R. J, Liuzzi, J. P, & Lichten, L. A. (2006) *Journal of Biological Chemistry* **281**, 24085–24089.
- [90] Hennigar, S. R & Kelleher, S. L. (2012) *Biol. Chem.* **393**, 565–578.
- [91] Kelleher, S. L, Velasquez, V, Croxford, T. P, McCormick, N. H, Lopez, V, & MacDavid, J. (2012) *J Cell Physiol* **227**, 1761–1770.
- [92] Gaither, L. A & Eide, D. J. (2001) *Biometals* **14**, 251–270.
- [93] Sekler, I, Sensi, S. L, Hershfinkel, M, & Silverman, W. F. (2007) *Mol Med* **13**, 337–343.
- [94] Liuzzi, J. P & Cousins, R. J. (2004) *Annu. Rev. Nutr.* **24**, 151–172.
- [95] Lichten, L. A & Cousins, R. J. (2009) *Annu. Rev. Nutr.* **29**, 153–176.
- [96] Fukada, T, Yamasaki, S, Nishida, K, Murakami, M, & Hirano, T. (2011) *J Biol Inorg Chem* **16**, 1123–1134.
- [97] Langmade, S. J, Ravindra, R, Daniels, P. J, & Andrews, G. K. (2000) *J Biol Chem* **275**, 34803–34809.
- [98] Lu, M & Fu, D. (2007) *Science* **317**, 1746–1748.

- [99] Argüello, J. M, Raimunda, D, & González-Guerrero, M. (2012) *Journal of Biological Chemistry* **287**, 13510–13517.
- [100] Ohana, E, Hoch, E, Keasar, C, Kambe, T, Yifrach, O, Hershfinkel, M, & Sekler, I. (2009) *J Biol Chem* **284**, 17677–17686.
- [101] Chao, Y & Fu, D. (2004) *J Biol Chem* **279**, 12043–12050.
- [102] Gaither, L. A & Eide, D. J. (2000) *J Biol Chem* **275**, 5560–5564.
- [103] Gaither, L. A & Eide, D. J. (2001) *J Biol Chem* **276**, 22258–22264.
- [104] Himeno, S, Yanagiya, T, & Fujishiro, H. (2009) *Biochimie* **91**, 1218–1222.
- [105] Zhao, N, Gao, J, Enns, C. A, & Knutson, M. D. (2010) *Journal of Biological Chemistry* **285**, 32141–32150.
- [106] Jeong, J, Walker, J. M, Wang, F, Park, J. G, Palmer, A. E, Giunta, C, Rohrbach, M, Steinmann, B, & Eide, D. J. (2012) *Proc Natl Acad Sci USA* **109**, E3530–8.
- [107] Montell, C. (2011) *Pflugers Arch.* **461**, 499–506.
- [108] Georgiev, P, Okkenhaug, H, Drews, A, Wright, D, Lambert, S, Flick, M, Carta, V, Martel, C, Oberwinkler, J, & Raghu, P. (2010) *Cell Metabolism* **12**, 386–397.
- [109] Fleig, A & Penner, R. (2004) *Trends Pharmacol Sci* **25**, 633–639.
- [110] Wagner, T. F. J, Drews, A, Loch, S, Mohr, F, Philipp, S. E, Lambert, S, & Oberwinkler, J. (2010) *Pflugers Arch.* **460**, 755–765.
- [111] Colsoul, B, Vennekens, R, & Nilius, B. (2011) *Rev. Physiol. Biochem. Pharmacol.* **161**, 87–110.
- [112] Bouron, A & Oberwinkler, J. (2013) *Pflugers Arch.*
- [113] Gyulkhandanyan, A. V, Lee, S. C, Bikopoulos, G, Dai, F, & Wheeler, M. B. (2006) *J Biol Chem* **281**, 9361–9372.
- [114] Priel, T & Hershfinkel, M. (2006) *Biochem Biophys Res Commun* **346**, 205–212.
- [115] Sheline, C. T, Ying, H. S, Ling, C. S, Canzoniero, L. M. T, & Choi, D. W. (2002) *Neurobiology of Disease* **10**, 41–53.
- [116] Sensi, S. L, Canzoniero, L. M, Yu, S. P, Ying, H. S, Koh, J.-Y, Kerchner, G. A, & Choi, D. W. (1997) *J Neurosci* **17**, 9554–9564.
- [117] Sensi, S. L, Ton-That, D, Sullivan, P. G, Jonas, E. A, Gee, K. R, Kaczmarek, L. K, & Weiss, J. H. (2003) *Proc Natl Acad Sci USA* **100**, 6157–6162.
- [118] Jiang, D, Sullivan, P. G, Sensi, S. L, Steward, O, & Weiss, J. H. (2001) *J Biol Chem* **276**, 47524–47529.
- [119] Apostolova, M. D, Ivanova, I. A, & Cherian, M. G. (1999) *Toxicol. Appl. Pharmacol.* **159**, 175–184.

- [120] Günther, V, Lindert, U, & Schaffner, W. (2012) *Biochim Biophys Acta* **1823**, 1416–1425.
- [121] Guerrero, A. L & Berg, J. M. (2004) *Biochemistry* **43**, 5437–5444.
- [122] Murphy, B. J, Kimura, T, Sato, B. G, Shi, Y, & Andrews, G. K. (2008) *Mol. Cancer Res.* **6**, 483–490.
- [123] Maret, W. (2008) *Exp Gerontol* **43**, 363–369.
- [124] Bossy-Wetzell, E, Talantova, M. V, Lee, W. D, Schölzke, M. N, Harrop, A, Mathews, E, Götz, T, Han, J, Ellisman, M. H, Perkins, G. A, & Lipton, S. A. (2004) *Neuron* **41**, 351–365.
- [125] Cortese-Krott, M. M, Suschek, C. V, Wetzell, W, Kröncke, K.-D, & Kolb-Bachofen, V. (2009) *Am J Physiol, Cell Physiol* **296**, C811–20.
- [126] Carter, K. P, Young, A. M, & Palmer, A. E. (2014) *Chem Rev.*
- [127] Dean, K. M, Qin, Y, & Palmer, A. E. (2012) *Biochim Biophys Acta* **1823**, 1406–1415.
- [128] Que, E. L, Domaille, D. W, & Chang, C. J. (2008) *Chem Rev* **108**, 1517–1549.
- [129] Thompson, R. B. (2005) *Current Opinion in Chemical Biology* **9**, 526–532.
- [130] McCormick, N, Velasquez, V, Finney, L, Vogt, S, & Kelleher, S. L. (2010) *PLoS ONE* **5**, e11078.
- [131] Walkup, G. K, Burdette, S. C, Lippard, S. J, & Tsien, R. Y. (2000) *J Am Chem Soc* **122**, 5644–5645.
- [132] Spiering, D & Hodgson, L. (2012) *Methods Mol. Biol.* **827**, 215–234.
- [133] Hodgson, L, Shen, F, & Hahn, K. (2010) *Current protocols in cell biology* pp. 14.11. 1–14.11. 26.
- [134] Lakowicz, J. R. (2007) *Principles of Fluorescence Spectroscopy*. (Springer).
- [135] Zhang, J, Campbell, R. E, Ting, A. Y, & Tsien, R. Y. (2002) *Nat Rev Mol Cell Biol* **3**, 906–918.
- [136] Dittmer, P. J, Miranda, J. G, Gorski, J. A, & Palmer, A. E. (2009) *J Biol Chem* **284**, 16289–16297.
- [137] Palmer, A. E, Giacomello, M, Kortemme, T, Hires, S. A, Lev-Ram, V, Baker, D, & Tsien, R. Y. (2006) *Chem Biol* **13**, 521–530.
- [138] Horikawa, K, Yamada, Y, Matsuda, T, Kobayashi, K, Hashimoto, M, Matsu-Ura, T, Miyawaki, A, Michikawa, T, Mikoshiba, K, & Nagai, T. (2010) *Nat Meth* **7**, 729–732.
- [139] Tian, L, Hires, S. A, Mao, T, Huber, D, Chiappe, M. E, Chalasani, S. H, Petreanu, L, Akerboom, J, McKinney, S. A, Schreiter, E. R, Bargmann, C. I, Jayaraman, V, Svoboda, K, & Looger, L. L. (2009) *Nat Meth* **6**, 875–881.
- [140] Yamada, Y, Michikawa, T, Hashimoto, M, Horikawa, K, Nagai, T, Miyawaki, A, Häusser, M, & Mikoshiba, K. (2011) *Front. Cell. Neurosci.* **5**, 18.

- [141] Newman, R. H, Fosbrink, M. D, & Zhang, J. (2011) *Chem Rev* **111**, 3614–3666.
- [142] Davidson, M. W & Campbell, R. E. (2009) *Nat Meth* **6**, 713–717.
- [143] Nagai, T, Yamada, S, Tominaga, T, Ichikawa, M, & Miyawaki, A. (2004) *Proc Natl Acad Sci USA* **101**, 10554–10559.
- [144] Palmer, A. E, Jin, C, Reed, J. C, & Tsien, R. Y. (2004) *Proc Natl Acad Sci USA* **101**, 17404–17409.
- [145] Miranda, J. G, Weaver, A. L, Qin, Y, Park, J. G, Stoddard, C. I, Lin, M. Z, & Palmer, A. E. (2012) *PLoS ONE* **7**, e49371.
- [146] Lindenburg, L. H, Hessels, A. M, Ebberink, E. H. T. M, Arts, R, & Merkx, M. (2013) *ACS Chem Biol* **8**, 2133–2139.
- [147] Mank, M, Santos, A. F, Dierenberger, S, Mrcic-Flogel, T. D, Hofer, S. B, Stein, V, Hendel, T, Reiff, D. F, Levelt, C, Borst, A, Bonhoeffer, T, Hübener, M, & Griesbeck, O. (2008) *Nat Meth* **5**, 805–811.
- [148] Tian, L, Hires, S. A, & Looger, L. L. (2012) *Cold Spring Harbor Protocols* **2012**.
- [149] Palmer, A. E & Tsien, R. Y. (2006) *Nature Protocols* **1**, 1057–1065.
- [150] Evers, T. H, Appelhof, M. A. M, de Graaf-Heuvelmans, P. T. H. M, Meijer, E. W, & Merkx, M. (2007) *J Mol Biol* **374**, 411–425.
- [151] Emmanouilidou, E, Teschemacher, A. G, Pouli, A. E, Nicholls, L. I, Seward, E. P, & Rutter, G. A. (1999) *Curr Biol* **9**, 915–918.
- [152] Nagai, T, Sawano, A, Park, E. S, & Miyawaki, A. (2001) *Proc Natl Acad Sci USA* **98**, 3197–3202.
- [153] Albeck, J. G, Burke, J. M, Aldridge, B. B, Zhang, M, Lauffenburger, D. A, & Sorger, P. K. (2008) *Mol Cell* **30**, 11–25.
- [154] Bravo-Cordero, J. J, Oser, M, Chen, X, Eddy, R, Hodgson, L, & Condeelis, J. (2011) *Curr Biol* **21**, 635–644.
- [155] Machacek, M, Hodgson, L, Welch, C, Elliott, H, Pertz, O, Nalbant, P, Abell, A, Johnson, G. L, Hahn, K. M, & Danuser, G. (2009) *Nature* **461**, 99–103.
- [156] Vilela, M, Halidi, N, Besson, S, Elliott, H, Hahn, K, Tytell, J, & Danuser, G. (2013) *Meth Enzymol* **519**, 253–276.
- [157] Harvey, C. D, Ehrhardt, A. G, Cellurale, C, Zhong, H, Yasuda, R, Davis, R. J, & Svoboda, K. (2008) *Proc Natl Acad Sci USA* **105**, 19264–19269.
- [158] Berg, J, Hung, Y. P, & Yellen, G. (2009) *Nat Meth* **6**, 161–166.
- [159] Morris, M. C. (2010) *Cell Biochem Biophys* **56**, 19–37.
- [160] Spiering, D, Bravo-Cordero, J. J, Moshfegh, Y, Miskolci, V, & Hodgson, L. (2013) *Methods in Cell Biology* **114**, 593–609.

- [161] Stein, F, Kress, M, Reither, S, Piljić, A, & Schultz, C. (2013) *ACS Chem Biol* **8**, 1862–1868.
- [162] Hodgson, L, Nalbant, P, Shen, F, & Hahn, K. (2006) *Meth Enzymol* **406**, 140–156.
- [163] Demaurex, N. (2005) *Cell Calcium* **38**, 213–222.
- [164] Perocchi, F, Gohil, V. M, Girgis, H. S, Bao, X. R, McCombs, J. E, Palmer, A. E, & Mootha, V. K. (2010) *Nature* pp. 1–7.
- [165] Baker, B. J, Mutoh, H, Dimitrov, D, Akemann, W, Perron, A, Iwamoto, Y, Jin, L, Cohen, L. B, Isacoff, E. Y, Pieribone, V. A, Hughes, T, & Knöpfel, T. (2008) *Brain Cell Biol* **36**, 53–67.
- [166] Kitano, M, Nakaya, M, Nakamura, T, Nagata, S, & Matsuda, M. (2008) *Nature* **453**, 241–245.
- [167] Lichtman, J. W & Conchello, J.-A. (2005) *Nat Meth* **2**, 910–919.
- [168] McCombs, J. E & Palmer, A. E. (2008) *Methods* **46**, 152–159.
- [169] Kao, J. P. Y, Li, G, & Auston, D. A. (2010) *Methods in Cell Biology* **99**, 113–152.
- [170] Gostimskaya, I. S, Grivennikova, V. G, Zharova, T. V, Bakeeva, L. E, & Vinogradov, A. D. (2003) *Anal Biochem* **313**, 46–52.
- [171] Gryniewicz, G, Poenie, M, & Tsien, R. Y. (1985) *J Biol Chem* **260**, 3440–3450.
- [172] Chen, I, Howarth, M, Lin, W, & Ting, A. Y. (2005) *Nat Meth* **2**, 99–104.
- [173] Miyawaki, A, Griesbeck, O, Heim, R, & Tsien, R. Y. (1999) *Proc Natl Acad Sci USA* **96**, 2135–2140.
- [174] Thomas, D, Tovey, S. C, Collins, T. J, Bootman, M. D, Berridge, M. J, & Lipp, P. (2000) *Cell Calcium* **28**, 213–223.
- [175] Filippin, L, Magalhães, P. J, Di Benedetto, G, Colella, M, & Pozzan, T. (2003) *J Biol Chem* **278**, 39224–39234.
- [176] Rudolf, R, Magalhães, P. J, & Pozzan, T. (2006) *J Cell Biol* **173**, 187–193.
- [177] Danuser, G. (2011) *Cell* **147**, 973–978.
- [178] Ljosa, V & Carpenter, A. E. (2009) *PLoS Comput Biol* **5**, e1000603.
- [179] Rittscher, J. (2010) *Annu Rev Biomed Eng* **12**, 315–344.
- [180] Eliceiri, K. W, Berthold, M. R, Goldberg, I. G, Ibáñez, L, Manjunath, B. S, Martone, M. E, Murphy, R. F, Peng, H, Plant, A. L, Roysam, B, Stuurman, N, Stuurmann, N, Swedlow, J. R, Tomancak, P, & Carpenter, A. E. (2012) *Nat Meth* **9**, 697–710.
- [181] Peng, H. (2008) *Bioinformatics* **24**, 1827–1836.
- [182] Schneider, C. A, Rasband, W. S, & Eliceiri, K. W. (2012) *Nat Meth* **9**, 671–675.

- [183] de Chaumont, F, Dallongeville, S, Chenouard, N, Hervé, N, Pop, S, Provoost, T, Meas-Yedid, V, Pankajakshan, P, Lecomte, T, Le Montagner, Y, Lagache, T, Dufour, A, & Olivo-Marin, J.-C. (2012) *Nat Meth* **9**, 690–696.
- [184] Perkel, J. M. (2011) *Nature Publishing Group* **8**, 541–543.
- [185] Schindelin, J, Arganda-Carreras, I, Frise, E, Kaynig, V, Longair, M, Pietzsch, T, Preibisch, S, Rueden, C, Saalfeld, S, Schmid, B, Tinevez, J.-Y, White, D. J, Hartenstein, V, Eliceiri, K, Tomancak, P, & Cardona, A. (2012) *Nat Meth* **9**, 676–682.
- [186] Carpenter, A. E, Jones, T. R, Lamprecht, M. R, Clarke, C, Kang, I. H, Friman, O, Guertin, D. A, Chang, J. H, Lindquist, R. A, Moffat, J, Golland, P, & Sabatini, D. M. (2006) *Genome Biol* **7**, R100.
- [187] Carpenter, A. E, Kamentsky, L, & Eliceiri, K. W. (2012) *Nat Meth* **9**, 666–670.
- [188] Lamprecht, M, Sabatini, D, & Carpenter, A. (2007) *Biotech.* **42**, 71–75.
- [189] Cardona, A & Tomancak, P. (2012) *Nat Meth* **9**, 661–665.
- [190] Shariff, A, Kangas, J, Coelho, L. P, Quinn, S, & Murphy, R. F. (2010) *Journal of Biomolecular Screening* **15**, 726–734.
- [191] Linkert, M, Rueden, C. T, Allan, C, Burel, J.-M, Moore, W, Patterson, A, Loranger, B, Moore, J, Neves, C, Macdonald, D, Tarkowska, A, Sticco, C, Hill, E, Rossner, M, Eliceiri, K. W, & Swedlow, J. R. (2010) *J Cell Biol* **189**, 777–782.
- [192] Swedlow, J. R, Goldberg, I. G, & Eliceiri, K. W. (2009) *Annu. Rev. Biophys.* **38**, 327–346.
- [193] Tian, Q & Huhns, M. N. (1986) *Computer Vision, Graphics, and Image Processing* **35**, 220–233.
- [194] Tzimiropoulos, G, Argyriou, V, & Stathaki, T. (2011) *IEEE Trans. on Image Process.* **20**, 1761–1767.
- [195] Hill, D. L, Batchelor, P. G, Holden, M, & Hawkes, D. J. (2001) *Phys Med Biol* **46**, R1–45.
- [196] Gonzalez, R. C & Woods, R. E. (2002) *Digital Image Processing*. (Prentice Hall, Upper Saddle River, NJ), 2 edition.
- [197] Uchida, S. (2013) *Dev. Growth Differ.* **55**, 523–549.
- [198] Acton, S. T & Ray, N. (2009) *Synthesis lectures on image, video, and multimedia processing* **9**, 1–116.
- [199] Otsu, N. (1979) *IEEE Transactions on systems, man and cybernetics* **smc-9**, 1–5.
- [200] Peng, J.-Y, Lin, C.-C, Chen, Y.-J, Kao, L.-S, Liu, Y.-C, Chou, C.-C, Huang, Y.-H, Chang, F.-R, Wu, Y.-C, Tsai, Y.-S, & Hsu, C.-N. (2011) *PLoS Comput Biol* **7**, e1002212.
- [201] Aizenman, E, Stout, A. K, Hartnett, K. A, Dineley, K. E, McLaughlin, B, & Reynolds, I. J. (2000) *Journal of Neurochemistry* **75**, 1878–1888.

- [202] Dineley, K. E, Votyakova, T. V, & Reynolds, I. J. (2003) *Journal of Neurochemistry* **85**, 563–570.
- [203] Dineley, K. E, Richards, L. L, Votyakova, T. V, & Reynolds, I. J. (2005) *Mitochondrion* **5**, 55–65.
- [204] Malaiyandi, L. M, Honick, A. S, Rintoul, G. L, Wang, Q. J, & Reynolds, I. J. (2005) *J Neurosci* **25**, 9507–9514.
- [205] Medvedeva, Y. V, Lin, B, Shuttleworth, C. W, & Weiss, J. H. (2009) *Journal of Neuroscience* **29**, 1105–1114.
- [206] Chang, D. T. W, Honick, A. S, & Reynolds, I. J. (2006) *J Neurosci* **26**, 7035–7045.
- [207] Caporale, T, Ciavardelli, D, Ilio, C. D, Lanuti, P, Drago, D, & Sensi, S. L. (2009) *Experimental Neurology* **218**, 228–234.
- [208] Malaiyandi, L. M, Vergun, O, Dineley, K. E, & Reynolds, I. J. (2005) *Journal of Neurochemistry* **93**, 1242–1250.
- [209] Masanta, G, Lim, C. S, Kim, H. J, Han, J. H, Kim, H. M, & Cho, B. R. (2011) *J Am Chem Soc* **133**, 5698–5700.
- [210] Tomat, E, Nolan, E. M, Jaworski, J, & Lippard, S. J. (2008) *J Am Chem Soc* **130**, 15776–15777.
- [211] Piljić, A, de Diego, I, Wilmanns, M, & Schultz, C. (2011) *ACS Chem Biol* **6**, 685–691.
- [212] Tantama, M, Hung, Y. P, & Yellen, G. (2011) *J Am Chem Soc* **133**, 10034–10037.
- [213] Meyer, A. J. (2008) *J Plant Physiol* **165**, 1390–1403.
- [214] Bolte, S & Cordelières, F. P. (2006) *J Microsc* **224**, 213–232.
- [215] Myers, S. A, Nield, A, & Myers, M. (2012) *J Nutr Metab* **2012**, 173712.
- [216] Thul, R, Bellamy, T. C, Roderick, H. L, Bootman, M. D, & Coombes, S. (2008) *Adv Exp Med Biol* **641**, 1–27.
- [217] Brini, M & Carafoli, E. (2000) *Cell. Mol. Life Sci.* **57**, 354–370.
- [218] Uhlén, P & Fritz, N. (2010) *Biochem Biophys Res Commun* **396**, 28–32.
- [219] Hu, H, Bandell, M, Petrus, M. J, Zhu, M. X, & Patapoutian, A. (2009) *Nat Chem Biol* **5**, 183–190.
- [220] Alvarez-Collazo, J, Díaz-García, C. M, López-Medina, A. I, Vassort, G, & Alvarez, J. L. (2012) *Pflugers Arch.* **464**, 459–470.
- [221] Dineley, K. E, Devinney, M. J, Zeak, J. A, Rintoul, G. L, & Reynolds, I. J. (2008) *Journal of Neurochemistry* **106**, 2184–2193.
- [222] Bozym, R, Hurst, T. K, Westerberg, N, Stoddard, A, Fierke, C. A, Frederickson, C. J, & Thompson, R. B. (2008) *Meth Enzymol* **450**, 287–309.

- [223] Nunemaker, C. S, Bertram, R, Sherman, A, Tsaneva-Atanasova, K, Daniel, C. R, & Satin, L. S. (2006) *Biophys J* **91**, 2082–2096.
- [224] Ashcroft, F. M & Rorsman, P. (2012) *Cell* **148**, 1160–1171.
- [225] Findlay, I, Ashcroft, F. M, Kelly, R. P, Rorsman, P, Petersen, O. H, & Trube, G. (1989) *Ann. N. Y. Acad. Sci.* **560**, 403–409.
- [226] Malaisse, W. J, Herchuelz, A, Devis, G, Somers, G, Boschero, A. C, Hutton, J. C, Kawazu, S, Sener, A, Atwater, I. J, Duncan, G, Ribalet, B, & Rojas, E. (1978) *Ann. N. Y. Acad. Sci.* **307**, 562–582.
- [227] Tengholm, A & Gylfe, E. (2009) *Mol Cell Endocrinol* **297**, 58–72.
- [228] Ramadan, J. W, Steiner, S. R, O’Neill, C. M, & Nunemaker, C. S. (2011) *Cell Calcium* **50**, 481–490.
- [229] Tamarina, N. A, Kuznetsov, A, Rhodes, C. J, Bindokas, V. P, & Philipson, L. H. (2005) *Diabetes* **54**, 3073–3081.
- [230] Idevall-Hagren, O, Barg, S, Gylfe, E, & Tengholm, A. (2010) *J Biol Chem* **285**, 23007–23018.
- [231] Wenzlau, J. M, Moua, O, Liu, Y, Eisenbarth, G. S, Hutton, J. C, & Davidson, H. W. (2008) *Ann. N. Y. Acad. Sci.* **1150**, 252–255.
- [232] Tamaki, M, Fujitani, Y, Hara, A, Uchida, T, Tamura, Y, Takeno, K, Kawaguchi, M, Watanabe, T, Ogihara, T, & Fukunaka, A. (2013) *J Clin Invest* **123**, 4513.
- [233] Li, D, Chen, S, Bellomo, E. A, Tarasov, A. I, Kaut, C, Rutter, G. A, & Li, W.-h. (2011) *Proc Natl Acad Sci USA* **108**, 21063–21068.
- [234] Lefebvre, B, Vandewalle, B, Balavoine, A.-S, Queniat, G, Moerman, E, Vantyghem, M.-C, Le Bacquer, O, Gmyr, V, Pawlowski, V, Kerr-Conte, J, & Pattou, F. (2012) *Journal of Endocrinology* **214**, 225–232.
- [235] Hardy, A. B, Wijesekara, N, Genkin, I, Prentice, K. J, Bhattacharjee, A, Kong, D, Chimienti, F, & Wheeler, M. B. (2012) *Am J Physiol Endocrinol Metab* **302**, E1084–96.
- [236] Petersen, A. B, Smidt, K, Magnusson, N. E, Moore, F, Egefjord, L, & Rungby, J. (2011) *APMIS* **119**, 93–102.
- [237] Bellomo, E. A, Meur, G, & Rutter, G. A. (2011) *Journal of Biological Chemistry* **286**, 25778–25789.
- [238] Fridlyand, L. E, Tamarina, N, & Philipson, L. H. (2010) *Am J Physiol Endocrinol Metab* **299**, E517–32.
- [239] Gwiazda, K. S, Yang, T.-L. B, Lin, Y, & Johnson, J. D. (2009) *Am J Physiol Endocrinol Metab* **296**, E690–701.
- [240] Zhang, M, Fendler, B, Percy, B, Goel, P, Bertram, R, Sherman, A, & Satin, L. (2008) *Biophys J* **95**, 4676–4688.

- [241] Hajnóczky, G, Robb-Gaspers, L. D, Seitz, M. B, & Thomas, A. P. (1995) *Cell* **82**, 415–424.
- [242] Pan, E, Zhang, X.-a, Huang, Z, Krezel, A, Zhao, M, Tinberg, C. E, Lippard, S. J, & McNamara, J. O. (2011) *Neuron* **71**, 1116–1126.
- [243] Li, X, Burnight, E. R, Cooney, A. L, Malani, N, Brady, T, Sander, J. D, Staber, J, Wheelan, S. J, Joung, J. K, & McCray, P. B. (2013) *Proc Natl Acad Sci USA* **110**, E2279–E2287.
- [244] Maret, W. (2013) *Adv Nutr* **4**, 82–91.
- [245] Brunelle, J. K, Bell, E. L, Quesada, N. M, Vercauteren, K, Tiranti, V, Zeviani, M, Scarpulla, R. C, & Chandel, N. S. (2005) *Cell Metabolism* **1**, 409–414.
- [246] Guzy, R. D, Hoyos, B, Robin, E, Chen, H, Liu, L, Mansfield, K. D, Simon, M. C, Hammerling, U, & Schumacker, P. T. (2005) *Cell Metabolism* **1**, 401–408.
- [247] Morgan, B, Ang, S. K, Yan, G, & Lu, H. (2009) *J Biol Chem* **284**, 6818–6825.
- [248] Powell, S. R. (2000) *J Nutr* **130**, 1447S–54S.
- [249] Eide, D. J. (2011) *Metallomics* **3**, 1124–1129.
- [250] Chiaverini, N & De Ley, M. (2010) *Free Radic. Res.* **44**, 605–613.
- [251] Tormos, K. V, Anso, E, Hamanaka, R. B, Eisenbart, J, Joseph, J, Kalyanaraman, B, & Chandel, N. S. (2011) *Cell Metabolism* **14**, 537–544.
- [252] Cairns, R. A, Harris, I. S, & Mak, T. W. (2011) *Nat Rev Cancer* **11**, 85–95.
- [253] Zhao, Y, Araki, S, Wu, J, Teramoto, T, Chang, Y.-F, Nakano, M, Abdelfattah, A. S, Fujiwara, M, Ishihara, T, Nagai, T, & Campbell, R. E. (2011) *Science* **333**, 1888–1891.
- [254] Adamo, A. M, Zago, M. P, Mackenzie, G. G, Aimo, L, Keen, C. L, Keenan, A, & Oteiza, P. I. (2010) *Neurotox Res* **17**, 1–14.
- [255] Franklin, R. B & Costello, L. C. (2009) *J. Cell. Biochem.* **106**, 750–757.
- [256] Yamashita, S, Miyagi, C, Fukada, T, Kagara, N, Che, Y.-S, & Hirano, T. (2004) *Nature* **429**, 298–302.
- [257] Atkinson, A, Khalimonchuk, O, Smith, P, Sabic, H, Eide, D, & Winge, D. R. (2010) *Journal of Biological Chemistry* **285**, 19450–19459.
- [258] Marvin, R. G, Wolford, J. L, Kidd, M. J, Murphy, S, Ward, J, Que, E. L, Mayer, M. L, Penner-Hahn, J. E, Haldar, K, & O’Halloran, T. V. (2012) *Chem Biol* **19**, 731–741.
- [259] Kim, J.-H, Jeon, J, Shin, M, Won, Y, Lee, M, Kwak, J.-S, Lee, G, Rhee, J, Ryu, J.-H, Chun, C.-H, & Chun, J.-S. (2014) *Cell* **156**, 730–743.
- [260] Evers, T. H, Appelhof, M. A. M, Meijer, E. W, & Merkx, M. (2008) *Protein Eng. Des. Sel.* **21**, 529–536.
- [261] Schmidt, A. M, Müller, H. N, & Skerra, A. (1996) *Chem Biol* **3**, 645–653.

- [262] Outten, C. E, Tobin, D. A, Penner-Hahn, J. E, & O'Halloran, T. V. (2001) *Biochemistry* **40**, 10417–10423.
- [263] Getz, E. B, Xiao, M, Chakrabarty, T, Cooke, R, & Selvin, P. R. (1999) *Anal Biochem* **273**, 73–80.
- [264] Krezel, A, Lesniak, W, Jezowska-Bojczuk, M, Mlynarz, P, Brasuñ, J, Kozlowski, H, & Bal, W. (2001) *Journal of Inorganic Biochemistry* **84**, 77–88.
- [265] McGuigan, J. A. S, Kay, J. W, & Elder, H. Y. (2006) *Progress in Biophysics and Molecular Biology* **92**, 333–370.
- [266] Bers, D. M, Patton, C. W, & Nuccitelli, R. (2010) *Methods in Cell Biology* **99**, 1–26.
- [267] Tsien, R & Pozzan, T. (1989) *Meth Enzymol* **172**, 230–262.
- [268] Martell, A. E & Smith, R. M. (2014) *Critical stability constants*. (New York, Plenum Press, New York).
- [269] Patton, C, Thompson, S, & Epel, D. (2004) *Cell Calcium* **35**, 427–431.
- [270] Moisescu, D. G & Pusch, H. (1975) *Pflugers Archiv* **355**, R122.
- [271] Cheng, K. L, Ueno, K, & Imamura, T. (1992) *CRC Handbook of Organic Analytical Reagents, Second Edition*. (CRC Press).

Appendix A

Purification of a Cytosolic Zinc Sensor Using an Intein Purification System

A.1 Introduction

Purified, active Zn^{2+} sensors must satisfy two conditions: the thiols in cysteine-containing Zn^{2+} finger binding domain(s) must be reduced, in order to coordinate Zn^{2+} , and hexahistidine affinity purification tags (His_6) must be absent. His_6 affinity purification tags can form dimers in the presence of nanomolar concentrations of free Zn^{2+} [260,261], and thus intermolecular FRET would interfere with binding assays designed to determine the affinity of the sensors binding domain for Zn^{2+} (intramolecular FRET). Although Zn^{2+} itself is not redox-active, oxidation of coordinating thiols from cysteine residues leads to the dissociation of Zn^{2+} under biological conditions. An oxidizing environment can inactivate sensors, and so Zn^{2+} -binding proteins are often purified and assayed in the presence of a reducing agent, such as dithiothreitol (DTT) or *tris*(2-carboxyethyl)phosphine (TCEP) [50, 66, 72, 136, 262]. In our laboratory, I have identified three main bottlenecks in the purification of Zn^{2+} sensor proteins: expression of soluble protein, proteolytic removal of His_6 tags, and reduction during and after purification to restore Zn^{2+} -binding.

Our established method has been bacterial expression of biosensors using a pBAD system (Life Technologies, Carlsbad, CA), modified to contain a Tobacco Etch Virus (TEV) protease cleavage site between the N-terminal His_6 tag and the biosensor. Bacterial lysate is loaded on to a Ni^{2+} -NTA column, washed, and eluted with imidazole. The eluted protein is buffer-exchanged into TEV protease buffer, and then it is incubated with TEV protease overnight (TEV protease cleavage appears to be particularly inefficient in our pBAD system). Then, the protein is loaded

on to another Ni^{2+} -NTA column and the flow through is collected and concentrated. Sometimes the protein is loaded on to a size-exclusion column and fractions containing full-length protein are pooled and concentrated. The concentrated protein is reduced with 300 mM DTT and buffer-exchanged to remove DTT, which creates a stable complex with Zn^{2+} [263,264].

In comparison, the IMPACT protein expression and purification system (New England Biolabs, Ipswich, MA) a chitin-binding domain is used instead of His_6 as an affinity tag, and a self-cleaving intein is used to remove the tag instead of TEV protease. This significantly simplifies the protein expression procedure. In addition, 50 mM DTT is used to induce intein self-cleavage, and so the purified protein is maintained in a reducing environment and does not need to be reduced in a separate step. Figure A.1 compares the two methods for purifying sensors. I purified NES-ZapCV2, a cytosolic Zn^{2+} sensor using the IMPACT system to test it as an alternative to our established method.

A.2 Cloning Strategy

The cytosolic Zn^{2+} sensor, NES-ZapCV2, is a modified version of the previously characterized ZapCY2 sensor [65,66]. NES-ZapCV2 has an N-terminal nuclear export signal (MLQLPPLERLTL) and contains Venus fluorescent protein (FP), circularly-permuted at amino acid 173, instead of citrine FP at its C-terminus Nagai:2004jr, Miranda:2012br. This sensor was assembled in the pcDNA3 plasmid vector backbone (Life Technologies, Carlsbad, CA).

I used the pTXB1 vector (New England Biolabs, Ipswich, MA) as a backbone for the NES-ZapCV2-intein bacterial expression plasmid. pTXB1 contains a multiple-cloning site between a T7 promoter and the sequence of a mini-intein from the *Mycobacterium xenopi GyrA* gene. The pTXB1-NES-ZapCV2 plasmid (shown in Figure A.2) was assembled in several steps. Briefly, NES-ZapCV2 was PCR-amplified with primers containing 5' *NheI* and 3' *SapI* restriction sites. The reverse primer contains a point mutation that changes the stop codon to one coding for leucine, and it also inserts phenylalanine N-terminal to the intein. The PCR product and pTXB1 were digested with *NheI* and *SapI* and ligated together.

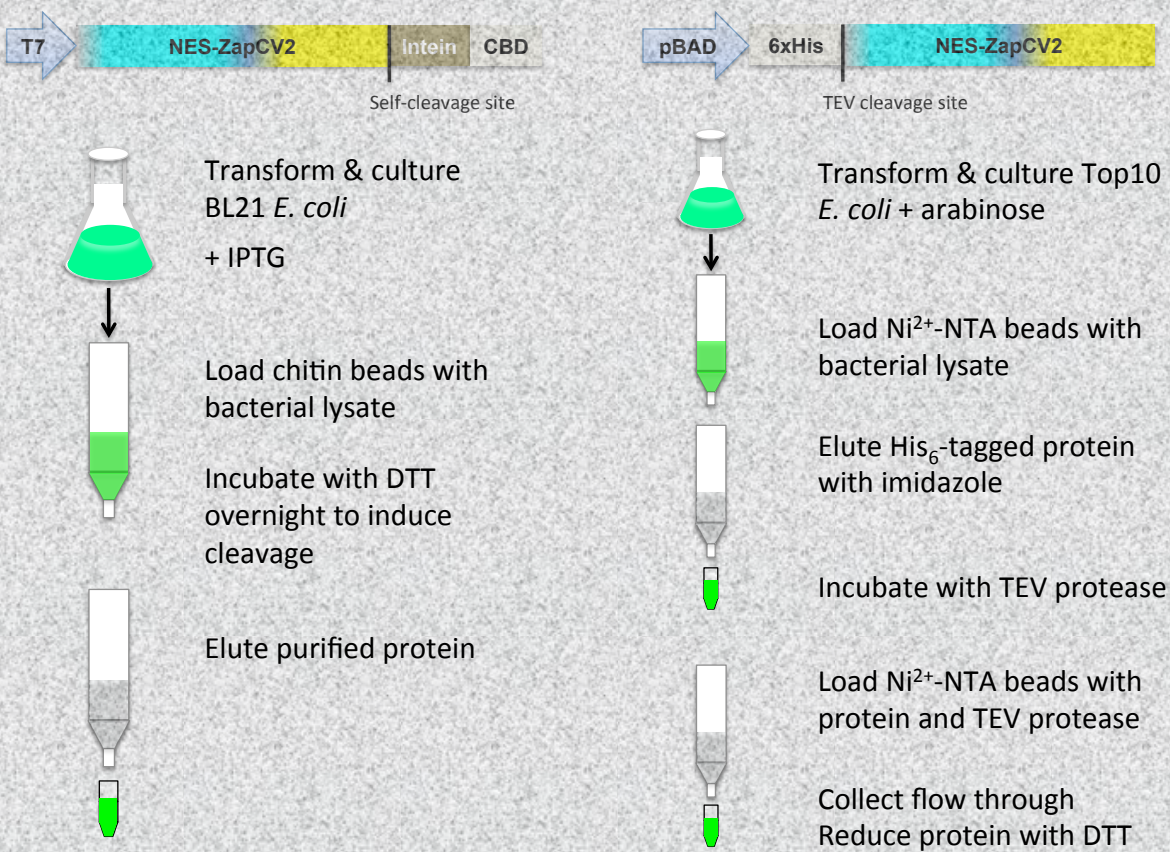


Figure A.1: Comparison of two strategies for purification of a Zn²⁺ sensor protein.

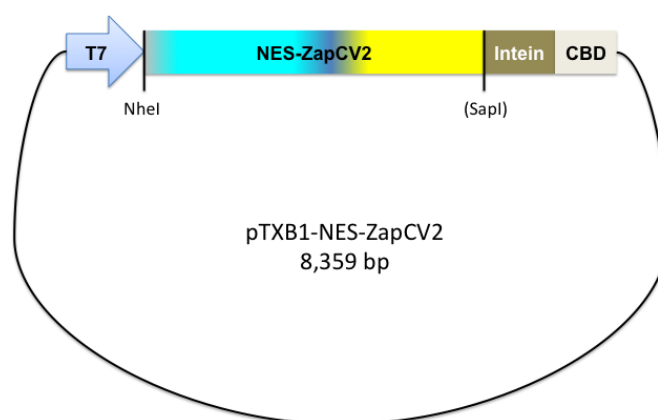


Figure A.2: Plasmid vector for bacterial expression of NES-ZapCV2 intein fusion protein. NES-ZapCV2 was PCR-amplified and ligated into the multiple-cloning site of pTXB1 (New England Biolabs, Ipswich, MA) using the *NheI* and *SapI* restriction sites. The *SapI* restriction site is lost after ligation. This plasmid also carries a lac operator downstream of the T7 promoter and ampicillin resistance (not shown in this figure).

A.3 Purification of NES-ZapCV2

A.3.1 Overview of *in vitro* Titrations

pTXB1-NES-ZapCV2 was transformed into chemically competent BL21 *E. coli* and plated on LB Amp (100 $\mu\text{g}/\text{mL}$). Single colonies were inoculated in 1 mL LB Amp, and these 1 mL cultures were used to inoculate 500 mL LB. These cultures were grown at 37 °C for 4 hours, induced with 250 μM IPTG and shaken at room temperature for 7.5 hours. The cultures were then harvested by spinning down 40 mL at a time in 50 mL conical tubes for 6 min at 5000 rpm at 4 °C.

Each pellet (500 mL culture) was resuspended in 10 mL lysis buffer using a 5 mL pipet. The resuspended pellet was gently shaken at room temperature for 45 min. Then, the lysate was centrifuged for 40 min at 11000 rpm (about 15000 x g) at 4 °C.

For each 500 mL culture, 2 mL chitin beads were loaded onto a column. Beads were washed with 10 volumes column buffer (20 mL total). Clarified lysate was loaded onto the column and washed with 40 mL column buffer followed by 20 mL cleavage buffer, without DTT. The beads were incubated overnight at room temperature in 2 mL cleavage buffer containing 50 mM DTT. After incubation, the flow through was collected and buffer-exchanged into titration buffer.

Beer's law can be used to calculate the concentration of fluorescent protein from an absorbance spectrum of the purified protein. An example is shown in Figure A.3.

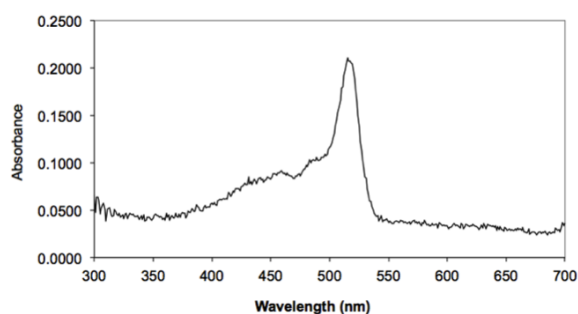


Figure A.3: Absorbance of purified NES-ZapCV2. The absorbance was measured using a Safire II microplate reader (Tecan). The eCFP absorbance peak is at 435 nm and the Citrine/YFP absorbance peak is at 515 nm.

A.4 Titration of NES-ZapCV2 *in vitro*

Genetically-encoded sensors of ions are almost always purified and characterized *in vitro* before being validated in cells [137, 138, 143, 253]. *In vitro* characterization has many advantages: the investigator can control the environment (pH, temperature, salt concentration, etc.), compare a variety of sensor designs, or evaluate specificity. Our *in vitro* assays are performed using a 96-well microplate reader, and so they can be performed quickly and precisely. The sensors may have different binding properties intracellularly, so new sensors are always characterized *in situ* in parallel (see Section 2.4).

In order to get an adequate signal in our microplate reader based assay for titrating FRET sensors, I require the purified sensor to be at a concentration of about a 1 μM . However, the K_D 's of these sensors are usually in the pM to μM range. Most binding assays use a concentration of protein (in this case, sensor) that is much less than its K_D ' so that $[\text{ion}]_{\text{free}} \approx [\text{ion}]_{\text{total}}$. I cannot make that assumption here. For this reason, I use metal-chelate buffer solutions to maintain specific $[\text{ion}]_{\text{free}}$ in our binding assay. I measure the fraction of sensor bound to the ion using the FRET ratio. Assuming the maximum FRET ratio is that of the bound sensor and the minimum FRET ratio is that of the unbound sensor, I calculate $\Delta R = R_{\text{max}} - R_{\text{min}}$ and the fraction of sensor bound (Equation A.1).

$$\text{Fractional Saturation} = \frac{R - R_{\text{min}}}{R_{\text{max}} - R_{\text{min}}} \quad (\text{A.1})$$

Then, I plot ΔR or the fraction bound against $[\text{ion}]_{\text{free}}$ to obtain our binding isotherm. Figure A.4 compares the binding curves when $[\text{ion}]_{\text{free}}$ is used (correct) and when $[\text{ion}]_{\text{total}}$ is used (incorrect).

Our laboratory's method of choice is to use metal-chelate buffer solutions to set sub- μM free ion concentrations, incubate purified sensor with these solutions, and measure emission spectra using a microplate reader. These data are used to calculate the fraction bound at each free ion concentration and determine the apparent dissociation constant, K_D' , and the empirical Hill co-

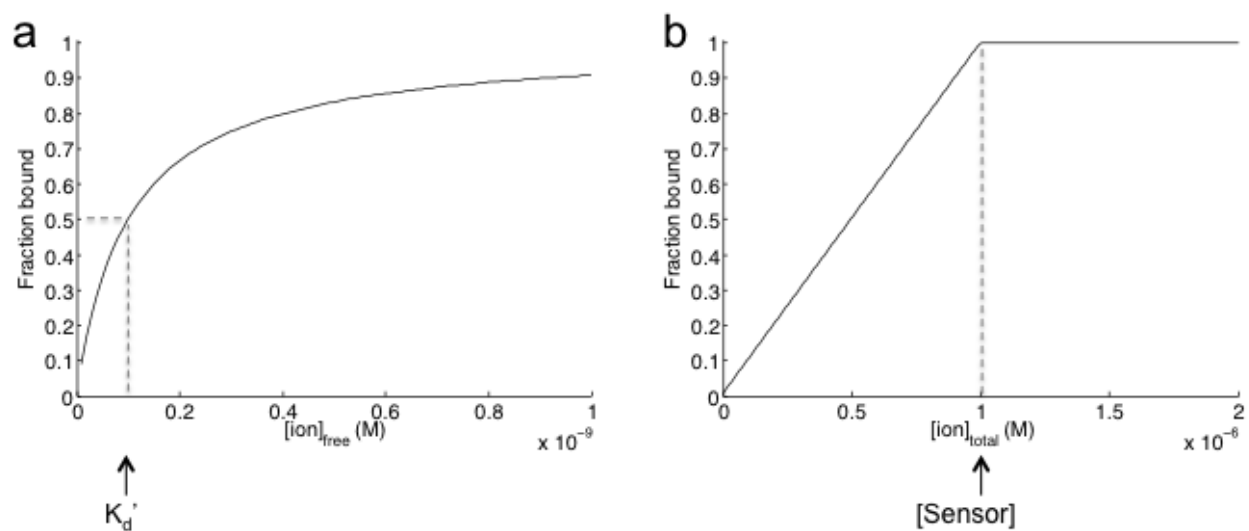


Figure A.4: Comparison of binding curves when fraction bound is plotted against $[\text{ion}]_{\text{free}}$ or $[\text{ion}]_{\text{total}}$ when the $[\text{sensor}]$ is in excess of the K_D' . In this example, $[\text{sensor}]$ is 1 μM and much greater than the K_D' (100 pM). In (a), where fraction bound is plotted against $[\text{ion}]_{\text{free}}$, the K_D' is the $[\text{ion}]_{\text{free}}$ when the half the sensor is bound. (b) shows a plot of fraction bound plotted against $[\text{ion}]_{\text{total}}$. The fraction bound increases linearly with $[\text{ion}]_{\text{total}}$ until it reaches $[\text{sensor}]$, which is 1 μM .

efficient, n . This section begins with a detailed explanation of how to make metal-chelate buffer solutions. Then, the results of an *in vitro* titration of NES-ZapCV2 are presented.

A.4.1 Preparation of Metal-Chelate Buffered Solutions

Metal-chelate buffers consist of a chelator (*e.g.* EDTA), the ion to be buffered, and sometimes a competing ion (*e.g.* Mg^{2+} or Sr^{2+}). The addition of a competing ion effectively increases the concentration of $[\text{ion}]_{\text{free}}$ that it can buffer. For this reason, all other divalent metals can affect $[\text{ion}]_{\text{free}}$ and must be eliminated from the metal-chelate buffers that are described in this protocol. The final concentration of the chelator must be much greater than the desired $[\text{ion}]_{\text{free}}$, just as in a pH buffer, where the concentration of the weak acid/conjugate base is much greater than the H_3O^+ concentration. In addition, the *total* $[\text{ion}]$ is orders of magnitude greater than the *free* $[\text{ion}]$.

Buffered Mg^{2+} and Ca^{2+} solutions have been used for a long time to perfuse cells during patch clamp and whole-cell voltage clamp experiments. Several methods of making these buffers have been published [137, 265–267] and can be used to make Zn^{2+} buffers [25, 32, 50, 66, 68, 72, 136].

The first step is to calculate the K_D' of the metal-chelator complex, and this value depends on the pH, temperature, and ionic strength of the solution. These values can be calculated from the stability constants in [268] or by using software such as MaxChelator [266, 269]. Some K_D' s for Ca^{2+} buffers can also be found in [265, 267]. The temperature and pH dependence of Ca^{2+} and Zn^{2+} buffers is shown in Tables A.1 and A.2.

Our laboratory uses the pH jump method [267, 270] of making metal-chelate buffers with chelators that are polyprotic acids, such as EDTA, EGTA, and HEDTA. This method only requires a pH meter.

Select the appropriate metal-chelate buffer(s) for the desired free Ca^{2+} or Zn^{2+} concentration ($[\text{Ca}^{2+}]_{\text{free}}$ or $[\text{Zn}^{2+}]_{\text{free}}$). For a sensor titration, at least 10 evenly-spaced concentrations should be chosen within the range of ~ 10 -fold above and below the expected K_D' . Some examples of Ca^{2+} and Zn^{2+} buffers are listed in Table A.3.

Prepare two 100X stock solutions for each buffer. For Ca^{2+} buffers, make 1 M stock solutions,

Table A.1: $[\text{Ca}^{2+}]_{free}$ buffering ranges of some metal chelate buffer systems at 20 °C and 25 °C and 0.1 M ionic strength. Each metal chelate buffer system can buffer $[\text{Ca}^{2+}]_{free}$ 10-fold above and below the K_D' . EDTA = ethylenedinitrilotetraacetic acid; EGTA = ethylene glycol-bis(2-aminoethylether)- N,N,N',N' -tetraacetic acid; HEDTA = N -(2-Hydroxyethyl)ethylenediamine- N,N',N' -triacetic acid.

Chelator	$K_d'(\text{Ca}^{2+})$ at pH 7.2 and 20°C	$K_d'(\text{Ca}^{2+})$ at pH 7.4 and 20°C	$K_d'(\text{Ca}^{2+})$ at pH 7.2 and 25°C	$K_d'(\text{Ca}^{2+})$ at pH 7.4 and 25°C
EDTA	32.2 nM	19.6 nM	32.6 nM	19.9 nM
EGTA	151 nM	60.5 nM	141 nM	56.7 nM
HEDTA	3.23 μM	2.03 μM	3.38 μM	2.12 μM

Table A.2: $[\text{Zn}^{2+}]_{free}$ buffering ranges of some metal chelate buffer systems at 20 °C and 25 °C and 0.1 M ionic strength. Each metal chelate buffer system can buffer $[\text{Zn}^{2+}]_{free}$ 10-fold above and below the K_D' . EDTA = ethylenedinitrilotetraacetic acid; EGTA = ethylene glycol-bis(2-aminoethylether)- N,N,N',N' -tetraacetic acid; HEDTA = N -(2-Hydroxyethyl)ethylenediamine- N,N',N' -triacetic acid.

Chelator	$K_d'(\text{Zn}^{2+})$ at pH 7.2 and 20°C (M)	$K_d'(\text{Zn}^{2+})$ at pH 7.4 and 20°C (M)	$K_d'(\text{Zn}^{2+})$ at pH 7.2 and 25°C (M)	$K_d'(\text{Zn}^{2+})$ at pH 7.4 and 25°C (M)
EDTA	4.99×10^{-14}	3.03×10^{-14}	4.83×10^{-14}	2.94×10^{-14}
EGTA	2.80×10^{-9}	1.13×10^{-9}	2.56×10^{-9}	1.03×10^{-9}
HEDTA	1.29×10^{-12}	8.07×10^{-13}	1.34×10^{-12}	8.44×10^{-13}

Table A.3: Metal-chelate buffers for sub- μM Ca^{2+} and Zn^{2+} solutions. The free Ca^{2+} and Zn^{2+} concentrations are accurate at 25 °C and 0.1 M ionic strength. Note the competing metal should have a weaker affinity for the chelator than the metal to be buffered. [267, 268, 271] are helpful references and resources.

Chelator	Ca^{2+} buffering range at pH 7.4	Zn^{2+} buffering range at pH 7.4	Zn^{2+} buffering range at pH 7.4 with competing metal
EDTA	0.002 to 0.18 mM	0.003 to 0.3 μM	
EGTA	0.006 to 0.5 mM	0.15 to 15 nM	9.7 to 1340 nM (with 2 mM Sr^{2+}) 2 to 134 μM (with 2 mM Ca^{2+})
HEDTA	0.3 to 25 mM	0.15 to 15 μM	0.05 to 7.5 nM (with 2 mM Ca^{2+})
NTA	20 to 1670 mM		

and for Zn^{2+} buffers, make 100 mM stock solutions. Stock solution 1 should have equimolar amounts of chelator and Ca^{2+} or Zn^{2+} , and stock solution 2 should contain chelator only. These two solutions are mixed in different proportions to make buffers for free ion concentrations from 10-fold below to 10-fold above its K_D' with the chelator. This is sometimes referred to as the "ratio method" for creating metal-chelate buffers [265].

The "pH jump method" should be used to prepare stock solution 1. This method can be used to make solutions of polyprotic acid chelators (EDTA, EGTA, HEEDTA) and metal ions, so that the concentrations of each are within 0.5% of each other. For example, when Ca^{2+} binds EGTA, two protons are released, causing a drop in the pH of the solution. Therefore, the change in pH upon Ca^{2+} addition ($\Delta\text{pH}/\Delta\text{Ca}^{2+}$) decreases when there are equal concentrations of Ca^{2+} and EGTA. First, weigh out the amount of chelator needed for the stock solution, and weigh out 95% of the amount of metal needed for the stock solution. Adjust the pH of the solution to the right range for that chelator (pH 5.0 for EDTA, pH 7.0–8.5 for EGTA). Prepare two solutions: 1.0 M KOH and 0.5 or 1.0 M of the divalent metal (e.g. 1.0 M CaCl_2 in water). Record the pH of the solution to the thousandths place. Add a specific amount of metal to the solution (e.g. 20 μl of 0.5 M ZnCl_2 , which is 0.010 mmole Zn^{2+}) and record the drop in pH. Adjust the pH to the appropriate range using the KOH solution. When the ratio of the change in pH to the change in metal decreases by 50%, the concentrations of metal and chelator are within 0.5% of each other.

Mix the two stock solutions in appropriate proportions (from 1:9 to 9:1) to buffer at specific $[\text{ion}]_{\text{free}}$.

A.4.2 Titration of NES-ZapCV2 Using a Microplate Reader

A fresh 100 mM TCEP solution was prepared for the titration. Purified NES-ZapCV2 was buffer-exchanged into column buffer (20 mM HEPES, 250 mM NaCl, pH 8.0) with 0.5 mM TCEP (75 l 100 mM TCEP into 15 mL column buffer) using an Ultracel YM-30 (MWCO 30,000) 0.5 mL concentrator. The protein was washed with 0.5 mL column buffer containing 0.5 mM TCEP 5 times by spinning at room temperature in a microcentrifuge (14,000 rcf x 8 min). 5 l of the

concentrated protein was diluted with 395 μl of titration buffer (50 mM HEPES, 100 mM NaCl, 10% glycerol, pH 7.4). A microplate reader (Safire II, Tecan) was used to measure the absorbance of the diluted protein to estimate protein concentration. The protein was diluted to 2.5 μM with titration buffer and 100 μl was aliquoted into each well of a 96 well plate.

Zn^{2+} buffer solutions were diluted to 2X (2 mM) with titration buffer containing 0.5 mM TCEP. The buffer solutions used in this titration are shown in Table A.4. Each measurement was performed in triplicate. A microplate reader was used to measure the emission spectrum upon excitation at 420 nm.

For each well, the FRET ratio was calculated by taking the ratio of the blank-subtracted YFP emission peak intensity (528 nm) by that of CFP (484 nm). The FRET ratios (or fraction bound calculated from maximum and minimum ratios) were plotted against $[\text{Zn}^{2+}]_{free}$. The data are fit with a single-site (Equation A.2) or two-site binding model (Equation A.3), where n is the empirical Hill coefficient.

$$\text{Fraction Bound} = \frac{[ion]^n}{(K_D')^n + [ion]^n} \quad (\text{A.2})$$

$$\text{Fraction Bound} = F_1 \frac{[ion]^{n_1}}{(K_D'1)^{n_1} + [ion]^{n_1}} + F_2 \frac{[ion]^{n_2}}{(K_D'2)^{n_2} + [ion]^{n_2}} \quad (\text{A.3})$$

This method was used to determine the K_D' of NES-ZapCV2 of 36 pM and n of 0.67 at 25 $^{\circ}\text{C}$ and pH 7.4. The fitted data are shown in Figure A.5.

The FRET ratios reported by ion sensors can be converted to $[ion]_{free}$ using K_D' and n values derived from *in vitro* sensor titrations, but at a different temperature, pH, or salt concentration, these values could differ significantly from the published values. Section 2.4 describes methods that can be used to determine a sensors K_D' *in situ* when the accuracy of free ion concentration estimation is critical. While there are many examples of no difference in the *in situ* and *in vitro* binding parameters, there are also well-documented examples of significant differences that substantially influence conversion to $[\text{Ca}^{2+}]$ [174–176].

Table A.4: $[\text{Zn}^{2+}]_{\text{free}}$ of Zn^{2+} buffered solutions used in the titration of NES-ZapCV2. Solution 1 contains equimolar amounts of Zn^{2+} and chelator. Solution 2 contains chelator only. Free Zn^{2+} concentrations are calculated at pH 7.4 and 25 °C.

Solution 1: Solution 2	Zn^{2+} -EGTA $[\text{Zn}^{2+}]_{\text{free}}$ (nM)	Zn^{2+} -HEEDTA $[\text{Zn}^{2+}]_{\text{free}}$ (nM)	Zn^{2+} -EDTA + 2 mM MgCl_2 $[\text{Zn}^{2+}]_{\text{free}}$ (nM)
1:9	1.00E-01	8.75E-05	3.00E-03
2:8	2.25E-01	1.97E-04	7.36E-03
3:7	3.86E-01	3.37E-04	1.37E-02
4:6	6.01E-01	5.25E-04	2.29E-02
5:5	9.01E-01	7.87E-04	3.68E-02
6:4	1.35E+00	1.18E-03	5.89E-02
7:3	2.10E+00	1.84E-03	9.74E-02
8:2	3.61E+00	3.15E-03	1.77E-01
9:1	8.11E+00	7.09E-03	4.20E-01

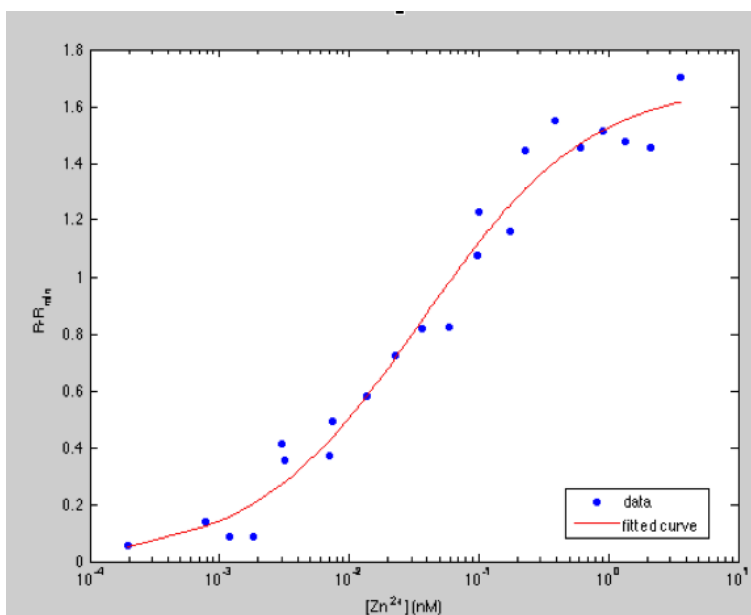


Figure A.5: Titration of NES-ZapCV2 *in vitro*. The titration data are fit with a single-site binding model with a K_D' of 36 pM and n of 0.67.

This protocol also describes how to make and use metal-chelate buffer solutions to set $[\text{ion}]_{free}$ to specific, sub-micromolar concentrations (Section A.4.1). These metal-chelate buffer solutions can also be used to control extracellular or intracellular ion concentrations for other applications (for example, to assess which $[\text{Ca}^{2+}]_{free}$ can trigger downstream cellular signaling).

Appendix B

Image Analysis Protocols

The protocols in this Appendix make use of the following software.

ImageJ

This protocol uses FIJI, which is a distribution of ImageJ [182,185].

GNU General Public License v2. Released 2011. Version 1.48r.

MATLAB

The protocols also require the Image Processing Toolbox.

The MathWorks, Inc. Released 2013. Version R2013b.

NIS-Elements Viewer

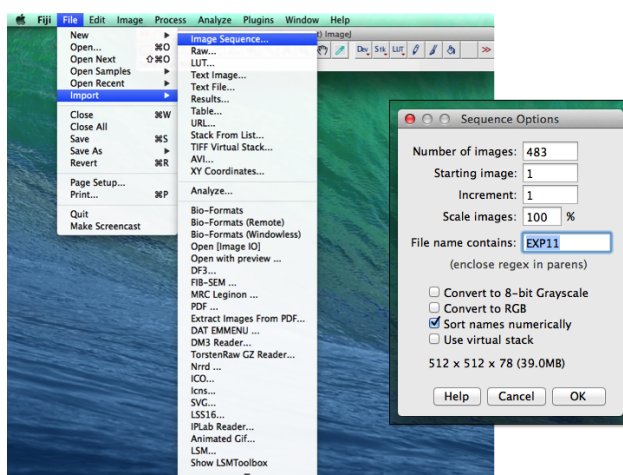
This software is a free program with limited capabilities, and it can open .nd2 files.

Nikon Instruments, Inc. Released 2013. Version 4.11.00.

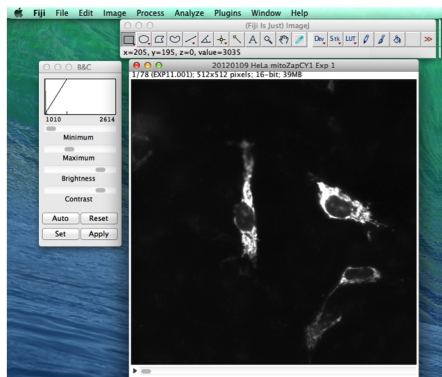
B.1 Selection of Regions of Interest with FIJI

This protocol describes one way to import images into FIJI, draw ROIs, and export measurements for each ROI.

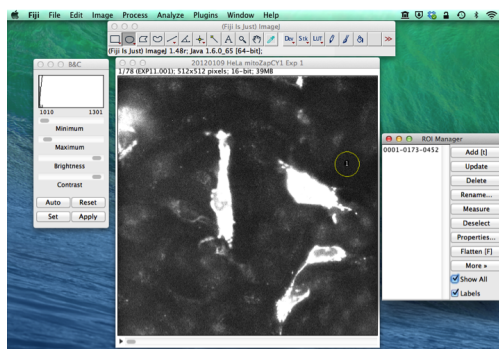
In this example, I'm importing 2 stacks of images collected on a widefield microscope using MetaFluor software (Molecular Devices). One stack contains all of the FRET images, and the other contains all the CFP images. All my FRET image filenames begin with EXP11. followed by a number that corresponds to the timepoint. ImageJ will create a stack that puts the images in numerical order.



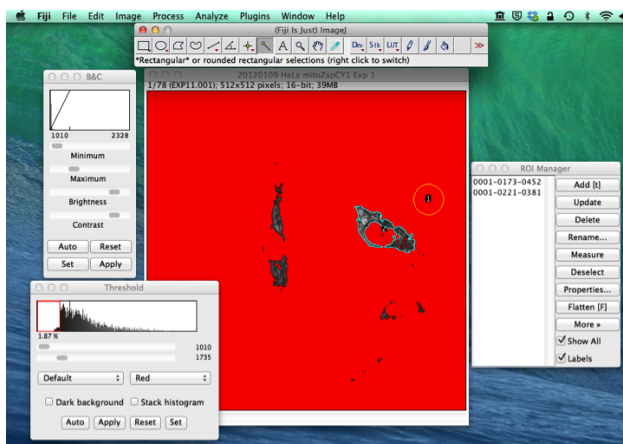
Adjusting the Brightness and Contrast does not change the pixel values in the image. The x-, y-, and z-positions and the pixel value at the cursor are shown in the bottom part of the toolbar. Image information is shown above the image in the image stack. There is a slider bar at the bottom of the stack that can be used to scroll through images.



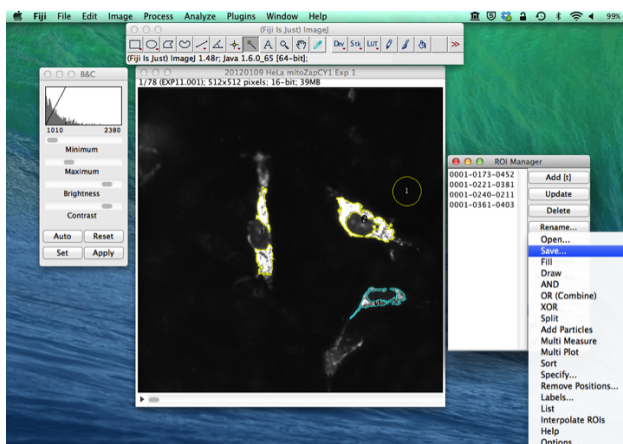
Next, select a background ROI. I change the contrast to make sure there aren't any dim cells in the background ROI. Scroll through the images to make sure nothing floats through the ROI. Typing "t" will automatically add an ROI to a list in the ROI manager.



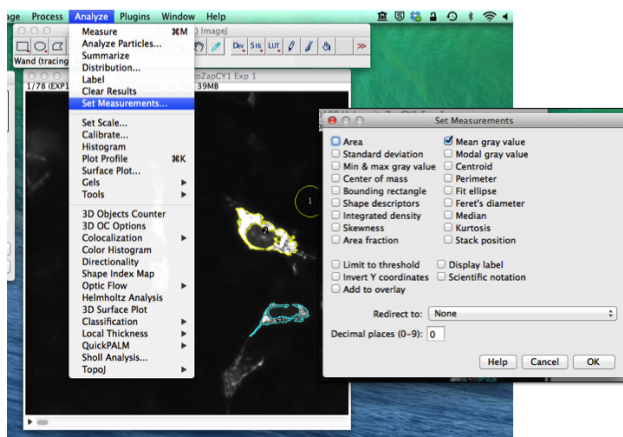
Continue using the drawing tools to select more ROIs. Sometimes I use the Threshold window and the magic wand tool to select ROIs (below). Scroll through the stack to make sure the ROIs stay within the boundary of the cell throughout the experiment.



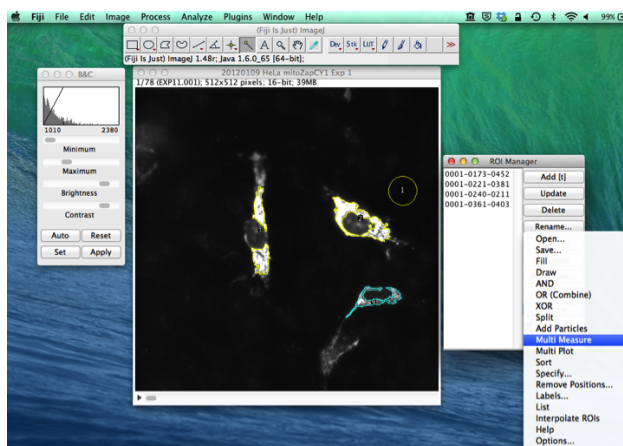
Save the ROIs. The menu shown in the figure below opens up after clicking the More>> button.



Next, select the measurements that ImageJ will make for each ROI.



Click on a stack of images, then click on the ROI manager. Click on Multi Measure under the More>> button. Save the results. The same ROIs can be selected in another stack just by clicking on the other stack. Multi Measure will make the ROI measurements on the last stack you've clicked on.



B.2 Automated Analysis of Manually-Selected ROIs in MATLAB

```

%% Stabilize images and select regions in ImageJ
%Use MultiMeasure to get average values of each region. Output is
%Image#,BGregion average intensity, Region1 average intensity, etc. First
%third of images are YFP FRET, second third are CFP, third third are YFP
%Use log file to get time of each image
%Output is: errorbar figure of mean FRET ratios, errorbar figure of mean
%YFP, xy of all FRET ratios, xy of all YFP

%load time and data files

%% separate data by channel, get rid of frame numbers from ImageJ
[images,x]=size(data);
FRET=data(1:images/3,2:x);
CFP=data(images/3+1:images*2/3,2:x);
YFP=data(images*2/3+1:images,2:x);
Regions=x-2;

%% Make background array
BG=[FRET(:,1) CFP(:,1) YFP(:,1)];

%% Make region arrays
for i=1:Regions;
    Region.(sprintf('Region%d',i))=[FRET(:,i+1) CFP(:,i+1) YFP(:,i+1)]-BG;
end

%% Calculate ratios and make YFP and CFP arrays
for i=1:Regions;
    Ratio(:,i)=Region.(sprintf('Region%d',i))(:,1)./Region.(sprintf('Region%d',i))(:,2);
    YFPm(:,i)=Region.(sprintf('Region%d',i))(:,3);
    CFPm(:,i)=Region.(sprintf('Region%d',i))(:,2);
end

%% Calculate fractional saturation
Ratio_min=min(Ratio);
Ratio_max=max(Ratio);
Diff=Ratio_max-Ratio_min;
for i=1:length(time);
    Frac(i,:)=(Ratio(i,:)-Ratio_min)./Diff;
end

%% Calculate means
Ratio_mean=mean(Ratio,2);
YFP_mean=mean(YFPm,2);
CFP_mean=mean(CFPm,2);
Ratio_err=std(Ratio,0,2)/sqrt(Regions);
YFP_err=std(YFPm,0,2)/sqrt(Regions);
CFP_err=std(CFPm,0,2)/sqrt(Regions);
Frac_mean=mean(Frac,2);
Frac_err=std(Frac,0,2)/sqrt(Regions);

%% Calculate Dynamic Range
DR = Ratio_max./Ratio_min;

%% Calculate Resting FRET Ratio
Resting = input('When did you add TPEN (in seconds)?');
LastResting=find(time<Resting,1,'last');
Resting_mean=mean(Ratio(1:LastResting,:),1);

```

```

%% Calculate Fractional Saturation at Resting
Resting_Frac = mean(Frac(1:LastResting,:),1);
disp(sprintf('Dynamic Range = %6.2f + %6.2f\nMean Frac = %6.2f + %6.2f\nMean min = %6.2f + %6.2f\nMean max = %6.2f + %6.2f\n',...
    mean(DR), std(DR), mean(Resting_Frac),std(Resting_Frac), mean(Ratio_min),std(Ratio_min),mean(Ratio_max),std(Ratio_max)))

%% New figure
figure
ax(1)=subplot(2,2,1);
    plot(ax(1),time,Ratio);
    title('FRET Ratio vs. time');...
ax(2)=subplot(2,2,2);
    plot(ax(2),time,Frac);
    title('Fractional Saturation vs. time');
ax(3)=subplot(2,2,3);
    errorbar(ax(3),time,Ratio_mean,Ratio_err);
    title('Mean FRET ratio vs. time');...
ax(4)=subplot(2,2,4);
    errorbar(ax(4),time,Frac_mean,Frac_err);
%     text(Resting,0.4,' \downarrow TPEN','FontSize',12);
    title('Mean Fractional Saturation vs. time');
    ylim([-0.5 1.1]);
    text(0,-.28,...
        [sprintf('Dynamic Range = %6.2f + %6.2f\nMean Frac = %6.2f + %6.2f\nMean min = %6.2f + %6.2f\nMean max = %6.2f + %6.2f',...
            mean(DR), std(DR), mean(Resting_Frac),std(Resting_Frac), mean(Ratio_min),std(Ratio_min),mean(Ratio_max),std(Ratio_max))],...
        'HorizontalAlignment','left',...
        'BackgroundColor',[.78 .89 .97],...
        'FontSize',8);
linkaxes(ax,'x')
xlim([-15 time(end)+15])
%save figure
print -dpdf AllPlots

```

B.3 Standardized Ratio vs. Time Plots

Contents

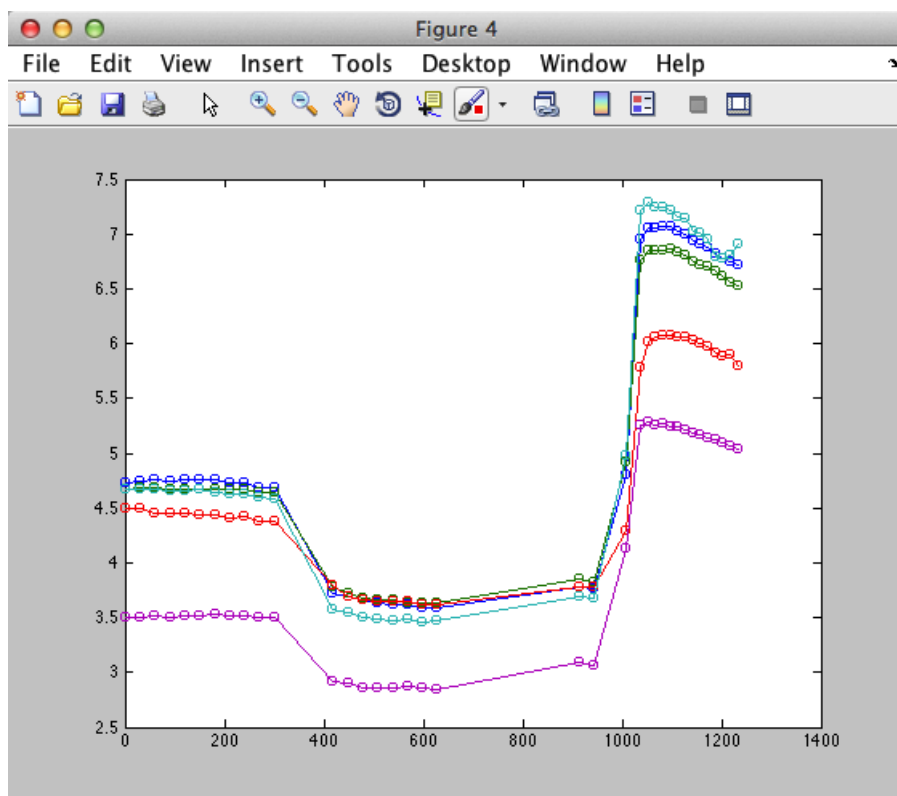
- [Create a labeled Ratio vs. Time plot.](#)
- [Enter Title](#)
- [Enter Labels](#)
- [Add Labels to Plot](#)
- [Save Figure](#)

Create a labeled Ratio vs. Time plot.

Make sure the variables "time" and "Ratio" are in the workspace. This script also puts the mean and standard deviation of the dynamic range, Rmin, and Rmax into the plot. The arrays DR, Ratio_min, and Ratio_max should contain an entry for each ROI plotted.

```
% Create a new figure
figure

% Plot Ratio vs. time with dots connected by a line.
plot(time,Ratio,'o-')
```



Enter Title

At the prompt, between single apostrophes, type in the title for the figure. For example: 'HeLa cells with ZapCV2'

```
ExperimentTitle=input('Title?')

title(ExperimentTitle)
ylabel('FRET ratio')
xlabel('Time (sec)')
```

```
Title?'ZapCV2 Calibration'
```

```
ExperimentTitle =
```

```
ZapCV2 Calibration
```

Enter Labels

Type the number of events and the text label for each event (also between single apostrophes). You can make superscript text like this: '100 μM Zn²⁺' and subscript text like this: 'ZnCl₂'

```
Events=input('How many events?')

for i = 1:Events
    Labels(i)={input('Event?')};
end
% Make sure your labels are correct:
Labels
```

```
How many events?3
```

```
Events =
```

```
3
```

```
Event?'TPEN'
```

```
Event?'Washout'
```

```
Event?'ZnCl2'
```

```
Labels =
```

```
'TPEN' 'Washout' 'ZnCl2'
```

Add Labels to Plot

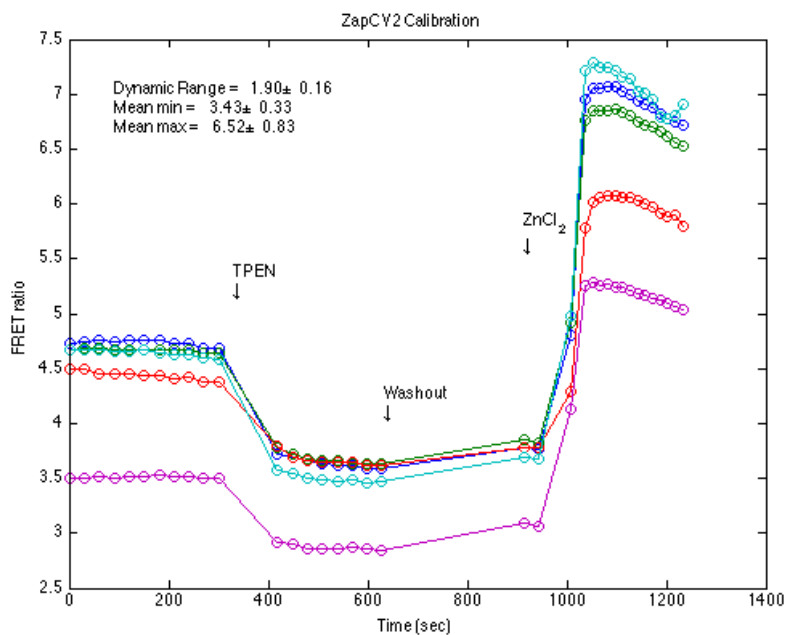
Click where you want the text using the crosshairs. Each click inserts a label in the same order of input. Each label will have a down arrow below the line of text, on the left side. You can change the text later by using plottools.

```

for i=1:Events
    gtext([Labels(i),'\downarrow'])
end

% This will create a box with mean and standard deviation of the dynamic
% range, Rmin, and Rmax. The crosshairs correspond to the top left corner
% of the text box.
gtext([sprintf('Dynamic Range = %6.2f%c%6.2f\nMean min = %6.2f%c%6.2f\nMean max = %6.2f%c%6.
2f',...
mean(DR), char(177),std(DR), mean(Ratio_min),char(177),std(Ratio_min),mean(Ratio_max),char(177
),std(Ratio_max))]

```



Save Figure

```
saveas(gcf,'LabeledRatioPlot','fig')
```

B.4 Automated Registration of YFP FRET and CFP images

Image registration

Load images to be aligned. In this example, we are using an image from the DV2 dual emission system. The upper image is the YFP FRET image and the lower image is the CFP image.

```
I=imread('Glucose0428T001C1.tif');
FRET=I(1:253,:);
CFP=I(254:506,:);
```

Calculate Geometric Transformation

```
[optimizer, metric] = imregconfig('multimodal');
optimizer.MaximumIterations=10000;

tform = imregtform(CFP,FRET,'affine',optimizer,metric)
CFP_reg = imwarp(CFP,tform,'OutputView',imref2d(size(FRET)));

tform.T

corr2(FRET,CFP)
corr2(FRET,CFP_reg)
```

```
tform =
```

```
affine2d with properties:
```

```
          T: [3x3 double]
Dimensionality: 2
```

```
ans =
```

```
    1.0031   -0.0022         0
    0.0010    1.0051         0
   -0.0420    4.3547    1.0000
```

```
ans =
```

```
    0.7203
```

```
ans =
```

```
    0.9740
```

B.5 Optimization of Image Segmentation

Optimization of image segmentation

Segmentation of an image for automatic ROI selection or making a mask can be computationally intensive (i.e. take a lot of time to run) or just not that good. I find that top-hat filtering is relatively fast and effective to process images before setting a threshold to make a binary image. A simple script can help determine which settings will work the best for your image.

Contents

- [Load an image](#)
- [Structuring element parameters](#)
- [See how changing the shape and size affect the mask](#)

Load an image

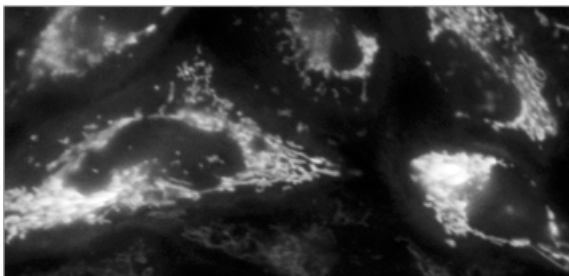
In this example, I am loading an image of mitochondria saved as originalFret.tif

```
% Load image into workspace
I=imread('originalFret.tif');
whos I

% Show image in a new figure
figure, imshow(I,[])

% Create a new image with better contrast
I2=imadjust(I);
```

Name	Size	Bytes	Class	Attributes
I	246x511	251412	uint16	



Structuring element parameters

Decide which size and shape of a structuring element you want to perform the morphological opening. A smaller size will bring out smaller features (like mitochondria); the structuring element size should be close to the diameter of the feature in pixels. I usually stick with the diamond or disk shape, but many different ones are available (look up strel in the MATLAB help).

```
size = input('What range of pixels?');
```

```
shape=input('What shape?');
```

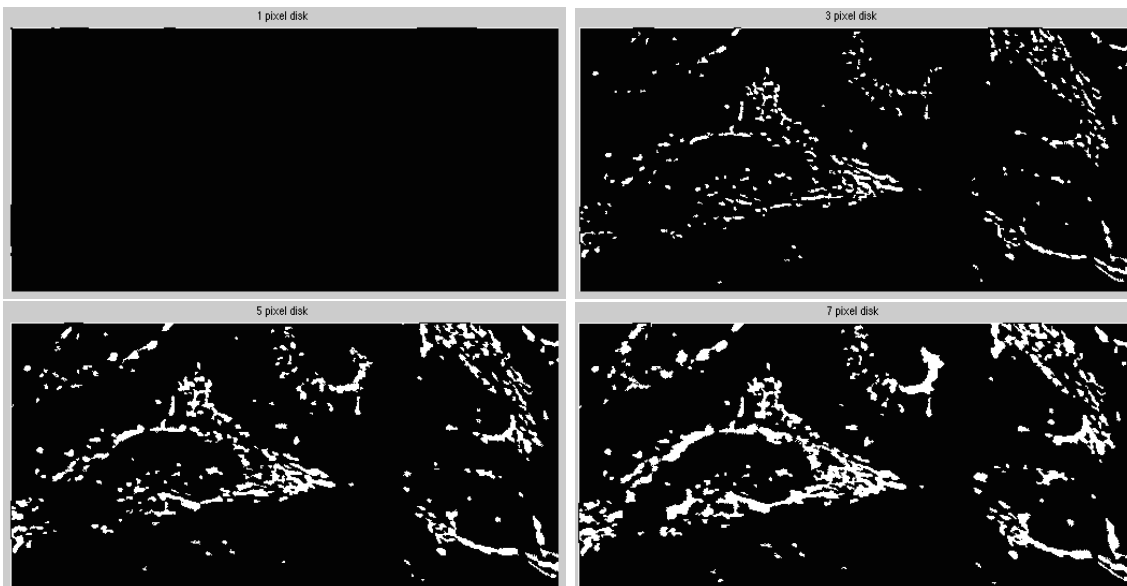
```
What range of pixels?1:2:20
What shape?'disk'
```

See how changing the shape and size affect the mask

```
figure

for i=size
    SE = strel(shape,i);
    I3=imtophat(I2,SE);
    pix2=nonzeros(I3);
    thresh=graythresh(pix2);
    bw=im2bw(I3,thresh);
    bw=bwareaopen(bw,4);
    disp(i)
    imshow(bw)
    title(sprintf('%d pixel %s',i,shape))
    pause
    %imwrite(FRET2,sprintf('FRET2_%03d.tiff',i))
    %imwrite(bw,sprintf('bw_%03d.png',i))
end

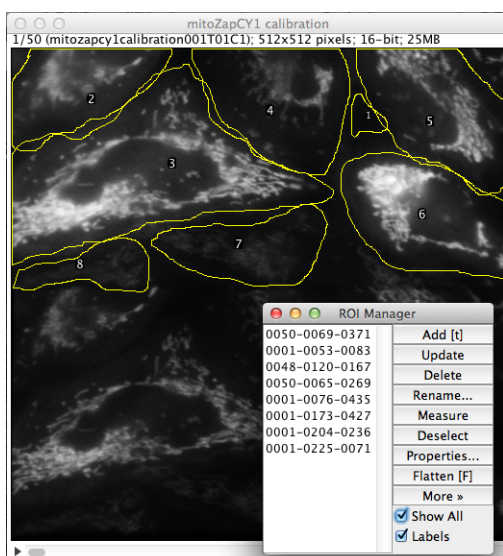
% Hit any key to move on to the next size. If you want to stop, press ctrl
% c
```



B.6 Automation of ROI Selection in an Image Where Cells are of Different Intensities

B.6.1 Select cells using ImageJ

Open the ROI Manager, under the Analyze drop-down menu and Tools. Select a background region with the freehand tool, and draw a boundary around each cell. Add each ROI to the ROI Manager. Save the regions by clicking on the More>> on the ROI Manager window.



B.6.2 Run MATLAB script

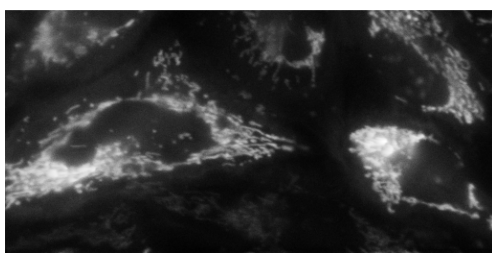
Contents

- [Creating a mask of an image with multiple cells of different intensities](#)
- [Load ROI information](#)
- [Process each ROI in the image](#)

Creating a mask of an image with multiple cells of different intensities

Only one image is processed in this example, but it can be incorporated into a loop to process all images.

```
figure
imshow(FRET, [])
```



Load ROI information

You will need the ReadImageJROI function, provided by Dylan Muir and available on MATLAB Central for free.

```
ROI_filename='RoiSetCells.zip'; %Case-sensitive
ROI=ReadImageJROI(ROI_filename);
StrelSize=5;
```

Process each ROI in the image

The first ROI is the background region, but you can skip this if you don't have a background region. Creation of a binary mask for a single cell is covered in another protocol in this section. This is just an iteration of that script for multiple cells.

```
for R=1:size(ROI,2); %Loop through all ROIs
    %Create new variables from the pixel coordinates of the ROI
    %boundaries
```

```

c=ROI{1,R}.mnCoordinates(:,1);
r=ROI{1,R}.mnCoordinates(:,2);
%Create a binary image using this ROI, setting all pixels outside
%the ROI to 0.
[J, BW]=roifill(FRET,c,r); %masked image

switch(R)

    % If there is no background region, skip this first section

    % From here
    case 1 % When R=1 (background region, do this)

        FRETm=immultiply(FRET,BW);

        % Save the mean background intensity in an array named bg
        bg(1)=mean2(nonzeros(FRETm));
    % To here

    case 2 % Replace with case 1 if there is no background region
        FRETm=immultiply(FRET,BW);
        pix=nonzeros(FRETm); % all pixel values in freehand ROI
        low=double(min(pix))/65536; % lowest intensity
        high=double(max(pix))/65536; % highest intensity
        FRETTr=imadjust(FRETm,[low high],[ ]);
        FRET2=imtophat(FRETTr,strel('disk',StrelSize));
        pix2=nonzeros(FRET2);
        thresh=graythresh(pix2);
        bwFRET=im2bw(FRET2,thresh);
        bw_all=bwareaopen(bwFRET,4);

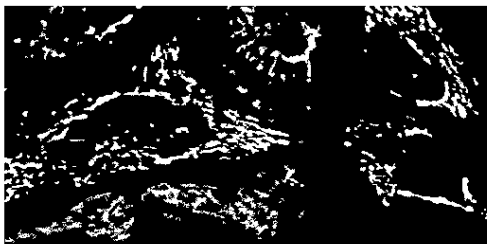
    otherwise
        FRETm=immultiply(FRET,BW);
        pix=nonzeros(FRETm); % all pixel values in freehand ROI
        low=double(min(pix))/65536; % lowest intensity
        high=double(max(pix))/65536; % highest intensity
        FRETTr=imadjust(FRETm,[low high],[ ]);
        FRET2=imtophat(FRETTr,strel('disk',StrelSize));
        pix2=nonzeros(FRET2);
        thresh=graythresh(pix2);
        bwFRET=im2bw(FRET2,thresh);
        bwFRET=bwareaopen(bwFRET,4);
        bw_all=or(bw_all,bwFRET);

end

end

figure,
imshow(bw_all)

```



B.7 Calculation of the Mean Intensity of an ROI Using a Binary Mask

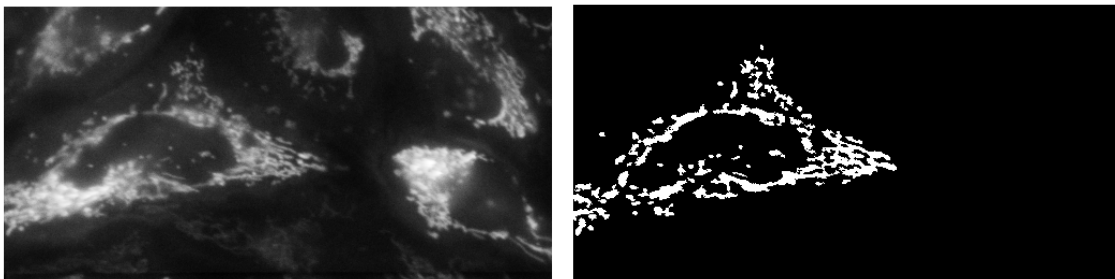
Contents

- [Calculation of the Mean Intensity of an ROI Using a Binary Mask](#)
- [Multiply the image and the binary mask to set all pixels outside the ROI to zero.](#)
- [Calculate the mean pixel value of all nonzero pixels](#)

Calculation of the Mean Intensity of an ROI Using a Binary Mask

First, load the image containing the ROI and the binary mask into the workspace using `imread`. Shown here is the FRET image from an experiment and a binary mask selecting the mitochondria of one cell.

```
figure, imshow(FRET,[])  
figure, imshow(bw)
```



Multiply the image and the binary mask to set all pixels outside the ROI to zero.

```
FRET_masked=immultiply(FRET,bw);  
figure, imshow(FRET_masked,[]);
```



Calculate the mean pixel value of all nonzero pixels

```
MeanFRET=mean(nonzeros(FRET_masked));
```

B.8 Creating Ratiometric Images for Movies

Contents

- [Creating Ratiometric Images in MATLAB](#)
- [Make background-subtracted ratiometric image](#)
- [Mask ratiometric image](#)

Creating Ratiometric Images in MATLAB

The FRET and CFP images used in this example were previously aligned using the protocol for image registration included in this Section. First, background-subtract the images.

```
disp(bg(1,:))

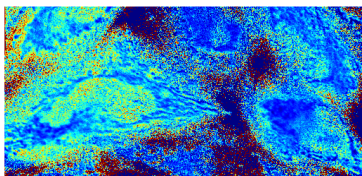
FRETS=FRET-bg(1,1);
CFPs=CFP_reg-bg(1,2);
```

```
1.0e+03 *
    5.3667    3.4887
```

Make background-subtracted ratiometric image

```
Ratio_s=uint16(double(FRETS)./double(CFPs)*1000);
% 1000 is the scaling factor: pixel values in the image correspond to
% 1000*FRET ratio

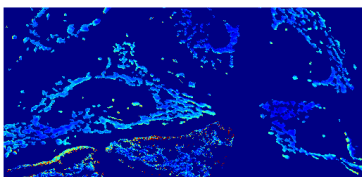
figure
imshow(Ratio_s,[1000 4000])
colormap 'jet'
```



Mask ratiometric image

bw_all is a previously created mask.

```
Ratio_sm_all=immultiply(Ratio_s,bw_all);
figure
imshow(Ratio_sm_all,[1000 4000])
colormap 'jet'
```



B.9 Example MATLAB Script for ROI Selection, FRET Ratio Calculation, and Ratiometric Image Creation

```

%% Analysis in FIJI
% .tiff images were exported using NIS Viewer, and then imported them into
% FIJI. There are two FOV in this experiment, one was supposed to be
% background, but the two FOV were acquired at slightly different times
% (and thus have different background intensities). Freehand ROIs were
% selected and saved. The boundaries of each image were estimated: FRET
% (1:253,:) and CFP (254:506,:)

%% Input information

length_time = input('How many timepoints?');
filename = input('What is the image sequence prefix?');
ROI_filename=input('What is the filename of the saved ImageJ ROIs?');
ROI=ReadImageJROI(ROI_filename);

%% Registration

% Align the FRET and CFP images using the first image of the sequence.

[optimizer, metric] = imregconfig('monomodal');
optimizer.MaximumIterations = 10000;
optimizer.MinimumStepLength = 5e-7;

% Load the first image
T=1;
switch(format)

    case 'DualView'
        I=imread(sprintf('%sT%03dC1.tif',filename,T));

        % Divide the image into FRET and CFP images
        FRET=I(1:256,:);
        CFP=I(257:end,:);

    case 'Sequential'
        FRET=imread(sprintf('%s1.%03d',filename,T));
        CFP=imread(sprintf('%s2.%03d',filename,T));

end

% Optimize the alignment and save "tform," which contains the information
% needed to translate the CFP image so that it aligns with the FRET image.
tform = imregtform(CFP,FRET,'rigid',optimizer,metric);

% Use imwarp to make a new image, "CFP_reg", that is aligned with the
% original FRET image.
CFP_reg = imwarp(CFP,tform,'OutputView',imref2d(size(FRET)));

% Display the overlay of the aligned images just to make sure it worked.
figure,imshowpair(imadjust(FRET), imadjust(CFP_reg),'Scaling','joint');
pause

% Press any key to continue.

%% Process all timepoints
% figure

```

```

for T=1:length_time;
    I=imread(sprintf('%sT%03dC1.tif',filename,T));
    FRET=I(1:253,:);
    CFP=I(254:506,:);
    CFP_reg = imwarp(CFP,tform,'OutputView',imref2d(size(FRET)));

    for R=1:size(ROI,2);

        c=ROI{1,R}.mnCoordinates(:,1);
        r=ROI{1,R}.mnCoordinates(:,2);
        [J, BW]=roifill(FRET,c,r); %masked image

        switch(R)

            case 1

                FRETm=immultiply(FRET,BW);
                CFPm=immultiply(CFP_reg,BW);

                bg(T,1)=mean2(nonzeros(FRETm));
                bg(T,2)=mean2(nonzeros(CFPm));

                FRETs=FRET-bg(T,1);
                CFPs=CFP_reg-bg(T,2);

                Ratio_s=uint16(double(FRETs)./double(CFPs)*1000);

            case 2

                FRETm=immultiply(FRET,BW);
                pix=nonzeros(FRETm); % all pixel values in freehand ROI
                low=double(min(pix))/65536; % lowest intensity
                high=double(max(pix))/65536; % highest intensity
                FRETm=imadjust(FRETm,[low high],[]);
                FRET2=imtophat(FRETm,strel('disk',StrelSize));
                pix2=nonzeros(FRET2);
                thresh=graythresh(pix2);
                bwFRET=im2bw(FRET2,thresh);

                CFPm=immultiply(CFP_reg,BW);
                pix=nonzeros(CFPm); % all pixel values in freehand ROI
                low=double(min(pix))/65536; % lowest intensity
                high=double(max(pix))/65536; % highest intensity
                CFPm=imadjust(CFPm,[low high],[]);
                CFP2=imtophat(CFPm,strel('disk',StrelSize)); % 3 looks better than 2
                pix2=nonzeros(CFP2);
                thresh=graythresh(pix2);
                bwCFP=im2bw(CFP2,thresh);

                bw2=bwCFP+bwFRET;
                bw2=bwareaopen(bw2,4);
                imshow(bw2)
                pause
                bw_all=bw2;

                MeanCFP(T,R-1)=mean(nonzeros(immultiply(CFPm,bw2)));
                MeanFRET(T,R-1)=mean(nonzeros(immultiply(FRETm,bw2)));
                Size(T,R-1)=length(nonzeros(bw2));

```

```

otherwise
    FRETm=immultiply(FRET,BW);
    pix=nonzeros(FRETm); % all pixel values in freehand ROI
    low=double(min(pix))/65536; % lowest intensity
    high=double(max(pix))/65536; % highest intensity
    FRETm=imadjust(FRETm,[low high],[]);
    FRET2=imtophat(FRETm,strel('disk',StrelSize));
    pix2=nonzeros(FRET2);
    thresh=graythresh(pix2);
    bwFRET=im2bw(FRET2,thresh);

    CFPm=immultiply(CFP_reg,BW);
    pix=nonzeros(CFPm); % all pixel values in freehand ROI
    low=double(min(pix))/65536; % lowest intensity
    high=double(max(pix))/65536; % highest intensity
    CFPm=imadjust(CFPm,[low high],[]);
    CFP2=imtophat(CFPm,strel('disk',StrelSize)); % 3 looks better than 2
    pix2=nonzeros(CFP2);
    thresh=graythresh(pix2);
    bwCFP=im2bw(CFP2,thresh);

    bw2=bwCFP+bwFRET;
    bw2=bwareaopen(bw2,4);
    %
    %     imshow(bw2)
    %     pause

    MeanCFP(T,R-1)=mean(nonzeros(immultiply(CFPm,bw2)));
    MeanFRET(T,R-1)=mean(nonzeros(immultiply(FRETm,bw2)));
    Size(T,R-1)=length(nonzeros(bw2));

    bw_all=or(bw_all,bw2);
end

end

Ratio_sm_all=immultiply(Ratio_s,bw_all);
imwrite(Ratio_sm_all,sprintf('RatioAllT%03d.tif',T),'Compression','none')

end

Ratio=MeanFRET./MeanCFP;

%% Calculate Ratios

Regions=size(Ratio,2);
Ratio_min=min(Ratio);
Ratio_max=max(Ratio);
Diff=Ratio_max-Ratio_min;
for i=1:length(time);
    Frac(i,:)=(Ratio(i,:)-Ratio_min)./Diff;
end
%% Calculate means
Ratio_mean=mean(Ratio,2);
Ratio_err=std(Ratio,0,2)/sqrt(Regions);
Frac_mean=mean(Frac,2);
Frac_err=std(Frac,0,2)/sqrt(Regions);

```

B.10 Generating Ratio vs. Time Plots for a Movie

Contents

- [Make Ratio vs. Time plots for each timepoint in an experiment](#)
- [Make and save a Ratio vs. Time plot](#)
- [Create and save a plot for each timepoint](#)

Make Ratio vs. Time plots for each timepoint in an experiment

Sequential Ratio vs. Time plots can be made into a movie using ImageJ. This movie can be combined with another movie (such as a movie of cells pseudocolored by FRET ratio), and they can be played simultaneously. First, the MATLAB workspace should contain a vector named "time" that contains the time at each acquisition. The workspace should also contain an array named "Ratio" that contains the FRET ratio of each ROI at each timepoint. Each column contains the FRET ratios of one ROI; each row contains the data at a different timepoint.

```
whos time
whos Ratio
```

Name	Size	Bytes	Class	Attributes
time	1x50	400	double	

Name	Size	Bytes	Class	Attributes
Ratio	50x5	2000	double	

Make and save a Ratio vs. Time plot

The plot axes and labels should be identical in all the plots. One way to do this is to plot all the timepoints and use the `plottools` command to edit the plot. Then, go to the File drop-down menu and "Generate Code..." This will create a new MATLAB function that contains the code to make the same plot. The example below plots all the data.

```
% Create a new figure
figure1 = figure('InvertHardcopy','off','Color',[1 1 1]);

% Create axes
axes1 = axes('Parent',figure1,'LineWidth',1,'FontSize',12);

% Set x and y limits of axes
xlim(axes1,[0 1200]); % time
ylim(axes1,[1.5 4.5]); % FRET ratio

% Make a box around the the plot
box(axes1,'on');
hold(axes1,'all'); % Don't change the plot axes to fit the data

% Plot the FRET ratio of each ROI over time. Put a marker at every
% timepoint and connect them with a line.
plot(time,Ratio,'Marker','o','LineWidth',1,'Parent',axes1);

% Create title
```

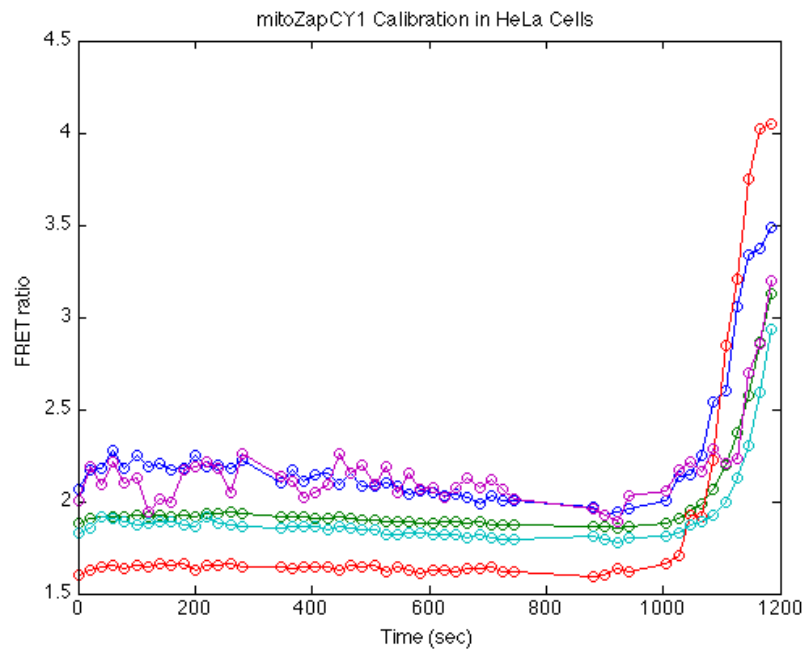
```

title('mitoZapCY1 Calibration in HeLa Cells','FontSize',12);

% Create ylabel
ylabel('FRET ratio','FontSize',12);

% Create xlabel
xlabel('Time (sec)','FontSize',12);

```



Create and save a plot for each timepoint

A "for loop" is used to make and save a new plot at each timepoint. These plots are numbered sequentially and will be saved in the same folder.

```

for t=1:length(time)

% Create a new figure
figure1 = figure('InvertHardcopy','off','Color',[1 1 1]);

% Create axes
axes1 = axes('Parent',figure1,'LineWidth',1,'FontSize',12);

% Set x and y limits of axes
xlim(axes1,[0 1200]); % time
ylim(axes1,[1.5 4.5]); % FRET ratio

% Make a box around the the plot
box(axes1,'on');
hold(axes1,'all'); % Don't change the plot axes to fit the data

```

```
% Plot the FRET ratio of each ROI over time, but only timepoints from 1
% to t. Put a marker at every timepoint and connect them with a line.
plot(time(1:t),Ratio(1:t,:), 'Marker', 'o', 'LineWidth', 1, 'Parent', axes1);

% Create title
title('mitozapCY1 Calibration in HeLa Cells', 'FontSize', 12);

% Create ylabel
ylabel('FRET ratio', 'FontSize', 12);

% Create xlabel
xlabel('Time (sec)', 'FontSize', 12);

% Save figure as a .pdf
print(gcf, '-dpdf', sprintf('Plot%02d.pdf', t));

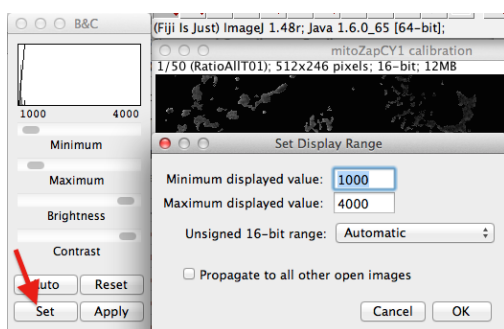
% Close the figure
close all

end
```

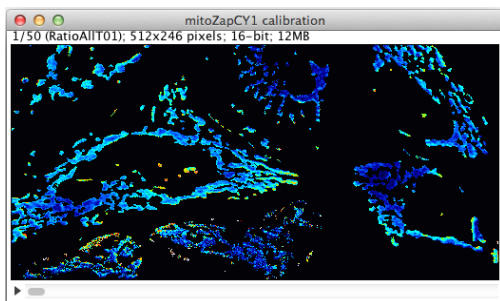
B.11 Techniques for Finishing Movies in ImageJ

Section B.8 describes how to use MATLAB to create set of images in which pixel values correspond to the FRET ratio. This protocol describes how to make this set of images into a movie.

- (1) Import the images as an Image Sequence... into ImageJ. These images should be 16-bit images. Adjust the contrast to the appropriate FRET ratio range by clicking on the Set button on the Brightness/Contrast window. The pixel value 1000 corresponds to a FRET ratio of 1; the pixel value 4000 corresponds to a FRET ratio of 4.

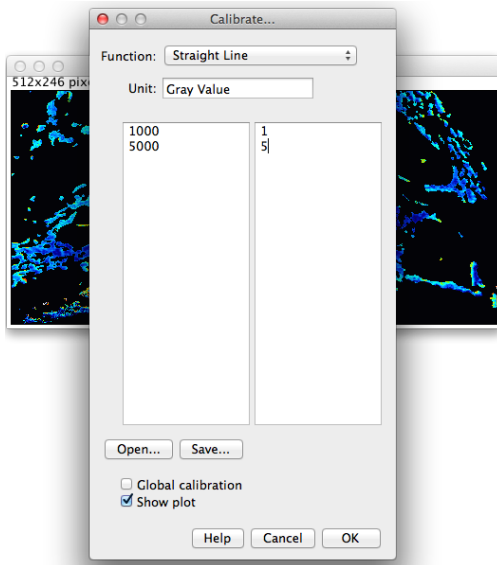


- (2) Select a lookup table to pseudocolor the images. By default, the images will be grayscale. To change the lookup table, go to the Image drop-down menu and select Lookup Tables. In this example, the royal lookup table was applied to the images.

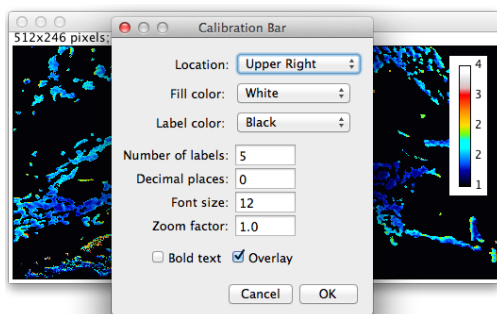


- (3) Create a calibration bar. I usually create a duplicate image in which to add the calibration bar so that I can place the calibration bar next to the movie in my presentation slide. Duplicate the image by going to the Image drop-down menu and selecting Duplicate... Then, go to the Analyze drop-down menu and select Calibrate... Enter the calibration

function as shown here:

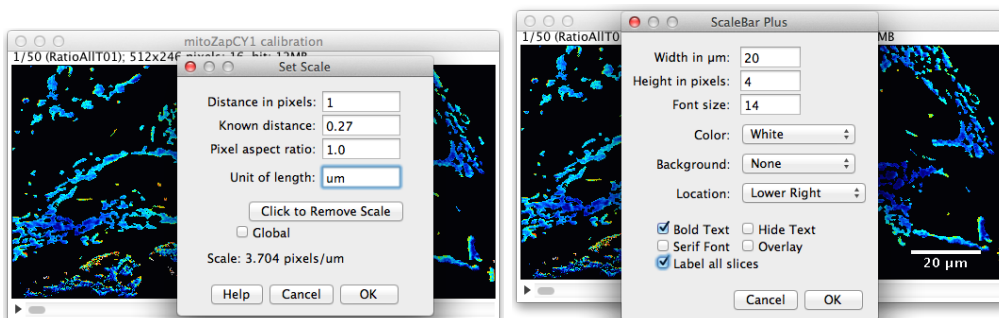


Go to the Analyze drop-down menu, select Tools, then select Calibration Bar...



Convert the image with the calibration bar from 16-bit to RGB Color by going to the Image drop-down menu and selecting Type. Save this image as a .png to preserve the color information.

- (4) Add a scale bar. Select the *stack* of radiometric images before going to the go to the Analyze drop-down menu and selecting Set Scale... Next, go to the Analyze drop-down menu, select Tools, then select Scale Bar...



- (5) Time-stamp images within the stack. Before performing this step, you may want to convert the stack to RGB Color and save it as a .tiff file. To save the image stack, go to the File drop-down menu, select **Save As**, and then select **Tiff...** This will save the stack of images in one .tiff file.

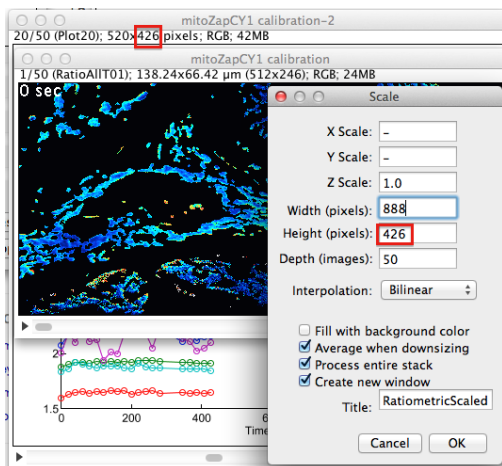
In this example, I am using the **Series Labeler** macro that can be found in the **Images** drop-down menu under **Stacks**.



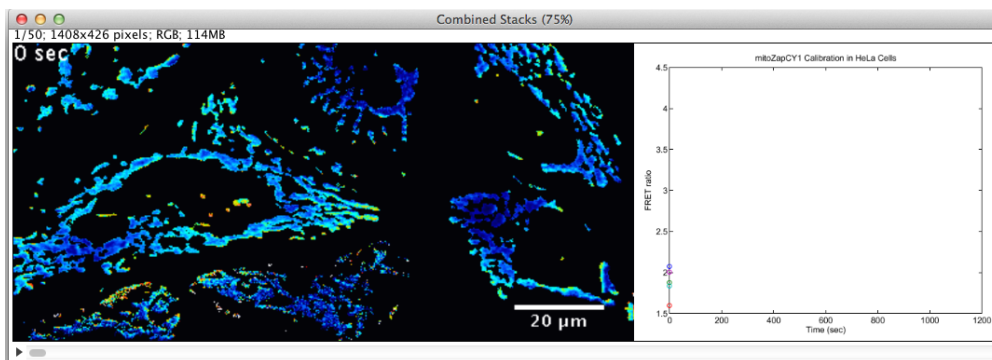
- (6) Save the image stack as an .avi file.
- (7) Make another movie that shows the ratiometric movie and a series of plots at the same time (refer to Section B.10 to see how this was done). Crop the image stack if necessary by first drawing a rectangle and then selecting **Crop** from the **Image** drop-down menu.

The ratiometric movie stack and the stack of plots must be the same dimensions in order to make them into one movie. In this example, I scaled the ratiometric movie stack to be the same height as the stack of plots (**Scale...** under the **Image** drop-down menu). Adjust

the Width (pixels) until the Height (pixels) matches that of the other stack (outlined in red).



- (8) The last step is to combine the two movies. Go to the Image drop-down menu, select Stacks, then Tools, then Combine... The combined movie will look like this:



Save the movie as an .avi file.

Appendix C

Miscellaneous Protocols

C.1 Making Imaging Dishes

Step 1: Use an industrial-strength hole punch to make a 0.375 inch hole in the bottom of a 35 mm cell culture dish, and then place the dish bottom-up.

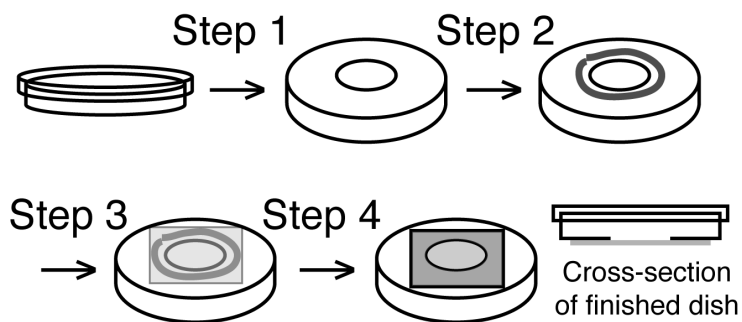
Step 2: Use an 18-gauge needle and syringe to judiciously apply pre-mixed SYLGARD 184 around the hole.

Step 3: Place a glass coverslip on top of the glue.

Step 4: Gently press down on the glass coverslip to remove air bubbles and to spread out the glue. Let the glue cure at room temperature for 48 hours or for 2–3 hours at 60 °C.

Step 5: Sterilize the dish with 70% ethanol and UV light.

Constructed dishes can be coated with reagents, such as polylysine, that improve the adherence of some cell types.



C.2 Widefield Microscopes Used in This Study

Many different microscopes are capable of capturing high-quality data from cells expressing genetically-encoded biosensors, but for most applications, a properly-equipped epifluorescence microscope generates excellent data. This system should be equipped with a mercury or xenon arc lamp and power supply, excitation and emission filters, dichroic mirrors, neutral density filters, plan apochromatic objectives, and a cooled CCD camera. Our laboratory uses two different epifluorescence microscopy systems, which are described in Figure C.1 and Table C.1. The filter sets used to image CFP/YFP biosensors are specified in Table C.2. Sputter-coated ET or brightline filters that provide high transmission will give rise to the brightest images.

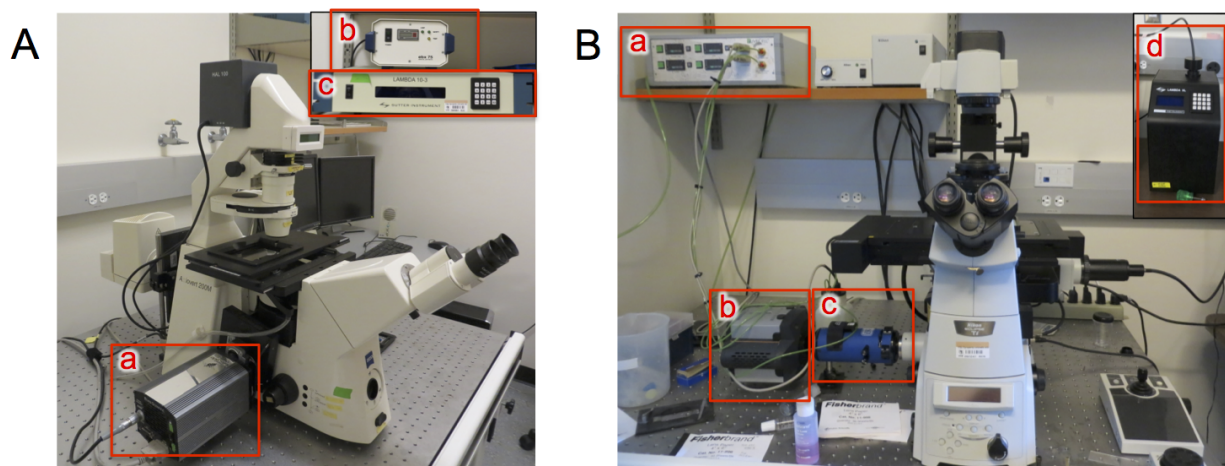


Figure C.1: Two widefield imaging systems used in this work. A) Zeiss Axiovert 200M inverted fluorescence microscope with the following components: a) a CCD camera, b) a Xenon arc lamp, and c) a filter wheel and shutter control system. B) Nikon Eclipse TiE inverted microscope with a) stage-top environmental chamber controlling temperature, %CO₂, and % humidity, b) an EMCCD camera, c) an emission splitting system for simultaneous imaging of YFP FRET and CFP emission, and d) a plasma light source with a liquid light guide. Refer to Table C.1 for further details.

Table C.1: Components of two widefield imaging systems used for CFP/YFP FRET sensors. These systems are pictured in Figure C.1.

	Zeiss Axiovert 200M	Nikon Eclipse Ti
Lamp	Xenon XBO 75 lamp (Zeiss)	Lambda XL with liquid light guide (Sutter Instruments)
Camera	Cascade 512B (Photometrics)	iXon3 EMCCD (Andor)
Objectives	20X air 40X oil 100X oil	20X air 60X oil
Software	MetaFluor (Molecular Devices)	NIS-Elements (Nikon)
Other	Lambda 10-3 filter wheel and shutter control system (Sutter Instruments)	DV2 emission splitting system (Photometrics) Perfect Focus System (Nikon) LiveCell Stage Top Incubation System (Pathology Devices)

Table C.2: Typical acquisition parameters for CFP/YFP FRET sensor imaging.

	YFP FRET	CFP (donor)	YFP (acceptor)	BF-DIC
Excitation filter	430/24	430/24	495/10	340/26
Emission filter	535/20	470/24	535/20	Open
Neutral density filter	1.3	1.3	1.3	N/A
Dichroic	450	450	515	Analyzer Trans
Gain	4X	4X	4X	1X
Transfer speed	1 MHz	1 MHz	1 MHz	1 MHz
Exposure time (ms)	200	200	200	300

C.3 Creating Stable Cell Lines With the PiggyBac System

C.3.1 Introduction

The PiggyBac system consists of two mammalian expression plasmids: a plasmid encoding the PiggyBac transposase (PB vector) and another plasmid encoding the gene of interest flanked by inverted repeats, which are recognized by the PB transposase. When the two plasmids are

co-transfected into a cell, the PB transposon is integrated into the cellular genome while the PB transposase expression is transient. Stable cells are blasticidin-resistant.

The protocol used to create a stable HeLa cell line expressing NES-ZapCV2 is included in the last section.

C.3.2 PiggyBac Transposon Cloning

The Liu laboratory kindly provided us with the PiggyBac plasmids. We have not sequenced the plasmid. However, we have successfully used the *EcoRI* and *SalI* restriction sites to clone FRET sensors into the plasmid:

$$5'—EcoRI—Gene\ of\ Interest—SalI—3'$$

C.3.3 Co-transfection of PB plasmids

Co-transfect both PB plasmids into the mammalian cell line of choice. I have used a 1:1 (mass) ratio of PB transposase: transposon plasmid, but some protocols indicate that you should transfect more of the transposon than the transposase.

The cells should express the gene of interest in 24-48 hours.

C.3.4 Selection with blasticidin

Begin the selection 48–72 hours after transfection. First, trypsinize the transfected cells, spin them down, and resuspend them in complete media containing blasticidin. Use the lowest concentration of blasticidin that will kill your untransfected cells within 2–3 days. Plate them in a fresh dish/flask (determine the size based on the number of cells you have).

You can perform the same selection on cells that weren't transfected (and shouldn't be blasticidin-resistant) to make sure that they all die within 2–3 days.

A second round of selection can be performed if necessary. Blasticidin treatment can mess up some cellular phenotypes. Cells could be sorted instead of (or in addition to) being selected.

Maintain stable cell lines in complete media without blasticidin.

C.3.5 Example: HeLa NES-ZapCV2 cell line

PB-NES-ZapCV2 cloning strategy

Primers used to add *Eco*RI and *Sal*I restriction sites to NES-ZapCV2:

PB-FRET-5'- *Eco*RI

ggaattgaattcaacttaagcttggtagccgag

PB-FRET-3'-*Sal*I (gaattc in the end of the reading frame is mutated to gaatcc)

gaagcgGTCGACcactgtgctggatatctgcaggattc

Sequence of NES ZapCV2 in pcDNA3.1 The primer annealing sequences are italicized.

ggagaccaagctggctagcgttta aacttaagcttggtagccgag
catgcttcaacttctcctcttgaacgttactctttcggatcccatggtgagcaagggcgaggagctgttcacc
gggtggtgcccatcctggtcgagctggacggcgacgtaaacggccacaggttcagcgtgtccggcgagggcgagg
gcatgccacctacggcaagctgacctgaagttcatctgcaccaccggcaagctgcccgtgcctggcccacct
cgtgaccacctgacctggggcgtgcagtgttcagccgctaccccaccacatgaagcagcagcacttcttcaag
tccgcatgcccgaaggtacgtccaggagcgtaccatcttctcaaggacgacggcaactacaagacctgcgccg
aggtgaagttcgagggcgacacctggtgaaccgcatcgagctgaaggcatcgacttcaaggaggacggcaacat
cctggggcacaagctggagtacaactacatcagccacaacgtctatatcaccgccgacaagcagaagaacggcacc
aagcccacttcaagatccgccacaacatcgaggacggcagcgtgcagctcgccgaccactaccagcagaacaccc
ccatcgccgacggccccgtgctgctgcccgacaaccactacctgagcaccagtcggcctgagcaaagaccccaa
cgagaagcgcgatcacatggtcctgctggagttcgtgaccgccgcccgcagcgcataaaaacaatgacttaaaacac
aatggaagaatgtcctgagcttctgtagctcactatttgacctacaagacatctttgaaggatcatgtctctc
aagatttcaaacacctatggaaccattagctcataattgggaggactgtgatttccttgagatgatacatgttc
catagtgaaacctatattaattgtcaacatggtatcgagctcatggacggcggcgtgcagctcgccgaccactaccag
cagaacacccccatcgccgacggccccgtgctgctgcccgacaaccactacctgagctaccagtcggcctgagca
aagaccccaacgagaagcgcgatcacatggtcctgctggagttcgtgaccgccgcccgggatcactctcgccatgga
cgagctgtacaaggtggcagcgggtggcatggtgagcaagggcgaggagctgtcaccggggtggtgccatcctg

gtcgagctggacggcgacgtaaacggccacaagttcagcgtgtccggcgagggcgagggcgatgccacctaaggca
agctgaccctgaagctgatctgcaccaccggcaagctgccctgcctggcccaccctcgtgaccaccctgggcta
cggcctgcagtgttcgcccgtaccccgaccacatgaagcagcagacttcttcaagtccgcatgccgaagge
tacgtccaggagcgcaccatcttcttcaaggacgacggcaactacaagaccgcccaggtgaagttcgagggcg
acacctggtgaaccgcatcgagctgaaggcatcgacttcaaggaggacggcaacatcctggggcacaagctgga
gtacaactacaacagccacaacgtctatatcaccgccgacaagcagaagaacggcatcaaggccaacttcaagatc
cgccacaacatcgagtaa *gaattctgcagatatccagcacagtgg*

PCR protocol*PCR mix:*

40.5 μ l water

5 μ l 10X Pfu buffer

1 μ l 25 μ M forward primer

1 μ l 25 μ M reverse primer

1 μ l 10 mM dNTPs

0.5 μ l template (pcDNA3-NES-ZapCV2)

1 μ l homemade Pfu

Thermal cycler program:

98 °C 2 min

30 cycles: (98 °C 20 sec; 60 °C 30 sec (usually 60-65 °C works); 72 °C 2 min)

72 °C 10 min

There were two major bands: 600 and 1700 bp. The 1700 bp band was gel-purified, digested with *Eco*RI and *Sal*I, and ligated into the PB transposase plasmid (which was digested with the same enzymes and treated with phosphatase).

Transfection Both of the PB plasmids were midipreped and resuspended at a concentration of 0.5 μ g/ μ l. A T25 flask of HeLa cells in complete media, at 30% density, was transfected with both plasmids using Lipofectamine LTX with Plus Reagent (Life Technologies).

1.5 mL OptiMEM was mixed well with 2 μ g of each PB plasmid (4 μ g total) and 4 μ l Plus reagent. After a 5 min incubation at room temperature, 11.25 μ l LTX reagent was added and the solution mixed well by pipetting. After a 30 min incubation, the mixture was added drop-by-drop to the T25 flask of HeLa cells. The media was changed 5 hours later.

The transfected cells were fluorescent when they were checked 2 days later. Most of them were dim.

Selection The optimal blasticidin concentration was determined by plating untransfected cells in complete media with different blasticidin concentrations (2-12 μ g/mL). 6 μ g/mL blasticidin

was sufficient to kill all the cells in 2 days.

4 days after transfection, the HeLa cells were trypsinized and transferred to a fresh T25 flask in complete media supplemented with 8 $\mu\text{g}/\text{mL}$ blasticidin.

Sorting Cells were sorted with FACS using the settings for YFP a week later. There was one major peak of fluorescent cells and very few non-fluorescent cells. About 50% of the cells with strong fluorescence were plated in a 10 cm dish. Aliquots of cells were frozen one passage later.

C.4 Imaging Buffer Recipes

C.4.1 Chelex-treated ultrapure H₂O

Mix 50 g of Chelex 100 resin (sodium form, 50-100 mesh) with 3-4 L of autoclaved ultrapure water (*e.g.* Milli-Q) in a large plastic container on a stir plate for at least 18 h. Let the resin settle to the bottom of the container for several hours. Use a bottle-top filter to remove all Chelex from the water, and store the filtered water in a plastic container. The resin can be reused several times.

C.4.2 Hank's Balanced Salt Solution (HBSS), Life Technologies Formulation

We purchase a 10X concentrated solution of HBSS, pH 7.4.

	Final Concentration (mM)
CaCl ₂	1.26
MgCl ₂ -6H ₂ O	0.49
MgSO ₄ -7H ₂ O	0.41
KCl	5.33
KH ₂ PO ₄	0.44
Na ₂ HPO ₄	0.34
NaHCO ₃	4.17
NaCl	137.93
Dextrose	5.56

C.4.3 HEPES-buffered HBSS (HHBSS), pH 7.4

10X HBSS (Life Technologies) is diluted to 1X with Chelex-treated water and supplemented with 20 mM HEPES and 2 g/L glucose. This buffer is routinely used for imaging experiments, with the exception of sensor calibrations.

	Final Concentration (mM)
CaCl ₂	1.26
MgCl ₂ -6H ₂ O	0.49
MgSO ₄ -7H ₂ O	0.41
KCl	5.33
KH ₂ PO ₄	0.44
Na ₂ HPO ₄	0.34
NaHCO ₃	4.17
NaCl	137.93
Dextrose	16.8
HEPES	20

C.4.4 HHBSS without Ca²⁺, pH 7.4

10X HBSS without Ca²⁺ or Mg²⁺ (Life Technologies) is diluted to 1X with Chelex-treated water and supplemented with 0.49 mM MgCl₂, 0.45 mM MgSO₄, 20 mM HEPES, and 2 g/L glucose. This buffer is used when depleting cells of Ca²⁺.

	Final Concentration (mM)
CaCl ₂	–
MgCl ₂ -6H ₂ O	0.49
MgSO ₄ -7H ₂ O	0.45
KCl	5.33
KH ₂ PO ₄	0.44
Na ₂ HPO ₄	0.34
NaHCO ₃	4.17
NaCl	137.93
Dextrose	16.8
HEPES	20

C.4.5 HHBSS without phosphate

This buffer is used during Zn^{2+} sensor calibrations or perturbations with Zn^{2+} because phosphate will precipitate and change the concentration of Zn^{2+} .

	Final Concentration (mM)
$\text{MgCl}_2 \cdot 6\text{H}_2\text{O}$	1.1
KCl	5.4
NaCl	137
HEPES	20
CaCl_2	1.26
Dextrose	16.8

C.4.6 Krebs-Ringer Buffer with HEPES, pH 7.4

This buffer is used during imaging of MIN6 cells. Dextrose concentration is adjusted with a 1M dextrose solution.

	Final Concentration (mM)
NaCl	130
KCl	4.8
CaCl_2	2
MgSO_4	1.2
HEPES	10
KH_2PO_4	0
NaHCO_3	5
BSA	0.10%
D-glucose	2

C.4.7 Alternative buffer for MIN6 Imaging, pH 7.4

	Final Concentration (mM)
NaCl	138
KCl	5
CaCl ₂	2
MgSO ₄	1
HEPES	10
D-glucose	0

C.4.8 Preincubation buffer for MIN6 cells, pH 7.4

Cells were incubated in this buffer for an hour before imaging in some experiments.

	Final Concentration (mM)
NaCl	114
KCl	4.7
CaCl ₂	2.5
MgSO ₄	1.2
HEPES	2
KH ₂ PO ₄	1.2
NaHCO ₃	25
BSA	0.02%
D-glucose	3